Experimental and Numerical Modeling in support of a Structural Design Framework for Submarine Pressure Hulls based on Nonlinear Finite Element Collapse Predictions

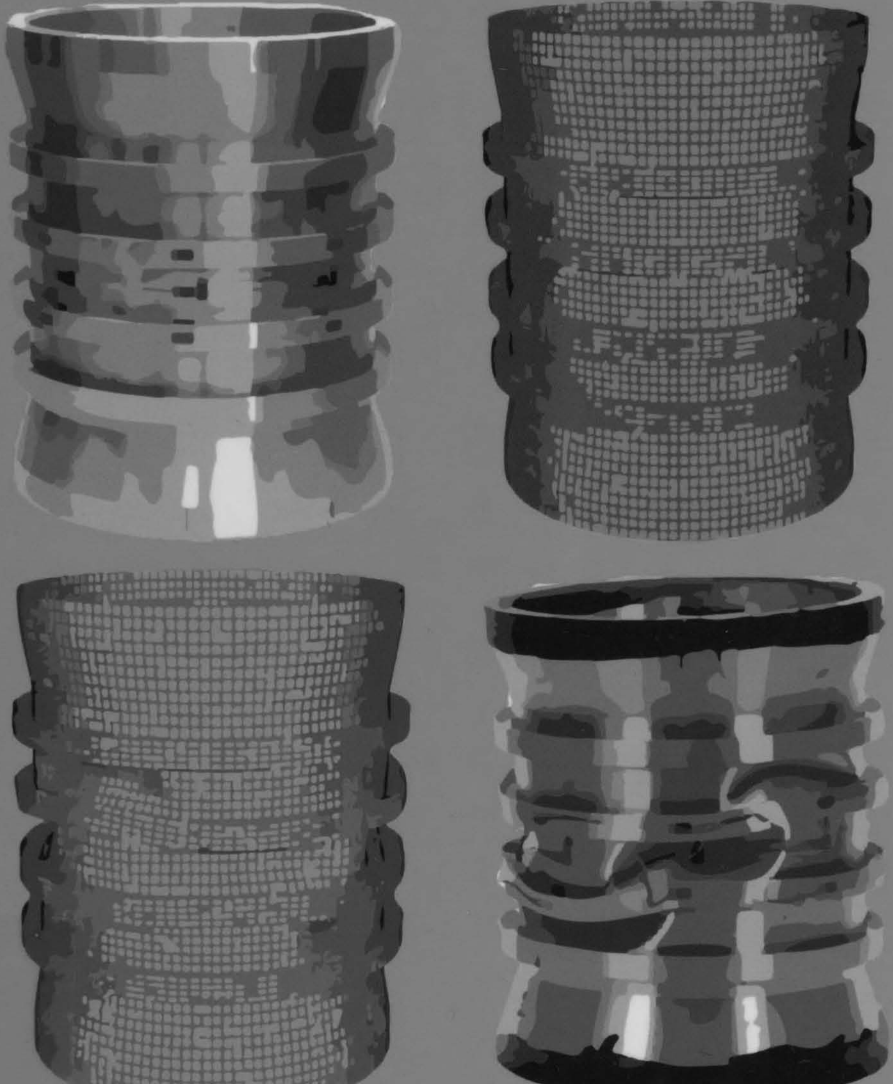

John R. MacKay

Invitation

On Thursday, June 28th, 2012 I will defend my thesis, entitled "**Experimental and Numerical Modeling in support of a Structural Design Framework for Submarine Pressure Hulls based on Nonlinear Finite Element Collapse Predictions**", as well as the accompanying propositions.

The ceremony will take place in the Senaatszaal of Aula auditorium at Delft University of Technology. The cermenony begins at 10:00h exactly.

Before the ceremony, I will present a short summary of my doctoral research. That will take place at 09:30. A reception will be held after the ceremony.

I am pleased to invite you to both the defence ceremony and the reception.

John MacKay
john.mackay@drdc-rddc.gc.ca

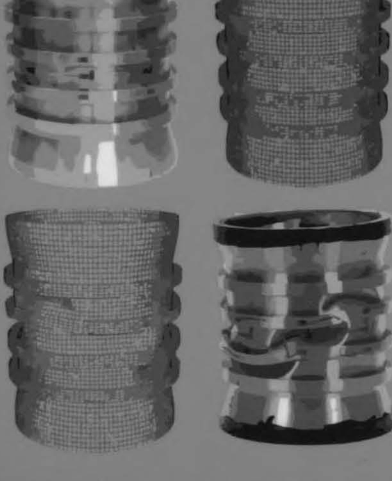

Propositions

accompanying the thesis entitled

Experimental and Numerical Modeling in Support of a Structural Design Framework for Submarine Pressure Hulls based on Nonlinear Finite Element Collapse Predictions

by John R. MacKay

1. Shell buckling predictions are sensitive to shape and material imperfections that are difficult to measure and to model, and will therefore continue to be confounded by non-trivial errors, despite improvements to theoretical and numerical models.
2. The requirement to characterize precisely the shape and condition of a shell, for a given level of accuracy in the buckling prediction, increases with the perfection of the shell.
3. It is impractical (and inappropriate) to develop generally applicable corrosion tolerances for submarine hulls because the effect of corrosion depends on the shape and failure mode of the hull and, furthermore, because an infinite number of corrosion cases can have the same effect on hull strength.
4. It is not enough for the designer (or the design standard developer) to understand the applicable physical processes and models; they must also understand the roles of randomness and uncertainty in order to produce a safe, reliable and efficient design.
5. The design community of naval architects, and other design engineers who must balance performance and safety, is, by necessity, conservative and will therefore continue to be reluctant to embrace new scientific methods.
6. Undue faith is placed in some traditional safety factors, simply because they are long-standing and catastrophic failures have not yet occurred.
7. Experiments are only as valuable as the care that is taken when performing the tests themselves and, even more importantly, when preparing the documentation.
8. Stability, as it applies to economies, polities, ecosystems and the atmosphere, is the critical phenomenon that human societies must understand in order to endure.
9. The increasing trend in the number of PhDs awarded [1] will be curbed by a similar growth in ADHD diagnoses [2].
    - [1] D. Cyranoski, N. Gilbert, H. Ledford, A. Nayar and M. Yahia, The PhD Factory, *Nature* 472 (2011) 276-279.
    - [2] P.N. Pastor and C.A. Reuben, Diagnosed Attention Deficit Hyperactivity Disorder and Learning Disability: United States, 2004–2006, *Vital Health and Statistics* Series 10, No. 237 (2008), National Center for Health Statistics, Hyattsville, Maryland.

These propositions are considered defendable and as such have been approved by the supervisor, Prof. dr. ir. A. van Keulen.

Stellingen

behorend bij het proefschrift getiteld

Experimental and Numerical Modeling in Support of a Structural Design Framework for Submarine Pressure Hulls based on Nonlinear Finite Element Collapse Predictions

door John R. MacKay

1. Het voorspellen van knik van schalen is gevoelig voor vorm- en materiaalonvolkomenheden die moeilijk te meten en te modelleren zijn. Ondanks de verbeteringen in theoretische en numerieke modellen, zullen de voorspellingen verder verstoord worden door niet-triviale fouten.
2. De noodzaak om, voor een bepaald nauwkeurigheidsniveau in het voorspellen van knik, de vorm en de conditie van een schaal precies te karakteriseren, neemt toe met de perfectie van de schaal.
3. Het is niet praktisch (en misplaatst) om algemeen toepasbare corrosietoleranties voor rompen van onderzeeërs te ontwikkelen omdat het effect van corrosie afhankelijk is van de vorm en de bezwijkvorm van de romp en omdat een oneindig aantal corrosiegevallen hetzelfde effect kan hebben op de sterkte van de romp.
4. Het is niet voldoende voor de ontwerper (of de ontwikkelaar van de ontwerpnorm) om de geldende fysische processen en modellen te begrijpen; om met een veilig, betrouwbaar en efficiënt ontwerp te komen, moeten zij ook het effect van variabiliteit en onzekerheid begrijpen.
5. De gemeenschap van scheepsbouwkundigen en andere ontwerpende ingenieurs die prestatie tegen veiligheid moeten afzetten, is per definitie behoudend en zal daarom huiverig blijven om nieuwe wetenschappelijke methodes te omarmen.
6. Er wordt teveel vertrouwd op bepaalde traditionele veiligheidsfactoren, gewoonweg omdat ze al zo lang bestaan en er nog geen catastrofaal falen is opgetreden.
7. Experimenten zijn zo waardevol als de zorg die wordt besteed aan de uitvoering van de tests zelf en, nog belangrijker zelfs, aan het opstellen van de documentatie.
8. Stabiliteit, zoals dat van toepassing is op de economie, bestuursvormen, ecosystemen en de atmosfeer, is het cruciale verschijnsel dat menselijke samenlevingen moeten begrijpen om stand te kunnen houden.
9. De trend om steeds meer PhDs toe te kennen [1] zal worden afgeremd door een vergelijkbare toename van het aantal ADHD diagnoses [2].

   [1] D. Cyranoski, N. Gilbert, H. Ledford, A. Nayar and M. Yahia, The PhD Factory, *Nature* 472 (2011) 276-279.

   [2] P.N. Pastor and C.A. Reuben, Diagnosed Attention Deficit Hyperactivity Disorder and Learning Disability: United States, 2004–2006, *Vital Health and Statistics* Series 10, No. 237 (2008), National Center for Health Statistics, Hyattsville, Maryland.

Deze stellingen worden opponeerbaar en verdedigbaar geacht en zijn als zodanig goedgekeurd door de promotor, Prof. dr. ir. A. van Keulen.

g10431

Experimental and Numerical Modeling
in support of a
Structural Design Framework
for
Submarine Pressure Hulls
based on
Nonlinear Finite Element Collapse Predictions

John R. MacKay

TU Delft Library
Prometheusplein 1
2628 ZC Delft

Experimental and Numerical Modeling in Support of a Structural Design Framework for Submarine Pressure Hulls based on Nonlinear Finite Element Collapse Predictions

Proefschrift

ter verkrijging van de graad van doctor
aan de Technische Universiteit Delft,
op gezag van de Rector Magnificus prof. ir. K.C.A.M. Luyben,
voorzitter van het College voor Promoties,
in het openbaar te verdedigen
op donderdag 28 juni 2012 om 10.00 uur

door John Robert MACKAY

Master of Applied Science in Civil Engineering
Dalhousie University, Halifax, Nova Scotia, Canada

geboren te Summerside, Prince Edward Island, Canada.

Dit proefschrift is goedgekeurd door de promotor:
Prof. dr. ir. A. van Keulen

Samenstelling promotiecommissie:
Rector Magnificus, voorzitter
Prof. dr. ir. A. van Keulen, Technische Universiteit Delft, promotor
Prof. dr .ir. M.A. Gutiérrez De La Merced, Technische Universiteit Delft
Prof. dr. ir. M.L. Kaminski, Technische Universiteit Delft
Prof. ir. J.J. Hopman, Technische Universiteit Delft
Prof. dr. ir. A. de Boer, Universiteit Twente
Prof. J. Arbocz, PhD, Technische Universiteit Delft
Dr. N.G. Pegg, PEng, Defence R&D Canada

Printed by *Ipskamp Drukkers*, Enschede, the Netherlands
Copyright © 2012 by John Robert MacKay

All rights reserved. No part of the material protected by this copyright notice may be reproduced or utilized in any form or by any means, electronic or mechanical, including photocopying, recording or by any information storage and retrieval system, without the prior permission of the author.

ISBN 978-94-6191-345-6

For my parents, Joyce and the late Sinclair MacKay, who instilled in me an appreciation for the value of an education. Also, for my late grandmother, Martha Bruce, a teacher, who assured me that “an education is an easy load to bear.”

Dit proefschrift is goedgekeurd door de promotor:
Prof. dr. ir. A. van Keulen

Samenstelling promotiecommissie:
Rector Magnificus, voorzitter
Prof. dr. ir. A. van Keulen, [illegible]
Prof. dr. ir. M.A. [illegible]
Prof. dr. ir. M.J. [illegible]
Prof. ir. J.J. [illegible]
Prof. dr. ir. A. de Boer, [illegible]
Prof. J. [illegible], PhD, [illegible]
Dr. N.S. [illegible]

Table of contents

Summary iii

Samenvatting...vii

Chapter 1: Introduction 1

Chapter 2: Conventional pressure hull design methods and numerical modeling 13

Chapter 3: Experimental methods for external pressure testing of buckling-critical shells 41

Chapter 4: Experimental study of the effect of corrosion damage on nearly shape perfect pressure hulls.........................77

Chapter 5: Experimental study of the sensitivity of intact and damaged pressure hulls to material strength 107

Chapter 6: Experimental study of the interaction of corrosion damage with pressure hull out-of-circularity 133

Chapter 7: Development of a numerical modeling methodology for pressure hulls 155

Chapter 8: Development of a numerical design framework and partial safety factor for pressure hulls 195

Chapter 9: Conclusions...235

References 249

Acknowledgements 263

Curriculum vitae.. 265

Summary

Background

The pressure hull is the watertight component of a naval submarine that resists external hydrostatic pressure associated with diving. Conventional pressure hulls are constructed of ring-stiffened cylinders and cones, closed with curved domes at the ends. The curved shell structure is fabricated by cold-rolling and welding high-strength steel plates and frames. The design load, shape and slenderness of a pressure hull lead to a mainly compressive stress field, and a critical failure mode associated with structural instability. The plating and frames are proportioned to take advantage of the material strength by preventing instability until yielding occurs. In that way, pressure hull failures combine aspects of elastic buckling and plastic collapse.

The conventional pressure hull design procedure uses simple analytical and numerical models; however, the prediction of hull strength relies on an empirical design curve. The empirical approach is needed to correct a classical buckling solution, which does not account for important factors such as material yielding, residual stresses and geometric imperfections. The design curve is based on hundreds of test results, which cover a range of material strengths, imperfection levels and dimensional scales. It is therefore applicable to a large range of potential hull designs, but the experimental scatter about the curve means that the accuracy is not great. Furthermore, the complexity of the shell equations precludes the derivation of closed form buckling solutions for all but the simplest geometries. Complex hull configurations must be idealized as uniformly ring-stiffened cylinders using the most pessimistic dimensions, giving the conventional design procedure another layer of inherent conservatism.

The current thesis aims to improve upon the conventional analytical-empirical methodology by presenting a design framework that allows pressure hull collapse to be predicted using nonlinear finite element (FE) analysis. FE analysis can accommodate the complex geometry, material, imperfections and structural response of real hulls. Furthermore, FE models can be used to assess the consequences of in-service damage due to, for example, collisions or corrosion, for which the conventional analytical methods are inappropriate. Before FE models can be used in design, modeling rules must be established that allow the collapse pressure to be predicted with controlled accuracy. Furthermore, a partial safety factor

(PSF) needs to be specified in order to account for error in FE collapse predictions. This thesis describes the development of a numerical pressure hull design framework, including FE modeling rules and a PSF.

Methodology

Numerical modeling rules were developed through a combination of literature review, previous experience and modeling studies benchmarked against test results. The numerical methodology is characterized by quasi-static incremental analysis of shell element FE models, including material and geometric nonlinearities. The standard numerical methodology is generally applicable to any FE software, but in the current work FE models were generated using an in-house pre-processor and analyzed using a commercial solver (ANSYS). The accuracy of the numerical methodology was assessed by comparing FE collapse predictions with experimental results.

Forty-seven small-scale ring-stiffened cylinders were tested to collapse in a pressure chamber in order to provide the benchmark test results. The test specimens were machined from alumimium tubing, and covered a range of failure modes, hull configurations, material strengths and geometric imperfections. Many cases of simulated corrosion damage (i.e., localized hull thinning) were also considered in order to study the effect of corrosion on hull strength, and to validate FE models for a type of damage assessment that is routinely required for in-service submarines. The pre-testing shape and material properties of each specimen were carefully measured and used to create high-fidelity FE models. The structural response at critical locations of each specimen was measured using strain gauges in order to assess the experimental failure mode and to provide additional data for validation of the FE models. A new "volume-control" pressure testing method was developed to improve control of specimen deformations, especially near the collapse load. With the volume-control method, the test specimen is pressurized from both the inside and the outside, and the internal pressure is regulated using hoses and valves to achieve the desired net external pressure.

The experiments and numerical modeling were carried out following a verification and validation (V&V) procedure. V&V is a formal way to establish credibility in a numerical model through experimental-numerical comparisons that lead to a quantitative accuracy assessment. In the current work, the experimental-numerical comparisons were fit to a normal probability distribution, which allowed the accuracy of a future FE prediction to be estimated based on a specific level of confidence. The statistical method was also applied to conventional design methods in order to provide a benchmark level of accuracy. The same statistical approach was used to define a PSF for FE collapse predictions.

Results and conclusions

The test results showed that corrosion thinning leads to higher stresses in the damaged area of the pressure hull and destabilizing bending moments under pressure loading. Those effects lead to early yielding and collapse compared to intact hulls. Corrosion damage has a greater effect on hulls failing by overall collapse of the combined shell plating and ring-stiffeners, compared to hulls that fail by interframe collapse of the plating between frames. Interframe-critical hulls have relatively heavy ring-stiffeners that can compensate for some of the loss of stiffness after the corroded shell plating has failed. The reserve strength in the frames is much smaller in overall-critical hulls. Corrosion damage interacts strongly with out-of-circularity (OOC) geometric imperfections, with much greater strength reductions when the corrosion is collocated with an inward, rather than an outward, OOC lobe. Overall collapse pressures in the experimental program were reduced by, on average, 0.85% for each 1% of the hull thinning, for a range of corrosion areas. Sufficient test data were lacking to determine the same relationship for interframe collapse. In any case, since the effect of corrosion damage was found to depend strongly on the hull configuration and OOC, it is not practical to produce generally applicable corrosion "knock-down" curves.

The standard FE methodology is accurate to within 10%, with 95% confidence, based on FE collapse predictions for all 47 test specimens. By comparison, the empirical curve used with the conventional design methodology is accurate to within 20%, with 95% confidence. The FE accuracy is better for hulls with significant geometric perturbations, e.g., corrosion thinning or large-amplitude geometric imperfections (6.2-9.5% accuracy, with 95% confidence), compared to nearly shape-perfect hulls (14% accuracy, with 95% confidence). Collapse predictions for nearly shape-perfect hulls are less accurate since it is difficult to measure and model the smaller defects that contribute to the onset of collapse. Because of that, all FE models, with and without large geometric perturbations, tend to over-predict collapse pressures by approximately 3-4%, on average. The FE models were able to predict the correct failure mode in all cases, and the location of collapse in the majority of cases. The presence of a known geometric perturbation also improves the prediction of collapse location.

A numerical design framework has been proposed, including a PSF to account for error and uncertainty in the FE collapse prediction. It was found that a PSF=1.134 would give the designer 99.5% confidence that the FE error is accounted for. The level of confidence was chosen to align with existing safety margins on fatigue cracking, a similarly catastrophic failure mode. The proposed framework also includes methods for dealing with geometric imperfections and residual stresses at the design stage.

Significance and future work

The proposed design framework would allow the submarine structural designer to base the pressure hull collapse prediction on FE analysis. Unlike conventional design methods, pessimistic idealizations of the complex hull configuration are not required with FE models. The FE approach is also more accurate than the conventional methods. Thus, a numerical design would be at the same time less conservative, more realistic and cover a wider range of possible design configurations than the current design practice. Those factors should lead to more efficient, less costly designs.

On the other hand, engineers responsible for through-life hull maintenance and safety could use FE models to realistically assess the hull capacity in light of measured geometric imperfections and known cases of damage. The as-built OOC magnitude and shape may be significantly less severe than the design assumption. A post-construction re-evaluation of the hull strength using FE models based on the measured shape of the hull could lead to greater operational limits, i.e., deeper diving depths. Furthermore, FE models, unlike conventional design methods, can account for structural redundancy, e.g., due to heavy frames. A numerical assessment may show that out-of-tolerance cases of corrosion damage do not require repair. That could create efficiencies in maintenance costs and schedules.

The test specimens from the current work did not have cold rolling or welding residual stresses, which can influence the collapse pressure of a hull. It has been proposed that an effective stress-strain curve approach can be used to capture residual stress effects in FE models; however, further work is required to validate that method against test results. Furthermore, the validation program should be extended to other pressure hull components like dome ends and watertight bulkheads. Finally, the current validation exercise was performed for a specific numerical methodology and software program (ANSYS). In the future, the experimental database generated for the current work could be used to extend the validation to other FE methodologies and codes.

Samenvatting

Achtergrond

De drukhuid is de waterdichte component van een onderzeeboot die weerstand biedt aan de externe hydrostatische druk geassocieerd met duiken. Conventionele drukhuiden worden gemaakt van met ringen verstevigde cilinders en kegels, afgesloten met dubbel gekromde delen aan de uiteinden. De drukhuid wordt verkregen door het koudwalsen en lassen van hoogwaardige stalen platen en spanten. De belasting, vorm en slankheid van een drukhuid resulteert in een spanningsveld dat wordt gedomineerd door drukspanningen, waardoor instabiliteit (knik) een kritische bezwijkvorm is. De scheepshuid en spanten worden zo geproportioneerd dat er geprofiteerd wordt van de materiaalsterkte en instabiliteit wordt voorkomen totdat er plastische vervorming optreedt. Op deze manier worden in het bezwijken van drukhuiden aspecten van elastische knik en plastisch bezwijken gecombineerd.

De traditionele ontwerpprocedure voor drukhuiden maakt gebruik van eenvoudige analytische en numerieke modellen; de voorspelling van de sterkte van de romp wordt gebaseerd op een empirische ontwerpkromme. De empirische benadering is nodig om een klassieke knikoplossing te corrigeren voor belangrijke factoren als plasticiteit, restspanningen en geometrische imperfecties. De ontwerpkromme is gebaseerd op honderden testresultaten die een scala aan materiaalsterktes, imperfecties en afmetingen omvatten. Hij is daarom van toepassing op een hele serie mogelijke scheepsrompontwerpen, maar de experimentele spreiding rondom de kromme betekent dat de nauwkeurigheid niet groot is. Daarnaast, sluit de complexiteit van de schaalvergelijkingen de afleiding van gesloten vorm knikoplossingen uit voor alle geometrieën behalve de meest eenvoudige. Ingewikkelde rompconfiguraties moeten worden geïdealiseerd als gelijkmatig ringversterkte cilinders met de meest pessimistische afmetingen en op die manier maken zij de conventionele ontwerpprocedure nog conservatiever.

Dit proefschrift tracht de conventionele analytisch-empirische methodologie te verbeteren door een ontwerpkader te presenteren dat het mogelijk maakt om het bezwijken van drukhuiden te voorspellen door gebruik te maken van de niet-lineaire eindige-elementen methode (EEM). EEM kan rekening houden met de complexe geometrie, het materiaal, imperfecties en de structuurresponsie van echte scheepsrompen. Bovendien kunnen EEM modellen worden gebruikt om de gevolgen in te schatten van schade tijdens de levensduur door, bijvoorbeeld, botsingen of corrosie, waarvoor de conventionele analytische methoden niet geschikt zijn. Voordat er bij het ontwerpen gebruik kan worden gemaakt van EEM modellen, moeten er modelleerregels vastgesteld worden die ervoor zorgen dat de bezwijkdruk met een voorgeschreven nauwkeurigheid kan worden voorspeld. Daarnaast dient er een partiële veiligheidsfactor (PVF) te worden gespecificeerd om onnauwkeurigheden in EEM bezwijkvoorspellingen te ondervangen. Dit proefschrift beschrijft de ontwikkeling van een numeriek drukhuidontwerpkader, inclusief EEM modelleringsregels en een PVF.

Methodologie

Er werden numerieke modelleringsregels ontwikkeld door een combinatie van literatuuronderzoek, ervaringen uit het verleden en modelstudies afgezet tegen testresultaten. De numerieke methodologie wordt gekenschetst door quasi-statische incrementele EEM analyses van schaalelementen, inclusief materiaal en geometrische niet-lineariteiten. De standaard numerieke methodologie kan in het algemeen gebruikt worden in combinatie met willekeurige EEM software. In dit proefschrift werden de EEM modellen gegenereerd door een eigen pre-processor en geanalyseerd met een commerciële solver (ANSYS). De nauwkeurigheid werd vastgesteld door EEM bezwijkvoorspellingen te vergelijken met experimentele resultaten.

Er werden zevenenveertig kleine ringverstijfde cilinders in een drukkamer getest op bezwijken om een referentiekader te creeëren. Deze cilinders werden machinaal vervaardigd van aluminium buismateriaal en bestreken een scala aan bezwijkvormen, scheepshuidconfiguraties, materiaalsterktes en geometrische imperfecties. Er werden ook vele gevallen van gesimuleerde corrosieschade (bv. locaal dunner worden van de scheepshuid) bekeken om het effect van corrosie op de sterkte te bestuderen, en om de EEM modellen te valideren voor een type van schadetaxatie die standaard vereist is voor in gebruik zijnde onderzeeboten. Voor iedere test werden de vorm- en materiaaleigenschappen van elk proefstuk gemeten en gebruikt om natuurgetrouwe EEM modellen te creëren. De responsie van de constructie werd gemeten op kritische punten, hierbij gebruik makend van rekstrookjes om de experimentele bezwijkvorm te bepalen en aanvullende informatie te verschaffen voor de validatie van de EEM modellen. Er is een nieuwe “volume-controle” drukproefmethode ontwikkeld om de controle op de vervorming van de proefstukken te verbeteren, vooral dichtbij de bezwijkbelasting. Met de volume-controle methode worden de testcilinders zowel van binnenuit als van buitenaf onder druk gezet en de interne druk wordt vervolgens gereguleerd door middel van slangen en ventielen om de gewenste netto externe druk te bereiken.

Bij de experimenten en numerieke modellering werd een verificatie- en validatie (V&V) procedure gevolgd. V&V is een formele manier om de geloofwaardigheid van een numeriek model vast te stellen door experimenteel-numerieke vergelijkingen die resulteren in een kwantitatieve nauwkeurigheidsbepaling. In dit proefschrift zijn de experimenteel-numerieke vergelijkingen gemodelleerd met een normale waarschijnlijkheidsspreiding, waardoor de nauwkeurigheid van een toekomstige EEM voorspelling geschat kon worden op basis van een specifiek betrouwbaarheidsniveau. De statistische methode is ook toegepast op de conventionele ontwerpmethodes om een referentiekader te hebben voor wat betreft het niveau van nauwkeurigheid. Dezelfde statistische benadering is gebruikt om een PVF te bepalen voor EEM bezwijkvoorspellingen.

Resultaten en conclusies

Het dunner worden door corrosie bleek te leiden tot hogere spanningen in het beschadigde deel en destabiliserende buigende momenten. Deze effecten leiden sneller tot vervormen en bezwijken dan bij intacte scheepshuiden. Corrosieschade heeft een groter effect op scheepshuiden die falen door een *overall* bezwijken van de gecombineerde huidplaten en ringverstijvers, dan op scheepshuiden die falen door *interframe* bezwijken. Interframe-kritische scheepshuiden hebben relatief zware ringverstijvers die kunnen compenseren voor een deel van het verlies aan stijfheid nadat de geroeste huidplaten zijn bezweken. De reststerkte in de spanten is veel kleiner in overall-kritische scheepshuiden. Corrosieschade werkt sterk in op *out-of-circularity* (OOC) geometrische imperfecties, met veel grotere sterkteverminderingen als de corrosie samengaat met een binnenwaartse in plaats van een buitenwaartse OOC lob. Het totaal aan bezwijkdruk in het experimentele programma is verminderd met gemiddeld 0.85% voor elke 1% van het dunner worden van de scheepshuid, voor een scala aan corrosiegebieden. Er waren niet voldoende testgegevens voorhanden om eenzelfde verhouding te bepalen voor interframe bezwijken. Daar het effect van corrosieschade sterk bleek af te hangen van de scheepshuidconfiguratie en OOC, is het in ieder geval niet praktisch om algemeen toepasbare "knock-down" krommes te produceren.

Gebaseerd op bezwijkvoorspellingen voor alle 47 testcilinders is de standaard EEM methodologie tot op 10% nauwkeurig, met een betrouwbaarheid van 95%. Ter vergelijking: de empirische kromme die gebruikt wordt bij de conventionele ontwerpmethodologie is tot op 20% nauwkeurig, met een betrouwbaarheid van 95%. De EEM nauwkeurigheid is beter voor scheepshuiden met significante geometrische imperfecties, b.v. door corrosie of grote geometrische imperfecties (6.2-9.5% nauwkeurigheid, met 95% betrouwbaarheid), dan voor bijna perfecte scheepshuiden (14% nauwkeurigheid, met 95% betrouwbaarheid). Bezwijkvoorspellingen voor bijna perfecte scheepshuiden zijn minder nauwkeurig omdat de kleine imperfecties moeilijk te meten en te modelleren zijn. Hierdoor hebben alle EEM modellen, met en zonder grote geometrische imperfecties, de neiging om de bezwijkdruk te overschatten met gemiddeld ongeveer 3-4%. De EEM modellen waren in staat om in alle gevallen de juiste bezwijkvorm te voorspellen, en de plaats van bezwijken in de meerderheid van de gevallen. Het voorspellen van de plaats van bezwijken wordt ook beter door de aanwezigheid van een bekende geometrische imperfectie.

Er wordt een numeriek ontwerpkader voorgesteld, inclusief een PVF om fouten en onzekerheden in de EEM bezwijkvoorspelling te ondervangen. Een PVF van 1.134 bleek de ontwerper een betrouwbaarheid te geven van 99.5%. Het betrouwbaarheidsniveau werd zo gekozen dat het overeenkomt met bestaande veiligheidsmarges voor wat betreft scheurvorming door vermoeiing, een soortgelijke catastrofale bezwijkvorm. Het voorgestelde kader omvat ook methodes om geometrische imperfecties en restspanningen in het ontwerpstadium aan te pakken.

Betekenis en toekomstig werk

Het voorgestelde ontwerpkader maakt het mogelijk dat de constructief ontwerper van een onderzeeboot de bezwijkvoorspelling van de drukhuid kan baseren op EEM analyse. Anders dan bij conventionele ontwerpmethodes zijn er bij EEM modellen geen pessimistische idealiseringen van de complexe scheepshuidconfiguratie nodig. De EEM benadering is ook nauwkeuriger dan de conventionele methodes. Een numeriek ontwerp is derhalve realistischer, minder conservatief en beslaat tegelijkertijd een groter scala aan mogelijke ontwerpconfiguraties dan de huidige ontwerppraktijk. Deze factoren zouden moeten leiden tot efficiëntere, goedkopere ontwerpen.

Aan de andere kant, kunnen de ingenieurs die verantwoordelijk zijn voor het *through-life* onderhoud van de scheepshuid en de veiligheid ervan, EEM modellen gebruiken om een realistische inschatting te maken van de scheepshuid in het licht van gemeten geometrische imperfecties en bekende schadegevallen. De *as-built* OOC grootte en vorm kan significant minder ernstig zijn dan aangenomen in het ontwerp. Een nieuwe evaluatie van de sterkte na de constructie met EEM modellen gebaseerd op de gemeten imperfecties kan resulteren in een verruiming van de operationele grenzen, b.v. grotere duikdiepten. Bovendien kunnen EEM modellen, in tegenstelling tot conventionele ontwerpmethodes, redundantie in de constructie, door b.v. zware spanten, modelleren. Een numerieke beoordeling kan aantonen dat *out-of-tolerance* door corrosie geen reparatie behoeft. Dit kan zorgen voor een grotere efficiëntie in onderhoudskosten en onderhoudsschema's.

De testcilinders uit dit proefschrift hadden door het koudwalsen of lassen geen restspanningen die de bezwijkdruk beïnvloeden. Er is voorgesteld om een effectief spanning-rekdiagrambenadering te gebruiken om de restspanningseffecten in EEM modellen te modelleren; er is echter verder onderzoek nodig om de resultaten van die methode te valideren. Daarnaast zou dit validatieprogramma moeten worden uitgebreid naar andere componenten van de drukhuid, zoals de uiteinden en de waterdichte scheidingswanden. Ten slotte zij opgemerkt dat de onderhavige validatie-oefening is uitgevoerd voor een specifieke numerieke methodologie en softwareprogramma (ANSYS). In de toekomst zou de experimentele database die voor dit proefschrift is opgesteld gebruikt kunnen worden om de validatie naar andere EEM methodologieën en codes uit te breiden.

[illegible] in het ontwerpstadium aan te passen.

Conclusie en toekomstig werk

Het voorgestelde ontwerpkader maakt het mogelijk dat de constructief ontwerper van een onderzeeboot de bezwijkvoorspelling van de drukhuid kan baseren op EEM analyse. Anders dan bij conventionele ontwerpmethodes zijn er bij EEM modellen geen pessimistische idealisaties van de werkelijke [illegible]configuratie nodig. De EEM benadering is ook nauwkeuriger dan de conventionele methodes. Een numeriek ontwerp is [illegible], realistischer, minder conservatief en biedt [illegible] een grotere reeks aan mogelijke ontwerpconfiguraties dan de huidige ontwerppraktijk. Deze factoren zouden kunnen leiden tot efficiëntere, goedkopere ontwerpen.

Aan de andere kant, kunnen de ingenieurs die verantwoordelijk zijn voor het [illegible] onderhoud van de [illegible] en de veiligheid ervan, EEM modellen gebruiken om een realistische [illegible] te maken van de [illegible] in het licht van gemeten [illegible] imperfecties en bekende schadegevallen. De [illegible] OOC [illegible] kan significant minder

Chapter 1

Introduction

Submarines are, of course, naval vessels that are designed to operate beneath the surface of the ocean. Submarines dive for reasons of stealth, whether acting offensively or defensively against enemy ships, aircraft, and shore-based targets, or for surveillance and espionage purposes. Underwater operation leads to several important differences between submarines and surface ships.

First of all, the tear-drop shape of a typical submarine, as shown in the schematic diagram in Figure 1, is optimized to reduce drag while operating below the surface [1]. By diving, a submarine, like an airplane or airship but unlike a surface vessel, manoeuvres in three-dimensional space. Large changes in the depth of the submarine are made by filling (diving) or emptying (surfacing) large seawater ballast tanks. When the ballast tanks are full, a submarine must be approximately neutrally buoyant, so that it does not tend to rise or fall in the water column. In that way, a submarine is like an airship. On the other hand, small corrections to the submarine's depth are made using hydrodynamic control surfaces that use lift in the same way as an airplane's wing. The control surfaces are also used to steer the submarine, while a propeller or screw provides forward thrust.

Submarines and surface ships also differ with respect to the loading that is applied to the vessel during operations. Surface ships are subjected to transient seawater pressures along the length of the hull that arise due to static (buoyancy) and dynamic (inertia, slamming) effects as the ship interacts with waves. Ballast, fuel, equipment, and stores load the internal ship structure. A ship's hull, decks and bulkheads are designed to resist the external and internal loads locally; more importantly, those structures must act together as a "hull girder" to resist global longitudinal bending moments that govern the ultimate strength of the ship [2].

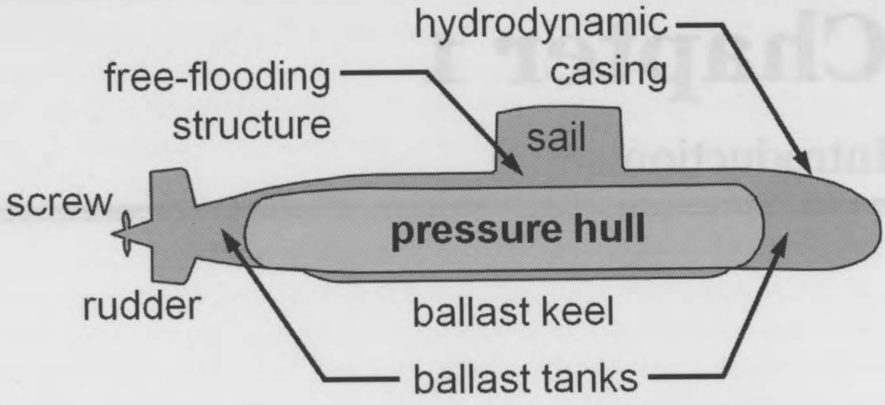

Figure 1: Structural and non-structural elements of a naval submarine.

Wave actions lead to millions of load cycles on a surface ship's hull over its service life. Because of that, fatigue considerations play a major role in structural design. Fatigue damage is exacerbated by slamming, a short-duration high-frequency vibration of the hull due to impact of waves on the bow of the ship [2]. Slamming can also induce whipping, a global vibration of the hull girder that is associated with large bending stresses. Furthermore, slamming can cause local structural damage at the impact location due to large accelerations and high pressures.

Submarines normally operate beneath the waves, so that longitudinal bending, fatigue and slamming are secondary design considerations. Most submarines have an outer hull or casing, as shown in Figure 1, which creates the hydrodynamic form of the submarine and may house the main ballast tanks. The casing is constructed of metal (usually steel) and/or composite material. It is free-flooding, meaning that it becomes filled with seawater while diving so that it is not subjected to a net hydrostatic pressure. The pressure hull, on the other hand, must be watertight since it houses personnel, propulsion machinery, weapons and sensor systems, and other sensitive equipment. Because it is watertight, the pressure hull is subjected to a net hydrostatic pressure when the submarine dives. The static pressure load drives the design of the pressure hull. That is in stark contrast to the design of surface ships, which is driven by dynamic forces and cyclic stresses. Both surface ships and submarines are constructed of plates, shells and beams, but submarine hulls tend to be relatively stocky due to the difference in loading that guides the design of the two types of vessels.

Research submersibles may need to dive several kilometres below the ocean surface [3], but naval submarines typically operate at shallower depths. The nominal diving depths of some submarines that were in service around the world at the time of writing are listed in Table 1. The nominal diving depths are listed as reported in [4]. Actual submarine diving depths are normally a secret due to their strategic importance for military operations. Nonetheless, the data in Table 1 provides a rough order-of-magnitude estimate of submarine diving depths, which can be seen to be measured in the hundreds of metres.

Table 1: Nominal diving depths of some modern submarines [4].

Submarine class	Country	Type[a]	Year[b]	Diving depth[c]
Victoria	Canada	SSK	1991	200 m
Kilo	Russia	SSK	1981	240 m
Ohio	United States	SSBN	1984	244 m
Collins	Australia	SSK	1996	250 m
Lada	Russia	SSK	2010	250 m
Han	China	SSN	1984	300 m
Rubis Améthyste	France	SSN	1983	300 m
Södermanland (A 17)	Sweden	SSK	1989	300 m
Trafalgar	United Kingdom	SSN	1984	300 m
Typhoon (Akula)	Russia	SSBN	1981	300 m
Walrus	Netherlands	SSK	1990	300 m
Delta IV (Delfin)	Russia	SSBN	1984	400 m
KSS-2 (Type 214)	North Korea	SSK	2007	400 m
Tridente (Type 209PN)	Portugal	SSK	2010	400 m
Borey	Russia	SSBN	2010	450 m
Los Angeles	United States	SSN	1977	450 m
Le Triomphant	France	SSBN	1997	500 m
Harushio class	Japan	SSK	1993	550 m
Sierra II (Kondor)	Russia	SSN	1993	750 m

[a] SSK: conventional diesel-electric submarine with anti-submarine warfare capability (some modern SSKs use air-independent propulsion)

SSN: nuclear-powered attack submarine

SSBN: nuclear-powered ballistic missile submarine

[b] Year the first submarine of class was commissioned.

[c] Nominal diving depth, according to [4].

Submarine pressure hull design

Conventional pressure hulls resist the hydrostatic pressure load using ring-stiffened axisymmetric shells fabricated by cold rolling and welding high-strength steel plates and T-section frames (Figure 2). The pressure loading leads to predominantly compressive stresses in those thin-walled structures, so that structural instability tends to govern the design. The ring-stiffeners strengthen the hull so that buckling does not occur until after the material has yielded. In that way, the hull's structural efficiency is optimized by taking full advantage of the material strength (weight optimization is important in the design of a submarine since it must be neutrally buoyant when dived). The critical failure mode of a well-designed pressure hull is therefore elasto-plastic collapse.

The conventional submarine structural design procedure, based on the British naval standard in [5], is described in Chapter 2. Briefly, the designer must predict the collapse pressure of the hull for a variety of failure modes that could occur depending on the relative strengths and proportions of the

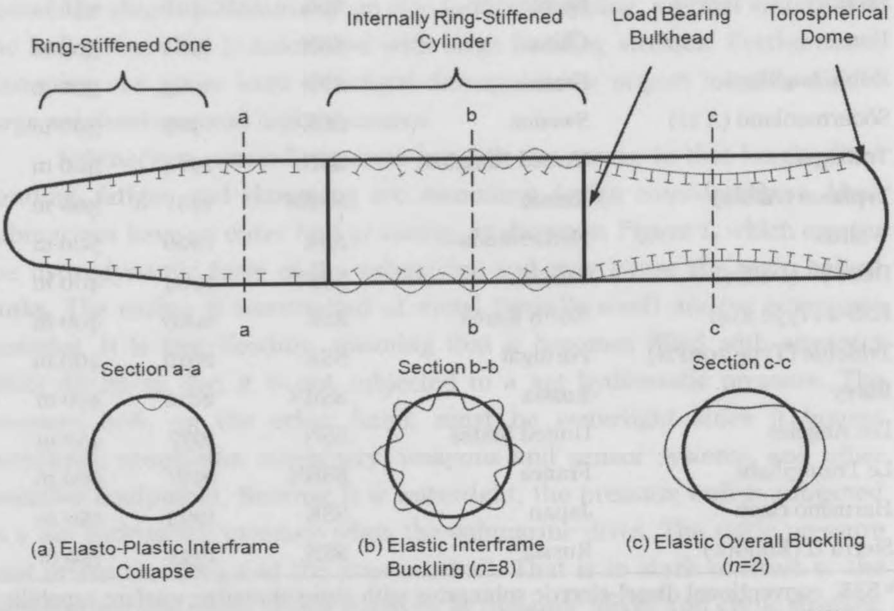
Ring-Stiffened Cone
Internally Ring-Stiffened Cylinder
Load Bearing Bulkhead
Torospherical Dome
a
b
c
a
b
c
Section a-a
Section b-b
Section c-c
(a) Elasto-Plastic Interframe Collapse
(b) Elastic Interframe Buckling (n=8)
(c) Elastic Overall Buckling (n=2)

Figure 2: A compartmentalized pressure hull structure showing a different failure mode in each compartment: (a) inelastic interframe buckling in the left-hand compartment, (b) elastic interframe buckling in the centre compartment, and (c) elastic overall buckling in the right-hand compartment.

hull plating and ring-stiffeners. Typical collapse modes that are important in hull design are shown in Figure 2. The "interframe" collapse strength of the hull plating between ring-stiffeners is predicted using a design curve that corrects classical shell buckling predictions through comparisons with collapse test results (Figure 3). The empirical approach is needed to account for plasticity, residual stresses and geometric imperfections. Those factors significantly influence the interframe hull strength but are not captured by the classical buckling equation. The "overall" collapse strength of the combined hull plating and ring-stiffener section is determined using a nonlinear elasto-plastic finite difference (FD) beam model [8]. Other failure modes, such as sideways tripping of the ring-stiffeners and collapse of dome bulkheads, must also be considered. The empirical interframe design curve and the FD method for overall collapse serve as benchmarks throughout this thesis against which the accuracy of numerical collapse predictions is compared.

Partial safety factors are applied to the collapse prediction for each failure mode in order to account for uncertainties in the hull loading and fabrication, as well as errors associated with the predictive models

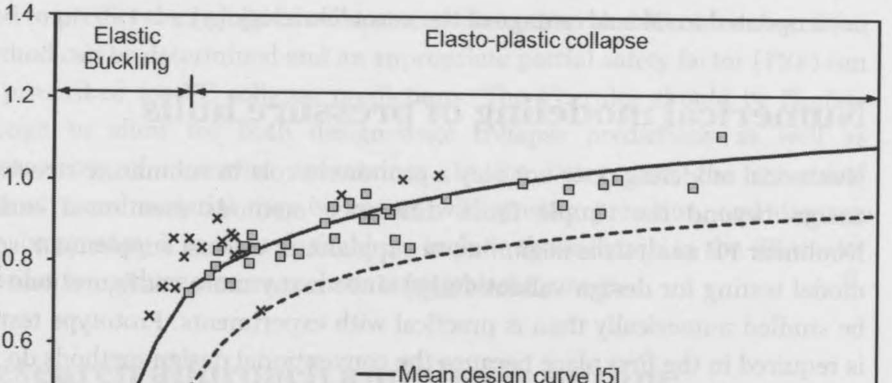

Figure 3: Mean and lower bound empirical knock-down curves for interframe collapse of ring-stiffened cylinders under external pressure.

themselves. The minimum resulting pressure is then converted to a deep diving depth (DDD) by dividing by the specific weight of seawater. DDD is the standard characterization of the submarine's structural strength and operational limit under normal operating conditions.

The conventional pressure hull design practice relies heavily on empirical curves to address the shortcomings of classical equations for shell buckling and yielding. The empirical design approach has been in use since the Second World War [9], with incremental updates to take advantage of new test results [10]. In the 1970s and 1980s, the analytical-empirical methodology was supplemented with simple numerical methods. Axisymmetric finite difference (FD) models allowed hull stresses and elastic buckling pressures to be predicted with greater accuracy [11], and the FD beam model discussed above was introduced to predict collapse for a global failure mode that is neglected by the empirical approach. Those modifications of the design procedure were appropriate for the level of sophistication of the numerical methods and the computing resources of the time. Since then, nonlinear finite element (FE) analysis of thin-walled structures has become well-established and computing power has increased exponentially; however, the submarine structural design philosophy has not been updated to take advantage of the new technology [5].

Numerical modeling of pressure hulls

Numerical modeling does not play a prominent role in submarine structural design beyond the simple finite difference methods mentioned earlier. Nonlinear FE analysis is beginning to supplant, or at least supplement, scale model testing for design validation [5] since many more configurations can be studied numerically than is practical with experiments. Prototype testing is required in the first place because the conventional design methods do not account for interaction between failure modes and between structural components. Nonlinear FE analysis is also used to assess the consequences of denting and corrosion damage to in-service hulls [12,13] since the conventional methodology cannot handle non-axisymmetric geometry and loading. Furthermore, FE models are frequently used in a research context to examine the effects of, for example, residual stresses and geometric imperfections on hull collapse [14-18].

It is desirable to introduce nonlinear FE analysis into the design procedure because it is capable of predicting the elasto-plastic collapse pressure of a pressure hull with complex geometry, imperfections and damage. If due care and attention is paid to the generation and analysis of the FE model, the numerical prediction can inherently consider all failure modes and the interaction between those modes. Furthermore, it will be shown in this thesis that FE predictions are more accurate than the conventional analytical-empirical and numerical methods.

The submarine design community is reluctant to use FE analysis. The developers of the UK submarine design standard cite the lack of FE validation against experiments as a major concern [5]. Designers also consider the experience and expertise required to properly model the hull, perform the collapse analysis, and interpret the results to be prohibitive [5,19]. Furthermore, there is a mistaken belief that the analyst requires some foreknowledge of how and where collapse will occur in order to predict it correctly [19]. In fact, one of the main benefits of the FE method is that the analyst need not have any preconceived notion of how or where the structure will collapse so long as the entire hull is modeled and certain steps are taken to ensure that the relevant failure modes are not neglected.

What is needed to alleviate the current concerns of the design community is a set of FE modeling rules that clearly describes how a pressure hull should be modeled, how the nonlinear analysis should be carried out, and how the results should be interpreted. Those rules must be used to predict the results of collapse experiments so that the accuracy of the method can be determined and an appropriate partial safety factor (PSF) can be prescribed for FE collapse predictions. The FE rules should be flexible enough to allow for both design-stage collapse predictions as well as assessments of in-service submarines. In the latter case, the structural geometry and material may be known with greater precision, and damage may be present; it is often desirable to include those details in the FE model in order to produce a more realistic strength assessment.

Research approach and thesis outline

The goal of this thesis is to establish a path to modernize submarine design philosophy through the incorporation of nonlinear FE analysis. The design community is reluctant to use FE analyses due to a lack of generally applicable modeling rules, and because the accuracy of the method has not been established by comparing FE predictions with test results. This thesis aims to address both of those concerns through a carefully conducted experimental program, complementary FE simulations, and a statistical analysis of the experimental-numerical results leading to a partial safety factor for design. The outcome of those tasks is a pressure hull design framework based on FE analyses, including FE modeling rules that are compatible with the PSF.

It is not being suggested that the conventional design procedure should be completely replaced. Rather, it is the hope of the author that nonlinear FE analysis will complement the existing analytical-empirical and numerical methods. For example, the designer may use the computationally inexpensive conventional methods in an initial optimization of the hull configuration. Nonlinear FE analysis may then be used to work out the detailed configuration and determine the final design strength of the hull. Furthermore, FE analysis would give the design authority a much-needed option for realistically assessing the capacity of in-service submarines that have sustained some type of damage.

The majority of the research presented here has been directed at developing FE modeling rules, and validating those rules through a collapse testing program and complementary FE simulations. A variety of hull configurations, failure modes and geometric imperfections were studied experimentally in order to cover a range of cases that may be encountered in design. Each test specimen was a ring-stiffened cylinder – the basic structural element of a pressure hull that tends to govern its structural capacity. Artificial corrosion was applied to some of the test specimens before collapse testing so that the FE methodology could be validated for a type of damage assessment that is likely to arise throughout the service life of a submarine. In fact, the impact of corrosion damage on hull strength is the focus of the chapters dealing with the experiments. Some of the test specimens are shown in Figure 4. Finally, significant effort was directed at investigating how the experimental-numerical comparisons could be used to quantify the accuracy of FE predictions and develop a PSF for design. In that context, this thesis is concerned with how to deal with uncertainty in several areas: error associated with the FE predictions, experimental scatter, and design uncertainty related to the fabrication and loading of the submarine. Those types of uncertainty were overcome in the current work using an approach based on statistics and probability.

Each chapter in this thesis, other than Chapter 1 (Introduction) and Chapter 9 (Conclusions), is adapted from a published, in press or submitted journal article [20-26]. In that way, each chapter is self-contained and can be read in isolation, but there is necessarily some repetition from chapter to chapter, especially in the introductory sections. Nonetheless, it is recommended that each chapter be read in its entirety to avoid unnecessary confusion that may result from skipping sections. Some minor wording changes have been made to the original papers to reflect the organization of

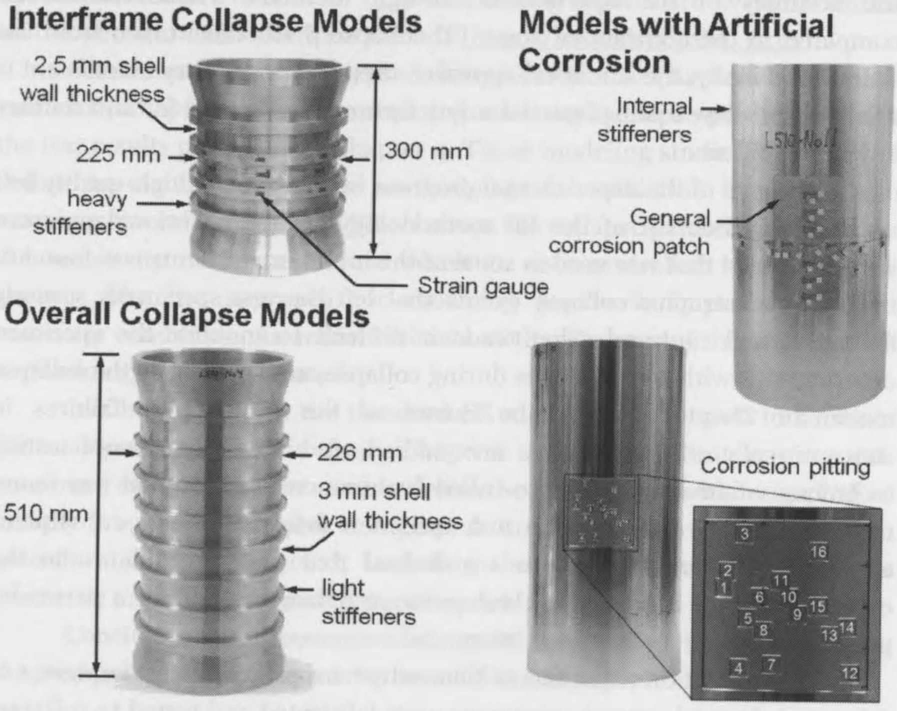
Interframe Collapse Models
2.5 mm shell wall thickness
225 mm
heavy stiffeners
300 mm
Strain gauge
Models with Artificial Corrosion
Internal stiffeners
General corrosion patch
Overall Collapse Models
510 mm
226 mm
3 mm shell wall thickness
light stiffeners
Corrosion pitting
3
16
2
1
11
6
10
9
15
5
8
13
14
4
7
12

Figure 4: Photographs of some typical aluminium test specimens used in the experimental program. Clockwise from top left: a cylinder with external ring-stiffeners that was designed to fail by interframe collapse; an internally stiffened cylinder with a rectangular patch of shell thinning representing general corrosion damage; a cylinder with smaller patches of thinning to simulate corrosion pitting followed by grinding; and an externally stiffened cylinder designed to fail by overall collapse.

this thesis and to maintain a consistent terminology and nomenclature. The abstracts have been retained as the initial paragraph within each chapter.

Chapter 2 [20] describes the conventional submarine pressure hull design procedure that has already been briefly introduced in the current chapter. The results of a survey of the literature, which was conducted to establish standard FE modeling procedures for pressure hulls and related structures, are also presented. That survey, along with the experience of the author and some of his colleagues, served as the starting point for establishing FE modeling rules in Chapter 7. The concept of verification and validation (V&V) of numerical models is also introduced in Chapter 2, and its application to numerical pressure hull predictions is considered. The statistical approach endorsed by the V&V methodology is used to estimate the accuracy of the conventional design methods. Those results are compared to the accuracy of some FE collapse predictions taken from the literature. Finally, the statistical approach used in the accuracy assessment is modified to allow a design partial safety factor to be derived for an arbitrary level of confidence.

The goal of the experimental program was to provide high-quality test results for validation of the FE methodology. The conventional pressure testing method that was used in some of the initial experiments was found to result in catastrophic collapse events that left the test specimens severely deformed and ruptured. That made it difficult to monitor the specimen deformations with strain gauges during collapse, and to identify the collapse mode. In Chapter 3 [21], the causes of the catastrophic failures in conventional testing apparatus are studied, and a novel pressure testing technique is introduced. The so-called "volume-control" method was found to allow better control of the test specimen deformations in subsequent experiments. Simple equations are derived that provide guidance to the experimenter for choosing the best pressure testing method for a particular pressure chamber and test specimen.

The validation experiments themselves are presented in Chapters 4 to 6 [22-24]. In total, 47 test specimens were fabricated and tested to collapse. Each test specimen was a ring-stiffened cylinder machined from aluminium tubing. As mentioned above, artificial corrosion was introduced into some of the test cylinders by locally machining away shell material. Since the as-machined specimens were nearly shape-perfect, some of the cylinders were mechanically deformed to introduce large-amplitude out-of-circularity. Figure 4 shows photographs of typical test specimens.

Chapter 4 [22] presents the results of collapse tests on as-machined cylinders with and without different types of corrosion damage. In Chapter 5 [23], some of the specimens from Chapter 4 are compared with new cylinders manufactured from a lower grade of aluminium in order to study the effect of material properties on intact and damaged hulls. Finally, Chapter 6 [24] looks at the interaction between corrosion damage and out-of-circularity imperfections.

It was not possible to present a detailed specimen-by-specimen description of the experiments in this thesis. Instead, typical examples are described, and the general trends are considered. A comprehensive account of the preparation, measurement and testing of each specimen can be found in the original experimental reports in [27-32]. A master list of test specimens, including key test results, photographs, and links to the relevant documentation is available in [33]. The testing reports are available online on the website of Defence R&D Canada (http://www.drdc-rddc.gc.ca).

The numerical modeling procedures identified in Chapter 2 are further refined in Chapter 7 [25] by comparing numerical collapse predictions with the test results presented in Chapter 4. Those modeling studies were used to define the standard numerical methodology for validation. Chapter 7 also examines the influence of the FE solver on the collapse prediction, as well as the sensitivity of the numerical result to user-controlled aspects of the analysis like the approach for modeling geometric imperfections and boundary conditions. An initial estimate of the accuracy of the standard FE methodology is also presented.

In Chapter 8 [26], the standard FE methodology is used to simulate the collapse experiments from Chapters 5 and 6. The experimental-numerical comparisons are used to derive the FE accuracy and design PSF as initially proposed in Chapter 2. A general framework for a numerical design procedure is also presented, including the prescription of design-stage geometric imperfections and material models.

Conclusions and recommendations for future work that arose during the preparation of this thesis are presented in Chapter 9.

[illegible]

deformations with strain gauges during collapse [illegible]

[illegible]

experimenter for choosing the [illegible]

The validation experiments [illegible] 4 to 6 [22-24]. In total, 47 test specimens were fabricated and tested to collapse. Each test specimen was a ring-stiffened cylinder machined from aluminium tubing. As mentioned above, artificial corrosion was introduced into some of the test cylinders by locally machining away shell material. Since the as-machined specimens were nearly shape-perfect, some of the cylinders were mechanically deformed to introduce large-amplitude out-of-circularity. Figure 4 shows photographs of typical test specimens.

Chapter 4 [22] presents the results of collapse tests on as-machined cylinders with and without different types of corrosion damage. In Chapter 5 [23], some of the specimens from Chapter 4 are compared with new cylinders manufactured from a lower grade of aluminium in order to study the effect of material properties on intact and damaged [illegible]. Finally, Chapter 6 [24] looks at the interaction between corrosion damage and out-of-circularity imperfections.

It was not possible to present a detailed specimen-by-specimen description of the experiments in this thesis. Instead, typical examples are described, and the general trends are considered. A comprehensive account of the preparation, measurement and testing of each specimen can be found in the original experimental reports in [29-32]. A master list of test specimens, including key test results, photographs, and links to the relevant

Chapter 2

Conventional pressure hull design methods and numerical modeling

An overview of current design practices for submarine pressure hulls is presented, along with the results of a survey of the literature that was conducted to determine standard nonlinear numerical modeling practices for those structures. The accuracies of the conventional submarine design formulae (SDF) and nonlinear numerical analyses for predicting pressure hull collapse are estimated by comparing predicted and experimental collapse loads from the literature. The conventional SDF are found to be accurate within approximately 20%, with 95% confidence, for intact pressure hulls. The accuracy of a wide range of nonlinear numerical methods, including axisymmetric finite difference and general shell finite element (FE) models, is found to be within approximately 16% with 95% confidence. The accuracy is found to be within 9% when only higher fidelity general shell FE models are considered. It is shown how the observations taken from the survey could serve as a starting point for establishing modeling guidelines, quantifying the accuracy of nonlinear FE analysis in pressure hull collapse calculations, and introducing this method into a design procedure by way of a partial safety factor. This chapter was originally published as a journal article in *Thin-Walled Structures* with co-authors Fred van Keulen and Malcolm Smith [20].

Introduction

The main load bearing structure in a naval submarine is the pressure hull, which is designed to resist hydrostatic pressure associated with diving. For hydrodynamic considerations, a modern submarine is roughly tear-drop shaped so that its pressure hull is constructed of a series of ring-stiffened cylindrical and conical shells, terminated with torispherical domes at either end, as shown in Figure 2 (p. 4). The design limit state is structural instability whereby the ring-stiffeners forestall buckling of the shell until yielding occurs, so that full advantage of the material strength is realized [34]. The failure mode of a typical pressure hull is therefore elasto-plastic collapse, which combines buckling instability, material plasticity, and nonlinear geometric effects associated with imperfections and large displacements and rotations.

The conventional design of pressure hulls involves a mixture of analytically-derived buckling and yield models, empirical relationships, and simple numerical analyses [5-7]; those methods are collectively referred to as the submarine design formulae (SDF). The SDF were developed for axisymmetric geometries and require simplifying and conservative idealizations of the real structure and structural behaviour to be made by the designer. The design and through-life analysis of pressure hulls could therefore benefit from the introduction of predictive (computational) models for collapse pressure and mode based on more realistic and flexible modeling of geometry, material, imperfections introduced during fabrication and assembly, and in-service damage and loading.

Improved collapse predictions could be achieved by the incorporation of nonlinear finite element (FE) analysis in the design procedure. Nonlinear FE analysis is currently used indirectly in hull design and analysis through the granting of tolerance concessions during fabrication, identifying failure modes and vulnerable regions of in-service structures, determining the effects of damage, and for general research purposes [13-18]. However, despite its widespread informal use and accepted benefits, the direct use of nonlinear FE analysis in the design of pressure hulls is not supported by design codes, primarily due to the lack of knowledge regarding the accuracy of FE collapse predictions [5]. Such knowledge could be derived by comparing experimentally determined collapse pressures and modes with numerical predictions based on a set of pre-defined FE modeling rules.

The goals of the current chapter are: (1) to establish the state of the art of numerical collapse predictions for pressure hulls, (2) to estimate the accuracy of those numerical models, and (3) to develop a method of incorporating numerical methods in pressure hull design codes through a partial safety factor (PSF). The methods used to assess the accuracy of numerical models and to derive a PSF are also applied to conventional analytical-empirical design methods. This is done in order to provide a baseline with which to compare the numerical results against, and in no way suggests that the present design methods should be replaced by numerical modeling. The ultimate goal is to provide an additional tool to the designer: a validated numerical model that can be used directly in design calculations.

Furthermore, while the current chapter provides an estimate of numerical model accuracy by using experimental-numerical comparisons from the literature, it is not being suggested that the resulting PSF reported here should be used as is in a design setting. The current chapter lays the groundwork for how numerical models may be incorporated in design in the future; further experimental and numerical modeling are required in order to properly complete the task.

This chapter is concerned with quantifying the accuracy of predictive methods for pressure hull design. As such, it begins with an overview of verification and validation theory and the metrics that will be used to quantify accuracy. A description of pressure hull design considerations and procedures is then presented, and the accuracy metrics are applied to the conventional design methods in order to provide a baseline to compare the FE results against. FE analyses of pressure hulls reported in the literature are reviewed in order to identify the most-commonly used numerical procedures. The results of that survey are also used to estimate the accuracy of the numerical methods. It is then shown how nonlinear FE analysis could be introduced into a design procedure by way of a partial safety factor. Conclusions and future work are described in the last section of this chapter.

Quantifying model accuracy

This section first presents an overview of the so-called verification and validation (V&V) theory, followed by an explanation of the terminology that will be used in this thesis to describe the accuracy of pressure hull strength predictions.

Verification and validation methods

Considerable effort has been devoted by a number of research groups to establish procedures for quantifying the accuracy of numerical modeling. The V&V procedures were first developed for computational fluid dynamics, but have more recently been applied to computational solid and structural mechanics [35,36]. The goal of the V&V process is to establish the credibility of a given numerical methodology by quantifying its accuracy for making predictions of the response of interest. Credibility is demonstrated by building evidence through the planning and conducting of experiments and numerical analyses, and comparing the results.

V&V is divided into two streams. Verification entails checking for errors in the numerical implementation of the physical model by, for example, comparison with analytical solutions and benchmark problems.

Verification also involves performing convergence studies on, for example, mesh refinement or load increment size. Validation follows verification, and is the process whereby experiments are conducted and compared with numerical results in order to assess the suitability of the physical model, including its numerical implementation, for the problem at hand. A key feature of V&V theory is that both numerical and experimental results contain errors; the experimental result is not considered to be infallible. As such, emphasis is placed on quantifying error in both numerical and experimental outcomes and on planning new, high quality, V&V-specific experiments. The V&V methods will be revisited in Section "Design using nonlinear finite element analysis" (p. 31) when discussing the use of numerical models in pressure hull design.

Accuracy metrics

The modeling uncertainty factor, X_m, is defined as the ratio of a single experimental value to the value predicted by a model [37-39]. The modeling uncertainty factor can be related to loading, material properties, geometry, *etc.*, but in the current context it is associated with the collapse pressure of a pressure hull. The mean value of the modeling uncertainty factor for a sample is referred to as the bias, and is an indication of the systematic modeling error, e.g., due to the inapplicability of the underlying theory of the predictive model. The random component introduced by experimental scatter, including uncertainties regarding the true geometric and material properties of the test model, is called the modeling uncertainty. It is defined by the coefficient of variation (COV) of the modeling uncertainty factor, taken as the standard deviation divided by the bias.

The bias and COV of a sample give an indication of systematic error and the scatter in predictions that can be expected for a given predictive model. However, it is also important to establish the degree of confidence associated with a particular level of accuracy [35,36]. This should take the form of a statistical statement, such as, "The prescribed methodology is accurate to 10% with 95% confidence." That means that the given sample of experimental-numerical comparisons indicates that the discrepancy between a future model prediction and the real value will not be greater than 10%, and furthermore, that there is a 95% probability that the sample that was chosen will reflect the true accuracy of the model. The confidence level may be increased, but there is a penalty to pay in that the predicted accuracy bounds will also increase.

The statistical statement discussed above is related to a prediction interval for X_m. A prediction interval gives the range within which a future value of a random variable is expected for a given confidence level. Prediction intervals are determined using a t-distribution for populations with a normal distribution where the mean and standard deviation can only be estimated from a finite sample. The t-distribution has the same form as the normal distribution, but with heavier tails to account for the uncertainty of using a finite sample. The prediction interval, with a $100(1-\alpha)\%$ confidence level, for a single future experimental-numerical comparison, $X_{m,n+1}$, is given by [40]:

$$\bar{x} - t_{\alpha/2,n-1} s\sqrt{1+1/n} \le X_{m,n+1} \le \bar{x} + t_{\alpha/2,n-1} s\sqrt{1+1/n} \quad (1)$$

Eq. (1) is valid for a sample of X_m from a normal distribution with sample size, n, bias, $\bar{x}$ and standard deviation, s.

Pressure hull limit states and conventional design practices

Pressure hull structure and limit states

The long, slender pressure hull of typical submarines is sub-divided lengthwise by watertight load-bearing bulkheads, as shown in Figure 2 (p. 4). This allows compartmentalization of the hull for hydrostatic stability considerations when hull damage occurs. Structural design is carried out on a compartment by compartment basis, under the assumption that the interaction between compartments is weak or is conservatively dealt with in the design process.

The failure mode of a ring-stiffened pressure hull is classified as either interframe or overall collapse, for configurations that result in inelastic buckling of the shell between stiffeners or the entire shell-stiffener component, respectively. Interframe and overall collapse modes are shown in Figure 2. Failure of the hull can also occur via collapse of the domes or by lateral buckling of the ring-stiffeners due to insufficient torsional stiffness of the ring, referred to as stiffener tripping. Larger safety factors are typically applied to these modes of failure so that they do not govern the design [11]. For this reason, the remainder of the discussion in this chapter will be focused on overall and interframe collapse.

Out-of-circularity (OOC) and residual stresses resulting from fabrication and assembly are the most important imperfections that must be considered for pressure hull design [14]. OOC imperfections introduce destabilizing bending moments that promote buckling instability and hasten material yielding. Residual stresses due to welding and especially cold rolling of the hull plating and ring-stiffeners lead to the early onset of yielding and collapse.

Conventional design methods for pressure hulls

The United Kingdom Ministry of Defence (UK MoD) compiled and developed much of the analytical and empirical methodology for determining the collapse strength of pressure hulls [10,11] that was eventually incorporated in civilian [6,7] and military [5] design codes. This section presents a brief review of the design methods, with reference to the design codes themselves, as well as some of the original work presented by Dr. S. Kendrick of the UK MoD.

Interframe collapse

For design, interframe collapse is typically predicted using empirical curves [5-7] that implicitly account for the influence of material plasticity and imperfections such as OOC and residual stresses. Two typical design curves, as well as some of the test data that were used to derive them, are shown in Figure 3 (p. 5). The design curves are plotted as the experimental collapse pressure, P_c, versus the classical elastic buckling load (the so-called von Mises pressure, P_{m1}), with both axes normalized with respect to a linear shell-theory yield pressure, P_{c5}. Models falling to the left of $P_{m1}/P_{c5} \approx 1$ on the horizontal axis are expected to fail by elastic buckling, and those falling to the right of that value, by elasto-plastic collapse. The empirical relationship defines the reduction in strength from the case of the perfect elastic structure, and is thus termed a "knock-down factor" approach to design.

The designer calculates the analytical buckling and yield pressures, and takes the predicted collapse pressure from the design curve. Some design codes specify the strength of the shell based on a curve that is fit to an approximate lower bound of all known relevant experimental data [6,7], while other codes use a curve fit to the mean of the data [5]. The lower-bound and mean curves, shown in Figure 3, use and require different safety factors.

Overall collapse

Overall collapse is typically precipitated by yielding of the ring-stiffeners. Kendrick [11] derived an analytical equation for the stress in the extreme fibres of the ring-stiffener, which includes the bending stresses associated with OOC. Overall collapse predictions are sometimes based on Kendrick's equation (e.g., Eq. 6.17 in [5]) with the collapse pressure taken as the pressure causing the onset of yielding in the ring-stiffener [6,7]. The overall collapse pressure is typically evaluated based on the maximum allowable OOC in the worst possible mode shape. Cold rolling residual stresses are dealt with using an additional safety factor.

Kendrick also derived a less conservative methodology for predicting overall collapse based on the full elasto-plastic capacity of the compartment. Kendrick's analysis uses a finite difference (FD) model of a single ring-stiffener and bay of plating [8]. The FD discretization is applied to the circumferential direction, while classical beam theory is used to predict the response of the ring under a pressure load, and the cross-section is sub-divided into discrete strips to track the progression of yielding. The nonlinear governing equations, which include the bending moments induced by an initial out-of-circularity, are solved incrementally, with the collapse pressure defined by the first limit point in the analysis. Residual stresses due to cold bending, calculated for example according to [41], may be included as an initial stress state in the model. Correction factors are used to account for the finite compartment length and the effective width of the shell plating that contributes to the circumferential bending resistance of the hull. Kendrick's finite difference method is prescribed by the design guidelines in [5].

A modified version of Kendrick's FD method for overall collapse [42] allows the circumferential extent of corrosion thinning, as well as the associated shell eccentricity, to be included explicitly in the model. The corrosion damage is assumed to be uniformly distributed over the length of the hull. This method was derived in order to allow assessments of in-service damage to be performed within the scope of conventional design methods.

Accuracy of the submarine design formulae

The accuracy of interframe and overall collapse predictions using the SDF are estimated in order to provide a baseline for comparison with numerical modeling results. Test results for interframe collapse are shown in Figure 3 (p. 5), along with the lower bound [6,7] and mean [5] empirical design curves. The experimental data, taken from Fig. 9.24 in [10], along with more recent results, were used to derive the design curves in [5-7]. It should be noted that the mean curve from [5], shown in Figure 3, differs slightly from the mean curve presented by Kendrick in [10]. Kendrick's mean curve is more conservative in the elastic region and falls below the true mean of the data in that region. That was done in order to allow the lower bound curve, which is used in [6,7,10] and lies 15% below Kendrick's original mean curve, to have a slope of 0.5 in the elastic region. In this chapter, only the more recent mean curve from [5] will be considered since it more closely reflects the true mean of the test data.

The experimental data are compared with the design curves in order to estimate their accuracies for future predictions. Two modeling uncertainty factors are calculated for every experimental data point in Figure 3 by dividing the experimental collapse pressure by the value predicted by the lower bound and mean curves. Those data are used to determine the bias, COV and prediction interval for each curve, as summarized in Table 2.

Since the lower bound curve is intentionally offset from the mean of the data, its statistical properties are significantly worse than those of the mean curve (Table 2). As expected, the mean curve has a bias close to unity, under-predicting collapse pressures by only 2%, on average. The bias of the lower bound curve indicates that it under-predicts the collapse pressure by, on average, 31%. That value is over twice the original 15% deviation of the lower bound curve from Kendrick's mean curve because the latter design curve was significantly conservative to begin with, as discussed above. The offset of the lower bound curve from the mean of the data amplifies the discrepancy between the curve and the test data. As a result, there appears to be greater scatter associated with the lower bound curve, since the COV for that curve is approximately twice that of the mean curve, at 17% and 8.5%, respectively. The prediction intervals in Table 2 indicate that the lower bound and mean curves are accurate to within approximately 76% and 20%, respectively, with 95% confidence. Both curves are more likely to under-predict, rather than over-predict, the collapse pressure, but the lower bound curve is significantly more conservative than the mean curve.

Table 2: Accuracy estimates for the submarine design formulae.

Mode and Method	n[a]	**Bias**[b]	**COV**[c]	**95% prediction interval for X_m**[d]
Interframe collapse				
Lower bound curve [6,7,10]	50	1.305	17.2%	$0.849 \leq X_{m,n+1} \leq 1.761$
Mean curve [5]	50	1.022	8.52%	$0.846 \leq X_{m,n+1} \leq 1.199$
Overall collapse				
FD, intact hulls [8]	9	1.046	4.76%	$0.925 \leq X_{m,n+1} \leq 1.167$
FD, corroded hulls [42]	10	1.121	17.5%	$0.657 \leq X_{m,n+1} \leq 1.585$

[a] n is the sample size. Experimental data for interframe collapse are taken from [10]. Experimental data for overall collapse of intact and corroded models are taken from [8,22] and [22], respectively.

[b] Bias is the mean modeling uncertainty factor, X_m, for a given sample.

[c] COV is the coefficient of variation for a given sample.

[d] The prediction interval for a future value of X_m for 95% confidence, based on Eq. (1).

The accuracy of overall collapse pressure predictions is assessed for Kendrick's elasto-plastic finite difference method, using the original methodology for intact hulls [8], as well as the modified version for corroded hulls [42]. Experimental-numerical comparisons are taken from [8,22] for intact ring-stiffened cylinders and from [22] for models with artificial corrosion damage. The results of the statistical analysis are shown in Table 2. Kendrick's method results in good accuracy (within 17%) for intact models, with a 95% confidence level; however, for corroded models, the accuracy is much poorer (within 59%), with the same level of confidence.

The experimental-analytical comparisons presented above are based on the ideal case, i.e., the experimental models are consistent with the assumptions of the predictive models. As such, the accuracy estimates are likely unconservative for real pressure hulls, which are not usually constructed of uniformly ring-stiffened cylinders. In order to account for that in design, a hull compartment with conical sections, variable frame spacing, *etc.*, is idealized as an equivalent ring-stiffened cylinder using the most pessimistic proportions. The net result of these and other approximations, such as lower-bound empirical methodology, is a layered conservatism. Some of this conservatism is intentionally built into the design process to account for the inaccuracy of the analytical methods, but it is compounded by the use of idealized geometry in the analytical models and due to the reliance on empirical design methods to account for imperfections in interframe collapse predictions.

Improvements to the contemporary design methods are unlikely to result in more efficient or reliable designs because they are limited by the above-mentioned conservatism and simplicity. Furthermore, the conventional methods are unable to handle some important design and analysis problems, such as realistic geometric imperfections, non-axisymmetric structure, interaction between structural components and modes of failure, novel structural configurations, and in-service loads and damage. Those problems can be dealt with using nonlinear FE analysis, which is discussed in the next section.

Finite element modeling of pressure hulls

The literature has been reviewed in order to assess the state of the art of numerical modeling of pressure hulls. In general, the discussion will be limited to papers dealing specifically with pressure hulls; however, where appropriate, articles concerning the more general field of buckling-critical shells will be included as well. The FE prediction of a shell buckling or collapse load is determined by taking several steps: choosing the physical model, performing the FE discretization and solving the resulting system of equations. The following review identifies standard methods for each of those aspects, and discusses the potential errors that may be introduced at each step. A summary of the surveyed articles is presented in Table 3, including the type of paper, topic and type of shell stability problem studied.

The majority of the reviewed analyses used commercially available FE packages: ABAQUS [56] was used in [16,18,48,49,52], ANSYS [57] was used in [13,42-44,47], MARC [58] was used in [55], NISA [59] was used in [53], STAGS [60] was used in [14,15] and Trident [61] was used in [51]. The finite difference axisymmetric shell analysis program BOSOR was used in [45,46]. This "black box" approach means that some of the details of the numerical method used, such as the nonlinear formulation or iteration scheme, were not always reported.

Physical model

The physical model includes the governing differential equilibrium equations relating stresses and loads, the continuity equations relating strains to displacements, and the constitutive equations. The complexity of the governing equations is often reduced by making assumptions about the system being studied, leading to the structural truss, beam, plate and, of particular relevance to the current study, shell theories.

Mechanical theory

Shell theory was used exclusively in almost all of the reviewed papers, with the exception of one article that considered a full solid mechanics approach [52] and another study, which used plane stress theory [55]. The approximations involved in the reduction to shell theory are an initial source of modeling error, albeit a small error if the shell assumptions reflect the physical reality, e.g., for classical shell theory with thin shell and small strain assumptions, the relative error does not exceed $(h/L)^2$ or h/R, where h, L and R are the shell thickness, the characteristic length of the shell deformation pattern, and the minimum principal radius of curvature, respectively [62].

In order to understand what those limitations imply for pressure hull analysis, some typical designs, which were generated for the reliability study in [63], can be examined. Assuming that the characteristic shell length is approximately equal to the stiffener spacing, the designs in [63] are bounded by $0.0085 \leq h/R \leq 0.0092$ and $0.0009 \leq (h/L)^2 \leq 0.0046$. This implies that the expected error in the prediction of the linear hull response due to shell theory approximations is on the order of one percent for typical pressure hulls.

Table 3: Overview of surveyed articles dealing with experimental and numerical modeling of shell structures under external pressure.

Source	**Topic**
Aghajari *et al.* [43]	Experimental and FE modeling of thin steel cylinders with lengthwise thickness variations
Boote *et al.* [44]	Experimental and FE modeling of moderately thick steel cylinders
Bushnell [45]	Experimental and finite difference modeling of ring-stiffened aluminium cylinders
Bushnell [46]	Experimental and finite difference modeling of ring-stiffened steel cylinders with residual stresses
Creswell and Dow [14]	FE modeling of ring-stiffened steel cylinders to investigate the effects of geometric imperfections and residual stresses
Gannon [47]	FE modeling of ring-stiffened steel cylinders to compare methods of incorporating cold rolling residual stresses
Graham [48,49]	Experimental and FE modeling of ring-stiffened steel cylinders
Graham *et al.* [15]	Experimental and FE modeling of ring-stiffened steel cylinders and domes
Le Grognec *et al.* [50]	Experimental and FE modeling of steel cylinders with residual stresses
Jiang *et al.* [51]	Experimental and FE modeling of ring-stiffened aluminium cylinders with discrete patches of thinning
Lennon and Das [18]	FE modeling of ring- and stringer-stiffened steel cylinders with residual stresses
MacKay *et al.* [13]	Experimental and FE modeling of ring-stiffened steel and aluminium cylinders with discrete patches of thinning
Moradi and Parsons [52]	Finite element and finite difference modeling of ring-stiffened aluminium cylinders to examine linear buckling
Morandi *et al.* [16]	Review of analytical, empirical, numerical and reliability methods for predicting collapse of ring-stiffened cylinders
Radha and Rajagopalan [53]	Comparison of analytical and FE collapse predictions for ring-stiffened steel cylinders under external pressure
Ross and Johns [54]	Experimental and FE modeling of ring-stiffened steel cylinders
Şanal [55]	Nonlinear FE modeling of steel cylinders under external pressure
Smith and MacKay [42]	Experimental, FE and finite difference modeling of ring-stiffened cylinders

Material law

Since pressure hulls fail in the plastic range, an appropriate inelastic material model must be specified, typically in combination with through-thickness shell integration to deal with plastic bending [64]. The inelastic model consists of the yield surface definition, flow rule and hardening rule [65].

The von Mises isotropic yield function (usually implying multiple through-thickness shell integration schemes) and associated flow rule was used in most of the studies reviewed here [13,16,42,45-47,50,51,54]. When modeling real structures, the measured stress-strain properties from tensile coupon tests were normally used in the numerical material model [13,16,42,43,48,49,51,54,55]. If the measured material properties were not available, nominal specified material properties were used [13,18,42,45,47]. Idealized material models were used for those studies that were not concerned with modeling real shells [14,46,52]. Both isotropic [13,16,42,45,46,50,54] and kinematic [14,47-49,51] hardening rules were used in the reviewed papers. Kinematic hardening was chosen when the Bauschinger effect was anticipated to play a role in the simulation of cold rolling fabrication procedures and/or the collapse behaviour.

Boundary conditions

Boundary conditions define the loads on the structure (force or Neumann boundary conditions) and the way in which it is supported (displacement or Dirichlet boundary conditions); furthermore, they are used to ensure a unique solution. Most pressure hull models use simply supported or clamped boundary conditions [13,16,42,45-47,51,54]. A more accurate representation of the boundary conditions was sought in some studies by explicitly modeling the shell support structures used in the experiments [48,49]. Model reduction, in tandem with symmetry constraints based on the applied imperfections and expected relevant buckling mode(s), was frequently used when full field measured imperfections were not modeled [14,18,45,50,52, 53,55]. Symmetry constraints must be used with caution, as they restrict both the possible imperfection and failure modes [64].

Pressure loads have a live nature, in that the loading direction changes as the structure deforms. For long wavelength buckling modes (n=2), live loads (also known as follower-forces) have been shown to decrease the critical nonlinear elastic buckling pressure of rings by up to 50% compared with dead loads, while the discrepancy between live and dead loads is less for higher values of n [66]. Jiang *et al.* [51] neglected the follower-force effect in their analyses of experimental models since the pre-collapse displacements were small. Otherwise, the inclusion or neglect of live loads in the pressure hull analyses reviewed here was not reported.

Finite element discretization

The FE discretization involves choosing the type of element, conducting mesh convergence studies, accounting for large displacements and rotations, and the treatment of imperfections.

Element selection

In this article, "shell elements" or "general shells" refer to shell elements that are discretized in two dimensions, but exist in a three-dimensional (3-D) domain. The most common types of general shell elements are the classically-derived shells, which involve a direct discretization of the 2-D shell equations and do not generally include transverse shear deformations, and the degenerate shells, which are derived by making 2-D shell assumptions after discretizing the 3-D shell continuum [64]. There are many variations of the general shell elements that incorporate different strategies to avoid some basic problems such as shear locking, membrane locking and spurious deformation modes [67-69]. For pressure hulls, the use of general shell elements is prevalent; they were used for at least some calculations in all but four [45,46,54,55] of the surveyed articles.

Further simplifications in shell element formulations can be achieved by assuming symmetry about an axis. The "axisymmetric" shell elements have a constant curvature with respect to the axis of symmetry. Axisymmetric shells are discretized along the axial direction, and operate in a two-dimensional domain. These elements, by definition, cannot model non-axisymmetric structures and imperfections, although Fourier series can be used to produce harmonic mode shapes for linearized buckling analyses. Axisymmetric shells are also commonly used in the analysis of pressure hulls [45,46,52,54], although less so in the last two decades.

"Solids" refers to continuum-based elements operating in 2-D (plane stress or axisymmetric) or 3-D space. Elements based on 3-D solid mechanics [52] and plane stress [55] were also used. Plane stress elements require significant simplification of the physical domain, e.g., in [55] plane stress elements were used to represent an infinite cylinder by discretizing a cross-section of the tube. The remainder of the current section dealing with FE modeling refers to the predominant general shells, including both degenerate and classical shell formulations.

Convergence studies

FE discretizations are subject to error related to the internal element interpolation of stresses and other parameters, by the use of shape functions. This type of error is reduced as the mesh density is increased. Mesh convergence studies are required to determine the mesh density for a particular model that yields a solution that is sufficiently close to the exact solution of the equations (not necessarily the correct solution of the problem being studied). The FE model should also be able to accurately represent the shape of both the anticipated mode of failure and any geometric imperfections [70], although a converged mesh should generally meet this requirement already. Mesh convergence studies were not generally mentioned in the reviewed articles. This does not mean that such investigations were not performed (in fact, figures in many of the papers indicate the use of dense meshes), but rather that the reader cannot be certain that they are considering well-converged numerical results.

Large displacements and rotations

The effects of large displacements and rotations must be considered in order to correctly predict the ultimate strength and failure mode of many buckling-critical shells [64,71], especially those in which geometric imperfections play an important role. Large displacement analyses normally use Lagrangian formulations, sometimes in combination with corotational schemes, where the reference frame moves and rotates with the element, and rigid body motion is separated from strain-producing modes [64,72]. All of the reviewed studies have included the nonlinear effects of large displacements and rotations.

Imperfections

Significant error in the collapse prediction will likely arise if imperfections, particularly out-of-circularity and residual stresses, are not modeled. For pressure hulls, that error can be as high as 20 to 30%, if either type of imperfection is neglected [14,73]. Furthermore, the influence of shell thickness variability, due to manufacturing procedures [44] or corrosion degradation [51], has also been found to be important for predicting pressure hull strength. Experiments have shown that the relative reduction in collapse pressure due to corrosion damage is approximately equal to the relative thinning, and that both the thinning itself and the shell offset due to one-sided thinning contribute to the strength reduction [22].

In the reviewed papers, measured out-of-circularity imperfections were fit to a Fourier series [51] or spline curve [48,49] function, which was subsequently applied to the nodal coordinates. When no measured data was available, imperfections were derived from some assumed or idealized pattern [14,47,55], such as a linear-elastic buckling mode.

The effects of cold rolling residual stresses are included in pressure hull FE models using several approaches. In some cases, the cold rolling process was explicitly, although approximately, simulated by applying an end rotation or moment to a clamped plate or stiffener [18,47-49]. The section was overbent into the plastic region and allowed to spring back to the desired radius. Other methods involve applying the pre-determined residual stress distribution as an initial stress condition [16,47,50], through equivalent thermal loads and an associated coefficient of thermal expansion [46], or using "effective" stress-strain curves [13,14,16,42,47]. Effective stress-strain curves account for early yielding caused by residual stresses by using a "softer" stress-strain curve in the material model during the nonlinear collapse analysis.

In [47], various methods for incorporating cold rolling stresses in a nonlinear FE collapse analysis of a pressure hull were compared. Collapse pressures for models with an initial stress state based on cold rolling stresses predicted by the method of [41] were within 7.5% of those based on explicit simulation of cold bending, even though the initial stresses were for the circumferential direction only. Models using effective stress-strain curves were found to give collapse pressures within 5.5% of the models with explicit simulation of cold bending.

Welding stresses at the stiffener-plate connection were included in three studies by applying thermal loads in the heat-affected zone in an elasto-plastic analysis [18,46,49]. In [46], inclusion of welding stresses did not change the predicted collapse pressure or mode compared with a similar model without the welding simulation. The predicted welding residual stresses were found to be yield-level in [49], but the collapse pressure of the welded hull was only reduced by approximately 1% compared to a similar model without welding stresses or distortions. The simulations in [18,46,49] are a simplification of the real welding process since they do not account for temperature-dependent material properties or the transient nature of weld deposition and cooling; and so, the abovementioned results must be interpreted cautiously.

Solution procedures

The product of the FE discretization is a set of simultaneous, nonlinear equations. The method chosen to solve this system will greatly affect the accuracy of the solution.

Nonlinear static solutions obtained through incremental application of the loads or displacements neglect inertial effects, but are otherwise similar to time-stepping procedures used in dynamic analyses, and are thus called "quasi-static". The nonlinear quasi-static buckling or collapse load is indicated by a bifurcation or a limit point on the fundamental equilibrium path, respectively. Bifurcation points on the solution path are identified by, for instance, checking for zero or negative eigenvalues of the system at regular nonlinear load increments [16,45,46,52]. The collapse load is typically taken as the maximum limit point on the calculated nonlinear load-deflection curve.

Quasi-static incremental application of the load was used in each of the pressure hull cases reviewed here. Dynamic analysis of buckling-critical shells has been shown to be unnecessary unless prediction of the post-buckling behaviour is of great interest; quasi-static analysis has been found to predict the pre-critical behaviour, critical load and mode, and for some cases even the post-critical path, as adequately as transient analysis [74-76].

The nonlinear solution is achieved by iteratively balancing the internal and external forces at a given load increment using a so-called Newton-Raphson approach. In the full Newton-Raphson method, the tangent stiffness is updated at each iteration, while in a modified Newton-Raphson method, the tangent stiffness is updated less frequently, e.g., at the beginning of each load increment [65]. While the iterative scheme was seldom reported in the reviewed papers, it is likely that nearly all of the analyses used a Newton-Raphson approach.

Reasonably small load increments are required to ensure convergence, especially for elasto-plastic behaviour. Furthermore, large load increments may allow bifurcation points on the equilibrium path to be stepped over, introducing additional non-conservative error in the strength prediction. The number of load increments preceding the onset of instability was not generally reported for these pressure hull studies, but values between 10 and 100 were noted [13,42,47-51].

There are several common methods used to follow the nonlinear solution path, including load control, displacement control and generalized displacement control. With the first two methods, the solution cannot be carried past limit points in the load and displacement, respectively, due to a singular tangent stiffness matrix at the limit point. With generalized displacement control, the load factor is related to the generalized displacement via a constraint equation that requires convergence to occur within a specified load-displacement "arc" [64,72]. The arc-length, or Riks' method [77,78] allows both snap-through and snap-back, and thus the entire quasi-static load-displacement history can be followed. The so-called "spherical" arc-length method operates in both the load and displacement domain, while the "cylindrical" arc-length procedure prescribes only the generalized displacements. With linearized arc-length methods, the solution is sought along a line that is orthogonal to the tangent or the secant of the load-displacement curve [65]. The arc-length methods have been shown to be capable of quasi-statically traversing snap-through and snap-back behaviour [65]. For pressure hulls, the equilibrium path is generally followed by the use of an arc-length method [13,14,16,18,42,43,48-51], but load control was also used in some cases [45-47,54].

Accuracy of nonlinear finite element buckling predictions

The preceding sections looked at the sources of error related to the numerical modeling methods. In this section, those studies reviewed in Table 3 that considered both experimentally- and numerically-derived critical loads were collected in order to estimate the accuracy of nonlinear FE collapse predictions for pressure hulls. When comparing numerical predictions with experimental results, the overall discrepancy will also include errors associated with the measurement and testing procedure. This includes the accuracy limitations of the instruments used to characterize the model geometry, material and collapse strength, as well as the impact of taking a discrete number of spatial and temporal sampling points. As such, the experimental error must also be considered when assessing a given numerical model.

The modeling uncertainty factor and COV for each set of numerical-experimental comparisons reported in the literature are summarized in Table 4, along with the statistical properties for the entire group. Note that the finite difference methods of [45,46] are included in this data set. The bias for the entire group is 0.964, indicating that the FE methods used in these studies are, on average, successful at predicting the critical load. The COV of 6.3% indicates that a certain degree of scatter exists in the data. This is to be expected due to experimental scatter, and since the FE models ranged in their complexity and no common set of rules or guidelines were used to predict the critical numerical load.

Table 4 also shows the statistical data for the model sub-sets corresponding with axisymmetric and general shell modeling. The use of general shells results in only a slight improvement in bias and COV over the axisymmetric shells. That result may be misleading, since the majority of the axisymmetric predictions were compared to relatively thick-shelled experimental models [45], with $0.019 \leq h/R \leq 0.080$. Thicker shell models are less sensitive to out-of-circularity imperfections, so that their neglect in the axisymmetic models had less impact on the accuracy of the results than would be expected for real pressure hulls.

The data in Table 4 can be used to establish prediction intervals for a single future experimental-numerical comparison. Based on Eq. (1) and using data for the entire sample, the 95% prediction interval is $0.843 \leq X_{m,n+1} \leq 1.086$, so that it can be said that a typical pressure hull analysis is accurate to within approximately 16% with 95% confidence. This result is somewhat better than the 20% accuracy of the mean empirical interframe collapse design curve, and similar to the 17% accuracy of Kendrick's overall collapse method for intact hulls (see Table 2). The accuracy statements are approximately the same for the axisymmetric and general shell model sub-sets.

In order to estimate the accuracy of pressure hull collapse predictions using reasonably high-fidelity general shell models, the studies in Table 4 that involved unnecessary approximations were eliminated. The study by Boote *et al.* [44] was not considered because out-of-circularity imperfections were neglected in the nonlinear analysis and the material model used in the analyses was not reported. The analyses by Morandi *et al.* [16] involved symmetry and an approximation of the measured OOC shape, and were thus

Table 4: Experimental-numerical comparisons from the literature.

Source	Model Type	Sample Size[a]	Bias[b]	COV[c]
Aghajari *et al.* [43]	3D	4	0.908	2.2%
Boote *et al.* [44]	3D	8	0.924	8.8%
Bushnell [45,46]	Axisymmetric	71	0.959	5.8%
Graham [48,49]	3D	14	0.979	4.1%
Jiang *et al.* [51]	3D	13	1.009	3.4%
Morandi *et al.* [16]	3D	4	0.986	3.8%
Ross and Johns [54]	Axisymmetric	3	0.973	18.8%
All of the above		*117*	*0.964*	*6.3%*
3D FE models		*43*	*0.972*	*6.0%*
Axisymmetric models		*74*	*0.960*	*6.5%*
Refs. [48,49,51]		*27*	*0.993*	*4.0%*

[a] Sample size is the total number of experimental-numerical comparisons presented in the referenced paper(s).

[b] Bias is the mean modeling uncertainty factor, X_m, for a given sample.

[c] COV is the coefficient of variation for a given sample.

discarded. Aghajari *et al.* [43] studied elastic buckling of thin, unstiffened shells, which are not representative of pressure hull structures, so those analyses were also ignored. That leaves the studies [48,49,51] which consider the most realistic representation of a pressure hull – a T-section ring-stiffened cylinder – and that include the relevant imperfections in the numerical model. The bias and COV for those models are 0.993 and 4.0%, respectively, and the 95% prediction interval is $0.909 \leq X_{m,n+1} \leq 1.077$, i.e., 9% accuracy. That accuracy is a significant improvement over the empirical curves and Kendrick's method for intact models. The FE data from [51] include models with non-axisymmetric damage in the form of corrosion thinning, for which the modified method of Kendrick has an accuracy of 59% (see Table 2).

Bearing in mind that the results reported in Table 4 were taken from a limited sample size, it is possible to make generalizations about the potential limits to the accuracy of the numerical methods. The near-unity bias of the sample considered here is encouraging, but the COV for the sample is somewhat large, resulting in an estimate of 16% accuracy with 95% confidence. It would be desirable to reduce the accuracy estimate considerably, to say 10% or less, if nonlinear FE methods are to be used in design. The results for [48,49,51] suggest that this is a reasonable goal.

The numerical-experimental results could be improved by the development of modeling guidelines to encourage consistent results, and the use of a common experimental method so that the experimental error is accounted for more precisely. Those tasks are considered in the proposed procedure for implementing numerical methods in pressure hull design, which is discussed in the following section.

Design using nonlinear finite element analysis

The incorporation of any structural analysis method into a design code requires the uncertainties associated with the modeling method to be accounted for so that the designer is reasonably assured that the as-built structure will be safe. Of course, the designer must also take into account uncertainties associated with, for instance, construction and loading. Modeling uncertainty in pressure hulls has traditionally been dealt with by using a lower-bound empirical method [6,7] or a partial safety factor associated with a mean empirical curve [5]. The PSF is generally taken as the maximum scatter from the mean curve, as in [5]; however, reliability methods can be used to develop a PSF for a particular structure and target reliability, as demonstrated by Morandi *et al.* [63].

Nonlinear FE analysis could be implemented in a pressure hull design code by, first, using the validation and verification methods to establish the accuracy of, and confidence in, numerical collapse predictions; and, second, by re-casting the results of the V&V process into a format that is suitable for design calculations. The second task may be addressed by deriving a partial safety factor based on the accuracy statement determined from V&V. The application of the V&V process to nonlinear FE predictions of pressure hull collapse is discussed in the following sub-section, followed by the presentation of a method for deriving a partial safety factor for design. Those methods are then compared with other existing or proposed procedures for incorporating numerical models in shell design codes.

Application of V&V methods to pressure hull collapse

V&V begins with a statement of the intended use of the numerical model [36]; in this case, "to predict the static collapse pressure of a submarine pressure hull under hydrostatic pressure associated with diving." The range of structural configurations, materials, loading and behaviours that are to be modeled must also be stated. For example, pressure hulls may be defined as ring-stiffened shell structures constructed of a roughly planar-isotropic metal. Furthermore, the current study is not concerned with validating models for predicting the response of the hull to other types of loading, such as shock loading from underwater explosions, and it is assumed that fluid-structure interaction is not important when predicting the response up to the collapse load.

V&V is performed for well-defined numerical modeling procedures, which are defined at the outset of the process, and is software-specific. In the end, the intended use of the model is to predict responses of in-service structures that will not be tested to failure. Those predictions are only credible if they are made using the same modeling methods and tools that were used in the V&V process.

For pressure hulls, the numerical modeling procedures may be established based on the trends identified in the literature survey described above, as well as by comparison of numerical and experimental data. Experimental models for validation should be representative of the structure and behaviour of real hulls. The primary response of interest, which will be used in accuracy assessments, must be measured and all experimental errors should be estimated. In the case of pressure hulls, the primary response is the collapse pressure. Confidence in the numerical model is increased by recording secondary experimental responses, such as the pressure-strain or pressure-displacement relationships. Comparison of those data with model predictions can show that the model is giving the right answer for the right reasons. Validation modeling should be performed without knowledge of the experimental results. This prevents "tuning" of the numerical model to match the experimental outcome.

The V&V guidelines prescribe a hierarchical breakdown of the system to be modeled into components and sub-components. V&V must be performed starting at the lowest level components in isolation, and work its way up to the complete "system" model. The components of a pressure hull are ring-stiffened cylinders and cones, load-bearing bulkheads, and dome ends. This thesis is focussed on a single component: the ring-stiffened cylinder. If the traditional design-by-component methodology for pressure hulls [5] is to be improved upon, additional V&V is required for domes and bulkheads, as well as the entire pressure hull system.

The V&V process is aimed at building confidence in a numerical model so that managers may use the results of modeling to make informed decisions regarding the safety, reliability, robustness, *etc.* of the object being modeled [36]. In that context, the V&V guidelines suggest that accuracy goals should be stated at the beginning, so that there can be an objective assessment of success or failure at the end of the process. In the case of failure, the numerical model is adjusted and the process is repeated. However, the scope of the current thesis extends beyond the V&V process: not only does the accuracy of the numerical model have to be derived, but that accuracy must be interpreted for use in a design setting, in this case by "translating" it into a partial safety factor. The starting point is a fairly well-defined set of modeling procedures for which the accuracy is unknown, and the end goal is the partial safety factor itself rather than a pass/fail decision.

The following section presents one potential method of deriving a PSF once the accuracy of the numerical model has been established. The accuracy estimates for nonlinear FE analysis that were presented earlier are used in an example PSF derivation, even though those data were not generated under a formal V&V process.

Derivation of a partial safety factor for design

The design strength of a pressure hull is given by dividing the predicted collapse pressure by a PSF for the prediction method itself, as well as PSFs that account for other uncertainties, such as those related to construction and loading. This thesis is only concerned with the PSF accounting for uncertainty in the predictive model. The challenge for the developers of design codes is to somehow convert the accuracy metrics (bias and COV) that are derived for a particular analysis method, such as those given in Table 4, into a PSF. One method of deriving such a PSF from a given sample is to determine the form of the distribution of X_m (e.g., normal, log-normal, Weibull) and to use that distribution to establish a lower-bound for a future observation based on a specified level of confidence. This differs from the conventional lower-bound empirical methodology, which simply fits a curve to the lower bound of all known experimental data. That method doesn't account for the statistical distribution of the results, and may give undue importance to outliers in the experimental data.

An initial indication of the form of a distribution of a sample is given by a histogram of the data, whereby the data range is divided into intervals and the number of values that fall within each interval is plotted. The shape of the histogram is suggestive of the distribution. A histogram of the X_m data from Table 4, shown in Figure 5, shows the bell shape of a normal distribution.

A more sensitive method to determine the form of a distribution is the probability plot. With this method, the sample data are ordered from smallest to largest, and given a standardized score, based on the assumed distribution, that reflects where each datum point is expected to occur in the distribution. The random variable is then plotted versus the standardized score, and if the points on the resulting probability plot are close to a straight line, the assumed distribution may be used for further statistical analysis [40]. Figure 6 shows a normal probability plot of X_m for the sample summarized in Table 4, with the modeling uncertainty factors plotted against the standardized normal score, z, for a normal distribution. That figure shows that the points fall close to a straight line, so that for the purposes of this chapter, the standard normal distribution can be used.

Since X_m is equal to the ratio of actual to predicted hull strength, lower values of X_m are associated with less conservative predictive models. The goal for design is to set the lower bound for X_m based on a desired level of confidence that no future prediction will be less than that lower bound. In statistics, this is referred to as a one-sided lower-bound prediction interval, and is given as follows [40]:

$$X_{m,n+1} \geq \bar{x} - t_{\alpha,n-1} s\sqrt{1+1/n} \quad . \tag{2}$$

Eq. (2) has a similar form as the prediction interval given in Eq. (1), except that the t-value is based on α rather than $\alpha/2$, since the interval is one-sided.

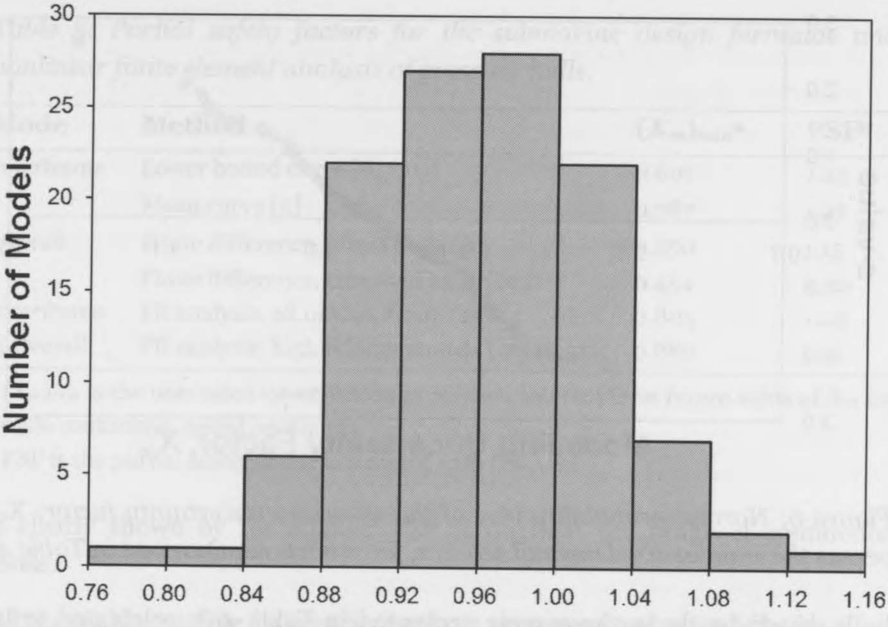

Figure 5: Histogram of modeling uncertainty factor, X_m, *for models summarized in Table 4.*

If the sample size, bias and standard deviation for a set of modeling uncertainty factors are substituted into the right-hand-side of Eq. (2), it gives the minimum value of X_m that can be expected for a confidence level of 100(1-α)%. That lower bound value will be referred to as $(X_m)_{min}$. The PSF for the predictive model is simply taken as the inverse of $(X_m)_{min}$. This method has the benefit of taking both the modeling error and uncertainty into account. Table 5 lists values of $(X_m)_{min}$ and the associated PSF for the SDF and FE analyses with α=0.005, i.e., a confidence level of 99.5%.

Table 5 shows that the PSF for the lower bound empirical curve is actually greater than the factor derived for the mean curve. This is paradoxical, since it is known that the lower bound curve is more conservative. The effect can be traced back to the large standard deviation associated with the lower bound curve, which is intentionally a poor fit to the experimental data. This method of deriving a PSF is not appropriate for a lower bound approach; however, it is suitable for the mean curve, as well as Kendrick's overall collapse method. The PSFs derived here for those methods are 1.27 and 1.15, respectively. The PSF for nonlinear FE analysis of pressure

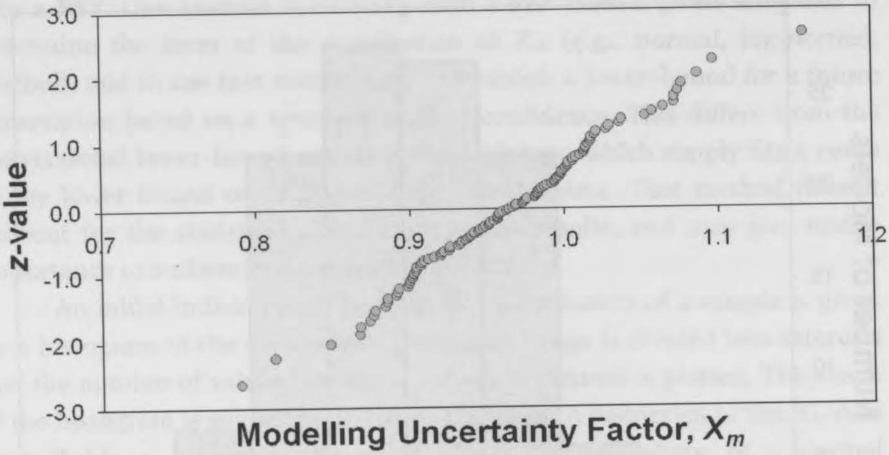

Figure 6: Normal probability plot of the modeling uncertainty factor, X_m*, versus the standardized normal score, z, for models summarized in Table 4.*

hulls, based on the entire sample presented in Table 4, is calculated to be 1.25. When only the higher fidelity models are considered, the PSF is 1.14.

PSFs associated with mean design curves are typically related to the maximum scatter. The mean curve of [5] agrees with the experimental data within approximately ±10% in the elasto-plastic region [10], where most conventional pressure hull designs fall. This implies a PSF of 1.1, which is significantly less than the PSF of 1.27 derived using a 99.5% level of confidence with the methods in this chapter. The statistical methods described above can be used to back calculate the level of confidence associated with a PSF of 1.1 for the mean curve, giving a value of approximately 90%. That level of confidence gives a PSF of 1.064 for the high fidelity numerical models.

The selection of a confidence level of 99.5% was somewhat arbitrary, although this value has been suggested for use with experimentally determined fatigue design curves for pressure hulls [5]. The mean interframe design curve has been used successfully for many decades, and in conjunction with a much smaller safety factor than the one derived here. That seems to indicate that 99.5% may be too stringent and that currently acceptable safety margins may be achievable using a smaller level of confidence. An acceptable level of confidence must be chosen for the collapse of pressure hulls, taking into consideration the safety and financial consequences of failure. Figure 7 shows the relationship between the PSF and the confidence level for the entire group of FE models, as well as the higher fidelity group. The benefit of using higher fidelity modeling methods

Table 5: Partial safety factors for the submarine design formulae and nonlinear finite element analysis of pressure hulls.

Mode	Method	$(X_m)_{min}$[a]	PSF[b]
Interframe	Lower bound curve [6,7,10]	0.697	1.43
	Mean curve [5]	0.787	1.27
Overall	Finite difference, intact hulls [8]	0.870	1.15
	Finite difference, corroded hulls [42]	0.454	2.20
Interframe & Overall	FE analysis, all models from Table 4	0.803	1.25
	FE analysis, high fidelity models [48,49,51]	0.880	1.14

[a] $(X_m)_{min}$ is the one-sided lower-bound prediction interval for a future value of X_m for 99.5% confidence, based on Eq. (2).

[b] PSF is the partial safety factor associated with $(X_m)_{min}$.

is clearly shown by the smaller PSF throughout the range of confidence levels.

Alternatives for incorporating numerical models in design

Graham [48,49] has suggested a PSF of 1.085 for nonlinear FE collapse predictions for pressure hulls. That value is based on the maximum percentage discrepancy between numerical and experimental collapse pressures for fourteen test models, using a more-or-less uniform set of numerical modeling procedures; i.e., it is based on a lower-bound methodology.

Graham's modeling approach resulted in good agreement between experimental and numerical collapse pressures, as shown in Table 4. If the statistical analysis described above is applied to Graham's data from [48,49], the resulting PSF is 1.17, which implies that twice the degree of conservatism is required compared to his PSF. Looked at from a different perspective, Graham's PSF is associated with a 90% level of confidence, rather than the 99.5% used in the example PSF derivations in this chapter, so that there is one chance out of ten that Graham's sample is not representative and that his PSF is too small. Nonetheless, it is interesting to note that the level of confidence associated with Graham's PSF is consistent with that of the typical PSF used with the mean interframe design curve.

The Eurocode for civil engineering shell structures [79] is the only case of a shell design code known to the author that allows the use of nonlinear FE analysis for shell strength calculations. A PSF for the numerical buckling/collapse prediction is prescribed for specific structural classes; in

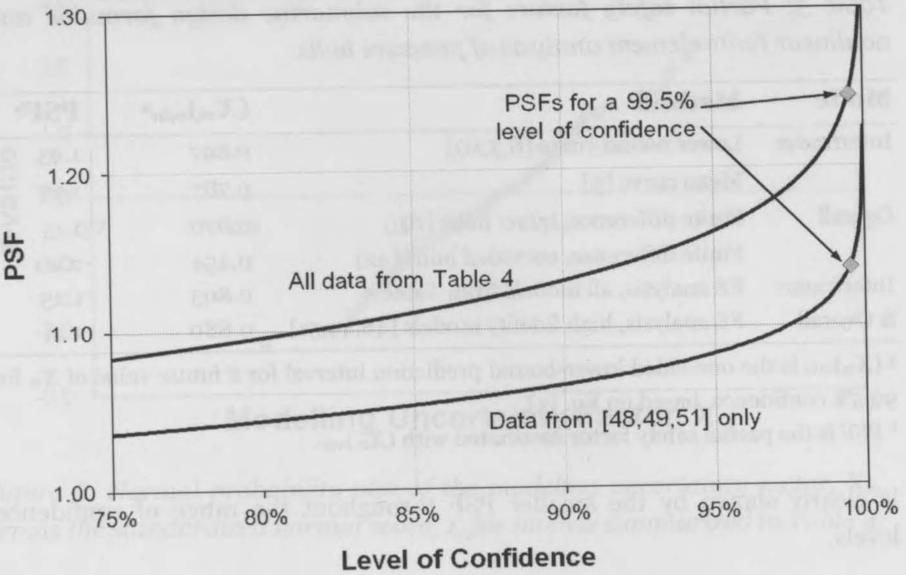

Figure 7: Variation of the partial safety factor (PSF) with the level of confidence that any future observation of X_m *will exceed* $(X_m)_{min}$*, for models summarized in Table 4.*

the absence of data for a particular structure, a value of 1.1 or greater is suggested. In addition to the PSF, the predicted FE strength is multiplied by a calibration factor, which is derived by comparing an FE model to a known buckling result (e.g., an experimental model). The Eurocode specifies certain modeling parameters, such as the application of geometric imperfections, but not the details of the FE modeling and solution. Presumably, the appropriateness of the FE model used for design is meant to be addressed by the calibration factor.

The Eurocode approach to numerical shell strength predictions is to allow the analyst discretion with regards to modeling and solution choices, and to account for this freedom by the use of a calibration factor. This differs from the approach outlined in this chapter, which is based on the development of a PSF for a specific set of modeling rules, so that a calibration factor is not required if those rules are followed. Negative aspects related to restricting the modeling methods would be, presumably, offset by a lesser degree of conservatism than would be required otherwise. Furthermore, the Eurocode calibration factor does not account for the normal statistical scatter found in real-world structures.

It has been shown in this chapter, that if a certain standard of modeling procedures are enforced, and a high-level of safety (99.5% level of confidence) is required, the PSF for nonlinear FE pressure hull collapse predictions can be taken as 1.14, which is somewhat greater than the Eurocode recommendation of 1.10. The PSF derived herein does not require a calibration factor, although the analyst is constrained to meet the aforementioned modeling criteria.

Conclusions and future work

The principal factors affecting numerical strength predictions for pressure hulls have been discussed in this chapter. A representative sample of practical nonlinear FE analyses of pressure hulls from the literature has been used to develop modeling trends, and to estimate the accuracy of the method in strength calculations.

With certain qualifications, such as the uncertainty regarding the errors in the experimental procedures, the typical pressure hull FE analysis was found to be accurate to within approximately 16% with 95% confidence. The accuracy can be improved to 9% by using higher fidelity shell models. The accuracy of numerical pressure hull collapse predictions compares favourably with the conventional approaches to pressure hull design, which are accurate to within approximately 20% with 95% confidence.

It has been suggested that the implementation of nonlinear FE analysis in pressure hull design procedures could address the inherent conservatism and inflexibility of the conventional design methods. The latter methods will likely be retained in novel design codes because of their simplicity and efficiency of use, as well as their value for use in iterative design procedures such as optimization routines and reliability analysis. Nonlinear FE analysis is expected to complement rather than replace the analytical methods, as in hierarchical design procedures [74].

A way forward for the incorporation of nonlinear numerical methods in the design procedure has been discussed. The suggested procedure builds on existing V&V concepts by introducing a straightforward way to develop a partial safety factor for design that accounts for the statistical distribution of the experimental-numerical comparisons. While this thesis deals specifically with submarine pressure hulls, the same process could be applied to any class of buckling-critical shell structure.

Unlike the analysts that generated the numerical predictions in Table 4, designers do not possess the measured material and geometric properties of the pressure hull before it is constructed. They must make assumptions about the material, using, for example, the minimum specified yield stress. And, since real imperfections cannot be anticipated precisely, characteristic values must be used. The Eurocode approach is to use the most pessimistic geometric imperfections that meet the specified design tolerances. An alternative approach is for the designer to consider the fabrication method when building the numerical model. Imperfection data banks [80] could be used to define more realistic geometric imperfections for a given method of manufacture. This would lead to less conservative designs than the use of worst-case imperfection assumptions. A consensus with respect to the most appropriate methods for modeling cold rolling and welding stresses in the numerical collapse analysis has not been reached, and is identified as an important topic requiring further research.

Chapter 3

Experimental methods for external pressure testing of buckling-critical shells

A review of conventional testing methods for applying external hydrostatic pressure to buckling-critical shells is presented. A new "volume-control" pressure testing method, aimed at preventing catastrophic specimen failures and improving control of specimen deformation near the critical load, is also introduced. The implementation of conventional and volume-control systems in an experimental program involving the destructive pressure testing of ring-stiffened cylinders is described. The volume control method was found to improve control of the specimen deformations, especially near the critical load, and catastrophic failures observed while using a conventional setup were avoided. The quasi-static tracking of post-collapse load-deformation relationships for snap-through buckling behaviour was possible while using a volume-control system, but precise control of dynamic shell deformations during buckling was not achieved for specimens failing with large buckling lobes. Expressions for estimating the available control over specimen deformations for pressure testing systems are presented. This chapter was originally published as a paper in *Experimental Mechanics* with co-author Fred van Keulen [21].

Introduction

Curved, thin-walled structures, which are under some manner of compressive loading, typically fail through instability in the form of elastic or inelastic buckling. These are the so-called "buckling-critical shells." This thesis is concerned with shells loaded under hydrostatic external pressure. This class of structures includes pressure hulls of naval submarines, commercial and research submersibles, and autonomous underwater vehicles, as well as certain civil engineering and aerospace structures and those used in the offshore oil and gas industry. Hydrostatically loaded shells are typically designed using empirically-derived curves, which invoke a knock-down factor approach on the classical elastic buckling load (e.g., Refs. [5-7]). A significant research effort has been devoted to experimentally determining buckling pressures in order to study the mechanics involved in buckling, validate analytical theory and support the empirical design methodology.

Conventional methods for applying hydrostatic pressure to shell structure prototypes or experimental specimens are reviewed in this chapter. These procedures have been widely and successfully used to determine shell strength; however, under certain conditions they exhibit some significant drawbacks, especially a tendency to allow the specimen to be catastrophically deformed and ruptured during the buckling event. Catastrophic failures are undesirable because they make it difficult or impossible to: (1) identify the mode and location of initial failure in order to identify weak structural features, (2) compare the initial buckling mode with analytical or numerical predictions, and (3) study the structural behaviour during and after the buckling event.

The chapter begins with an explanation of load-, displacement- and generalized displacement-control, which are key concepts for the discussion of hydrostatic pressure testing to follow. Conventional pressure testing apparatus are then reviewed, followed by a description of the "volume-control" method, which was developed to address the deficiencies of conventional pressure testing methods. Simple expressions are presented for estimating the degree of control over the specimen deformation that can be expected for various pressure testing systems. The relative merits of conventional and volume-control systems are shown by examining the results of an experimental program, wherein both types of systems were used to test ring-stiffened cylinders. The chapter concludes with recommendations for choosing an appropriate pressure testing system for a particular problem.

Load- versus displacement-control

Structural strength testing and analysis can be divided into two broad categories when considering the application of the load: (1) "load-control" and (2) "displacement-control". Equilibrium path-following schemes used in nonlinear finite element (FE) analysis are the computational counterparts to experimental methods for the application of load. As such, the difference between load and displacement-control can be demonstrated to a large extent by examining a popular benchmark problem for nonlinear FE analysis of shells: a hinged cylindrical panel under a central load (Figure 8). This problem has been widely studied [81] because, depending on the particular geometry and material, these panels exhibit either or both types of dynamic "snapping": snap-through and snap-back, associated with limit points in the load and displacement, respectively. The thick line in Figure 8 represents the theoretical static equilibrium path for the panel defined by the parameters listed in Table 6 [81].

Load-control

Load-control refers to the monotonic application of a load to a structure. In nonlinear FE analysis, the load is applied incrementally and an iterative scheme is employed to achieve equilibrium, i.e., a balance of external loads and internal stresses [82]. When a local maximum in the load-displacement relationship (e.g., the load limit point in Figure 8) is reached, an experimental load-control system or FE analysis does not reduce the applied

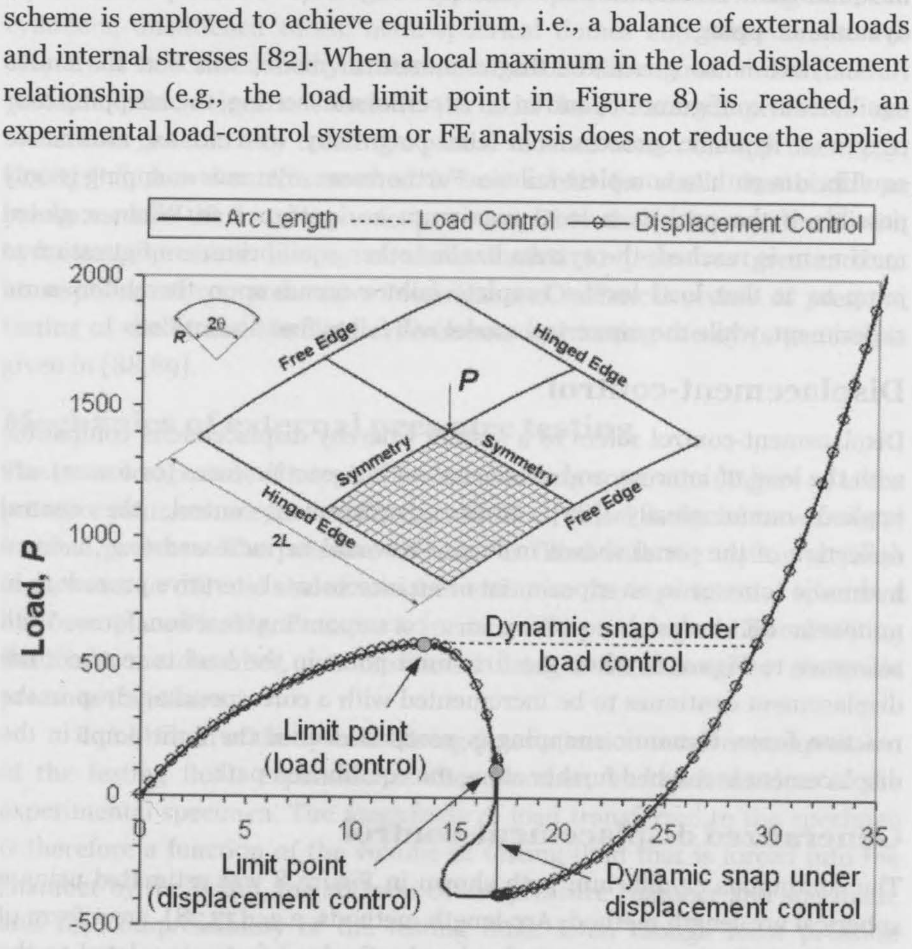

Figure 8: Benchmark load-displacement curve for the hinged cylindrical panel described by the parameters in Table 6, and under a central load.

Table 6: Geometry and material properties of hinged cylindrical panel.

Radius, R	2540
Length, L	254
Sweep angle, θ	0.1 radians
Thickness, h	6.35
Young's modulus, E	3102.75
Poisson's ratio, ν	0.3

load to follow the true, though unstable, equilibrium path; instead, equilibrium is maintained by "jumping" to an adjacent configuration that is in equilibrium, is stable and is at the same or greater load level. This is called dynamic snapping.

There is no guarantee that a numerical model will find the stable equilibrium configuration, and in an experimental setting, the snapping may trigger a dynamic process that can potentially lead to an alternative equilibrium path or complete failure. Furthermore, dynamic snapping is only possible if the peak is a local maximum as in Figure 8. When a global maximum is reached, the system has no other equilibrium configuration to jump to at that load level. Complete failure occurs soon thereafter in an experiment, while the numerical model will fail to find a solution.

Displacement-control

Displacement-control refers to a system whereby displacements compatible with the load of interest, and associated with a reaction force (or forces), are applied monotonically [82]. Under displacement-control, the central deflection of the panel shown in Figure 8 would be increased (e.g., using a hydraulic actuator in an experiment or an incremental-iterative procedure in nonlinear FE analysis), resulting in a corresponding reaction force. With reference to Figure 8, when the first limit point in the load is reached, the displacement continues to be incremented with a corresponding drop in the reaction force. Dynamic snapping is postponed until the limit point in the displacement is reached further along the equilibrium path.

Generalized displacement-control

The continuous equilibrium path shown in Figure 8 was estimated using a spherical arc-length method. Arc-length methods, e.g., [77,78], are a form of generalized displacement-control, whereby the load factor is related to the generalized displacements via a constraint equation that requires convergence to occur within a specified load-displacement "arc". The so-called "spherical" arc-length method operates in both the load and displacement domain, while the "cylindrical" arc-length procedure prescribes only the generalized displacements. Both methods have been shown capable of quasi-statically traversing snap-through and snap-back behaviour [65]. Generalized displacement-control is commonly used in numerical analyses, but it is more difficult to implement experimentally since more than one displacement parameter must be controlled, not to mention simultaneous control of the load.

External pressure testing techniques

Hydrostatic pressure tests are typically performed on ring-stiffened cylinders, unstiffened tubes, hemi-spherical domes and other shells. For cylindrical structures, the hydrostatic design load differs from radial (lateral) pressure, which does not include the axial load. External pressures are sometimes generated by creating a partial vacuum within the specimen, e.g., [43,83-87]; however, this method is only useful for shells that buckle at pressures less than atmospheric pressure. This thesis is concerned with hydrostatic pressure testing of shells loaded to pressures greater than atmospheric. A comprehensive historical and technical review of pressure testing of shells, and buckling experiments and testing theory in general, is given in [88,89].

Mechanics of external pressure testing

The main component of a typical pressure testing apparatus (Figure 9) is the pressure chamber: a cylindrical, typically steel, vessel designed to withstand internal pressure. The pressure chamber is filled with the testing medium (e.g., water or oil) and sealed at either end once the experimental specimen has been placed inside. Pressure is increased by pumping additional testing fluid into the chamber, and monitored using a manometer or electronic pressure transducer.

Equilibrium of the system during pressurization involves compression of the testing fluid, expansion of the chamber, and deformation of the experimental specimen. The magnitude of load transferred to the specimen is therefore a function of the volume of testing fluid that is forced into the chamber by the pump, the stiffness of the pressure chamber and specimen, and the compressibility of the testing fluid. Even though most pressure testing systems are controlled by monitoring the applied pressure and adjusting the pumping rate, loading is actually achieved by applying a volume-change to the specimen via the testing apparatus, i.e., the testing fluid. As such, this system is a form of generalized displacement-control.

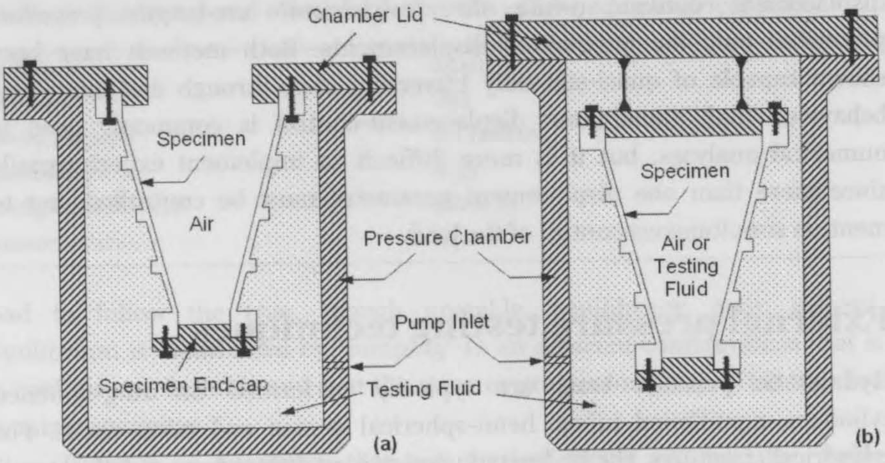

Figure 9: Conventional (a) open-ended and (b) closed-ended pressure testing apparatus.

The compressibility of a fluid is defined by its bulk modulus, B, and initial volume, V_o. The quotient of these values can be considered an equivalent stiffness, k^*, when relating the pressure applied to a fluid, δP, to the corresponding incremental volume change, δV [90]:

$$\delta P = \frac{B}{V_o}\delta V = k^* \delta V \tag{3}$$

The main difference between a conventional pressure testing system and a typical displacement-control test apparatus is the relatively greater compliance of the pressure testing fluid compared to traditional testing frames. This is due to the high compressibility of fluids compared to solids, as shown by the relatively low values of bulk modulus for fluids (e.g., the bulk moduli of water and steel are approximately 1.6 GPa and 170 GPa, respectively). The discrepancy is compounded in pressure chambers having a large ratio of testing fluid to specimen volume, since this further reduces the stiffness of the pressure testing system compared to the specimen. This results in a relatively large amount of strain energy being built up in the testing fluid during pressurization. Traditional testing frames can improve control of the load and displacement by increasing the frame stiffness, i.e., adding material. Conversely, in a pressure testing system this can be achieved by taking away test rig material, i.e., reducing the volume of testing fluid.

In conventional pressure testing, the prescribed deformation must be transferred through the elastic and highly compressible fluid component, rather than directly controlling the deformation of the specimen. This is a problem for pressure testing of buckling-critical shells, since buckling involves a rapid change in the manner of load resistance, from largely membrane stresses to a combination of membrane and bending stresses, and is often accompanied by a substantial loss of overall stiffness [91]. This system may be treated as quasi-static up to the occurrence of buckling, at which point the system behaves dynamically. The large and rapid deformations associated with buckling trigger the release of strain energy stored in the compressed testing fluid, resulting in undesirable catastrophic failure if some method of reducing, slowing down or absorbing the released energy is not present [27]. Some researchers have been able to reduce the damage at collapse by minimizing the volume of testing fluid, either by selectively proportioning their specimens and/or pressure chamber [95], or adding solid filler material to the test chamber [108]. However, these options are not always practical, e.g., when using an existing pressure chamber, or when filler blocks would interfere with the instrumentation.

Since conventional pressure testing systems are a form of generalized displacement-control, they are capable, in principle, of surpassing limit points in the load, although this does not rule out the possibility of snapping at limit points in the generalized displacements. In practice, the catastrophic nature of shell buckling events in combination with the associated release of energy stored in the testing fluid, means that the equilibrium path is not neatly traced beyond limit points when using traditional pressure testing methods.

Conventional external pressure testing methods

Pressure testing apparatus are constructed in either of two typical arrangements: (1) "open-ended" chambers, e.g., [44,54,92-106], and (2) "closed-ended" chambers, e.g., [107-126]. Figure 9(a) shows an open-ended pressure chamber, whereby the end-closure is designed to be directly attached to the specimen. The other end of the specimen must be sealed with an end-cap when testing a cylinder or truncated cone. Figure 9(b) shows a closed-ended arrangement, whereby both ends of the specimen are sealed with end-caps and the entire assembly is placed in the pressure chamber, which has a solid end-closure. Sealing of the end-caps and end-closures using o-rings or sealing compounds is normally required to achieve pressurization.

Open-ended pressure chambers allow access to the specimen during testing for observation (e.g., video recording) and instrumentation (e.g., strain gauges and displacement sensors); however, the specimens are necessarily "air-backed" in this system, so that it is difficult to control or absorb the energy released at collapse to check catastrophic failure. Closed-ended test setups can mitigate these effects by filling, or partially filling, the specimen with the testing fluid before pressurization, e.g., [120-126]. This helps to dampen the post-collapse motions. The compression of a fully fluid-backed specimen results in an internal pressure load on the specimen, which works against the applied external pressure. The net or differential pressure is taken as the chamber pressure less the internal specimen pressure. As with conventional air-backed arrangements, the deformation is applied to the specimen indirectly via the chamber testing fluid.

Some researchers have used an arrangement that involves venting the inside of a fluid-filled specimen to the exterior of the pressure chamber, e.g., [120-123]. This type of setup, shown in Figure 10(a), ensures that there is no back pressure in the specimen, at least during the quasi-static pre-buckling stage, and so it behaves like an air-backed system up to collapse while also dampening the specimen motions during the collapse event. Even so, as with the other conventional systems, direct control of the specimen deformation is not possible. A secondary advantage of this system is that the volume of fluid expelled from the specimen during testing (i.e., the volume change of the specimen) can be monitored and used to roughly estimate the load-deformation behaviour and identify the failure pressure [121].

Kinra [126] performed shell buckling tests using a closed-ended system and fluid-filled specimen with an outlet. The setup was the same as that shown in Figure 10(a), except that a valve controlled the flow of testing fluid at the outlet. Testing proceeded by closing the valve and applying pressure to the system. This pre-pressurizing stage is analogous to a fully fluid-backed closed-ended system, as discussed above, i.e., there is a net load on the specimen. After pre-pressurizing the system to the desired level, the valve was opened, letting the pressurized fluid escape from the specimen. This simultaneously reduced the chamber pressure and increased the load on the specimen. The valve was then closed, and the procedure was repeated with increasing levels of system pre-pressure until the specimen failed while the specimen fluid was being bled.

The system used by Kinra helped control the pre- and post-buckling motions, but had some drawbacks. Firstly, there was a risk of the specimen collapsing during pre-pressurization since it experienced a net load during this stage. Only the chamber pressure was monitored during testing, so the

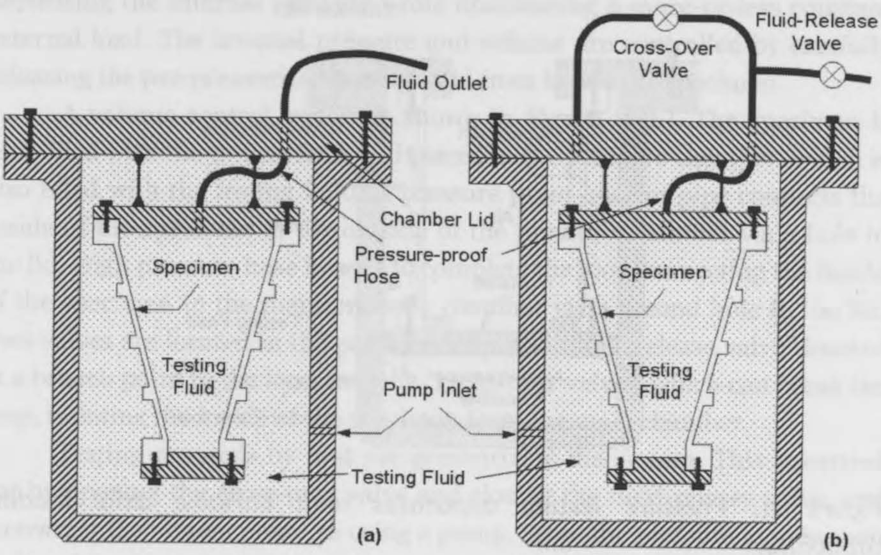

Figure 10: (a) Modified and (b) volume-control closed-ended pressure testing apparatus.

net load on the specimen would not have been known if it failed during pre-pressurization. Furthermore, the benefit of this system over other arrangements was the greater control of specimen deformation that was achieved by loading the specimen via the internal fluid; this advantage would be negated if the specimen failed during pre-pressurization. To ensure that the specimen did not fail at this stage, the final collapse load was approached incrementally. Finally, since only the chamber pressure was monitored, the collapse pressure could only be measured as bounded by the final two pressure increments in the chamber.

A substantially different method of applying hydrostatic pressure involves the application of radial pressure to the shell wall via a pressure chamber, in combination with some method of independently applying the axial load, e.g., using hydraulic actuators [127-134] or a second pressure chamber for the axial load [135,136]. Figure 11 shows an example of this type of system that uses two pressure chambers and two pumps to control the radial and axial load independently. This setup is typically used for the testing of offshore structures, which may be required to resist axial loads in excess of those due to hydrostatic pressure. This type of system is more flexible than conventional pressure testing methods since the axial load is not a fixed function of the radial load; however, it is more difficult to implement since the two loads must be controlled simultaneously.

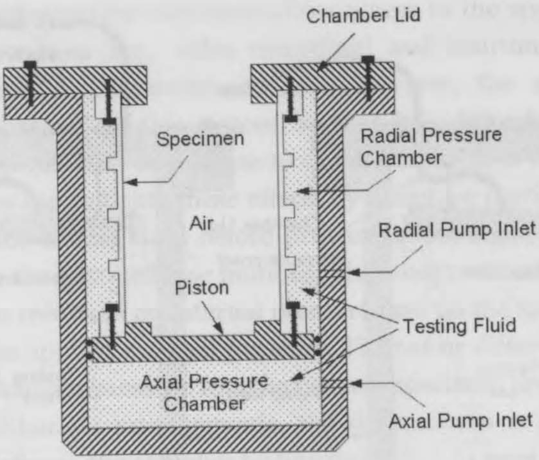

Figure 11: Pressure testing apparatus with variable axial loading capability.

A volume-control external pressure testing method

The main drawback of conventional pressure testing methods is that the deformation is applied to the specimen through a relatively compliant fluid medium that is uniformly loaded; that is, the stiffness of the testing system can only be increased by decreasing the volume of testing fluid, which, as mentioned earlier, is not always practical. The release of energy stored in the compressed testing fluid results in catastrophic buckling failures for air-backed specimens. For fluid-backed specimens, the post-buckling motions can be dampened, but the specimen deformation is still controlled indirectly by regulating the pressure in the chamber fluid via the pumping rate.

A pressure testing setup whereby the specimen deformation is managed more directly would allow the response of the specimen in the collapse and post-collapse regions to be better controlled and therefore studied more effectively. This chapter presents such a system, referred to hereafter as the "volume-control" pressure testing technique. The goal of this system is to control the bulk specimen deformation, i.e., the generalized displacements, by controlling the volume of the specimen. Such a system was used by Kinra [126], but it had some significant drawbacks that were related to the specimen being loaded during the pre-pressurization stage. In the volume-control system advocated in this chapter, the deficiencies of Kinra's method are addressed by uniformly loading the inside and outside of the specimen during pre-pressurization, i.e., no net load is applied to the specimen during pre-pressurization. The specimen is then loaded by decreasing the internal pressure while maintaining a more-or-less constant external load. The internal pressure and volume are controlled by carefully releasing the pre-pressurized testing fluid from inside the specimen.

A volume-control system is shown in Figure 10(b). The specimen is first filled with the testing fluid and placed in the pressure chamber, which is also filled with the testing fluid. A pressure proof hose or pipe connects the inside of the specimen to the outside of the pressure chamber via a hole in the lid. High pressure hose is used to complete the loop connecting the inside of the specimen to the main pressure chamber via a second hole in the lid. Two valves are located in the pressure loop: the "fluid-release valve" located at a branch point in the loop, and the "cross-over valve", which can break the loop, isolating the inside of the specimen from the main chamber.

Testing proceeds by first pre-pressurizing the system. This is carried out by opening the cross-over valve and closing the fluid-release valve, and increasing the system pressure using a pump. Since the pressure loop is open during this stage, the system pressure increases with a net pressure of zero on the specimen. Once the system is pre-pressurized to the desired load, the pump can be turned off for the duration of the test.

External pressure is applied to the specimen by closing the cross-over valve and opening the fluid-release valve, allowing the pressurized fluid to escape from the specimen. This allows the specimen to deform and the fluid inside the specimen to expand, resulting in a decrease of internal specimen pressure and thus an increase in the net external pressure load on the specimen. Pressure in the main chamber and the specimen are monitored throughout loading; the net load on the specimen at any time is equal to the chamber or tank pressure less the specimen's internal pressure.

Of course, the amount of pre-pressure must be greater than the expected test or collapse load to allow for a loss in chamber pressure as the specimen contracts. The required additional pre-pressure depends on the volume and stiffness of both the chamber and the specimen. The load can be reversed at any point by closing the fluid-release valve and opening the cross-over valve, allowing the system to achieve equilibrium.

The rate of pressure loading is controlled by the amount of fluid released from the specimen (thus, "volume-control"). The volume-control technique is therefore a form of generalized displacement-control whereby the controlled parameter is the volume of fluid removed from the specimen rather than the volume of fluid pumped into the chamber, as in conventional pressure testing methods. If the specimen volume is significantly less than the chamber volume, the specimen fluid will be significantly less compliant than the fluid in the chamber. This is analogous to using a stiffer testing frame in a displacement-control test, and should allow better control of specimen deflections than with conventional methods. Loading with the volume-control method proceeds by slowly releasing the pre-pressurized fluid from the system, which is an improvement over the conventional method of forcing extra fluid into the system using a pump.

Control of specimen deformation using various pressure testing methods

For any given test rig for shell buckling experiments, it is desirable to estimate the amount of control over the specimen displacement that is available in order to compare systems and make informed choices when planning an experimental program. In this context, "control" is a measure of how completely the applied displacement of a test rig is passed on to the shell specimen. Ideally, the test rig will be infinitely stiff, so that the applied displacements are passed on to the specimen in a one-to-one manner. This is important because, even though the stiffness of the test rig does not influence the quasi-static pre-buckling path or the buckling load, the dynamic post-buckling behaviour of the specimen will be affected by the test rig stiffness [89]. The same applies to the specific case of externally pressurized shells, the relevant test rig in this case being the testing fluid. The post-buckling behaviour is influenced through the release of the built-up strain energy in the testing fluid, as mentioned earlier, so that the test rig, i.e., the fluid, should be as stiff as possible in order to minimize the accumulation of energy.

The degree of control of the generalized shell displacement for external pressure tests is estimated in this chapter in two ways: (1) by determining the change in volume of the specimen, Δu_2, relative to the applied volume change in the testing system, Δu_1, for the pre-buckling path (also applicable to limit-point buckling that does not involve a sudden loss of specimen load-carrying capability); and (2) by determining the change in specimen volume, Δu_2, as a result of the abrupt loss of load-carrying capability experienced during collapse, while Δu_1 is fixed at zero. Δu_1 is the amount of fluid pumped into the pressure chamber for conventional systems and the volume of fluid released from the specimen for volume-control systems.

Perfect specimen control in the pre-buckling range is indicated by a $(\Delta u_2/\Delta u_1)$ ratio of unity; that is, one unit of volume change in the testing apparatus results in one unit of specimen deformation. However, $(\Delta u_2/\Delta u_1)<1$ is normal for the practical setting since the testing fluid must have a finite compressibility and the specimen a finite stiffness (at least before buckling occurs). The degree of control of a particular system can be estimated by how close this value approaches unity, which is analogous to an infinitely stiff testing rig.

Spring diagrams for pressure testing systems

The ($\Delta u_2/\Delta u_1$) ratio, referred to hereafter as the "relative displacement", can be estimated by studying equilibrium and associated rate equations for equivalent spring diagrams representing pressure testing systems. Spring diagrams developed for conventional and volume-control systems are shown in Figure 12 and Figure 13, respectively. The stiffness of the springs representing the chamber fluid, specimen fluid and specimen are indicated by k_{cf}, k_{sf} and k_s, respectively. Figure 12(c), representing a conventional fluid-filled system with an outlet, includes a dashpot with damping constant, c_{sf}, to indicate the damping action of the specimen fluid.

In these diagrams, the specimen is represented as a coil, indicating a nonlinear spring. The internal force in the specimen spring, F_s, is a nonlinear function, g, of its elongation, Δl_s=-u_2. The specimen is not represented in the pre-pressurization stages for the volume-control arrangement, since the net load on it is zero. The stiffness of the pressure chamber itself, which is normally relatively large, is neglected. These diagrams and the following derivations refer to displacements and forces; however, these parameters are analogous to volumes (or generalized-displacement) and pressures in a pressure testing system.

Development of the equilibrium equations

For the pressure testing systems discussed here, equilibrium dictates that the force in the chamber fluid spring, F_{cf}, must be balanced by the force in the specimen spring, F_s, plus the force in the specimen fluid spring, F_{sf}, if applicable:

$$F_{cf} = F_s + F_{sf} \qquad (4)$$

The evaluation of each of the forces in Eq. (4) depends on the pressure testing system being studied. This is straightforward for conventional systems: the force in a spring is the product of its stiffness and net elongation, Δl. However, for a volume-control system, the total force in the chamber fluid and specimen fluid springs is the force resulting from pre-pressurizing the system, F_o, plus the internal spring force as the specimen is loaded. The force expressions for the various pressure testing systems are summarized in Table 7.

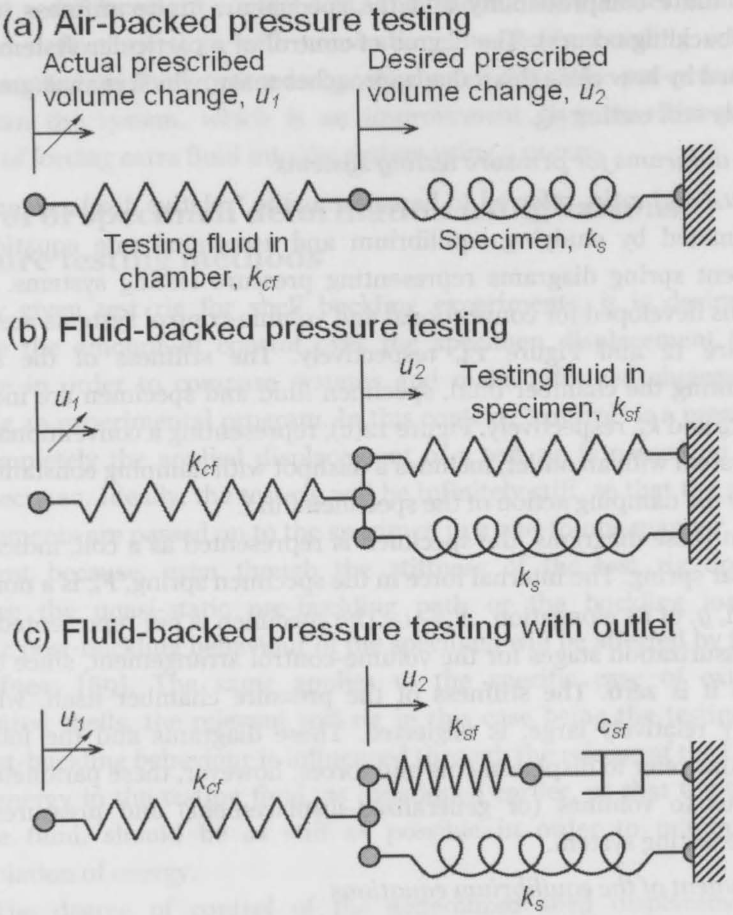
(a) Air-backed pressure testing
Actual prescribed volume change, u_1
Desired prescribed volume change, u_2
Testing fluid in chamber, k_{cf}
Specimen, k_s
(b) Fluid-backed pressure testing
u_2
Testing fluid in specimen, k_{sf}
u_1
k_{cf}
k_s
(c) Fluid-backed pressure testing with outlet
u_2
u_1
k_{sf}
c_{sf}
k_{cf}
k_s

Figure 12: Schematic spring diagrams of conventional pressure testing systems (a sloping arrow indicates the control variable).

Pre-buckling relative displacement expressions

An equilibrium expression for each pressure testing method is given by substituting the appropriate spring force expressions from Table 7 into Eq. (4). The sensitivity of the system to an incremental volume change can be studied by taking the derivative of each term in the equilibrium expression with respect to time, which results in a rate equation for each method. For example, the equilibrium equation for a conventional air-backed system is shown below:

$$k_{cf}\left(u_2 - u_1\right) = g[\Delta l_s] = g[-u_2]. \tag{5}$$

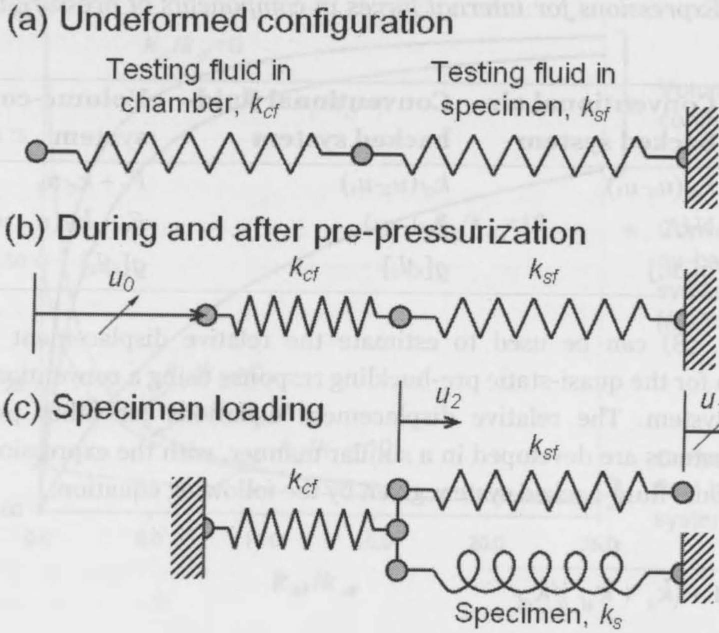
(a) Undeformed configuration
Testing fluid in chamber, k_{cf}
Testing fluid in specimen, k_{sf}
(b) During and after pre-pressurization
u_0
k_{cf}
k_{sf}
(c) Specimen loading
u_2
u_1
k_{sf}
k_{cf}
Specimen, k_s

Figure 13: Schematic spring diagram of a volume-controlling pressure testing system (a sloping arrow indicates the control variable).

Taking the time derivatives of the displacement and force terms in Eq. (5) yields the following rate equation:

$$k_{cf}\left(\dot{u}_2-\dot{u}_1\right)=\dot{g}\left[-u_2\right]=-\frac{dg}{d\Delta l_s}\dot{u}_2=-k_s\dot{u}_2 \qquad (6)$$

In Eq. (6), the derivative of the specimen spring force, *g*, with respect to its elongation, Δl_s is replaced by the tangent stiffness of the specimen, k_s. The resulting rate equation can be written in incremental notation in order to study the effects of small changes in the displacement:

$$k_{cf}\left(\Delta u_2-\Delta u_1\right)\approx -k_s\Delta u_2 \qquad (7)$$

Finally, by rearranging the terms in Eq. (7), the relationship between the relative displacement and the various spring stiffnesses can be expressed:

$$\frac{\Delta u_2}{\Delta u_1}\approx\frac{k_{cf}}{k_{cf}+k_s}=\frac{1}{1+k_s/k_{cf}} \qquad (8)$$

Table 7: Expressions for internal forces in components of pressure testing systems.

Force	**Conventional air-backed system**	**Conventional fluid-backed system**	**Volume-control system**
F_{cf}	$k_{cf}(u_2-u_1)$	$k_{cf}(u_2-u_1)$	$F_0+k_{cf}u_2$
F_{sf}	N/A	$k_{sf}(-u_2)$	$F_0+k_{sf}(u_1-u_2)$
F_s	$g[\Delta l_s]$	$g[\Delta l_s]$	$g[\Delta l_s]$

Eq. (8) can be used to estimate the relative displacement of the specimen for the quasi-static pre-buckling response using a conventional air-backed system. The relative displacement equations for other pressure testing systems are developed in a similar manner, with the expression for a conventional fluid-backed system given by the following equation:

$$\frac{\Delta u_2}{\Delta u_1}\approx\frac{1}{1+\left(k_s+k_{sf}\right)/k_{cf}}. \tag{9}$$

The relative displacement equation for the volume-control system is shown below:

$$\frac{\Delta u_2}{\Delta u_1}\approx\frac{1}{1+\left(k_s+k_{cf}\right)/k_{sf}}=\frac{k_{sf}}{k_{cf}}\left(\frac{1}{1+\left(k_s+k_{sf}\right)/k_{cf}}\right). \tag{10}$$

The system used by Kinra [126] behaves like a conventional fluid-backed system, i.e., Eq. (9), during pre-pressurization and like a volume-control system, i.e., Eq. (10), during the loading stage.

The relative performance of the various systems in the pre-buckling range may be studied by examining the behaviour of the relative displacement equations. Figure 14 shows the relative displacement for each system as the ratio of specimen fluid to chamber fluid stiffness (k_{sf}/k_{cf}) is varied, while fixing the ratio of specimen to chamber fluid stiffness (k_s/k_{cf}) at finite values. Figure 14, along with Eqs. (8) and (9), indicates that specimen control for a conventional air-backed system will always be better than for a similar conventional fluid-backed system, since the chamber fluid in a fluid-backed system must work against both the specimen and specimen fluid stiffness. This suggests that the main advantage of a fluid-backed system (without an outlet) is the damping effect of the fluid during buckling. A fluid-backed system with an outlet behaves like an air-backed system for the quasi-static pre-buckling region, and is thus governed by Eq. (8). So, it has the advantage of greater pre-buckling specimen control relative to a fluid-

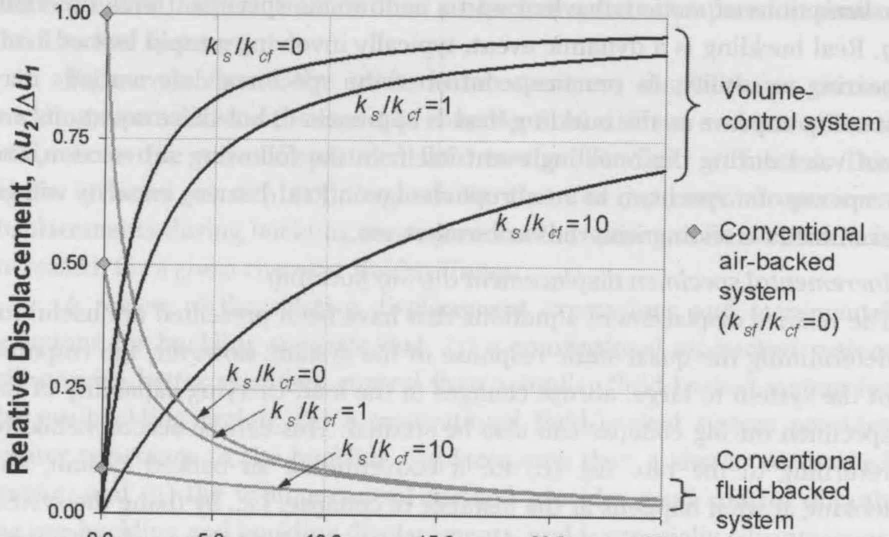

Figure 14: Relative displacement of pressure testing systems determined by varying the ratio of specimen fluid to chamber fluid stiffness while fixing other parameters.

backed system without an outlet, and also provides damping to buckling motions.

Eqs. (9) and (10) indicate that the relative displacement of a volume-control system is given by the relative displacement of a similar conventional fluid-backed system, multiplied by the ratio of the stiffnesses of the fluid in the specimen and the chamber. If it is assumed that the same testing fluid is used in the specimen and the chamber, this implies that a conventional fluid-backed system will perform better in the pre-buckling stage if the volume of chamber fluid is less than the volume of fluid in the specimen. Conversely, if the internal volume of the shell specimen is less than the volume of fluid in the pressure chamber, the volume-control method will show better performance. This is shown in Figure 14 by the coincidence of the relative displacement of the volume-control and fluid-backed systems at (k_{sf}/k_{cf})=1. This figure also shows that when the specimen stiffness is negligible compared to the fluid stiffnesses, a conventional air-backed system will have the greatest relative displacement.

A common feature of Eqs. (8) through (10) is that control of specimen deformation is predicted to increase as the specimen stiffness, k_s, approaches zero, i.e., as the buckling load is approached. These expressions are based on assumptions of static behaviour and a continuous specimen force function, g. Real buckling is a dynamic event, typically involving a rapid loss of load-bearing capability. In practice, control of the specimen deformations may steadily improve as the buckling load is approached, but these equations are not valid during the buckling event itself. In the following sub-section, the response of a specimen to an abrupt change in load-bearing capacity will be examined for testing with the various systems.

Incremental specimen displacement during buckling

The relative displacement equations that have been presented are useful for determining the quasi-static response of the system; however, the response of the system to large, abrupt changes in the load-carrying capability of the specimen during collapse can also be studied. This can be accomplished by returning to the rate Eq. (6) for a conventional air-backed system, and looking at what happens at the instance of collapse, i.e., by fixing the system displacement, u_1, and determining the incremental specimen displacement relative to a change in the internal specimen force function, g. The rate equation is given by:

$$k_{cf}\left(\dot{u}_2 - \dot{u}_1\right) = \dot{g}. \tag{11}$$

The incremental change in specimen displacement for a given change in specimen load-bearing capability is given by setting $\dot{u}_1$ in Eq. (11) equal to zero, and switching to incremental notation:

$$\Delta u_2 \approx \frac{\Delta g}{k_{cf}}. \tag{12}$$

A similar procedure yields the following expression, which applies to conventional fluid-backed as well as volume-control systems:

$$\Delta u_2 \approx \frac{\Delta g}{k_{cf} + k_{sf}}. \tag{13}$$

Eq. (13) can also be applied to a conventional air-backed system by substituting a value of zero for k_{sf}. Since the incremental displacement of the specimen at collapse is inversely proportional to the sum of the stiffnesses of the various fluids in the system, any fluid-backed system will tend to arrest the buckling displacements better than an air-backed system. These incremental equations do not take dynamic effects, i.e., inertia and the damping effects of the internal specimen fluid, into account, which would further reduce the performance of an air-backed system compared to similar fluid-backed systems.

Figure 15 shows the incremental specimen displacement during buckling, normalized with respect to chamber fluid stiffness and incremental load, versus the ratio of specimen fluid to chamber fluid stiffnesses. This figure is based on Eq. (13), and shows that the incremental specimen displacements during buckling are reduced as the specimen fluid stiffness is increased, for a given chamber fluid stiffness.

A review of the relative displacement expressions and incremental equations for buckling suggests that: (1) a conventional air-backed system will provide better specimen control than a similar fluid-backed system for the pre-buckling region; (2) a conventional fluid-backed system provides greater resistance to the buckling displacements than a similar air-backed system; and (3) the volume-control method provides good control of both the pre-buckling and buckling displacements, and is especially advantageous for large values of (k_{sf}/k_{cf}), i.e., for large pressure chambers in relation to specimen volume.

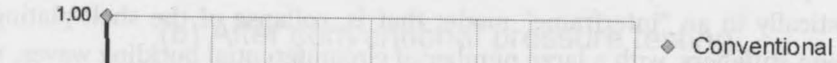

Figure 15: Incremental specimen displacement during buckling, normalized with respect to chamber fluid stiffness and incremental load, versus the ratio of specimen fluid to chamber fluid stiffnesses.

Experimental studies

An experimental program was undertaken whereby stiffened shells were pressure tested to collapse using a conventional closed-ended air-backed method for some specimens [27] and the volume-control method for others [28]. These experiments allowed comparison of the volume-control method with a conventional technique, and provided validation (or invalidation) of several conjectured features of the former method; namely its ability to: (1) apply external pressure to a shell specimen, (2) prevent catastrophic buckling failures, (3) preserve the initial collapse mode of the shell specimen, and (4) allow control of the specimen deformation, especially near the critical load. The following sections present a brief overview of the test specimens, followed by the results of the testing program, especially with respect to validation of the various features of volume-control testing listed above.

Test specimens and experimental setup

The pressure testing of three different types of experimental shell specimens, referred to hereafter as "short", "long" and "unstiffened", is examined*. The short specimens (Figure 16) were ring-stiffened cylinders, designed to fail inelastically in an "interframe" mode; that is, collapse of the shell plating between stiffeners, with a large number of circumferential buckling waves, $n \geq 5$ [10]. Long specimens (Figure 17) were ring-stiffened cylinders that were designed to fail inelastically in an "overall" mode; that is, the combined collapse of rings and shell, with $n \leq 4$ [10]. This testing program was also designed to study the strength-reducing effect of material loss due to corrosion by machining away shell and stiffener material on selected specimens. As such, the long ring-stiffened cylinders have been artificially "corroded" by machining away material on the stiffener flange in a "dog-bone" pattern, as shown in the inset of Figure 17(a).

The unstiffened specimen (Figure 18) was an aluminium tube of uniform shell thickness, having roughly the same dimensions as the long ring-stiffened cylinder. The unstiffened specimen was designed to fail by

---

* The short and long cylinders are described in greater detail in Chapter 4, starting on p. 77. The short cylinders tested using the conventional and volume-control methods are referred to as L300-No2 and L300-No1, respectively, in Chapter 4 and other chapters. The long cylinder tested with the conventional method is L510-No2, and its nominally identical counterpart, L510-No3, was tested with the volume-control method. Testing of the unstiffened cylinder is not covered elsewhere in this thesis, but numerial simulations of the specimen are presented in Chapter 7, starting on p. 153. The cylinder is referred to as L510-Test in that chapter.

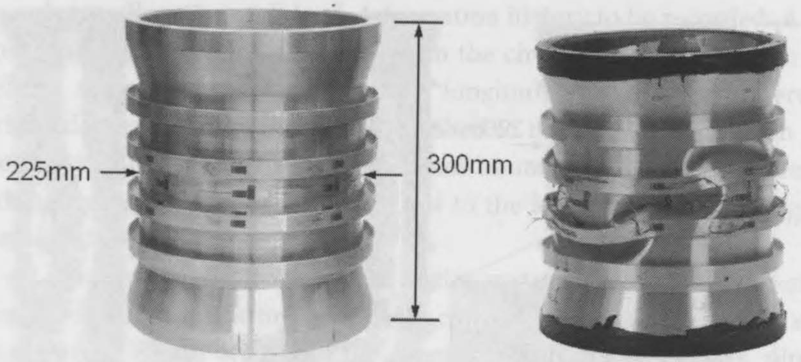

(a) Before pressure testing

(c) After volume-control pressure testing

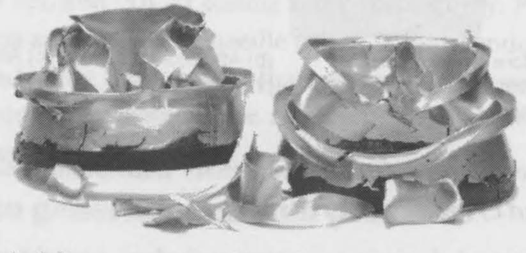

(b) After conventional pressure testing

Figure 16: Typical short cylinder specimens (a) before and (b and c) after pressure testing.

elastic buckling with three or four buckling waves about the circumference, distributed in a half wave over the length.

All test specimens were machined from solid aluminium tubing. The overall sizes of the short, long and unstiffened specimens are shown in Figure 16(a), Figure 17(a) and Figure 18(a), respectively. Detailed descriptions of the test specimens are given in [27,28]. Measurement of the fabricated specimens indicated that the maximum initial geometric imperfections were less than 0.1 times the mean shell thickness for all specimens discussed in this chapter.

Two short and two long ring-stiffened cylinders have been tested, using both conventional and volume-control methods for comparison. A single unstiffened cylinder was tested using the volume-control method. Before testing, whether conventional or volume-control, heavy steel end-caps were attached to either end of the specimen with bolts, and the end-cap joints were made watertight using an adhesive polymer sealant.

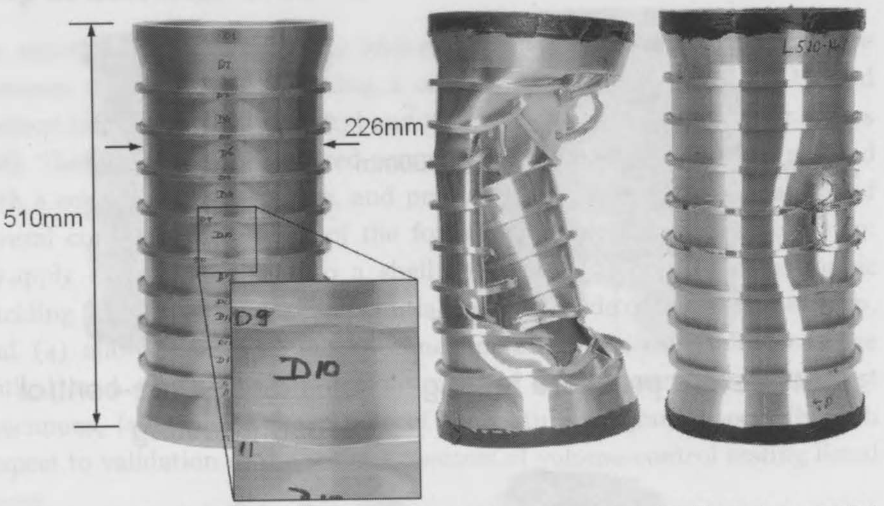

(a) Before pressure testing, with inset showing "dog-bone corrosion"

(b) After conventional pressure testing

(c) After volume-control pressure testing

Figure 17: Typical long cylinder specimens with simulated corrosion (a) before and (b and c) after pressure testing.

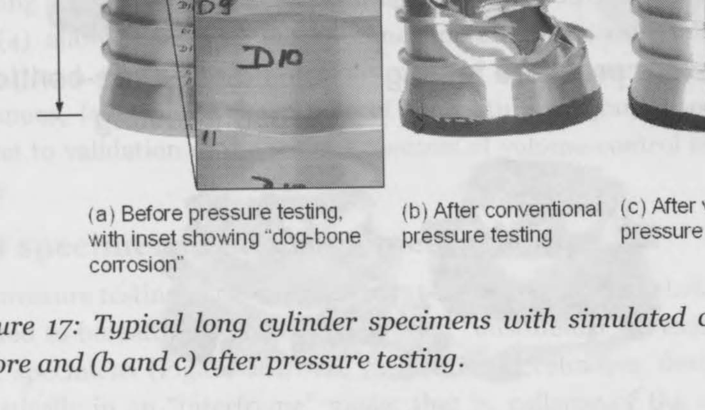

(a) Before pressure testing

(b) After volume-control pressure testing

Figure 18: Unstiffened specimen (a) before and (b) after pressure testing.

Strain gauges were attached to selected cylinders at critical locations in order to allow their full load-deformation history to be recorded. A typical specimen had strain gauges oriented in the circumferential direction on the central stiffener flanges, as well as longitudinally and circumferentially oriented gauges on the outside of the shell in the central bay. Strain gauges were distributed about the circumference in uniform 30° or 45° increments. Additional strain gauges were attached to the long cylinder in the region of simulated corrosion.

The volume-control pressure testing system used in these experiments was produced by outfitting an existing conventional pressure testing system, as shown in Figure 9(b), with the necessary high pressure hoses, pipes and valves as shown in Figure 10(b). The pressure chamber has an internal volume of approximately 1600L, while the short and long specimens displaced about 12L and 20L of testing fluid, respectively. Precise control of the fluid flow was achieved using needle valves. A non-conductive mineral oil was used as the testing fluid, rather than water. This prevented shorting of the electronic equipment without the requirement to seal strain gauges and lead wires against water infiltration.

Capability to generate external pressure

The full loading history, including system pre- and de-pressurization, was not recorded for the specimens discussed in this chapter; however, Figure 19 shows a typical loading history for the volume-control system used in these tests, recorded during the pressure testing of a similar ring-stiffened cylinder[*]. The markers on the time axis (t_o, t_1, *etc.*) indicate milestones in the testing procedure. These milestones, as well as time intervals (e.g., t_2-t_3), will be referred to in the following discussion. Table 8 summarizes the status of the pump and valves during the various stages of testing.

The cross-over valve is open for system pre- and de-pressurization (t_o-t_1 and t_5-t_6, respectively), which is indicated by the coincidence of the chamber and specimen pressures in Figure 19. This valve is closed during specimen loading (t_2-t_4), which is undertaken by releasing the testing fluid from inside the specimen via the fluid-release valve. The pre-collapse portion of the loading history (t_2-t_3) shows a steadily decreasing loading rate. This results from setting the fluid-release valve once, at the onset of loading, after which the internal specimen pressure is continuously decreasing and, correspondingly, the flow rate of the fluid escaping from the specimen.

---

[*] The loading history shown in Figure 19 is for specimen L300-No6A, which is described in Chapter 5, starting on p. 107.

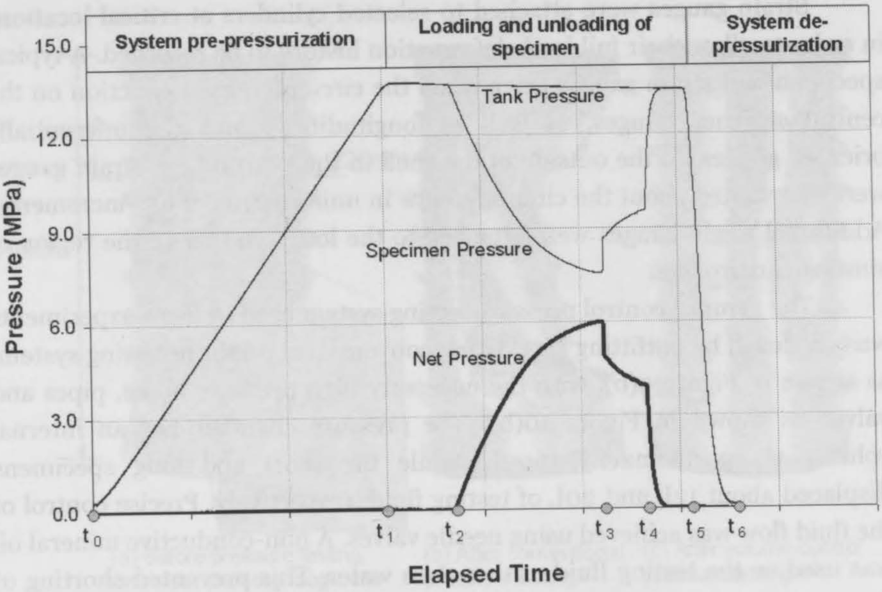

Figure 19: Complete load history for a typical volume-control pressure test.

Table 8: Stages of a volume-control pressure test.

Time Interval	Process	Pump	Cross-over valve	Fluid-release valve
t_0-t_1	System pre-pressurization	On	Open	Closed
t_1-t_2	Checking equipment	Off	Open	Closed
t_2-t_3	Loading (pre-collapse)	Off	Closed	Open
t_3-t_4	Loading (post-collapse)	Off	Closed	Open
t_4-t_5	Unloading	Off	Open	Closed
t_5-t_6	System de-pressurization	Off	Open	Open

Collapse of the specimen is indicated by a sharp drop in net pressure at t_3, followed by a steadily dropping net pressure as the specimen is loaded into the post-collapse region (t_3-t_4). The fluid-release valve is closed at t_4, preventing further deformation of the specimen, and the cross-over valve is opened allowing the system to reach equilibrium and thus unloading the specimen (t_4-t_5).

The general capability of the volume-control system to apply external hydrostatic pressure to a shell specimen is indicated by the net pressure load shown in Figure 19. The response of the strain gauges indicated that the experimental pressure-strain relationships were in good agreement with numerical predictions for these specimens [51]*.

Prevention of catastrophic buckling failure

Figure 16(b) and Figure 17(b) show typical specimens after conventional air-backed pressure testing, which resulted in catastrophic failures with a high degree of material rupture, such that the immediate post-collapse shape was difficult to identify. Figure 16(c) and Figure 17(c) show typical short and long specimens after volume-control pressure testing; these cylinders were nominally identical to those shown in Figure 16(b) and Figure 17(b), respectively. Catastrophic failures were avoided while using the volume-control method, so that the final post-testing configurations were easily distinguishable. This was due to a combination of damping and stiffness associated with the internal specimen fluid, which slowed down and arrested the collapse event, respectively.

Preservation of the initial collapse mode

The shape of certain specimens, up to and including the collapse load, has been shown by the strain gauge data to be a more-or-less regular sinusoidal pattern in the circumferential direction, while the deformations in the post-collapse region were dominated by a single lobe of this collapse shape. For example, Figure 20 shows the distribution of circumferential strain in the unstiffened cylinder just before collapse and again after collapse had occurred and the specimen was completely unloaded. At collapse, the strain gauges indicate that the specimen has been deformed into roughly four circumferential waves, while the final configuration after unloading indicates that a single lobe of the collapse mode has dominated the post-collapse behaviour. This was confirmed by inspection of the cylinder after it was removed from the pressure chamber.

Figure 18(b) shows the unstiffened cylinder after it was tested to collapse and removed from the pressure chamber, and then loaded in the pressure chamber a second time to determine its “residual strength”. The residual strength test resulted in significant permanent deformation, with the formation of three circumferential lobes. This will be discussed further in the context of snap-through buckling.

While control of the post-collapse deformations has been significantly improved with respect to a conventional air-backed pressure testing method,

---

* See also Chapter 7, p. 153.

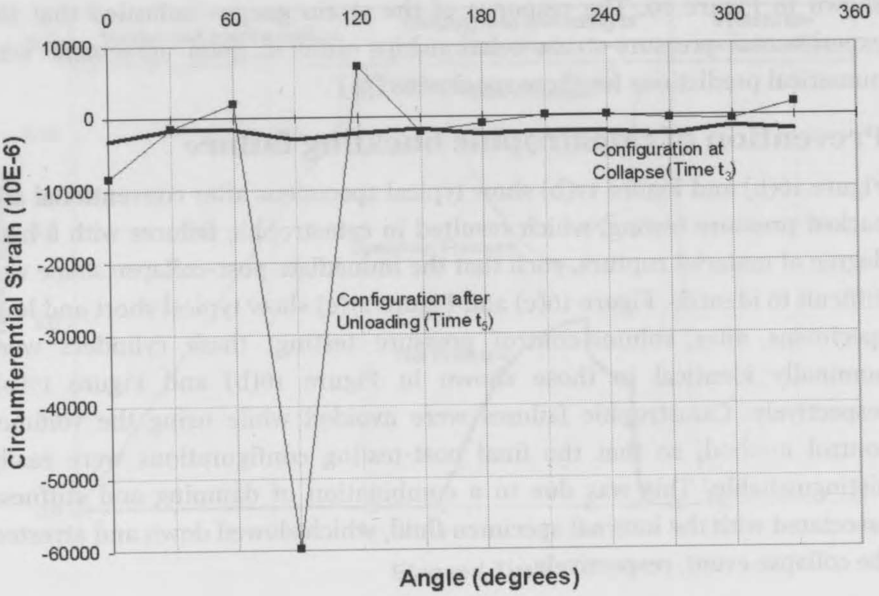

Figure 20: Circumferential distribution of circumferential strain outside the shell at mid-length in the unstiffened cylinder.

the preservation of the initial collapse mode in the cylinder specimens after volume-control testing was not always possible, even when the testing was stopped immediately after the occurrence of collapse. This is a consequence of using the volume-control method of testing, which regulates the generalized displacement, and represents a test rig with finite stiffness, i.e., the finite stiffness of the testing fluid in the specimen. This emphasizes the importance of tracking pre- and post-collapse deformations with strain gauges in order to fully understand the collapse behaviour of the specimens and to make authentic comparisons between experimental and numerical results.

Of course, evidence of a purely elastic instability event would not be shown by the final specimen configuration after testing, since the specimen would be returned to its original shape after the load was removed. In the case of the unstiffened cylinder, collapse occurred while the material, at least at strain gauge locations, was still in the elastic range. The volume-control system allowed the buckling deformations to be controlled to such an extent that the strains could be traced and the collapse mode determined; however, the violence of the buckling event was not mitigated to the degree that permanent deformations were avoided.

Control of specimen deformation near the critical load

Figure 21 shows partial load histories for the short and long cylinders tested using the volume-control method; system pre- and de-pressurization stages are not shown, and only the net pressures are plotted for the loading and unloading stages. Times corresponding to milestones in the testing procedure (see Table 8) are indicated for each test. The "kink" in the load history for the long cylinder at approximately 240 seconds is due to an adjustment that was made to the fluid-release valve to increase the flow (and loading) rate.

For the short cylinder, the formation of the initial buckling lobe is indicated in the net pressure history by a slight drop in pressure at t_3. The cylinder was loaded slightly into the post-collapse region (t_3-t_4), and then unloaded (t_4-t_5) by opening the cross-over valve. Figure 16(c) shows the short cylinder after it was loaded a second time (i.e., to determine its residual strength), well into the post-collapse region, resulting in the formation of several lobes in a classical interframe buckling pattern.

During collapse, the rapidly decreasing shell volume due to inward buckling encounters resistance from the pressurized fluid inside the specimen. If the testing fluid were infinitely stiff, this would represent a limit

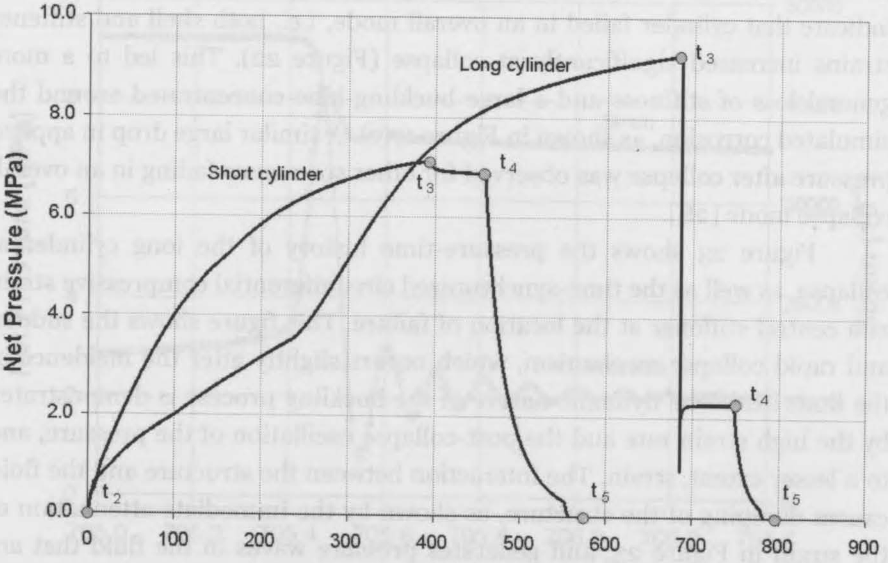

Figure 21: Partial load history for short and long cylinders during volume-control testing.

point in the generalized displacement. Inward buckling results in a sharp increase in the internal specimen pressure, and corresponding decrease in net pressure.

Tests undertaken with a conventional air-backed setup provided very little information after the peak collapse load was reached, as the rapid and catastrophic buckling event caused the strain gauges and lead wires to be torn from the cylinders. Using the volume-control method, it was possible to trace the specimen behaviour during and after collapse. Strain gauges located about the circumference of the short cylinder indicated that initial collapse (at time t_3 in Figure 21) resulted in a proportionally greater increase in shell strains compared to stiffener strains (Figure 22). The largest shell strains were concentrated in one or two adjacent locations, indicating a small, localized buckle in the shell. These features are characteristic of interframe collapse. The strain data also indicate that the initial buckling mode was amplified in the post-collapse region, and resulted in permanent deformation that was observable after the test was completed. Since the buckling mode for the short cylinder was a small, localized lobe or dimple, the corresponding reduction in specimen volume was negligible.

The load history in Figure 21 shows that the drop in net pressure at collapse (at time t_3) was much greater for the long cylinder. Circumferentially distributed strain gauges on the shell and ring-stiffeners indicate that cylinder failed in an overall mode, i.e., both shell and stiffener strains increased significantly at collapse (Figure 22). This led to a more general loss of stiffness and a large buckling lobe concentrated around the simulated corrosion, as shown in Figure 17(c). A similar large drop in applied pressure after collapse was observed for other specimens failing in an overall collapse mode [28].

Figure 23 shows the pressure-time history of the long cylinder at collapse, as well as the time-synchronized circumferential compressive strain at a central stiffener at the location of failure. This figure shows the sudden and rapid collapse mechanism, which occurs slightly after the incidence of the limit load. The dynamic nature of the buckling process is demonstrated by the high strain rate and the post-collapse oscillation of the pressure, and to a lesser extent, strain. The interaction between the structure and the fluid causes damping of the structure, as shown by the immediate attenuation of the strain in Figure 23, and generates pressure waves in the fluid that are more slowly attenuated.

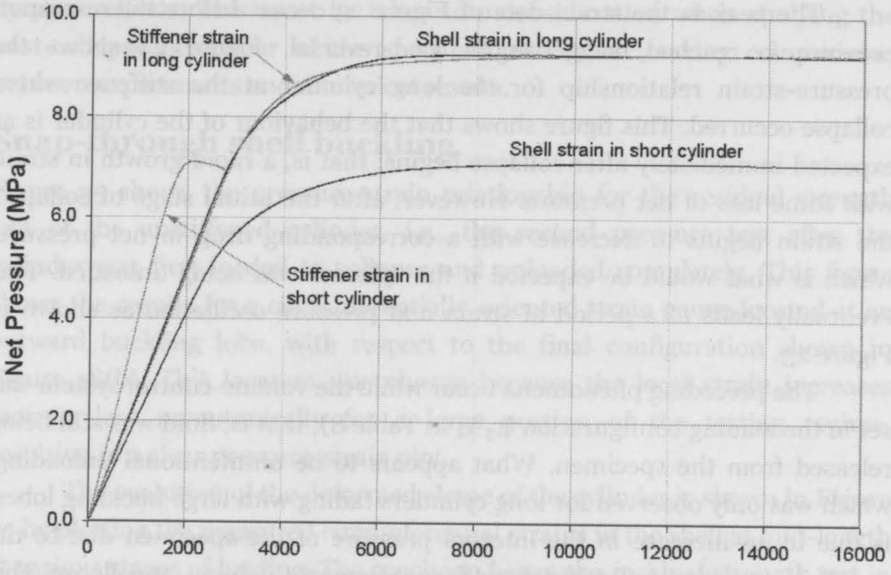

Figure 22: Pressure-strain plots at location of initial collapse for short and long cylinders.

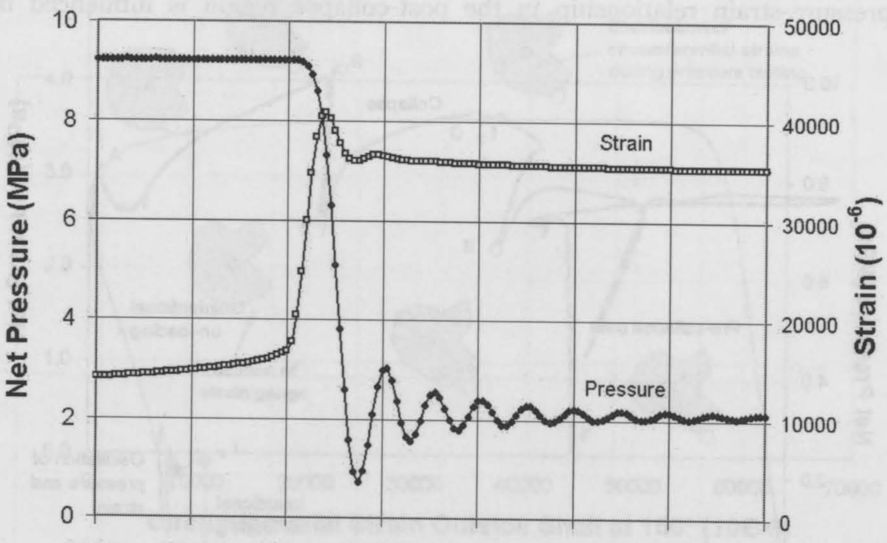

Figure 23: Pressure and strain history for long cylinder at collapse (100Hz sampling rate).

The peak in the strain data of Figure 23 occurs before the minimum pressure is reached, suggesting a load-reversal. Figure 24 shows the pressure-strain relationship for the long cylinder at the stiffener where collapse occurred. This figure shows that the behaviour of the cylinder is as expected immediately after collapse begins; that is, a rapid growth in strain with some loss of net pressure. However, after the initial stage of collapse, the strain begins to decrease with a corresponding drop in net pressure, which is what would be expected if the cylinder was being unloaded. This eventually leads to a period of strain and pressure oscillation as shown in Figure 23.

The preceding phenomena occur while the volume-control system was set in the loading configuration (t_3-t_4 in Table 8); that is, fluid was still being released from the specimen. What appears to be unintentional unloading, which was only observed for long cylinders failing with large buckling lobes, is due to an increase in the internal pressure of the specimen due to the rapidly decreasing shell stiffness and, consequently, volume, at collapse. This arises due to the stiffness of the internal specimen fluid, and is a necessary outcome of arresting the collapse event before the specimen is completely ruptured. The volume-control system can slow down and arrest buckling, but it cannot completely control the buckling event, so that the resulting pressure-strain relationship in the post-collapse region is influenced by

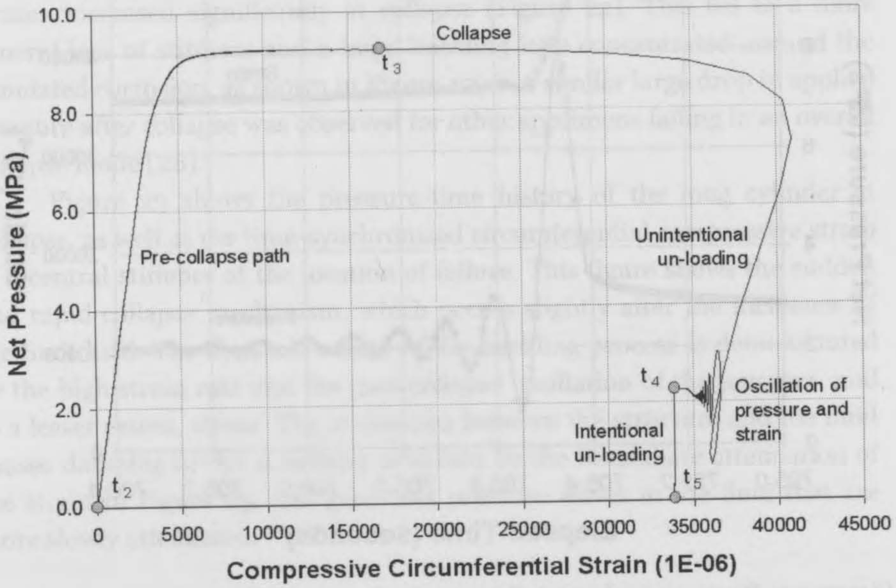

Figure 24: Pressure-strain relationship at the stiffener of the long cylinder.

dynamic effects. This must be taken into consideration when studying the post-collapse behaviour of the specimen and when making comparisons between experiments and numerical results.

Snap-through shell buckling

Figure 25 shows the pressure-strain relationship for the residual strength test of the unstiffened cylinder, i.e., the second pressure test after the cylinder was first loaded to collapse and unloaded completely. This figure shows the results for a circumferentially-oriented strain gauge located at an outward buckling lobe, with respect to the final configuration shown in Figure 18(b). This location was chosen because the local strain increases more-or-less monotonically for a large portion of the testing regime, resulting in a clear pressure-strain plot.

The evolution of the deformed shape of the cylinder is shown in Figure 25 by plotting the measured circumferential strains in the shell at mid-length at various stages of loading. The specimen began the residual strength test in the configuration indicated by the circumferential strain distribution after initial testing (Figure 20); that is, having a single dominant imperfection

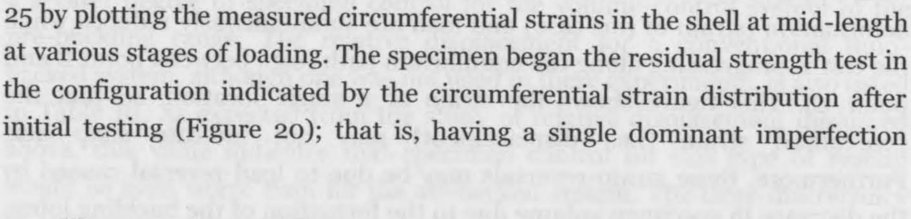

Figure 25: Residual strength test of the unstiffened specimen, showing the pressure-strain curve for a single strain gauge throughout the loading history (solid line) and the circumferential strain distribution in the shell at selected points on the curve.

lobe. This shape was preserved in the initial stages of the residual strength test, i.e., up to the first limit point in the load, at point A in Figure 25. A second buckling lobe began to form as the load recovered, reaching a second limit point in the load at B, after which the load began to drop. The second buckling lobe is clearly indicated by the circumferential strain distribution at the local load minima at point C. Additional limit points in the load are shown in Figure 25 as the test progresses, with the final configuration of three unevenly distributed buckling lobes at point F matching the observed post-testing shape of the specimen, as shown in Figure 18(b).

Figure 25 suggests that the several maxima and minima in the pressure-strain history are mainly due to the formation of additional buckling lobes (snap-through), which is evidence of the generalized displacement-control nature of the testing apparatus. Figure 25 also shows what appears to be the occurrence of "snap-back" behaviour, whereby the deformation (strain in this case) and load are simultaneously reduced while the test is progressing along the equilibrium path (e.g., between point B and point C). This figure shows the strain at a single location, so that the generalized strain (i.e., displacement) may not indicate snap-back. Furthermore, these strain-reversals may be due to load reversal caused by the decrease in specimen volume due to the formation of the buckling lobes, as discussed above.

Relative displacement of experimental apparatus

The experimental studies discussed above indicate that the volume-control system provided better control of the specimen displacements, especially near the critical load, than a conventional air-backed system. This section will use the expressions for relative displacement ($\Delta u_2/\Delta u_1$) derived above to determine if they predict a similar outcome, and to judge if another option, e.g., a conventional fluid-backed system, would have provided even better results.

The various stiffness and volume parameters for the pressure testing apparatus used in the experiments described in this chapter are listed in Table 9. The specimen stiffness in Table 9 is for the unstiffened cylinder, and was approximated as the change in volume of the specimen under a uniform external pressure, as predicted using a linear static finite element analysis with general shell elements. The equivalent stiffness shown in Eq. (3) was used to evaluate the fluid stiffnesses listed in Table 9.

Table 10 lists the relative displacement for the various pressure testing systems, determined using Eqs. (8) through (10). These values indicate that the relative displacement for the conventional air-backed system used in the

Table 9: Stiffness parameters for experimental pressure testing systems.

Parameter	Actual exp. apparatus	Hypothetical exp. apparatus
B_{cf}, B_{sf} (mineral oil)	1620 MPa	1620 MPa
$V_{0,cf}$	1.583×10^{9} mm^3	1.341×10^{7} mm^3
$V_{0,sf}$	1.716×10^{7} mm^3	1.716×10^{7} mm^3
k_{cf}^*	1.023×10^{-6} N/mm^5	1.208×10^{-4} N/mm^5
k_{sf}^*	9.441×10^{-5} N/mm^5	9.441×10^{-5} N/mm^5
k_s^*	1.143×10^{-4} N/mm^5	1.413×10^{-4} N/mm^5

experiments was two orders of magnitude less than the relative displacement for the volume-control system used in later experiments. This would suggest a greater degree of specimen control for the volume-control system in the pre-buckling range. The relative displacement for a conventional fluid-backed system, although one was not used in these experiments, is also listed in Table 10. As expected from the study of relative displacement discussed above, this value indicates that specimen control for this type of system would be even worse than for the air-backed system. The large discrepancy in relative displacement between the conventional and volume-control systems is due to the significantly greater stiffness of the specimen fluid and/or specimen compared to the chamber fluid, i.e., due to the relatively large pressure chamber.

The incremental specimen volume change at collapse due to a complete loss of load-carrying capability by the specimen, Δu_2, is also presented in Table 10 for each system. These values, calculated using Eqs. (12) and (13), indicate that fluid-backed systems, whether conventional or volume-control, reduce the change in specimen volume at collapse by two orders of magnitude relative to an air-backed system. This, in combination with dynamic effects that play a role during buckling, explains the catastrophic failures observed for air-backed specimens.

Since the degree of specimen control for conventional pressure testing systems may be improved by decreasing the volume of testing fluid, a hypothetical smaller pressure chamber was studied. Stiffness parameters for the second pressure chamber (Table 9) are identical to the actual pressure testing rig, except that the volume of the pressure chamber is reduced so that the clearance around the test specimen is much smaller – approximately 10% of the maximum specimen radius. This increases the stiffness of the pressure chamber fluid to such an extent that the relative displacements for

Table 10: Relative displacement parameters for experimental pressure testing systems.

Pressure testing system	**Pre-buckling ($\Delta u_2/\Delta u_1$)**	**Buckling (Δu_2)**
Actual apparatus		
Conventional air-backed	8.872×10^{-3}	7.819×10^{6} mm^3
Conventional fluid-backed	4.878×10^{-3}	8.383×10^{4} mm^3
Volume-control	4.501×10^{-1}	8.383×10^{4} mm^3
Hypothetical apparatus		
Conventional air-backed	5.138×10^{-1}	6.624×10^{4} mm^3
Conventional fluid-backed	3.665×10^{-1}	3.718×10^{4} mm^3
Volume-control	2.865×10^{-1}	3.718×10^{4} mm^3

the conventional systems are dramatically improved with respect to the actual apparatus, and even somewhat better than the volume-control system (see Table 10). The fluid-backed systems are still better at arresting the collapse displacements (Δu_2), but the degree of improvement over the air-backed systems is less than an order of magnitude.

Conclusions and recommendations

Conventional pressure testing systems were reviewed and expressions developed to estimate the degree of specimen control available for these systems. A volume-control pressure testing apparatus was developed and implemented successfully in a shell buckling testing program. This system allowed the amount of testing fluid leaving the specimen, and thus the shell deformation, to be controlled up to, and slightly beyond, the limit load of the cylinder. Precise control of the shell deformation and applied load in the dynamic post-collapse region was not achieved for specimens that formed large buckling lobes compared to the specimen volume. This has been attributed to the sudden loss of stiffness, and subsequent decrease in specimen volume, due to inward buckling, and is thought to be a necessary consequence of arresting the collapse process before the shell is ruptured.

The authors have used the proposed volume-control system to replace a conventional pressure testing setup used earlier in their testing program. The modified test apparatus eliminated the large, undesired post-collapse deformations and material rupture that occurred in the earlier testing. The post-collapse shape was preserved in all cases; however, this shape did not necessarily match the initial collapse mode at the peak load. As such, caution is required when interpreting the experimental results, and strain gauges were found to be invaluable for tracking the full load-deformation history of test specimens and identifying the mode of failure. Testing of the post-collapse strength of the cylinders was possible, with tracking of several load peaks and valleys in this region, which was not possible with a previously used conventional pressure testing setup.

The simple expressions for relative displacement and incremental specimen displacement during buckling developed in this chapter have been shown to be at least qualitatively correct. They can be used to produce a rough estimate of the performance of a given pressure testing system, keeping in mind that as the value of relative displacement, ($\Delta u_2/\Delta u_1$), approaches unity, the control of pre-buckling specimen displacements improves. The magnitude of buckling displacement, Δu_2, has been shown to be reduced by filling the specimen with the testing fluid.

In general, when planning experiments, it is recommended that a conventional fluid-backed pressure testing system be used when the pressure chamber is only slightly larger than the test specimens. A fluid-backed system with an outlet may be the best option for this situation, as it offers the better pre-buckling specimen control associated with an air-backed system, as well as at least some of the damping characteristics of a closed fluid-backed system. An air-backed system with an open-ended pressure chamber has the advantage of access to the interior of the specimen for instrumentation and observation during testing. This setup may be a good option if catastrophic specimen failures can be avoided by minimizing the volume of testing fluid in the chamber.

When the specimen is much smaller than the pressure chamber, as was the case in the experiments described in this chapter, it is recommended that a volume-control system be used if control over the specimen pre-buckling deformation is important. The volume-control system has the additional benefits that the pump is not running during the loading stages and that the specimen displacements are controlled using needle valves rather than turning the pump on and off. These considerations may influence the choice of pressure testing system when the relative displacements are similar for all types of pressure testing, e.g., the hypothetical apparatus in Table 9. Kinra's system [126] behaves similarly to the volume-control system, and is simpler to implement; but since the specimen is loaded during the pre-pressurization stage in Kinra's method, its advantages must be weighed against the risk of premature specimen collapse or yielding during pre-pressurization so that the actual collapse load cannot be determined.

For any existing pressure testing apparatus, greater control of the specimen deformation can be achieved by decreasing the volume of the chamber fluid and specimen fluid (or by increasing its bulk modulus) for conventional and volume-control systems, respectively. This volume reduction could be achieved by, for example, using a stiff steel insert in the pressure chamber or specimen, although this may interfere with instrumentation and wiring. Besides improving the control of specimen deformation, reducing the volume of testing fluid has a universal benefit, in that less strain energy is stored up in the testing system to be released at collapse. This helps to mitigate catastrophic specimen failures and allows better tracking of the post-collapse behaviour.

Chapter 4

Experimental study of the effect of corrosion damage on nearly shape perfect pressure hulls

A submarine may have to operate for a period of time with local corrosion damage in the pressure hull if a suitable repair method is unavailable or too expensive for implementation. This chapter describes collapse tests on twenty ring-stiffened aluminium cylinders, which were conducted to study the effect of corrosion damage on hull strength and stability. Artificial hull thinning was found to reduce the collapse strength of experimental models through high local stresses in the corroded region, leading to early onset of yielding and inelastic buckling. Bending associated with the eccentricity due to one-sided thinning was found to further increase the local stresses in the hull. Overall collapse pressures were more severely affected by corrosion damage than interframe collapse pressures. The percentage reduction in overall collapse pressure, compared with intact experimental models, was found to be closely related to the percentage depth of thinning. The accuracy of conventional collapse pressure predictions for the experimental models was significantly better for intact than for corroded cylinders. This chapter was originally published as an article in *Marine Structures* with co-authors Malcolm Smith, Fred van Keulen, Theo Bosman, and Neil Pegg [22].

Introduction

The pressure hull is the main load-bearing structure in a naval submarine. The basic structural component is a ring-stiffened cylindrical metallic shell under an external hydrostatic pressure load (Figure 2, p. 4). The ring-stiffeners forestall buckling of the shell until the material exhibits yielding, thereby taking advantage of the full material strength and increasing the structural efficiency [34]. The ultimate structural limit state of an efficiently designed pressure hull is therefore elasto-plastic collapse, which involves interaction between buckling instability and the nonlinear effects of material yielding and large displacements. The failure mode is classified as either interframe or overall collapse, for configurations that result in inelastic buckling of the shell between stiffeners or the entire shell-stiffener component, respectively. Interframe and overall collapse modes are shown in Figure 2. Failure of the hull can also occur via a lateral buckling of the ring-stiffeners due to insufficient torsional stiffness of the ring, referred to as stiffener tripping. Large safety factors are typically applied to this mode of failure so that it does not govern the design [11].

Submarine pressure hulls are susceptible to corrosion if inadequately protected. Corroded pressure hull material, once detected, is removed by grinding; if the damage is significant it may be corrected by weld build-up of the plate thickness (weld "cladding" or "buttering") or by replacement of the shell plating. These procedures involve welding, whereby residual stresses, deformations and geometric imperfections are introduced in the hull. Furthermore, the material properties of the hull may be changed as a result of the heat input from welding. As these factors may be detrimental to strength and stability, and because of the high cost of replacing damaged shell plates, it may be preferable to operate the pressure hull with a reduced plating thickness rather than effect a repair. This requires investigation into the structural response of hulls with unrepaired corrosion damage, as well as validated analysis methods for determining the strength and stability of damaged hulls in order to provide corrosion tolerance guidance to engineers.

Some investigations into the effect of discrete local patches of shell thinning on hull strength and stability have been performed using numerical methods. MacKay *et al.* [13] studied the effect of thinning on ring-stiffened cylinders using nonlinear finite element analysis. The study concluded that hull thinning reduces interframe collapse pressure by reducing the bending and membrane stiffness of the shell, leading to the early onset of yielding and collapse in the corroded region. Overall collapse pressure was also reduced, although to a lesser extent than interframe collapse, through a reduction in the bending stiffness of the combined shell-stiffener section. However, the effect of corrosion on overall collapse was understated, since the corrosion thinning was applied uniformly to both sides of the shell.

Smith and MacKay [42] studied the effect of corrosion thinning on overall collapse using a modified version of Kendrick's elasto-plastic finite difference method for predicting overall collapse pressures [8]. Kendrick's method accounts for the nonlinear effects of out-of-circularity (OOC) and residual stresses due to cold rolling, which are critical factors when determining overall collapse pressures. The modified method allows the circumferential extent of one-sided thinning, as well as the associated eccentricity, to be included explicitly in the finite difference model.

That study showed that, in general, overall collapse pressure decreases with increasing depths of thinning; however, the effect of corrosion thinning was found to be dependent on its circumferential extent and its orientation with respect to out-of-circularity. Overall collapse strength does not monotonically decrease with the circumferential extent of thinning. The load-path eccentricity resulting from one-sided thinning effectively increases or decreases the imperfection magnitude depending on whether the corrosion is in-phase or out-of-phase with the OOC. This leads to cases whereby, as the thinning is extended around the cylinder, the collapse pressure actually increases relative to cases with smaller extents of thinning. In a similar manner, shell thinning that is out-of-phase with OOC (i.e., collocated with an outward bulge) can increase the collapse pressure, while out-of-phase shell thickening can decrease the collapse pressure with respect to a similar intact model. Furthermore, shell thinning was found to have a greater effect on collapse strength for models having small magnitudes of OOC, due to its relatively greater influence on OOC.

While the studies reported in [13,42] provide useful insight into the behaviour of corroded pressure hulls, the numerical methodologies used in those studies have not been validated against experiments. A large body of experimental data on the collapse of intact shells under external pressure is available in the literature [3,10,15,44,48,88,89,93,95,98,113,134,137]; however, those experiments were focused on (nominally) axisymmetric models with (nominally) uniform shell thicknesses. The only case known to the author whereby the researchers intentionally varied the thickness of a metallic shell model under external pressure is a study by Aghajari *et al.* [43]. Those authors presented experimental (and numerical) results for thin cylindrical steel shells under external pressure with step-wise axisymmetric thickness variations over the shell length. Aghajari *et al.* found that the elastic buckling mode and pressure were influenced by the degree of local thinning; unfortunately, the study did not include benchmark test models with uniform shell thicknesses, so the net effect of thinning on buckling pressure cannot be deduced.

The influence of regions of locally reduced plating thickness on pressure hull strength and stability has not been previously studied experimentally. The current chapter describes a study aimed at filling that void. The present experiments are aimed at gaining a qualitative understanding of the collapse mechanisms for corroded pressure hulls, and at quantifying the effects of corrosion on hull strength and stability.

Furthermore, these experiments will provide data for validation of nonlinear finite element (FE) analysis of corroded hulls. This chapter does not include any numerical modeling, but initial nonlinear FE simulations of some of the specimens described herein have already been performed [51]*.

In the present study, twenty small-scale T-section ring-stiffened cylinders were machined from aluminium tubing and tested to collapse under external pressure [27-29]. Several pressure hull configurations and failure modes were studied, as well as various magnitudes of artificial corrosion thinning in simple geometric patterns. The experiments have been designed to isolate the effects of corrosion thinning by minimizing the influence of other factors that complicate hull collapse, such as large-amplitude out-of-circularity and residual stresses. Some of the specimens covered in this chapter are shown in Figure 26.

The chapter begins with a description of the experimental models and procedures. The test results for intact and corroded models are then presented, followed by a discussion of the effect of corrosion on hull strength and stability. The accuracy of conventional design methods for determining the collapse strength of the intact and corroded experimental models is also discussed. Finally, conclusions and plans for future work are presented.

Experimental models and methods

The experimental models have the same structural configuration as the main component of a real pressure hull: a cylindrical shell with T-section ring-stiffeners. The axisymmetric geometries for these models are shown in Figure 27. Collapse pressure and mode vary with several aspects of the structural configuration, especially the shell thickness and the stiffness of the ring-stiffeners. Those parameters were varied in the experimental program in order to investigate the effect of corrosion on different configurations and modes of failure. The twenty experimental models considered in this chapter are listed in Table 11, along with the axisymmetric configuration, corrosion damage, and material batch for each specimen.

Each specimen was machined from extruded aluminium alloy (6082-T6) tubing on a CNC lathe, which produces specimens with near-perfect circular geometry and insignificant residual stresses compared to structures fabricated by cold forming and welding. This allows the strength-reducing effects of the artificial corrosion to be isolated from other factors. Corrosion damage was introduced on selected cylinders by machining material from either the shell or ring-stiffener. The following sections describe the model geometry and material, and the testing procedures.

---

* Numerical modeling is also described in Chapter 7 of this thesis (p. 154).

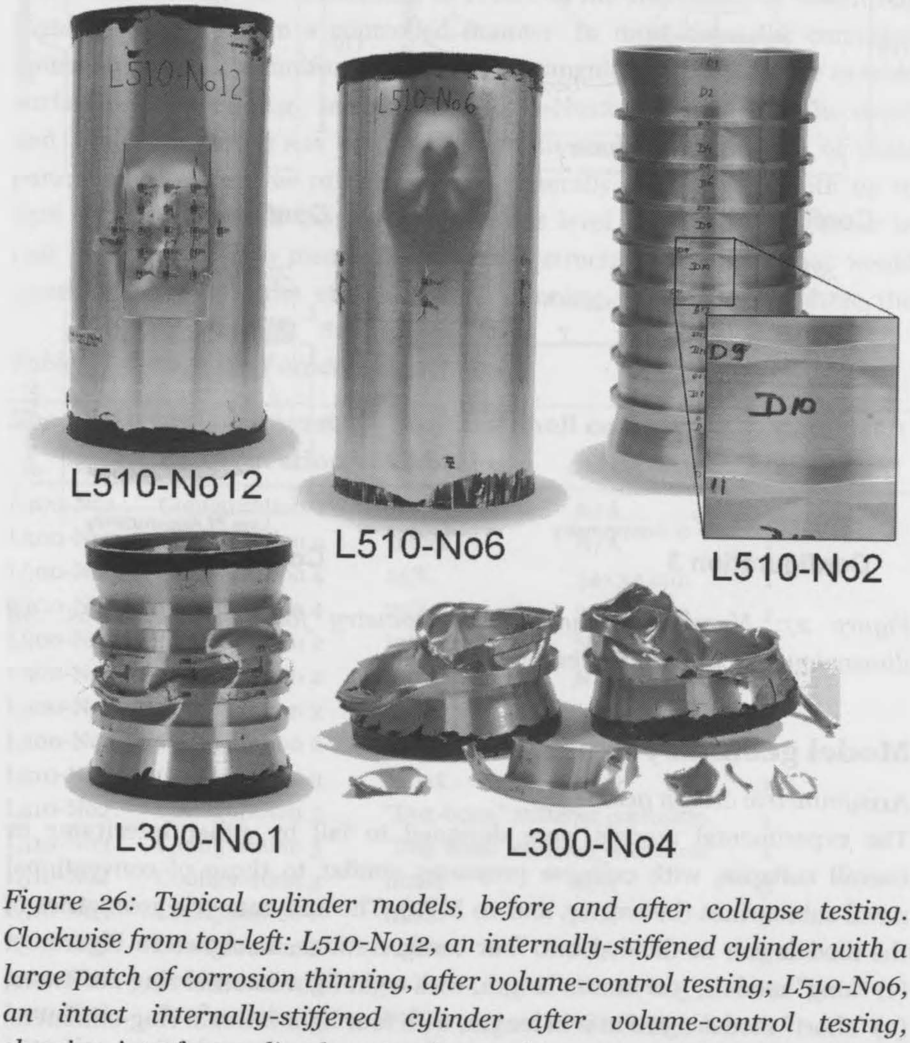

Figure 26: Typical cylinder models, before and after collapse testing. Clockwise from top-left: L510-No12, an internally-stiffened cylinder with a large patch of corrosion thinning, after volume-control testing; L510-No6, an intact internally-stiffened cylinder after volume-control testing, showing interframe dimples superimposed on an overall collapse mode; L510-No2, before testing, showing dog-bone stiffener corrosion at inset; L300-No4, a short cylinder with heavy stiffeners and a small patch of shell corrosion, showing the specimen after testing with a conventional apparatus; L300-No1, a short intact cylinder failing by interframe collapse, and showing the specimen after testing with a volume-control apparatus.

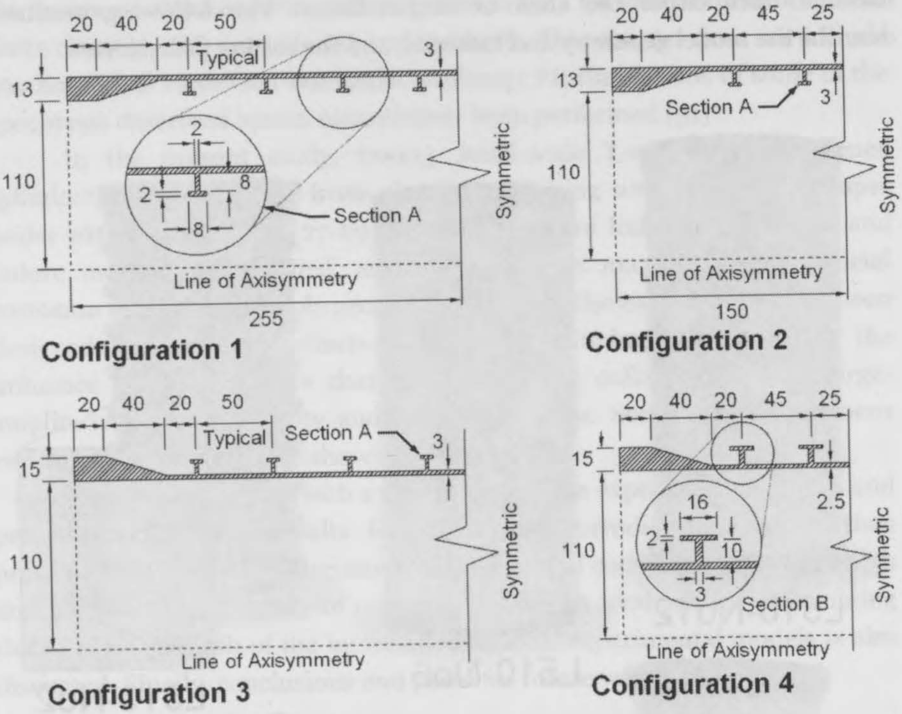
20 40 20 50
Typical
3
13
2
8
2
8
110
Section A
Symmetric
Line of Axisymmetry
255
Configuration 1
20 40 20 45 25
13
Section A
3
110
Symmetric
Line of Axisymmetry
150
Configuration 2
20 40 20 50
Typical
Section A
3
15
110
Symmetric
Line of Axisymmetry
Configuration 3
20 40 20 45 25
15
2.5
16
2
10
3
110
Section B
Symmetric
Line of Axisymmetry
Configuration 4

Figure 27: Nominal axisymmetric geometry for test specimens. All dimensions are in millimetres.

Model geometry

Axisymmetric design geometry

The experimental models were designed to fail by either interframe or overall collapse, with collapse pressures similar to those of conventional naval submarines (between 5 and 10 MPa). The axisymmetric geometries of the models can be divided into four configurations, as shown in Figure 27: (1) "long" models, 510 mm in length, with eight light internal ring-stiffeners; (2) "short" models, 300 mm in length, with four light internal ring-stiffeners; (3) long models with external ring-stiffeners; and (4) short models with four heavy external ring-stiffeners. Figure 26 shows some of the models before and after collapse testing.

Short, externally stiffened specimens had relatively heavy stiffeners (Figure 27, Configuration 4) to encourage failure by inelastic interframe buckling of the shell. All other cylinders had a thicker shell and lighter stiffening (Figure 27, Configurations 1-3), which favoured inelastic overall collapse of the combined shell and ring-stiffeners. All cylinders had thick end-rings that tapered gradually to the mean shell thickness to prevent undesired end-bay failure.

Artificial corrosion damage

Corrosion damage was introduced in twelve of the specimens by machining material from them in a controlled manner. In most cases the corrosion damage consisted of uniformly thinned rectangular patches on the outside surface of the shell (e.g., see specimen L510-No12 in Figure 26). The depth and area of thinning was varied in order to study the influence of these parameters. The degree of damage was generally quite severe, with up to 25% reduction in shell thickness. While this level of damage may occur in real hulls, it was also meant to produce a structural response that would clearly demonstrate the effects of hull thinning, as well as facilitate the

Table 11: Summary of experimental models.

Specimen	**Axisymmetric configuration**[a]	**Nominal shell corrosion**[b]		**Material batch no.**[c]
		Thinning	**Area**	
L300-No1	Configuration 4	Intact	N/A	1
L300-No2	Configuration 4	Intact	N/A	1
L300-No3	Configuration 4	25%	34×34 mm	1
L300-No4	Configuration 4	25%	34×34 mm	1
L300-No5	Configuration 2	Intact	N/A	3
L300-No6	Configuration 2	Intact	N/A	3
L300-No7	Configuration 2	25%	37×37 mm	3
L300-No8	Configuration 2	25%	37×37 mm	3
L510-No1	Configuration 3	Intact	N/A	1
L510-No2	Configuration 3	"Dog-bone" stiffener corrosion		1
L510-No3	Configuration 3	"Dog-bone" stiffener corrosion		1
L510-No4	Configuration 3	Intact	N/A	3
L510-No5	Configuration 1	Intact	N/A	2
L510-No6	Configuration 1	Intact	N/A	3
L510-No7	Configuration 1	20%	42×42 mm	2
L510-No8	Configuration 1	20%	42×42 mm	3
L510-No9	Configuration 1	13.3%	100×100 mm	2
L510-No10	Configuration 1	13.3%	100×100 mm	3
L510-No11	Configuration 1	13.3%	200×100 mm	2
L510-No12	Configuration 1	13.3%	200×100 mm	3

[a] See Figure 27.

[b] Shell corrosion is applied in a rectangular area, orthogonal to ring-stiffeners and centred at mid-length of the cylinder. "Intact" models do not have artificial corrosion. Corrosion area is specified by the axial times the circumferential extents.

[c] Measured material data for each batch are listed in Table 13.

reproduction of the damaged configuration in numerical models. More realistic cases of thinning can then be studied using the validated numerical methods. Nominal dimensions of the corrosion patches are listed in Table 11; actual dimensions deviated from these values somewhat.

Since ring-stiffeners, especially those external to the hull plating, are also susceptible to corrosion, this was artificially introduced by machining flanges to a "dog-bone" shape on the central stiffeners of two long externally stiffened cylinders (see specimen L510-No2 in Figure 26). The corrosion consisted of a reduction in the flange breadth, up to a maximum of 50%, in a circular pattern over a circumferential arc of approximately 20°. Other stiffener properties, such as flange thickness and web depth, were the same in corroded and intact regions.

Measured imperfections

Each specimen was measured for out-of-circularity type geometric imperfections, as well as shell thickness, using a coordinate measurement machine (CMM). The rated accuracy of the CMM is ±0.0025 mm when using standard measurement probes; however, it has been estimated that the accuracy drops to ±0.02 mm for a setup using longer probes, which was required to measure these cylinders. Radial measurements were taken at 10° intervals about the circumference at axial locations corresponding to ring-stiffeners and the centre of each bay of shell plating. Shell thicknesses were derived by comparing internal and external radial measurements of the shell.

Fourier series decompositions of the measured radii were performed in order to determine the contributions of the various modes of imperfections; i.e., n-value, or number of circumferential waves [138]. Fourier amplitudes (A_n) are defined by the following Fourier expansion:

$$R_\theta = b_0 + \sum_{n=1}^{\infty} A_n \cos(n(\theta - \phi_n)) \tag{14}$$

In Eq. (14), R_θ is the radius at a given angle, θ; b_o is the mean radius; A_n and ϕ_n are the Fourier amplitude and phase angle, respectively, for a given n-value.

The results of the Fourier decompositions at the stiffener flanges are listed in Table 12, along with the nominal flange radii and maximum out-of-circularity. The precision of the machining fabrication process, especially with respect to the near-perfect circularity of the as-built cylinders, is indicated by the mean values of radius (n=0), none of which exceed ±0.06% of the specified value. Furthermore, the maximum out-of-circularity for all specimens was less than or equal to 0.15% of the shell radius, which is well below the standard design value of 0.5% [5].

The results in Table 12 also show that the machining process resulted in a dominant n=2 or n=3 imperfection for all of the specimens, and

Table 12: Measured radii and out-of-circularity at stiffener flange locations, including the results of Fourier decompositions.

Specimen	**Nominal radius (mm)**	**Mean Fourier amplitude, A_n (mm), at stiffener flanges**[a]						**OOC**[b]
		n=0	n=2	n=3	n=4	n=5	n=6	
L300-No1	124.5	124.485	0.023	0.008	0.003	0.001	0.001	0.06%
L300-No2	124.5	124.501	0.040	0.011	0.002	0.002	0.001	0.07%
L300-No3	124.5	124.468	0.009	0.009	0.004	0.002	0.001	0.03%
L300-No4	124.5	124.501	0.031	0.016	0.003	0.002	0.001	0.05%
L300-No5	110.0	109.945	0.046	0.055	0.011	0.005	0.003	0.13%
L300-No6	110.0	109.948	0.046	0.049	0.014	0.005	0.003	0.15%
L300-No7	110.0	109.943	0.044	0.033	0.016	0.006	0.004	0.11%
L300-No8	110.0	109.951	0.035	0.043	0.011	0.007	0.003	0.08%
L510-No1	123.0	123.008	0.035	0.013	0.003	0.002	0.001	0.08%
L510-No2	123.0	123.007	0.034	0.014	0.003	0.001	0.001	0.05%
L510-No3	123.0	123.015	0.051	0.014	0.002	0.001	0.001	0.10%
L510-No4	123.0	123.024	0.051	0.032	0.009	0.004	0.003	0.09%
L510-No5	110.0	110.002	0.080	0.004	0.005	0.002	0.001	0.11%
L510-No6	110.0	109.911	0.059	0.018	0.010	0.006	0.001	0.12%
L510-No7	110.0	109.967	0.055	0.005	0.004	0.003	0.001	0.09%
L510-No8	110.0	110.035	0.026	0.066	0.011	0.005	0.001	0.12%
L510-No9	110.0	109.986	0.042	0.006	0.003	0.001	0.001	0.06%
L510-No10	110.0	110.004	0.046	0.050	0.016	0.003	0.003	0.12%
L510-No11	110.0	109.958	0.028	0.009	0.003	0.002	0.002	0.08%
L510-No12	110.0	109.938	0.034	0.048	0.018	0.006	0.003	0.09%

[a] Fourier decomposition was performed at each stiffener location at the stiffener flange; i.e., using outer and inner radial measurements for externally and internally stiffened cylinders, respectively. For a given n-value, the mean Fourier amplitude for all stiffener locations is reported. The n=0 values represent the mean radius of the stiffener flanges for each cylinder. Fourier amplitudes for n=1, which represent the offset of the measurement apparatus from the axis of revolution, are not reported.

[b] OOC is taken as the maximum absolute value of the deviation from the mean radius, expressed as a percentage of the mean radius. OOC was calculated using the raw measured radius less the n=1 Fourier component.

contributions for modes $n>4$ are negligible. Fourier amplitudes for individual n-values are less than 0.1% of the shell radius for all specimens.

Materials

The cylinders were fabricated from three separate batches of extruded 6082-T6 aluminium alloy tubing. This material was chosen because it is easy to machine and, since it is a ductile strain-hardening material, behaves somewhat similarly to traditional pressure hull materials (i.e., high-strength steel) for failure by elasto-plastic collapse[*].

Tensile coupons were machined from the original aluminium tubing, and in some cases from the thick end-rings of the cylinder specimens themselves after pressure testing, in the axial and circumferential directions. Young's modulus and the 0.2% offset yield stress for each batch and coupon direction are listed in Table 13. These data indicate anisotropy in the cylinder material, with the yield strength in the circumferential direction less than the axial direction, likely a result of the extrusion process. The anisotropy was most pronounced for batch numbers 1 and 2, with the circumferential yield stress approximately 10% less than the yield stress in the axial direction. Engineering stress-strain curves showing a somewhat weaker anisotropy in the batch no. 3 material are shown in Figure 28. The coupon test results also indicate variation in the mean material properties between batches, within about 10%.

Poisson's ratio was measured using strain gauge rosettes bonded to two flat tensile coupons machined from tests specimens from batch no. 2, giving a value between 0.32 and 0.34.

Table 13: Summary of tensile testing for coupons taken from the axial and circumferential directions of the cylinders, showing the statistical data for each batch of aluminium material.

Batch no./direction	**Young's modulus (MPa)**			**0.2% Yield stress (MPa)**		
	Samples	**Mean**	**StDev**	**Samples**	**Mean**	**StDev**
1/Axial	6	73200	3100	10	304	5
1/Circumferential	3	72700	460	3	272	2
2/Axial	4	70700	750	7	327	12
2/Circumferential	6	67900	2000	6	297	5
3/Axial	9	74300	1600	9	317	3
3/Circumferential	3	80600	4500	3	303	1

---

[*] The aluminium used for the test specimens is compared with high-strength submarine steel in Chapter 5 of this thesis (p. 107).

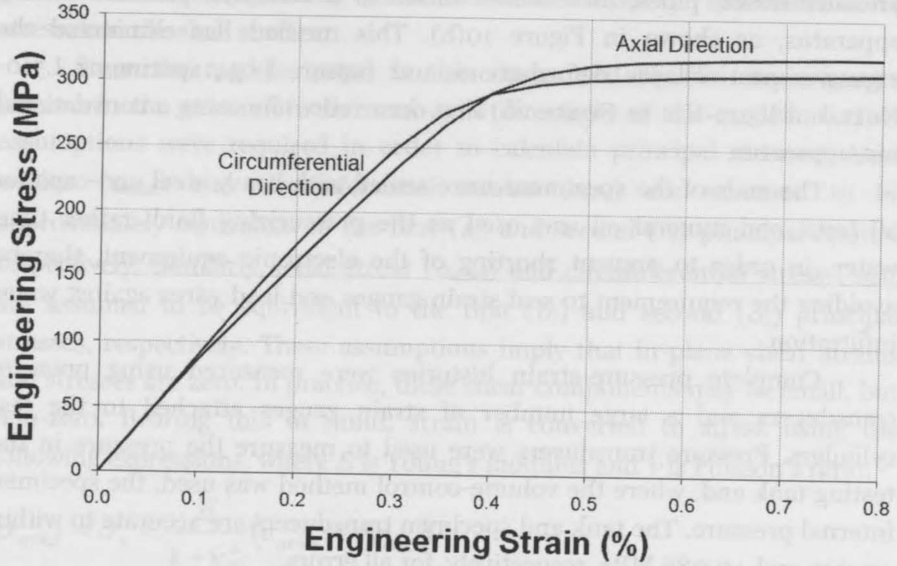

Figure 28: Measured engineering stress-strain curves for coupons taken from the axial and circumferential directions of the batch no. 3 aluminium tubing.

Pressure testing

In earlier experiments [27], specimens were loaded to collapse by applying external hydrostatic pressure to sealed and air-filled specimens. During collapse, a large amount of energy, which is stored in the testing fluid and the cylinder itself, is released. Since there is nothing to resist or slow down the collapse mechanism in an air-filled specimen, the model is catastrophically deformed and ruptured. With this approach it was difficult to determine the failure mode from post-test inspection (e.g., specimen L300-N04 in Figure 26).

A revised experimental procedure was used for subsequent tests [28,29], with the goal of preventing catastrophic failures. In this so-called "volume-control" method, which is shown schematically in Figure 10(b), p. 49, and described in [21] (see also Chapter 3, p. 41), a fluid-filled specimen is uniformly pressurized inside and outside to a level greater than the specimen collapse pressure. The fluid inside the specimen is then isolated from the tank by closing a "cross-over" valve. The loading stage begins by releasing the pressurized fluid from inside the specimen using a second "fluid-release" valve, resulting in a net pressure load on the shell. The volume-control apparatus is realized by connecting a network of high-pressure hoses, pipes, and needle valves to a standard pressure testing apparatus, as shown in Figure 10(b). This method has eliminated the excessive post-collapse deformations and rupture (e.g., specimens L510-N012 and L300-N01 in Figure 26) that occurred while using a conventional test apparatus.

The ends of the specimens were sealed with heavy steel end-caps for all tests, and mineral oil was used as the pressurizing fluid, rather than water, in order to prevent shorting of the electronic equipment, thereby avoiding the requirement to seal strain gauges and lead wires against water infiltration.

Complete pressure-strain histories were measured using pressure transducers and a large number of strain gauges attached to the test cylinders. Pressure transducers were used to measure the pressure in the testing tank and, where the volume-control method was used, the specimen internal pressure. The tank and specimen transducers are accurate to within ±0.043 and ±0.086 MPa, respectively, for all errors.

A typical intact cylinder was instrumented with strain gauges at eight or twelve equally spaced increments about the circumference at the expected sites of yielding and collapse: the stiffener flanges, the shell in the central bay and, in some cases, the shell opposite the stiffeners. Cylinders with artificial corrosion had additional gauges in that area. In general, gauges fixed to the shell were 2-gauge 90° tee rosettes, aligned in the circumferential and axial directions, while uni-axial gauges oriented in the circumferential direction were fixed to the ring-stiffener flanges. The strain measurements are accurate to within ±0.5% of the reported strain values.

Data processing

Strain and pressure data were simultaneously acquired at a sampling rate of 100 Hz. These data were used to estimate the onset of yielding by converting strains to stresses and comparing them with the measured yield stress. A von Mises yield criterion was used, as discussed below.

Stresses in the ring-stiffeners were assumed to be uni-directional (circumferential), and Hooke's law was used to estimate stress. Yielding of the stiffeners was assumed to have occurred when the stress associated with the circumferential strain in the flange reached the circumferential yield stress.

Yielding in the shell is governed by a multi-dimensional stress state. The shell portions of the experimental specimens are treated as ideal shell structures, and thus the in-plane stresses, rather than the through-thickness stresses, are considered to be of primary importance. This implies a plane stress state whereby yielding can be determined from the two-dimensional stresses on the shell surface.

Since the models tested in this study used bi-axial strain gauges aligned in the circumferential and axial directions of the models, further assumptions were required in order to calculate principal stresses. Axial strains (ε_{axial}) and circumferential strains (ε_{circ}) are assumed to be approximately equivalent to the first (ε_1) and second (ε_2) principal strains, respectively. Similarly, axial stress (σ_{axial}) and circumferential stress (σ_{circ}) are assumed to be equivalent to the first (σ_1) and second (σ_2) principal stresses, respectively. These assumptions imply that in-plane shear strains and stresses are zero. In practice, these shear components may be small, but non-zero. Bearing this in mind, strain is converted to stress using the following expressions, where E is Young's modulus and ν is Poisson's ratio:

$$\sigma_{axial} = \sigma_1 = \frac{E}{1-\nu^2}\left(\varepsilon_{axial} + \nu\varepsilon_{circ}\right),$$

$$\sigma_{circ} = \sigma_2 = \frac{E}{1-\nu^2}\left(\varepsilon_{circ} + \nu\varepsilon_{axial}\right). \qquad (15)$$

Yielding of the shell at a strain gauge location was assumed to have occurred when the von Mises equivalent stress reached the 0.2% yield stress of the material in the circumferential direction. For plane stress states, the von Mises equivalent stress, σ_{eqv}, reduces to the following expression:

$$\sigma_{eqv} = \sqrt{\sigma_1^{\ 2} + \sigma_2^{\ 2} - \sigma_1\sigma_2}. \qquad (16)$$

Poisson's ratio was assumed to be 0.3 for stress calculations for cylinders from batch no. 1, while the measured value of 0.32 was used for stress calculations for batches no. 2 and no. 3. The yield stress for a particular specimen was taken as the mean circumferential yield stress for the batch from which it was fabricated.

The experimental yield pressure, P_y, is associated with the first occurrence of yielding, as determined using the procedure described above, at any measured strain gauge location on the shell or stiffeners. The experimental collapse pressure, P_c, refers to the peak measured load.

Design formulae predictions

Predicted collapse pressures for intact cylinders reported in this document are based on a contemporary submarine design code [5]. Interframe collapse pressures (P_{ci}) are based on a design curve that accounts for interaction between elastic buckling and shell yielding by applying an empirically-derived "knock-down factor" to the classical von Mises elastic shell buckling pressure (the mean design curve in Figure 3, p. 5). The reported interframe collapse mode, n, is based on the minimum von Mises buckling pressure used with the empirical curve. Overall collapse pressures (P_{co}) are based on Kendrick's elasto-plastic finite difference method [8], which accounts for out-of-circularity. The predicted overall collapse mode is associated with the minimum overall collapse pressure for circumferential modes n=2 to n=6. An out-of-circularity of 0.1% of the mean shell radius was used in overall collapse calculations.

The design code rules had to be adapted in order to make predictions for the corroded models. Interframe collapse predictions were arrived at using the nominal thickness in the corroded region, which implies that the corrosion was applied uniformly throughout the shell. The modified Kendrick method [42] was used for overall collapse predictions for corroded cylinders, so that the circumferential pattern of thinning was captured, but applied uniformly over the cylinder length. For overall collapse predictions for cylinders with flange corrosion, the flange breadth reduction was modeled as an equivalent thinning of the flange in the corroded region. Otherwise, all predicted collapse pressures are based on the nominal axisymmetric geometry and the mean circumferential material properties for the batch.

Experimental results

Intact models

This section presents experimental results for intact models, i.e., models without artificial corrosion damage. Experimental yield and collapse pressures for all intact models are summarized in Table 14, along with the design formulae predictions.

Interframe collapse

Only the short cylinder models with heavy ring-stiffeners (L300-No1 and -No2) failed in an interframe collapse mode, and only one of those models, L300-No1, was instrumented with strain gauges. The average collapse pressure for these models was approximately 7.5 MPa. The interframe collapse mode, with lobar buckling of the shell, for specimen L300-No1 is shown in Figure 26. That figure shows the model after it was pressurized well into the post-collapse region using the volume-control method. Specimen

L300-No2 was tested using the original apparatus, so that the model was torn apart during collapse.

Figure 29 shows the pressure-strain relationship for the instrumented specimen L300-No1 at the initiation site for interframe collapse, as well as the adjacent stiffener. The pressure-strain relationship, which is plotted up to and slightly beyond the peak load, is linear until just prior to the onset of

Table 14: Measured and predicted collapse pressures and modes for intact cylinders.

Specimen	**Test results**[a]			**Interfr. collapse**[b,d]			**Overall collapse**[c,d]		
	P_y (MPa)	P_c (MPa)	n	P_{ci} (MPa)	n	X_m	P_{co} (MPa)	n	X_m
L300-No1	5.79	7.11	4	6.20	9	1.15	7.86	4	0.90
L300-No2	N/A	7.87	N/A	6.20	9	1.27	7.86	4	1.00
L300-No5	7.44	8.99	3	7.99	9	1.13	8.57	5	1.05
L300-No6	7.53	9.14	3/4	7.99	9	1.14	8.57	5	1.07
L510-No1	8.27	9.05	2/3	7.69	8	1.18	8.18	3	1.11
L510-No4	8.12	9.79	3	8.56	8	1.14	9.11	3	1.08
L510-No5	8.08	9.08	3	7.59	9	1.20	8.16	3	1.11
L510-No6	7.41	8.48	3	7.99	9	1.06	8.45	3	1.00
Bias						*1.16*			*1.04*
COV						*5.2%*			*6.6%*

[a] The collapse pressure, P_c, is taken as the maximum load applied to the specimen. The yield pressure, P_y, is taken as the minimum load at which the von Mises equivalent stress at strain gauge locations exceeded the circumferential yield stress determined from coupon testing. The experimental circumferential wave number, n, is associated with the largest Fourier amplitude for decomposition of circumferential strains at the collapse load. Two values are shown when shell and stiffener wave numbers are different; e.g., "3/4" indicates dominant $n=3$ and $n=4$ modes in the shell and stiffener, respectively. Wave numbers up to half the number of circumferential gauges were permitted.

[b] Predicted interframe collapse pressures, P_{ci}, are based on the mean empirical curve from [5], while the predicted n-value is based on the minimized von Mises elastic buckling pressure used with the empirical curve.

[c] Predicted overall collapse pressures, P_{co}, and n-values are based on Kendrick`s elasto-plastic finite difference method [8].

[d] The modeling uncertainty factor, X_m, is taken as the quotient of the experimental and predicted collapse pressures. The bias is the mean value of X_m for a group, while the coefficient of variation, COV, is the standard deviation divided by the mean.

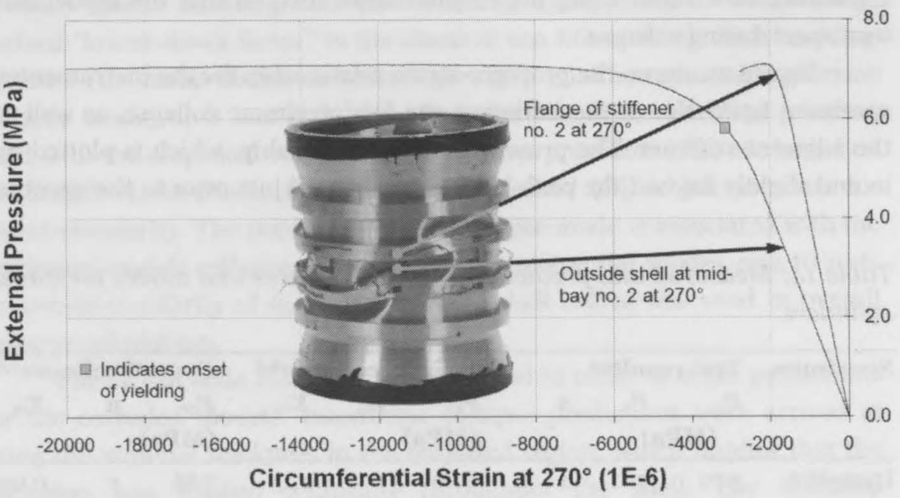

Figure 29: Pressure-strain relationship at the collapse initiation site for an intact specimen failing by interframe collapse (L300-N01).

yielding in the shell. This figure also shows the relatively greater deformation of the shell compared to the ring-stiffener, especially after the onset of shell yielding, which is typical of interframe collapse. The stiffeners did not yield at gauge locations until the specimen was loaded well into the post-collapse region (not shown in Figure 29).

Overall collapse

All intact cylinders with light stiffeners (L300-N05, L300-N06, L510-N01, L510-N04, L510-N05 and L510-N06) failed in an overall collapse mode, regardless of overall cylinder length. All of these cylinders were tested using the volume-control test method except L510-N01.

A typical overall collapse mode, with large deformation of both the shell and ring-stiffeners, is shown by specimen L510-N05 in Figure 30. The circumferential distribution of strains at the shell and an internal ring-stiffener at the collapse load are plotted at the top of Figure 30. These data show a collapse mode dominated by n=3 strains, with strain minima outside the shell corresponding with maxima on the ring-stiffener, as would be expected due to circumferential bending. The photograph at the bottom of Figure 30 shows the cylinder after it has been loaded into the post-collapse region using the volume-control method, with one lobe of the n=3 collapse mode dominating the post-peak deformation.

Figure 30 also shows selected pressure-strain relationships up to and slightly beyond the peak load. The difference between the pressure-strain

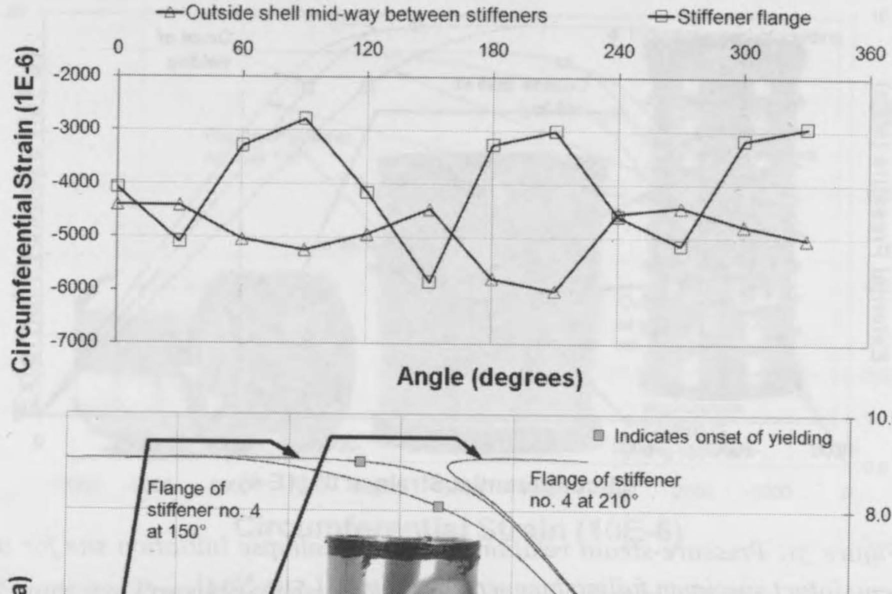

Figure 30: Circumferential distribution of strain at the collapse load of 9.08 MPa (top) and pressure-strain relationship (bottom) for a long, internally-stiffened intact specimen failing by overall collapse (L510-No5). The pressure-strain data is shown up to and slightly beyond the peak load, for gauges located near the collapse initiation site.

relationships for the shell and stiffeners is much smaller than it is for the cylinders that failed by interframe collapse (Figure 29), especially after yielding has occurred. This is as expected for overall collapse. Figure 30 also shows that, even though the shell has yielded early on, collapse is precipitated by yielding of the stiffener flange.

Similar structural behaviour was observed with other specimens that failed by overall collapse. For example, Figure 31 and Figure 32 show

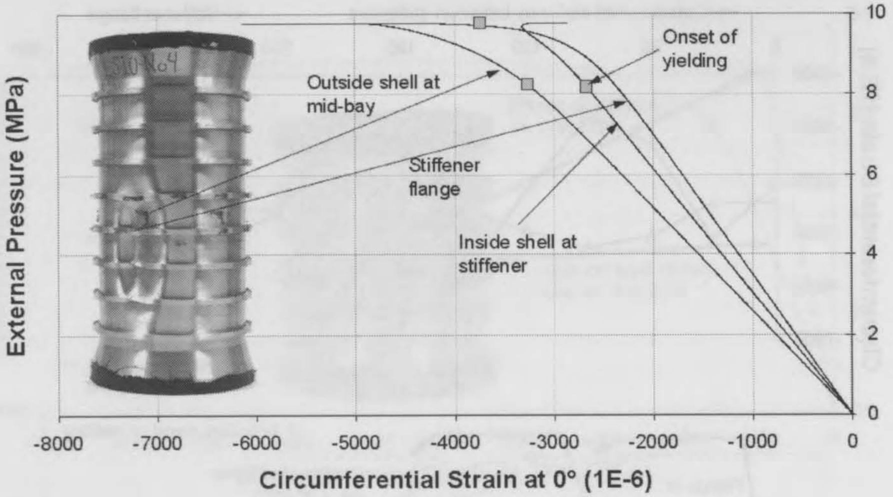

Figure 31: Pressure-strain relationship at the collapse initiation site for a long intact specimen failing by overall collapse (L510-No4).

pressure-strain relationships for an externally stiffened long cylinder and an internally stiffened short cylinder, respectively. In both of these models the shell mid-way between stiffeners yields early on, with collapse following closely after the onset of yielding in the stiffener flange. The shell opposite to a stiffener yields at a pressure closer to the collapse load in the internally stiffened cylinder (Figure 32) compared to the externally stiffened cylinder (Figure 31). Some of these cylinders showed post-collapse configurations characterized by several adjacent interframe buckling lobes superimposed on global deformation of the shell and stiffeners (see specimen L510-No6 in Figure 26). It may be inferred that some interaction between interframe and overall failure modes occurred, even though the latter mode was dominant at collapse.

Corroded models

In this section, the results for cylinders with intentionally thinned regions of shell or damaged ring-stiffeners are summarized. As with the intact specimens, cylinders with heavy and light ring-stiffeners failed by interframe and overall collapse, respectively, and so the discussion will be divided along those lines. The experimental yield and collapse pressures for corroded models, along with design formulae predictions, are presented in Table 15.

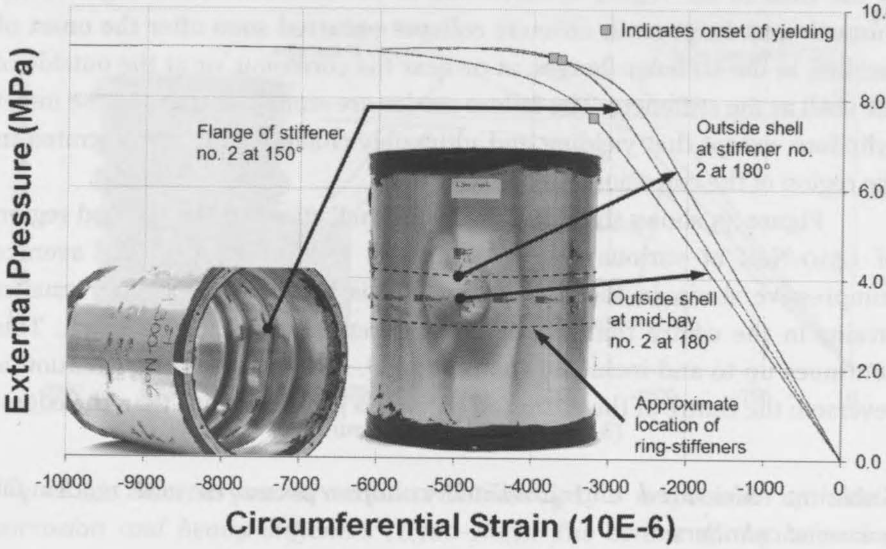

Figure 32: Pressure-strain relationship at the collapse initiation site for a short intact specimen failing by overall collapse (L300-No6).

Interframe collapse

Specimens L300-No3 and -No4 had heavy ring-stiffeners and 25% shell thinning in a square patch spanning approximately 70% of the width of the central frame-bay. These cylinders failed by interframe collapse. Figure 33 shows the pressure-strain relationship up to collapse at selected locations on specimen L300-No3. The strain gauge data indicate that yielding occurred first at the centre of the corrosion patch. The pressure-strain behaviour at this location became increasingly nonlinear as the load was increased, until a local strain reversal in the corroded shell occurred at approximately 5.5 MPa. The strain gauge data indicate that the stiffeners did not yield prior to collapse; instead, collapse occurred after the onset of yielding in the intact shell away from the corroded region. This air-backed specimen failed violently, having a post-testing configuration similar to L300-No4, shown in Figure 26.

Overall collapse

Specimens L300-No7 and -No8, and specimens L510-No7 to -No12 had light ring-stiffeners and shell corrosion, and failed in an overall collapse mode. Figure 34 shows pressure-strain relationships at critical structural locations for specimen L510-No8, which is typical of the group. The structural behaviour of L510-No8 was approximately linear until yielding was initiated in the shell in the region of corrosion, at the circumferential edges of the thinned area. In general, ultimate collapse occurred soon after the onset of yielding in the stiffener flanges, at or near the corrosion, or at the outside of the shell at the stiffeners. The failure modes are similar to those of the intact cylinders, except that yielding and ultimately collapse were concentrated in the region of the corrosion.

Figure 35 shows the circumferential shell strain in the thinned region of L510-No8 at various stages of testing. Before collapse, the average compressive strain in the corroded region is higher, with slightly smaller strains in the centre than at the circumferential edges of the patch. This continues up to and including the peak load. After collapse, the situation is reversed: the centre of the corrosion patch has greater strains than the edges.

Table 15: Measured and predicted collapse pressures and modes for corroded cylinders.

Specimen	**Test results**[a]		**Interfr. collapse**[b]			**Overall collapse**[c]		
	P_y **(MPa)**	P_c **(MPa)**	P_{ci} **(MPa)**	n	X_m	P_{co} **(MPa)**	n	X_m
L300-No3	4.43	6.77	4.00	10	1.69	5.93	6	1.14
L300-No4	N/A	6.94	4.00	10	1.74	5.93	6	1.17
L300-No7	4.57	7.30	5.29	10	1.38	4.93	5	1.48
L300-No8	4.56	7.11	5.29	10	1.34	4.93	5	1.44
L510-No2	N/A	8.59	7.61	8	1.13	7.78	4	1.10
L510-No3	7.85	9.25	7.61	8	1.22	7.78	4	1.19
L510-No7	5.33	7.07	5.49	9	1.29	7.58	3	0.93
L510-No8	4.97	7.21	5.82	9	1.24	7.81	3	0.92
L510-No9	6.58	7.68	6.18	9	1.24	7.29	3	1.05
L510-No10	6.29	7.81	6.53	9	1.20	7.38	3	1.06
L510-No11	6.34	7.58	6.18	9	1.23	7.29	3	1.04
L510-No12	5.93	7.29	6.53	9	1.12	7.38	3	0.99
Bias					*1.32*			*1.13*
COV					*15.2%*			*15.8%*

---

[a] See notes in Table 14. Experimental *n*-values were not determined for corroded models since they were asymmetric.

[b] See notes in Table 14. The shell thickness in the corroded region was used for all calculations.

[c] Predicted overall collapse pressures, P_{co}, and *n*-values are based on Kendrick`s elasto-plastic finite difference method, modified for discrete corrosion patches [42].

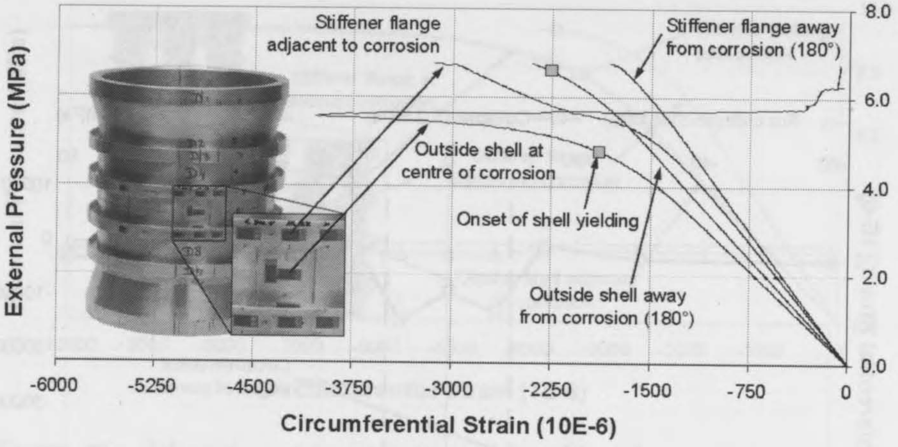

Figure 33: Selected pressure-strain relationships for a specimen with shell corrosion and heavy stiffeners (L300-N03). The centre of the corrosion patch corresponds to 0°.

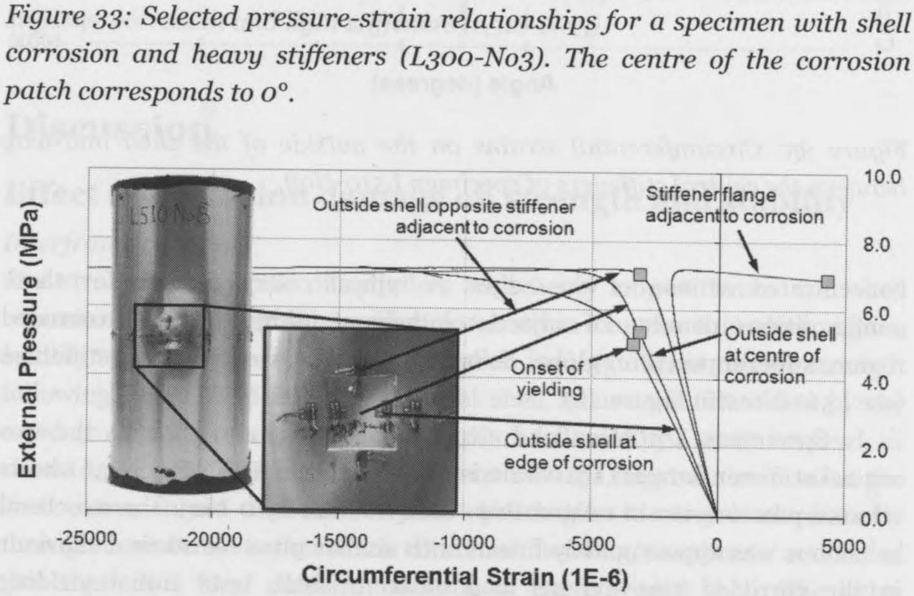

Figure 34: Selected pressure-strain relationships for a specimen with shell corrosion and light stiffeners (L510-N08).

The above characteristics typify the structural behaviour of cylinders with shell corrosion and light stiffeners. In short cylinders with light stiffeners (L300-N07 and -N08), the switch in the location of the maximum strains in the corroded shell occurs before, rather than after, collapse. Long cylinders with larger regions of corrosion (L510-N09 to -N012) also show larger compressive strains near the edges of the thinned shell. Here, yielding initiates at the corrosion edges, and the deformation at collapse is

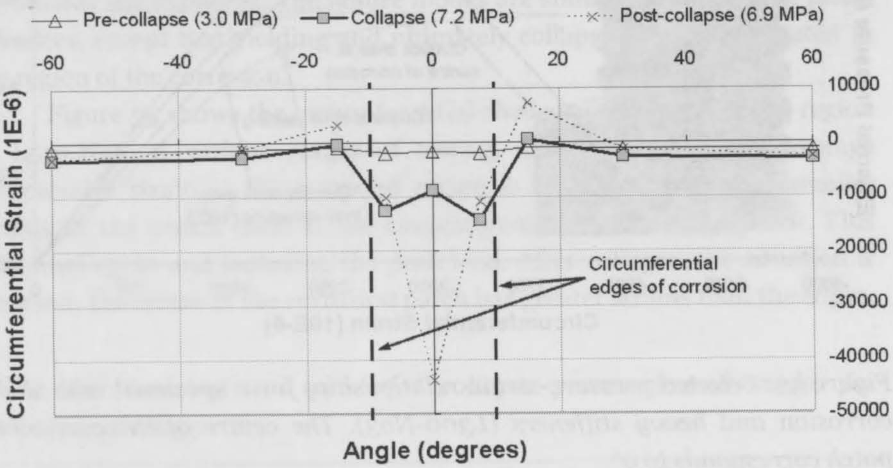

Figure 35: Circumferential strains on the outside of the shell mid-way between the central stiffeners of specimen L510-No8.

concentrated at one of the edges. A typical collapse mode for these configurations consists of adjacent interframe dimples in the corroded region, superimposed on global deformation of the shell and ring-stiffeners (see L510-No12 in Figure 26).

Specimens L510-No2 and -No3 had artificial corrosion in the two central stiffener flanges (L510-No2 is shown in Figure 26). Figure 36 shows selected pressure-strain relationships for specimen L510-No3. The structural behaviour was approximately linear, with similar pressure-strain behaviour in the corroded ring-stiffener and adjacent shell, until initial yielding occurred at the shell. Collapse occurred immediately following the onset of yield in the corroded ring-stiffeners, just outside the region of corrosion. During collapse, the ring-stiffeners in the corroded region tripped sideways. The similarity of shell and stiffener strains, and the observed post-collapse shape, indicates an overall collapse mode.

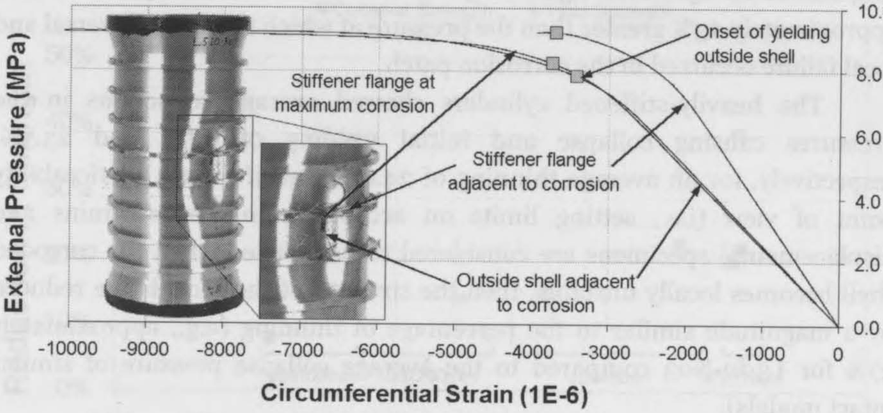

Figure 36: Selected pressure-strain relationships for a specimen with stiffener corrosion and light stiffeners (L510-N03).

Discussion

Effect of corrosion damage on strength and stability

Interframe collapse

The structural response of cylinders with heavy ring-stiffeners and shell corrosion is characterized by high local strains in the thin-shell region, leading to local failure of the corroded shell, and significant reserve strength following initial local failure. The local shell failure was identified by the rapid growth of strain at the corrosion patch followed by a strain reversal, as shown in Figure 33. Two possible explanations for the strain reversal at the shell corrosion are that the corroded shell begins to carry load primarily through membrane rather than combined bending/membrane action; or that there is a local outward buckling of the corroded shell. The latter explanation is supported by the post-testing shapes of the short models with heavy stiffeners and corrosion, which show outward deformation of the corroded shell.

Unfortunately, these models were tested using the original testing method, which resulted in catastrophic failures. As a result, strain gauge data is unavailable after the onset of collapse, and it is not known when the local outward deformation in the corroded shell occurred –it may be a product of the dynamic post-collapse behaviour. Nonetheless, both explanations –a shift to membrane behaviour and local buckling– involve load being redistributed from the corroded shell to the surrounding intact shell and ring-stiffeners. Specimen L300-N03 was able to withstand a pressure load approximately 23% greater than the pressure at which the strain reversal and local failure occurred in the corrosion patch.

The heavily-stiffened cylinders showed average reductions in the pressures causing collapse and initial yielding of 8.5% and 23.5%, respectively, for an average thinning of 24.8%. But, if from a serviceability point of view (i.e., setting limits on acceptable in-service strains and displacements) specimens are considered to have failed when the corroded shell becomes locally unstable, then the strength of the models are reduced by a magnitude similar to the percentage of thinning (e.g., approximately 27% for L300-N03 compared to the average collapse pressure of similar intact models).

Overall collapse

For models with shell thinning that failed by overall collapse, the experimental data clearly show that the average local strain in a corroded region is greater than in intact regions of the same specimen. This increase can be partially attributed to shell thinning alone. Large strains observed at the edges of the thinned shells suggest that the shell eccentricity due to one-sided thinning introduces bending moments at these locations, which lead to even higher stresses. High local stresses due to the combination of thinning and eccentricity lead to early onset of yielding in the corroded region, and hence earlier onset of elasto-plastic collapse compared to intact cylinders. Bending strains due to the shell eccentricity are likely also significant for interframe collapse models, but edge strains were not measured during testing of those cylinders.

Figure 37 shows the relationship between the maximum shell thinning for overall collapse models and the resulting reduction in yield and collapse strength, as compared to similar intact specimens. This figure clearly shows the trends of decreasing strength with increased corrosion thinning, as well as the greater impact on yield compared to collapse strength. Least-squares linear regression of the collapse and yield data in Figure 37 results in slopes of 0.99 and 2.38, respectively. This suggests that the reduction in collapse pressure for models failing by overall collapse is, on average, equivalent to the percent depth of thinning, and that the average percent reduction in yield strength is over twice that value.

The experimental data seem to indicate that the disproportionate effect of corrosion on yield compared to collapse strength is related to the redistribution of the load shed by the corroded shell, after initial yielding, to

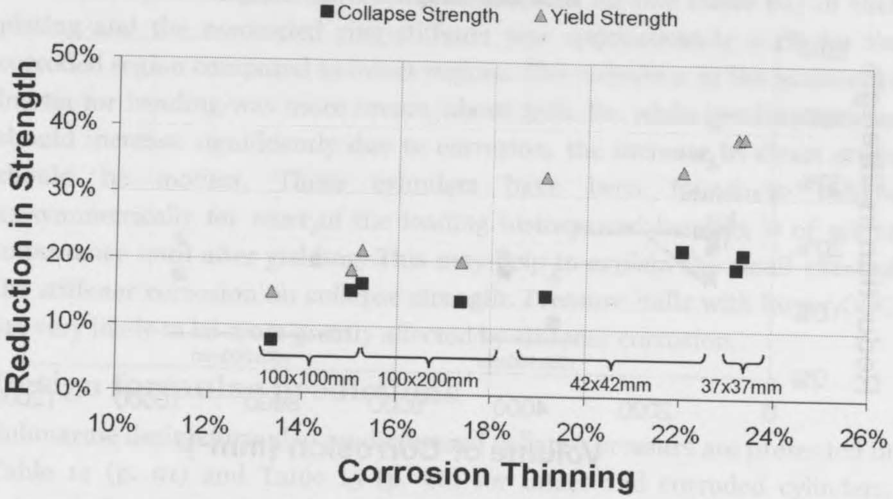

Figure 37: Relationship between cylinder strength and shell thinning for specimens with light, internal ring-stiffeners and failing by overall collapse. The patch sizes are shown at the bottom of the chart by specifying the circumferential and axial extents.

the adjacent ring-stiffeners and shell. Ultimate collapse was delayed until the intact stiffeners or shell began to yield.

It was pointed out in [42] that one-sided corrosion thinning effectively increases out-of-circularity. For long cylinders in this study with 0.4 mm thinning, the neutral axis of the combined shell and stiffener is locally shifted towards the centre of the specimen by approximately 0.3 mm. This is equivalent to an out-of-circularity of 0.25% of the mean shell radius, which is significantly greater than the measured OOC values (see Table 12). It is therefore not surprising that models failing by overall collapse were more greatly affected by thinning than models failing by interframe collapse, since the latter are less sensitive to OOC.

Figure 38 shows a plot similar to Figure 37, but replaces corrosion thinning on the horizontal axis with total volume of corrosion. This figure shows data for a variety of patch areas and depths. There is no obvious trend relating increased corrosion volume to decreases in overall collapse and yield strength; in fact, the four cylinders with the greatest volumes of corrosion showed smaller decreases in collapse pressure than all other cylinders except one. Furthermore, three cylinders with nearly identical volumes of corroded material (980 ± 13 mm^3) show a large variation in strength reduction.

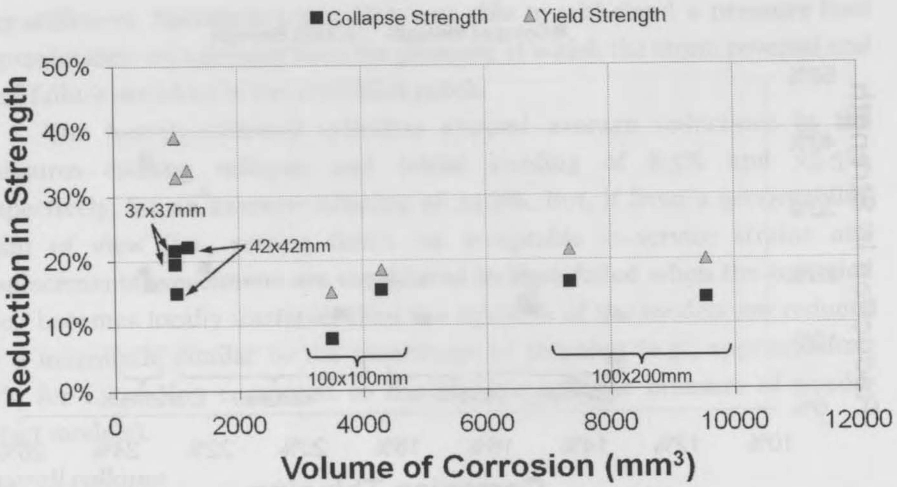

Figure 38: Relationship between cylinder strength and volume of corrosion for specimens with light, internal ring-stiffeners and failing by overall collapse. The patch sizes are also shown by specifying the circumferential and axial extents.

Taken together, the trends observed in Figure 37 and Figure 38 suggest that the magnitude of thinning has a greater impact on overall collapse strength than the total volume of material lost to corrosion. The circumferential extent of thinning may also be an important factor, as indicated in [42], but this parameter was not sufficiently varied in the models to draw any conclusions. Nonetheless, the relative importance of depth versus volume of corrosion is an important consideration when assessing the operational consequences of corrosion thinning for in-service structures. There are insufficient data points to draw a similar conclusion for interframe collapse.

The strength and stability of cylinders with dog-bone corrosion of the ring-stiffeners were less markedly affected by corrosion than for cases of shell thinning. On average, the collapse strength of cylinders with stiffener corrosion (L510-No2 and L510-No3) was 5.3% less than similar intact specimens (L510-No1 and L510-No4). The yield pressure of the instrumented cylinder (L510-No3) was reduced by a similar magnitude. Furthermore, that cylinder actually collapsed at a higher pressure than the intact specimen L510-No1, possibly due to variability in the material properties for a batch. Nonetheless, this observation makes it more difficult to make definitive conclusions about the strength-reducing tendency of stiffener corrosion.

The reduction in total cross-sectional area for one frame bay of shell plating and the associated ring-stiffener was approximately 4.4% for the corroded region compared to intact regions. The reduction in the moment of inertia for bending was more severe, about 33%. So, while bending stresses should increase significantly due to corrosion, the increase in direct stress should be modest. These cylinders have been found to behave axisymmetrically for most of the loading history, and bending is of minor importance until after yielding. This may help to explain the small effect of the stiffener corrosion on collapse strength. Pressure hulls with larger OOC are very likely to be more greatly affected by stiffener corrosion.

Design formulae predictions

Submarine design formulae predictions of collapse pressure are presented in Table 14 (p. 91) and Table 15 (p. 96) for intact and corroded cylinders, respectively, along with the experimental values. The predicted collapse pressures are based on the methodology described in Section "Design formulae predictions" on p. 89.

Table 14 and Table 15 also list the "modeling uncertainty factor", X_m, for individual specimens. X_m is taken as the experimental collapse pressure divided by the predicted collapse pressure. The mean value of X_m for a group is referred to as the bias, and is an indication of the ability of the method to, on average, correctly predict the collapse pressure. The coefficient of variation (COV) provides a measure of the scatter in the collapse predictions, and is defined as the quotient of the standard deviation of X_m and the bias.

Intact models

Table 14 indicates that the design methods almost uniformly under-predict the collapse pressures of the intact cylinders. This is reflected in biases greater than unity, with the interframe and overall methods under-predicting the actual collapse pressures by, on average, 16% and 4%, respectively. The empirical interframe design curve is based on cylinder models with a wide variety of manufacturing methods and qualities, so that the predicted collapse pressure includes scatter associated with large OOC amplitudes (up to 0.5% of the mean shell radius) and residual stresses. Since the overall collapse predictions used more realistic OOC values, and did not include the effects of residual stresses, more accurate collapse predictions were achieved. The overall collapse methodology also tended to predict the circumferential wave number with greater accuracy than the interframe methods, which are based on elastic buckling assumptions. Scatter in X_m was of a similar magnitude for both failure modes, as indicated by COVs between 5% and 7%.

The design calculations predict the intact cylinders with light stiffeners to fail by interframe collapse, since the interframe design collapse pressures are between 5% and 7% less than the corresponding overall collapse predictions. The discrepancy between the predicted (interframe) and actual (overall) collapse modes for this group of cylinders can be attributed to the excessive pessimism of the interframe empirical curve for these carefully constructed cylinders. Nonetheless, the similarity of the predicted overall and interframe collapse pressures helps to explain the apparent failure mode interaction (i.e., yielding of both the shell and stiffeners prior to collapse, with interframe dimples superimposed on a global buckling lobe) that was observed in collapse tests of the lightly-stiffened cylinders.

Corroded models

The data in Table 15 indicate that the design methods under-predict the collapse pressures of corroded cylinders to an even greater extent than for intact cylinders. Interframe collapse predictions are overly pessimistic, by 32% on average, due to the application of the corroded geometry in an axisymmetric manner, as well as the previously mentioned conservatisms related to the empirical methodology. The overall collapse methodology was more accurate, under-predicting collapse by 13% on average, since the corrosion damage and OOC could be modeled with greater precision. Scatter in the analytical-experimental correlation was also greater for corroded compared to intact cylinders, with COVs between 15% and 16% for both failure modes.

Conclusions and future work

The experimental data suggest that corrosion thinning of the shell reduces pressure hull collapse pressure due to the depth of thinning and to the resulting shell eccentricity when thinning is one-sided. Alternatively, one-sided thinning can be viewed as equivalent to uniform thinning and an accompanying out-of-circularity imperfection. The sensitivity of shell buckling to thickness and imperfections is well documented. Viewed either way, these factors introduce high stresses and destabilizing bending moments at the corroded region, thus contributing to the early onset of yielding and ultimate collapse.

The observed reductions in overall collapse and yield pressures due to shell thinning were as high as 20% and 40%, respectively, compared to intact specimens. This implies serious operational consequences for in-service pressure hulls, whether the design load is related to the yield pressure or the collapse limit state. Furthermore, for the cases studied here, the volume of material lost to corrosion seems to have less influence on overall collapse strength than the depth of thinning, although the influence of the circumferential extent of thinning is still unclear.

The effect of shell thinning on interframe collapse was found to be less severe in this study, mainly because heavy stiffeners in models failing in that mode were able to pick up the load shed by the corroded shell. This result should be interpreted with caution since ring-stiffeners in real pressure hulls, even if they are designed to fail by interframe collapse, are not typically as heavy as those of the experimental models, since optimal designs are achieved by having similar overall and interframe collapse pressures. Furthermore, when local failure of the corroded shell was taken to indicate failure of the entire model, the percentage reduction in strength was similar for models failing by interframe and overall collapse.

Artificial corrosion of the ring-stiffeners was not found to significantly reduce the collapse strength of cylinders in this study; this is likely due to the predominance of direct rather than bending stresses. Pressure hulls with larger OOC and residual stresses due to industrial fabrication procedures are likely to be more greatly affected by stiffener damage.

The empirical method for interframe collapse has been shown to be pessimistic when predicting collapse of the intact cylinders, under-predicting the collapse pressure by between 6 and 27%. Overall elasto-plastic collapse predictions were, on average, more accurate, being within -11 and +10% of the measured value. Both methods were less accurate at predicting collapse pressures for corroded models, with the interframe and overall methods predicting the actual collapse pressures within -74 and -12%, and -48 and +8%, respectively.

The OOC of the cylinders discussed in this chapter was very small due to fabrication by machining. The effect of thinning is thought to be most severe for cylinders with small-amplitude imperfections, since the effective increase in OOC is most pronounced [42]. Further testing will examine the effects of large-amplitude OOC on the collapse of intact and corroded cylinders, as well as more realistic patterns of corrosion (see Chapter 6, p. 133). The effect of material properties on corroded and intact cylinders is also being studied by testing cylinders constructed of lower yield-strength aluminium (see Chapter 5, p. 107). The nonlinear finite element methodology described in [51], which was used to analyse some of the experimental models described in the present study, will be further validated against the current and new test specimens (see Chapter 7, p. 155, and Chapter 8, p. 195, respectively). Validated FE modeling and analysis methods can then be used to conduct numerical experiments to fill in the gaps of the testing program and extend the scope of the investigation.

Chapter 5

Experimental study of the sensitivity of intact and damaged pressure hulls to material strength

Twenty ring-stiffened cylinders were machined from high- and low-grade aluminium alloy tubes. The cylinders, which are representative of naval submarine pressure hulls, were tested under external hydrostatic pressure in order to study the effect of material strength on overall elasto-plastic collapse. Artificial general corrosion damage was introduced in selected specimens by machining away material from the outside of the cylinder shell in rectangular patches of uniform depth. Comparisons of similar intact and corroded specimens indicated that collapse pressures for corroded cylinders were reduced by approximately $0.86\delta_c$, where δ_c is the depth of thinning divided by the original shell thickness, for a variety of patch sizes and depths and material strengths. The collapse strength of corroded cylinders was found to be more sensitive to the shape of the stress-strain curve than for intact specimens. Higher levels of strain hardening and ductility were found to improve the performance of damaged cylinders. Finally, one corroded cylinder was repeatedly loaded past the yield limit in order to study the effect of cyclic plastic loading on collapse. The permanent deformations, as measured with strain gauges, grew with each constant-amplitude load cycle; however, the additional deformations tended towards zero with increasing number of cycles, and a subsequent collapse test indicated that the cyclic loading did not affect the collapse pressure. This chapter is based on the manuscript of a paper co-authored with Fred van Keulen. The paper has been accepted by the *Journal of Offshore Mechanics and Arctic Engineering* and is currently in press [23].

Introduction

Corrosion damage to naval submarine pressure hulls is best prevented using preservative coatings or impressed current cathodic protection. If those measures fail, corrosion can result in a significant degradation of the exposed hull material. Once detected, the corroded material is removed by grinding. The resulting loss of thickness can be corrected by locally applying weld material to the hull in order to build up its thickness to the original value. However, the heat input associated with weld repair can result in residual stresses and distortions, as well as changes to the material properties in the heat-affected zone. The sensitivity of submarine hull strength and stability to those by-products of the repair procedure is not yet known [139]. On the other hand, damaged hull plating can be completely replaced, rather than repaired, but that option is expensive and does not eliminate welding stresses and distortions. Thus, in many cases it is preferable to operate submarines with some corrosion damage, whether in the form of small corrosion pits or larger areas of general corrosion.

The effect of discrete patches of general corrosion damage on the strength and stability of pressure hulls has been studied using numerical models in [13,42]. Hull collapse strength was found to be reduced through high local stresses in the corroded region, as well as by the effective increase in out-of-circularity (OOC) imperfections associated with one-sided thinning. However, because experimental results for corroded hulls were not available until recently [22], numerical models could not be properly validated and modeling procedures were uncertain.

In [22] (see Chapter 4, p. 77), general corrosion damage was artificially introduced into ring-stiffened cylinders that were machined from aluminium tubing and tested to collapse in a pressure chamber. Aluminium was chosen since it is easy to machine, and since it is a strain hardening material that behaves like high-strength steels used in real pressure hulls. The results of those experiments confirmed that the failure mechanisms were predicted correctly by the numerical models in [13,42]. The test results were used to validate nonlinear finite element (FE) models of the test specimens [25] (see Chapter 7, p. 155).

The tests in [22] showed that overall collapse, which is characterized by a general elasto-plastic buckling of the ring-stiffeners and shell plating, is more sensitive to corrosion thinning than interframe collapse, whereby the shell plating buckles inelastically while the ring-stiffeners initially remain intact. The percentage reduction in overall collapse pressures was approximately equal to the percentage of shell thinning for a variety of corrosion patch sizes.

Pressures for yielding of the corroded specimens on the other hand were reduced by over twice the percentage thinning. The disproportionate effect of corrosion damage on yield pressure, compared to collapse pressure, has two potential consequences. First, it suggests that the effect of corrosion damage on hull strength will be sensitive to the material behaviour, and particularly the post-yielding shape of the stress-strain curve, i.e., strain hardening. Second, it suggests that a corroded hull could be plastically deformed during diving, even if the deep diving depth (DDD) has been restricted to account for the expected reduction in collapse pressure (but not the yield pressure). Those permanent deformations pose a risk, since the associated residual stresses and displacements could interact with elasto-plastic collapse mechanisms, over one or multiple dives, to induce collapse at the restricted DDD, despite the apparent safety margin on the collapse pressure.

The aim of the current chapter is to experimentally study the effect of material strength and behaviour on overall collapse of corroded submarine hulls, and to investigate the possibility of cyclic plastic collapse of damaged hulls. To that end, twenty ring-stiffened cylinders were machined from two different grades of aluminium tubing having significantly different yield stresses and strain hardening behaviour. General corrosion damage was introduced into selected specimens by machining material from the outside of the cylinders. Some of the test specimens are shown in Figure 39, and their axisymmetric geometries are given by Configurations 1 and 2 in Figure 27, p. 82. The specimens were tested to collapse in a pressure chamber in order to determine the effect of the corrosion damage on strength and stability. One of the corroded specimens was cyclically loaded past the yield limit in order to study the potential for collapse resulting from the build-up of permanent deformations.

This chapter begins with a description of the test specimens and experimental methods in the next section, after which the experimental results are presented. The effect of material strength on the collapse of intact and corroded hulls is then discussed, along with the potential for cyclic plastic failure of corroded hulls. The discussion is followed by conclusions and plans for future work.

Test specimens and experimental methods

The test specimens considered in the current work are summarized briefly in the following sections. Detailed descriptions of the measured specimen geometry and material are presented in [28-30,32]. Twelve of the specimens were fabricated from AA-6082-T6 aluminium. Collapse testing results for those specimens were presented in Chapter 4 [22], and serve as a benchmark against which to compare test results for eight new specimens fabricated from the lower grade AA-6082-F28 aluminium. The T6 and F28 materials are compared in Section "Material properties", p. 114. Summaries of the T6 and F28 test specimens are given in Table 16 and Table 17, respectively, including the type and magnitude of corrosion damage, the measured yield stress of the cylinder material, and the experimental yield and collapse pressures. Nominally identical T6 and F28 specimens are differentiated by an "A" suffix appended to the name of F28 cylinders.

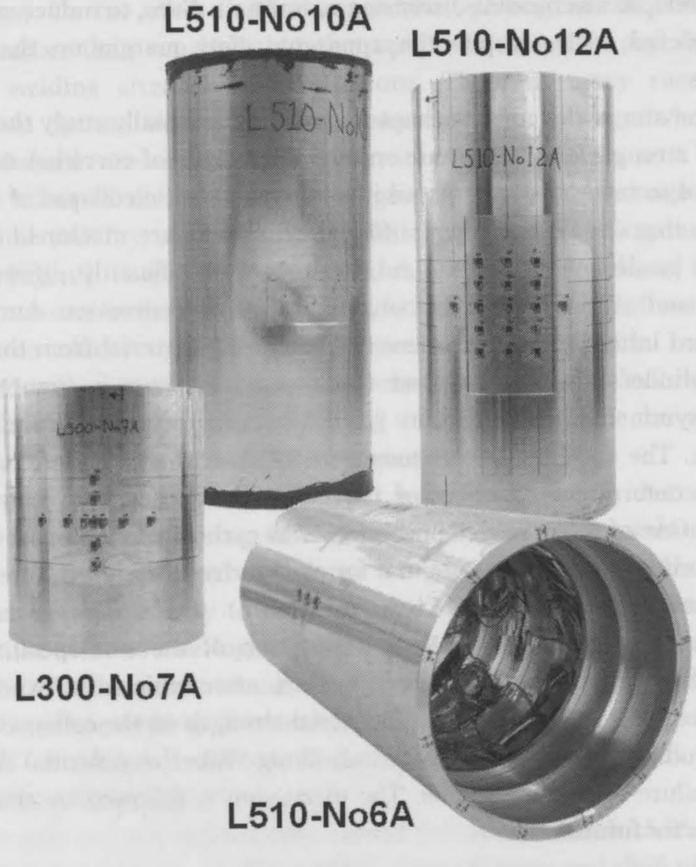

Figure 39: Photographs of typical test specimens. Clockwise from middle-left: L510-No10A, with Patch C general corrosion, after collapse testing; L510-No12A, with Patch D general corrosion, before testing; the intact specimen L510-No6A, showing the internal ring-stiffeners and strain gauge wiring, before testing; and L300-No7A, with Patch A corrosion damage, before testing.

Table 16: Summary of corrosion damage and test results for AA-6082-T6 specimens[a] *[22].*

Specimen	Corrosion Type	δ_c	σ_y (MPa)	P_b (MPa)	P_y (MPa)	P_c (MPa)
L300-No5	Intact	N/A	303	7.64	7.44	8.99
L300-No6	Intact	N/A	303	7.68	7.53	9.14
L300-No7	Patch A	23.2%	303	7.66	4.57	7.30
L300-No8	Patch A	23.3%	303	7.58	4.56	7.11
L510-No5	Intact	N/A	297	7.43	8.08	9.08
L510-No6	Intact	N/A	303	7.41	7.41	8.48
L510-No7	Patch B	22.1%	297	7.48	5.33	7.07
L510-No8	Patch B	19.1%	306	7.49	4.97	7.21
L510-No9	Patch C	15.1%	297	7.63	6.58	7.68
L510-No10	Patch C	13.4%	303	7.49	6.29	7.81
L510-No11	Patch D	15.3%	297	7.44	6.34	7.58
L510-No12	Patch D	17.3%	303	7.56	5.93	7.29

[a] Corrosion damage cases are described in Table 18. δ_c is the maximum measured corrosion thinning, σ_y is average measured circumferential yield stress, P_b is the boiler pressure as defined by Eq. (17) on p. 123, P_y is the applied pressure at which the strain gauges first detected yielding in the experiments, and P_c is the experimental collapse pressure.

Table 17: Summary of corrosion damage and test results for AA-6082-F28 specimens[a].

Specimen	Corrosion Type	δ_c	σ_y (MPa)	P_b (MPa)	P_y (MPa)	P_c (MPa)
L300-No5A	Intact	N/A	171	4.34	4.44	5.54
L300-No6A	Intact	N/A	182	4.61	4.52	5.98
L300-No7A	Patch A	26.9%	225	5.65	3.32	5.56
L300-No8A	Patch A	24.3%	188	4.74	3.09	5.06
L510-No6A	Intact	N/A	238	6.07	6.48	7.31
L510-No8A	Patch B	21.8%	172	4.36	2.87	4.11
L510-No10A	Patch C	16.1%	224	5.67	4.81	5.97
L510-No12A	Patch D	19.6%	221	5.72	4.64	5.74

[a] See note (a) in Table 16.

Axisymmetric geometry

The axisymmetric geometry of each test specimen was produced by turning extruded aluminium tubes on a CNC lathe. The specimens were produced in two standard lengths of 300 and 510 mm, resulting in the so-called L300 and L510 series of cylinders, respectively. The nominal dimensions for the L510 and L300 series are given by Configurations 1 and 2, respectively, in Figure 27, p. 82. The axisymmetric geometries of the two series were similar, except that with the L300 series, there were only four ring-stiffeners and only the central bay was 50 mm in breadth; the other two bays measured 45 mm. The T-section ring-stiffeners and shell thickness were proportioned to promote overall collapse. The thick, tapered end-rings were designed to prevent undesired end-bay failure, and to allow thick steel end-caps to be bolted on to the cylinders before pressure testing.

Corrosion damage

General corrosion was simulated by machining away some of the shell material from the outside of selected specimens. Other specimens were left intact in order to establish the baseline strength of undamaged cylinders. The corrosion damage was applied in rectangular patches of uniform depth, centred at the cylinder mid-lengths. Each specimen had only one corrosion patch, and four different patch sizes were studied, as defined by their nominal dimensions in Table 18. The measured levels of thinning, which are presented in Table 16 and Table 17, deviated somewhat from the nominal values given in Table 18.

Table 18: Descriptions of nominal corrosion damage cases.

Corrosion	Description[a]
Intact	No corrosion damage
Patch A	34×34×0.75 mm corrosion patch, with 25% nominal thinning (patch size was 37×37 mm for AA-6082-T6 specimens in Table 16)
Patch B	42×42×0.6 mm corrosion patch, with 20% nominal thinning
Patch C	100×100×0.4 mm corrosion patch, with 13.3% nominal thinning
Patch D	100×200×0.4 mm corrosion patch, with 13.3% nominal thinning

[a] Corrosion patch sizes are specified by the circumferential times the axial extents, times the depth. All corrosion patches were located on the outside of the cylinder shell, and were centred at the cylinder mid-length, mid-way between the two central ring-stiffeners.

Chapter 5

Measured geometry

A coordinate measurement machine (CMM) was used to characterize the as-machined geometry of the test specimens. Radial measurements were taken on the inside and outside of each test specimen on a uniform grid with thirty-six points about the circumference, and axial locations corresponding with ring-stiffeners and mid-bay positions. Those measurements allowed discretized maps of the OOC and shell thickness (by comparing inner and outer radii) to be derived for each specimen. The accuracy of the CMM is ±0.02 mm.

Vibrations that occurred during the machining process (i.e. chatter) led to cylinders with out-of-circularity characterized by two complete waves about the circumference (n=2). In general, the OOC shapes were approximately constant over the length of the cylinders, although the OOC magnitude tended to be greatest near the cylinder ends. The longer L510 series of cylinders had to be machined in two stages, with the specimens flipped lengthwise and re-clamped after machining half the length. As a result, a phase angle shift in the n=2 shape was sometimes observed near the center of the L510 cylinders. Measurements taken at the outside of the shell and the inside of the ring-stiffener flanges showed similar OOC shapes and magnitudes. The n=2 OOC mode of the test specimens is consistent with the imperfect shapes of actual submarine hulls, which tend to be dominated by the same mode [16], mainly due to longitudinal welding of the hull [73].

The maximum radial eccentricity of the shell was found to be between 0.0003a and 0.0014a for all specimens, where a is the mid-plane shell radius. Those values are considerably less than the standard OOC magnitude of 0.005a used to design hulls against collapse [5]. On the other hand, the specimen OOC magnitudes are much closer to the typical build tolerance of one-third of the design value, or 0.0017a [5]. The out-of-circularity and shell thickness of specimen L300-No6A, based on measurements at the central bay, are shown in Figure 40. That specimen had the typical n=2 OOC mode at a magnitude (0.0007a) in the middle of the range for these cylinders. The magnitudes of corrosion thinning listed in Table 16 and Table 17 were derived by comparing the minimum measured shell thickness in a corrosion patch with the mean measured shell thickness in intact regions of the cylinder.

The CMM measurements indicated that the as-machined radii and shell thicknesses of all specimens were within 0.1% and 5% of the nominal values, respectively, except for L510-No8A. The shape measurements for that cylinder revealed that one of the short, 20 mm end-bays (see Figure 27,

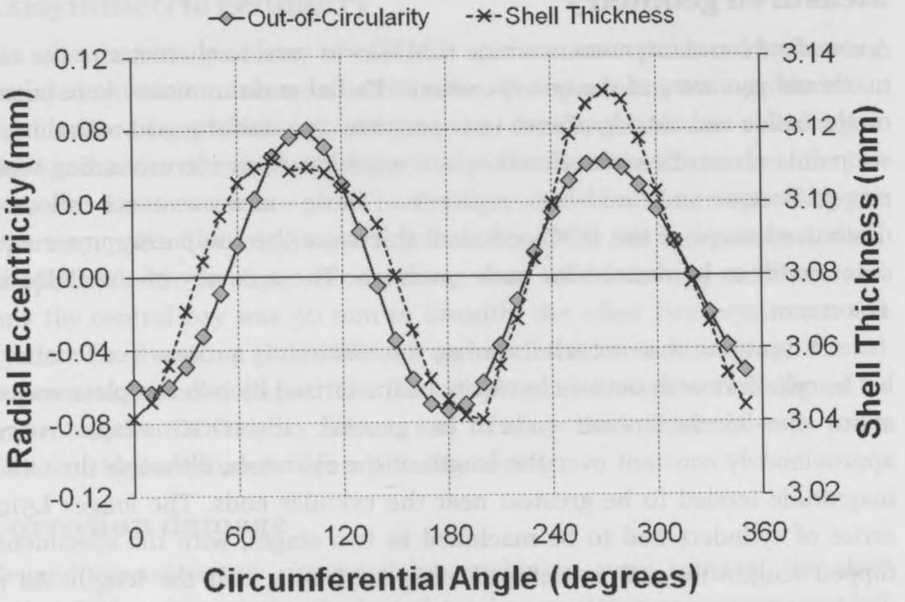

Figure 40: Measured out-of-circularity and shell thickness at the centre of the central bay of L300-N06A.

p. 82) was approximately 2 mm thick, rather than the design value of 3 mm. The unintentional thinning was from the inside of the shell and arose due to an error in the CNC machining. Otherwise, the shell thickness and radius of L510-N08A were within the previously mentioned tolerances.

Material properties

Aluminium alloy AA-6082-T6 has a minimum yield stress in tension of 250-260 MPa, a minimum tensile strength of 290-310 MPa, and an elongation at break of 10% [140]. AA-6082-F28 is a similar grade of aluminium, but it is not subjected to the T6 heat treatment. Thus, the tube manufacturer does not guarantee minimum material properties for the F28 aluminium.

Tensile coupon testing for AA-6082-T6 specimens indicated that the as-machined cylinders were anisotropic, with a yield stress in the circumferential direction that was approximately 10% less than the axial yield stress. The anisotropy likely resulted from the extrusion process for the original tubes. Furthermore, it was found that there could be as much as 10% variation in material properties between separate batches of the same material. Those considerations led to the adoption of a practice whereby tensile coupons were machined from the end-rings of each test specimen after collapse testing in order to determine specimen-specific material properties. The end-rings of the specimens were not plastically deformed during collapse testing, so the material properties measured with those coupons may be considered to represent the pre-testing state of the cylinders. The diameter and gauge length of the undersized, circular cross-section coupons were 4 mm and 20 mm, respectively. The coupons were loaded using displacement control at a rate of 0.36 mm/minute, based on the crosshead displacement of the testing frame. After the onset of yielding, the loading rate was increased to approximately 1.2 mm/minute.

The data for the AA-6082-T6 specimens in Table 16 are based on representative coupon samples for an entire batch of tubing, while the yield stresses for AA-6082-F28 cylinders in Table 17 are specimen-specific. The yield stress data in both tables are based on coupons taken from the circumferential direction of the cylinders or tubes.

The measured yield stresses for the F28 material were uniformly lower than for the heat treated T6 aluminium, and there was considerable variation in yield stress between individual AA-6082-F28 specimens. It is possible that the F28 cylinders were machined from two batches of tubing, since there appears to be two distinct groups of circumferential yield stresses, with values ranging from 171 to 188 MPa and 221 to 238 MPa. Figure 41 shows engineering stress-strain curves for coupons taken from the axial and circumferential directions of an AA-6082-F28 tube from the higher yield stress batch. It is clear from Figure 41 that the F28 material shares the anisotropy of the T6 grade, and that the axial yield stress is approximately 10% greater than the circumferential value.

Typical engineering stress-strain curves for AA-6082-T6 and the high- and low-yield stress batches of the F28 material are plotted in Figure 42. That figure shows a trend whereby the magnitude of strain hardening and ductility decrease as the yield stress of the aluminium increases. Figure 42 also shows a measured stress-strain curve for a typical submarine pressure hull material, Q1N high strength steel [141]. While that steel has a greater elastic modulus and yield stress than the aluminium alloys, the overall shape of the stress-strain curves are similar. The steel and aluminium material will be further compared in the discussion starting on p. 122.

The average measured values of Young's modulus for the T6 and F28 groups were 72.2 and 68.1 GPa, respectively. Those values are close to the typical handbook value of approximately 70 GPa [142]. Poisson's ratio was not measured for the F28 aluminium, but coupon tests for AA-6082-T6 gave results between 0.32 and 0.34.

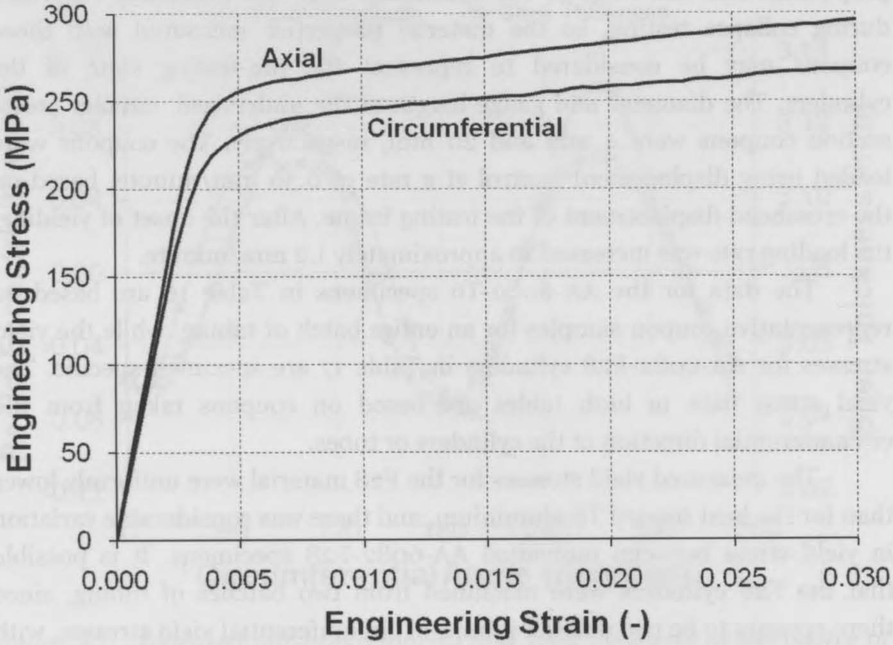

Figure 41: Average measured engineering stress-strain curves for tensile coupons taken from the axial and circumferential directions of an AA-6082-F28 cylinder.

Pressure testing

Pressure testing was conducted in a pressure chamber using a "volume-control" method, whereby each test specimen was pressurized from both the inside and the outside, and the internal pressure was regulated using a series of hoses and valves to achieve the desired net external pressure. In Chapter 3 [21], the volume-control method was shown to give better control of post-collapse deformations than conventional air-backed pressure testing. The average loading rate at the start of each experiment was approximately 3 MPa/minute. The loading rate tended to decline as the testing proceeded and, by the time collapse occurred, was only a small fraction of the initial value. Thus, the specimen loading was effectively static, as originally intended. A non-conductive mineral oil was used as the pressure testing fluid in order to prevent shorting of the data acquisition equipment used to monitor strain gauges and pressure transducers.

Before testing each cylinder, 38 mm thick, mild steel end caps were attached to both ends of the specimen with bolts. The cylinders were

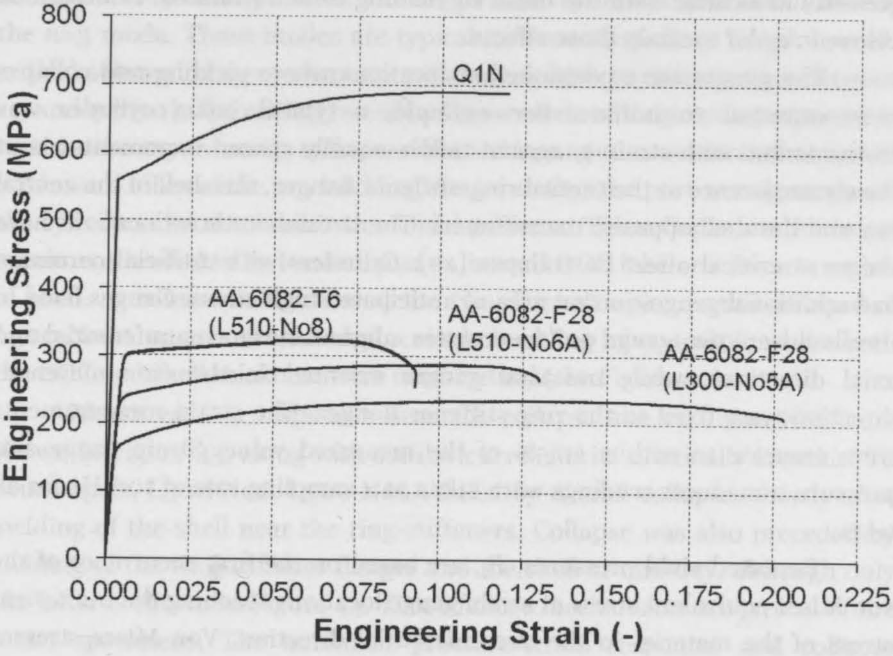

Figure 42: Typical engineering stress-strain curves for aluminium alloys and a high-strength naval quality steel; showing measured data for coupons taken from the circumferential direction of aluminium test cylinders, and the average curve for coupons taken from the rolling and transverse directions of a Q1N steel plate.

therefore approximately clamped at the ends (that is supported by the results of the numerical modelling in Chapter 7 of this thesis [25]). Watertight integrity at the end-cap joint was achieved using an adhesive polymer sealant. Pressure transducers were used to measure the pressures inside and outside of the test specimens, in order to derive the net external pressure load. The reported collapse pressures, P_c, are based on the maximum measured net load and are accurate to within ±0.09 MPa. All specimens except L300-No8A were pressurized monotonically until they collapsed. L300-No8A was the cylinder chosen for cyclic loading, the details of which are given in Section "Experimental results" starting on p. 118.

Each cylinder was instrumented with between 64 and 72 strain gauges in order to track specimen deformations during loading and to provide information on the collapse mode. Typical intact submarine hulls collapse soon after the onset of yielding [10], but it is not clear how strain hardening and corrosion affect that relationship. The measured strain data allow the pressure associated with the onset of yielding to be estimated, as described below, in order to study those effects.

The gauges were positioned at locations where yielding and collapse were expected to initiate. For example, a typical intact cylinder was instrumented with strain gauges at twelve equally spaced increments about the circumference at the central ring-stiffener flanges, the shell in the central bay and the shell opposite the stiffeners. The stresses in those locations have the most critical affect on collapse [10]. Cylinders with artificial corrosion had additional gauges in that area of anticipated high stress. Gauges fixed to the shell were two-gauge 90° tee rosettes, aligned in the circumferential and axial directions, while uni-axial gauges oriented in the circumferential direction were fixed to the ring-stiffener flanges. The strain measurements were accurate to within ±0.5% of the measured value. Strain gauge and pressure transducer readings were taken at a sampling rate of 100 Hz for all tests.

Reported yield pressures, P_y, are based on the first occurrence of the von Mises equivalent stress at strain gauge locations reaching the 0.2% yield stress of the material in the circumferential direction. Von Mises stresses were calculated using the generalized Hooke's law with the measured circumferential and axial strains, and assuming a plane stress condition whereby the in-plane shear stresses were negligible. The procedure for calculating stresses from measured strain values is described in greater detail in Chapter 4, Section "Data processing" (p. 88) [22]. It is acknowledged that, by measuring strain at a limited number of locations and by neglecting shear strains, the yield pressures are likely over-estimated. On the other hand, the critical stress locations have been measured, so the errors in the estimated yield pressures are not likely excessive. Furthermore, those data allow comparison of the relative onset of yielding at the same location on different specimens, and provide valuable insight into the collapse mechanisms.

Experimental results

The experimental collapse and yield pressures are listed in Table 16 and Table 17. Each specimen failed by overall collapse, with large deformations of both the shell plating and ring-stiffeners. In this section, the pressure-strain (P–ε) response of typical intact and corroded specimens will be presented, as well as the cyclic loading of L300-No8A.

The circumferential distribution of strain showed that, before collapse, the deformations in the shorter L300 specimens were characterized by sinusoidal $n=4$ or $n=5$ modes. The longer L510 cylinders were dominated by the $n=3$ mode. Those modes are typical of short to medium length overall-critical submarine compartments with, say, length to radius ratios between 1.5 and 4.5 [10]. The critical overall collapse mode of longer compartments is $n=2$. In the experiments, collapse deformations were concentrated at one of the inward lobes of the pre-buckling shape, so that the post-testing shapes of the cylinders did not exhibit sinusoidal patterns. The collapse site for intact specimens tended to be located near an inward OOC lobe or a thinner region of shell, or some combination of the two. For example, overall collapse of L300-No6A was concentrated at a single buckling lobe at 180°, where both the OOC and shell thickness were most critical (see Figure 40).

Measured P–ε responses near the collapse site on L300-No6A are shown in Figure 43, along with similar curves for its nominally identical T6 counterpart, L300-No6. L300-No6A failed by overall collapse, shortly after yielding of the shell near the ring-stiffeners. Collapse was also preceded by yielding of the ring-stiffener flanges and the shell at mid-bay, although only the latter is shown in Figure 43. Those failure mechanisms are typical of the intact specimens. The nonlinear pressure-strain responses and collapse

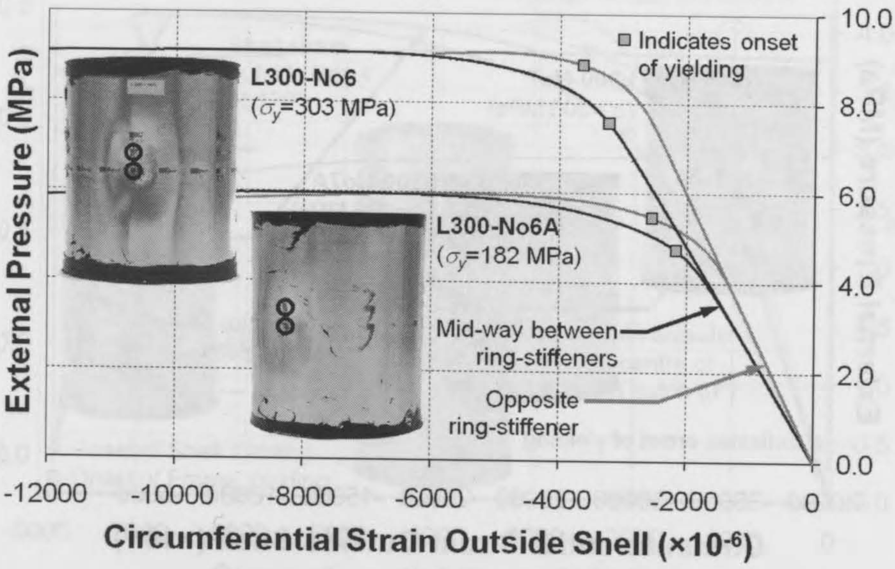

Figure 43: Measured pressure-strain curves for strain gauges near the collapse sites of geometrically identical intact specimens machined from AA-6082-T6 (L300-No6) and AA-6082-F28 (L300-No6A); also showing photographs of the specimens after collapse testing.

modes of the low- and high-grade aluminium cylinders were qualitatively the same. Furthermore, the P–ε responses were quantitatively identical in the initial linear-elastic region, and differed only with respect to the pressure at which yielding occurred.

All specimens with corrosion collapsed in the region of shell thinning, except for L510-No8A, which is discussed separately below. The post-testing photograph of L510-No10A in Figure 39 shows several small interframe buckling lobes superimposed on a large overall collapse lobe. The collapse deformations were concentrated near one edge of the corrosion patch, due to the effect of the shell eccentricity at that location. That type of collapse is typical of cylinders with Patch C and D corrosion.

The collapse modes of cylinders with smaller corrosion patches were centred around the area of shell thinning, as shown by the post-testing photograph of L300-No7A (Patch A) in Figure 44. The P–ε curves shown in that figure indicate that the corroded shell of L300-No7A yielded well before the onset of collapse, which was precipitated by yielding of the intact shell near the ring-stiffeners and adjacent to the corrosion damage. The strain reversal at the corrosion patch just before collapse is likely associated with

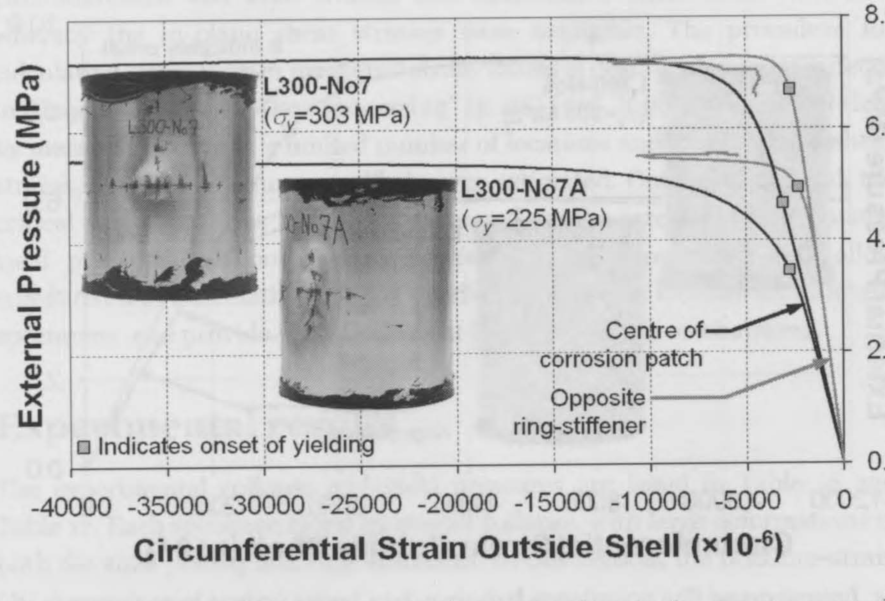

Figure 44: Measured pressure-strain curves for strain gauges near the collapse sites of geometrically identical corroded specimens (Patch A) machined from AA-6082-T6 (L300-No7) and AA-6082-F28 (L300-No7A); also showing photographs of the specimens after collapse testing.

tensile membrane stresses that developed as the bending resistance of the corroded shell diminished. The response of L300-No7, its T6 counterpart, is also shown in Figure 44. As with the intact cylinders in Figure 43, the initial responses of the corroded F28 and T6 cylinders are similar, and the overall shape of the respective P–ε curves are the same. The strain reversal at the corrosion patch occurs after collapse in the T6 cylinder, but otherwise, the cylinder responses differ only in the onset of yielding and subsequent collapse.

L510-No8A was the only corroded specimen not to collapse at the corrosion damage. Its post-testing shape and P–ε response are shown in Figure 45. Despite the large strains and early yielding near the corrosion patch, L510-No8A collapsed at an intact region of the cylinder near the end-bay with unintentional shell thinning (see p. 113). The end-bay thinning was not discovered until after the cylinder was instrumented, so P–ε information is not available at that location. The level of unintentional thinning was quite severe, approximately 36%, so it is not surprising that the cylinder failed near the end-bay; however, it is not clear why the cylinder failed so far away

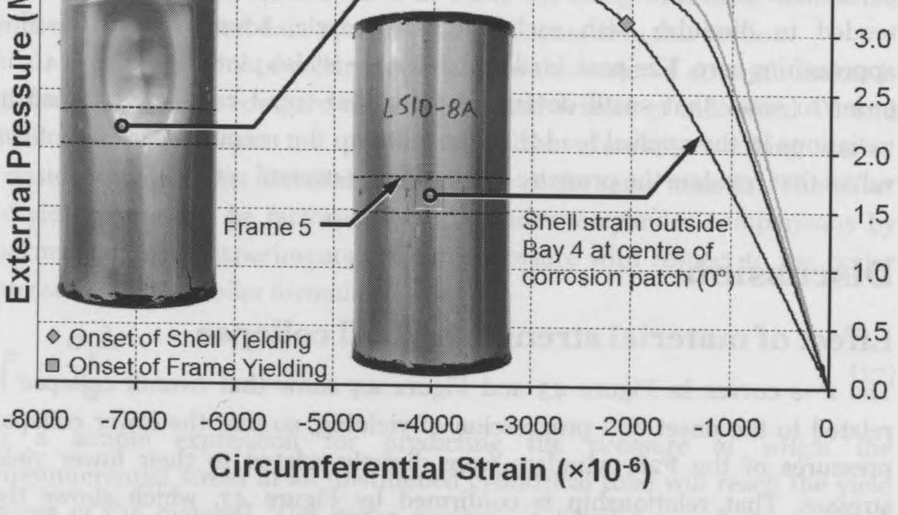

Figure 45: Measured pressure-strain curves for strain gauges near the corrosion patch and the collapse site of specimen L510-No8A; also showing photographs of the specimen after collapse testing.

from the corrosion damage since neither the OOC nor the intact shell thickness were critical at the collapse location.

L300-No8A was cyclically loaded ten times from zero to 4.76±0.09 MPa. The cyclic load level was chosen to ensure that a significant amount of plastic strain occurred in the corrosion patch and surrounding intact shell during the first load cycle. The goal was to produce as much permanent deformation as possible without actually causing the cylinder to collapse during the first load cycle, so that the likelihood of a cyclic failure was optimized. The average cyclic pressure was 54% greater than the pressure causing initial yielding. The cylinder did not collapse during the cyclic loading, but a subsequent destructive test was performed to determine its ultimate strength. The collapse pressure listed in Table 17 is based on that destructive test, whereby the cylinder collapsed at the location of corrosion. The collapse test indicated that the average cyclic load was only 6% less than the overall collapse strength of the cylinder.

The maximum circumferential strain measured at the outside of the corrosion patch during the initial load cycle was approximately 0.012, much greater than the uni-axial circumferential yield strain of approximately 0.003. The residual strain after unloading was approximately 0.007, or 60% of the maximum strain. The incremental residual strain, taken as the residual strain after load cycle *i*, less the residual strain after cycle *i*-1, for each subsequent load cycle is shown in Figure 46. Despite the significant permanent deformation after the first load cycle, the additional deformation tended to diminish with each successive cycle, towards a final value approaching zero. The peak load for each cycle is also plotted in Figure 46, in order to show that small deviations from that trend can be attributed to variations in the applied load that arose due to the manual operation of the valves that regulate the pressure in the volume-control setup.

Discussion

Effect of material strength on hull collapse

The $P-\varepsilon$ curves in Figure 43 and Figure 44 show that overall collapse is related to the onset and progression of yielding, so that the lower collapse pressures of the F28 cylinders were directly related to their lower yield stresses. That relationship is confirmed by Figure 47, which shows the experimental collapse pressures versus the measured circumferential yield stresses for intact specimens. The curve fitting parameters for the regression

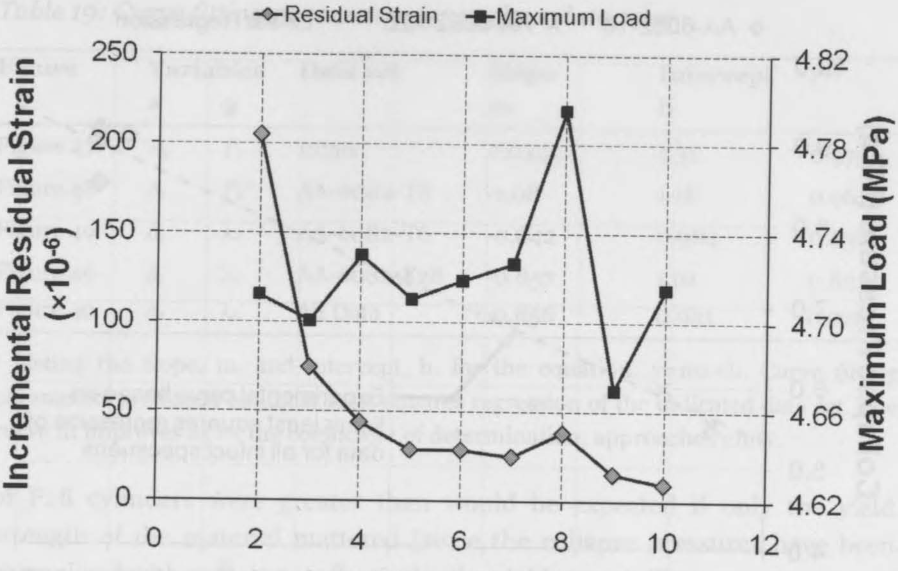

Figure 46: Incremental residual circumferential strain at the outside of the corroded shell after each load cycle that was applied to test specimen L300-No8A; also showing the maximum applied pressure load for each cycle.

line shown in Figure 47 are listed in Table 19, along with those associated with other figures and data sets that will be discussed in this section.

The sensitivity of collapse pressure to the material strength makes it difficult to directly compare the experimental results of individual T6 and F28 specimens, since the properties of the aluminium tubing varied considerably between materials and batches of the same material. The effect of yield stress can be factored out of cylinder-to-cylinder comparisons by normalizing each experimental collapse pressure with respect to the boiler pressure, P_b. The boiler formula,

$$P_b = \frac{\sigma_y h}{a} \tag{17}$$

is a simple expression for predicting the pressure at which the circumferential stress in an unstiffened cylindrical tube will reach the yield stress of the material. The boiler pressure is listed for each T6 and F28 specimen in Table 16 and Table 17, respectively. It was calculated by taking σ_y as the measured circumferential yield stress, h as the mean measured

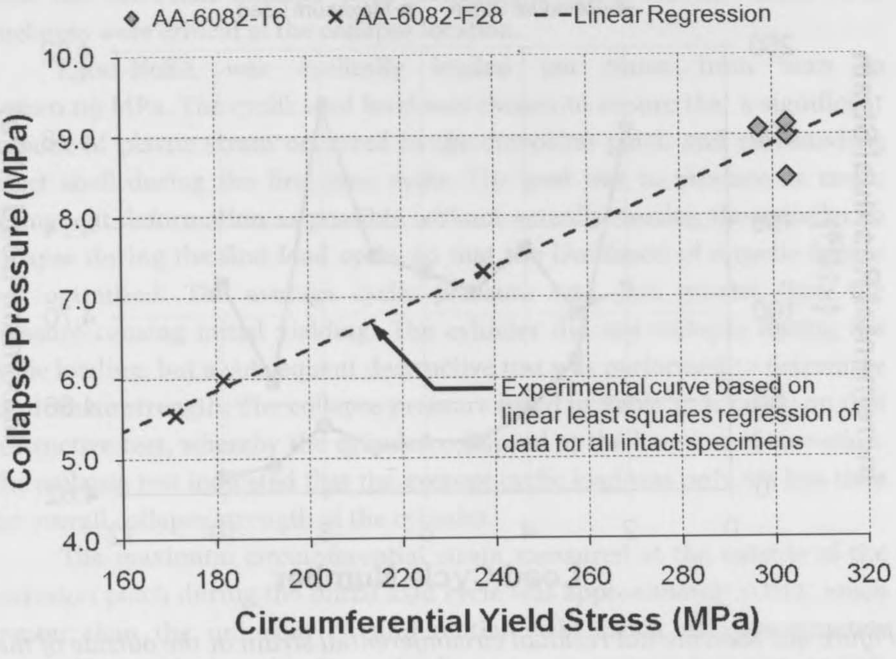

Figure 47: Collapse pressure as a function of circumferential yield stress for cylinders machined from high- and low-grade aluminium.

shell thickness in intact regions of the specimen, and a as the nominal mid-plane shell radius.

A normalized collapse pressure,

$$P_c * = \frac{P_c}{P_b} \tag{18}$$

was then derived for each test specimen by dividing the measured experimental collapse pressure by the boiler pressure. The normalized collapse pressures are plotted against the maximum measured corrosion thinning, δ_c, in Figure 48. That figure includes all T6 and F28 specimens with the exception of L510-No8A, which has been omitted due to the uncertainty associated with unintentional end-bay thinning. Intact specimens have been assigned thinning values of zero.

The experimental curve in Figure 48 has been fit to the T6 data in order to provide a baseline against which to compare the F28 results. The curve fitting parameters for that trend-line are listed in Table 19. The F28 results fall above the trend-line for the T6 data, and, for the most part, outside the scatter of the T6 results. That suggests that the collapse strengths

Table 19: Curve fitting parameters for various data sets[a].

Figure	**Variables** x	y	**Data set**	**Slope** m	**Intercept** b	r^2
Figure 47	σ_y	P_c	Intact	0.0252	1.31	0.975
Figure 48	δ_c	P_c*	AA-6082-T6	-1.08	1.18	0.961
Figure 49	δ_c	λ_c	AA-6082-T6	-0.842	0.984	0.636
Figure 49	δ_c	λ_c	AA-6082-F28	-0.857	1.01	0.832
Figure 49	δ_c	λ_c	All Data	-0.856	0.991	0.726

[a] Listing the slope, m, and intercept, b, for the equation: y=mx+b. Curve fitting parameters are based on linear least squares regression of the indicated data set. The curve fit improves as r^2, the coefficient of determination, approaches unity.

of F28 cylinders were greater than would be expected if only the yield strength of the material mattered (since the collapse pressures have been normalized with respect to, effectively, the yield stress). The average ratios of ultimate tensile strength to yield stress for the T6 and F28 cylinders were 1.11 and 1.35, respectively, so that it can be concluded that the strain hardening effect resulted in the relatively high normalized collapse pressures for F28 specimens.

In Figure 49, a corrosion "knock-down factor", λ_c, for each corroded specimen is plotted against the shell thinning. λ_c was calculated as the quotient of the normalized collapse pressures for a corroded specimen and its intact counterpart(s) from the same batch of aluminium. For example, λ_c for L300-No7 was determined by dividing its P_c* by the average value of P_c* for L300-No5 and L300-No6. The slopes of the T6 and F28 trend-lines in Figure 49 are approximately equal (see Table 19); however, the T6 curve is approximately 2.5% more conservative than the F28 curve. That suggests that the effect of corrosion damage on hull strength diminishes with increasing levels of strain hardening. That may seem intuitive, but it would be expected that strain hardening effects would be factored out of comparisons between intact and corroded specimens fabricated from the same material. The benefit of increased strain hardening arises from the relatively early onset of yield in corroded specimens compared to intact cylinders. Corroded specimens make greater use of their plastic reserves, so that strain hardening has a greater opportunity to play a role in delaying collapse.

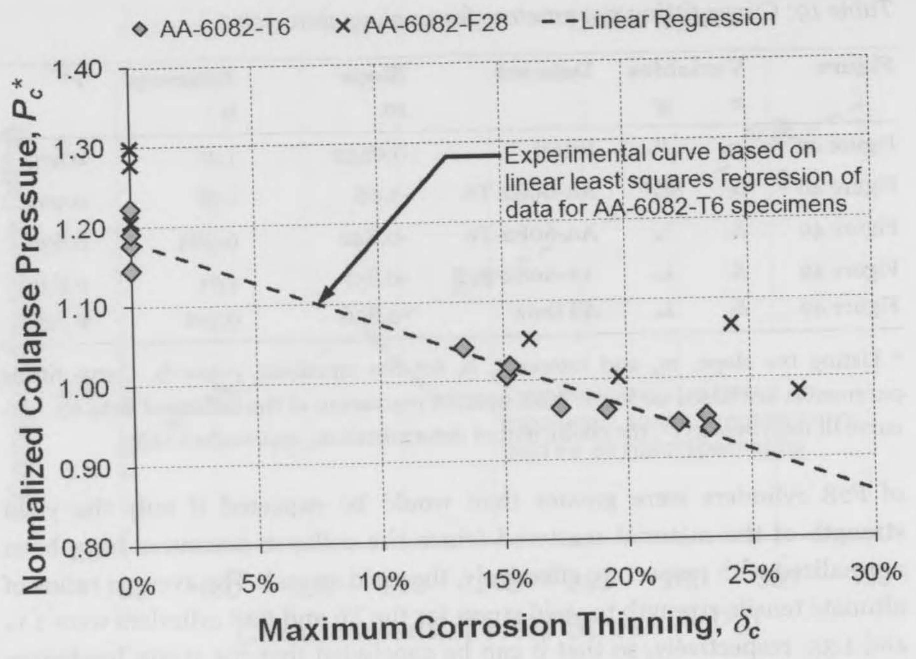

Figure 48: Normalized collapse pressure, P_c*, *taken as the collapse pressure divided by the boiler pressure, versus the magnitude of corrosion thinning,* δ_c*, for cylinders machined from high- and low-grade aluminium.*

The preceding discussion indicates that the severity of the reduction in overall collapse pressure for a given level of thinning is related to the shape of the stress-strain curve. If the corrosion knock-down curves in Figure 49 are to be used directly or indirectly for damage assessments of real pressure hulls, it must be demonstrated that the aluminium materials are sufficiently similar to real hull materials. The overall collapse mechanisms in the test specimens considered here have been shown to be qualitatively identical to collapse mechanisms in real pressure hulls made of steel; that is, elasto-plastic buckling brought on by yielding of the ring-stiffeners and/or the shell plating near the stiffeners. The collapse of real hulls is affected by residual stresses that arise from fabrication procedures such as cold rolling [14] and welding [73]. Corrosion damage could interact with those stresses, or even change their magnitude and distribution due to the loss of material, but it is expected that residual stress effects would be largely factored out in a comparison of collapse pressures for intact and corroded hulls. Furthermore, the goal of the current study is to examine the interaction of corrosion

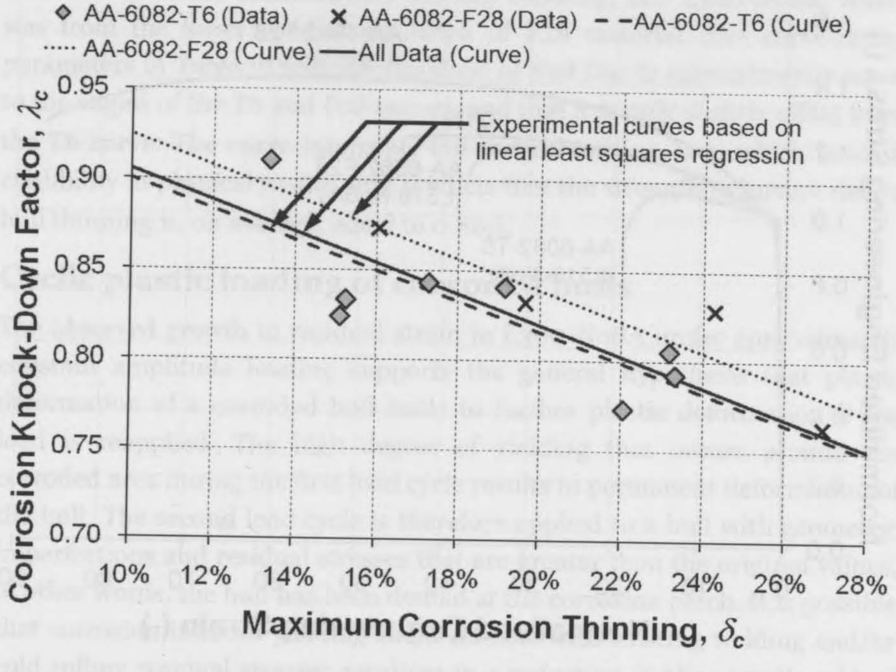

Figure 49: Corrosion knock-down factor, λ_c, as a function of the magnitude of shell thinning, δ_c, for cylinders machined from high- and low-grade aluminium. The experimental curve labelled "All Data" is based on results for all T6 and F28 cylinders in Table 16 and Table 17, respectively, except for L510-No8A and L300-No8A.

damage and material strength in isolation from other factors that complicate collapse.

The critical factor to consider in the current context is whether the behaviour of the aluminium material itself is similar to the response of real hull materials. The experiments show that the post-yield shape of the stress-strain curve has a significant impact on collapse behaviour, especially for corroded specimens. The aluminium and steel stress-strain curves in Figure 42 are re-plotted in Figure 50, whereby the stress and strain data for each material curve have been normalized by dividing by the material's yield stress and yield strain, respectively. The normalization procedure provides a common frame of reference, whereby the ultimate tensile strengths, relative to the corresponding yield stresses, can be compared, as well as the post-yielding shape of the curves in general. For example, Figure 50 shows that the tensile strength of the T6 material is somewhat less than 10% greater

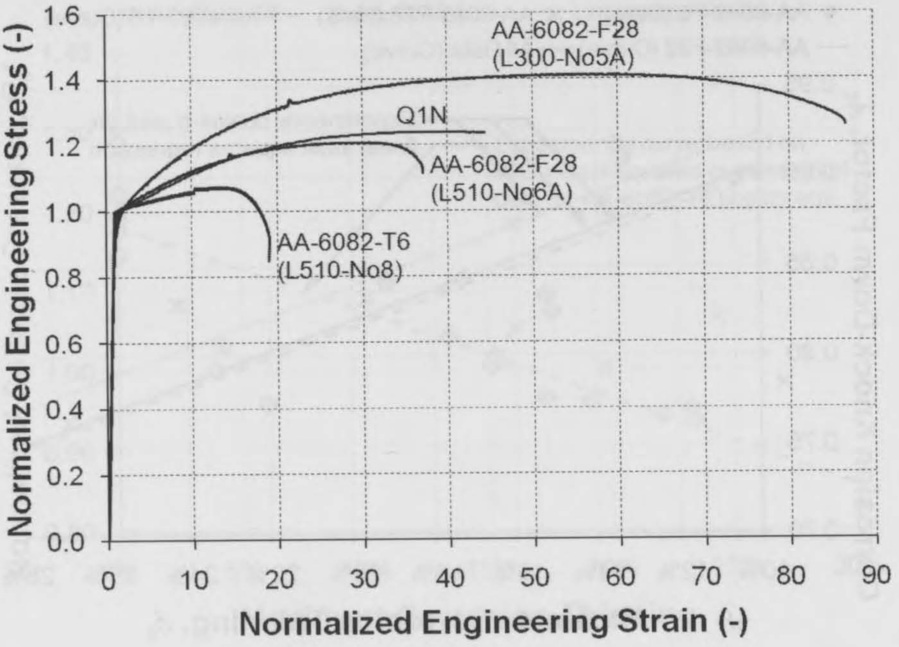

Figure 50: Normalized engineering stress-strain curves for aluminium alloys and a high-strength naval quality steel. The measured engineering stress and strain data have been normalized by dividing by the yield stress and yield strain of the material, respectively.

than its yield stress, while the F28 materials have tensile strengths that are between 20% and 40% greater than their yield stresses.

Figure 50 highlights the differences in strain hardening and ductility between the T6 and F28 materials. It also suggests that the aluminium grade most like the typical high-strength steel used in submarines is the high yield stress batch of F28 aluminium. Furthermore, the T6 material has significantly less strain hardening and ductility than the high-strength steel, while the opposite trend is observed for the low yield stress F28 material. The test results for T6 specimens have been shown to produce a more conservative corrosion knock-down curve than the F28 specimens. Furthermore, the material curves for the lower yield stress F28 material are non-conservative with respect to high strength steel. Therefore, it is concluded that the low yield stress F28 results should not be used for producing empirical corrosion assessment curves.

The experimental curve in Figure 49 labelled "All Data" is based on results for all T6 and F28 cylinders except for L510-No8A, which was omitted due to the unintentional end-bay thinning, and L300-No8A, which was from the lower yield stress batch of F28 material. The curve-fitting parameters in Table 19 indicate the slope of that line is approximately equal to the slopes of the T6 and F28 curves, and that it is only slightly offset from the T6 curve. The curve intercepts the vertical axis at $\lambda_c \approx 1$, which lends it credibility in physical reality, and predicts that the strength reduction due to hull thinning is, on average, equal to $0.86\delta_c$.

Cyclic plastic loading of corroded hulls

The observed growth in residual strain in L300-No8A under approximately constant amplitude loading supports the general hypothesis that plastic deformation of a corroded hull leads to further plastic deformation if the load is reapplied. The high degree of yielding that occurs around the corroded area during the first load cycle results in permanent deformation of the hull. The second load cycle is therefore applied to a hull with geometric imperfections and residual stresses that are greater than the original values; in other words, the hull has been dented at the corrosion patch. It is possible that corrosion induced yielding could interact with existing welding and/or cold rolling residual stresses resulting in a reduction in the overall residual stresses, but for the sake of this discussion it will be assumed that shakedown has not occurred. Yielding and large displacements, especially those associated with out-of-circularity, drive the nonlinear response of pressure hulls, so that the hull is subjected to somewhat greater stresses and displacements during the second load cycle, leading to an increase in the size of the dent. The critical questions to answer are: (1) whether the size of the dent will eventually stabilize with repeated loading or if the loading-yielding cycle represents a feedback loop producing ever larger dents, and (2) if it is possible that the dent can grow large enough to precipitate elasto-plastic collapse at the cyclic load level rather than the original collapse pressure.

The first question is addressed by Figure 46, where it is shown that the growth in residual strain tended towards zero with increasing number of cycles. It should be made clear that the residual strains themselves were not diminished, just the rate at which they grow with additional load cycles. Thus, the reduction in incremental residual strain with increasing number of load cycles does not suggest that shakedown has occurred. The incremental residual strains became smaller and smaller because the initial permanent deformation was too small to initiate the kind of self-sustaining growth in plastic strains hypothesized earlier. Furthermore, the strain hardening exhibited by the F28 material may have played a role in reducing the incremental plastic strain.

The second question is addressed by the collapse test that was performed on L300-No8A after the cyclic loading, which gave a normalized collapse pressure (1.07) that was slightly greater than the normalized collapse pressure of its nominally identical counterpart L300-No7A (P_c*=0.98). That shows that the cylinder strength was not reduced by the cyclic loading, likely because the residual displacements were not great enough to significantly affect the nonlinear response during the collapse test.

In the test case, the growth of the dent petered out quickly so that the overall collapse strength of the cylinder was not appreciably affected by the cyclic loading. In general, the size of the initial dent, and thus the potential for cyclic failure, would be related to the material properties and geometry of the hull, as well as the severity of the corrosion damage. Displacements in the shell plating of hulls failing by interframe collapse are relatively greater than with overall collapse, so the former collapse mode may be more sensitive to cyclic collapse. However, test specimens in Chapter 4 [22] that failed by interframe collapse were found to have a large plastic reserve due to the heavy ring-stiffeners, which could compensate for some of the cyclic damage. The dent size is expected to be more sensitive to corrosion depth than area, since deformations in larger patches have been shown to be concentrated in a limited area near the patch edges.

Conclusions and future work

Test results have shown that the collapse of intact and corroded submarine pressure hulls is sensitive to the material strength. That sensitivity is related to not only the yield stress, but also the plastic reserve of the material; higher levels of strain hardening and ductility were found to increase the overall collapse strength of the test specimens, especially those with general corrosion damage. The effect of a given level of corrosion thinning was found to be less severe for cylinders with relatively greater levels of strain hardening. Numerical models for corrosion damage assessments of real hulls should include an accurate description of the full stress-strain behaviour; in the absence of detailed material data, a simplified material model that assumes an elastic-perfectly-plastic response will be conservative.

The overall collapse mechanisms of the aluminium test specimens were shown to be the same as those found in real pressure hulls made of high-strength steel. Furthermore, the material responses of the various aluminium alloys used in the experimental work, despite having lower material strengths than high-strength steel, were shown to be qualitatively similar to the latter material. The out-of-circularity of the test specimens has also been shown to be similar to imperfections found in as-built submarines. Finally, it is thought that the residual stresses found in real hulls, which are not present in the test specimens, will not influence the relative performance of intact and corroded hulls. Those considerations justify the application of the experimental results to real pressure hulls. In other words, the improved performance of the F28 cylinders is indicative of the performance of high-strength steel hulls, since those materials have approximately the same degree of strain hardening. Furthermore, the empirical corrosion knock-down curve presented in Figure 49 is expected to be similar to curves for real hulls with similar levels of OOC and failing by overall collapse.

The cyclic plastic loading of a corroded test specimen represents a severe case, as the depth of artificial corrosion (24%) was much greater than allowable levels of thinning for real pressure hulls, and the applied cyclic load was very large with respect to the collapse load (within approximately 6%). Thus, since cyclic loading past the yield pressure has not resulted in uninhibited growth of plastic strains or premature collapse of the test specimen, it is not likely that those effects are a concern for real pressure hulls failing by overall collapse. All things considered, it is concluded that the experimental results justify the use of corrosion knock-down curves based on the collapse pressure rather than the yield pressure of the hull, even though the latter pressure is more greatly affected by corrosion damage.

The current work was aimed at studying the static collapse strength of corroded pressure hulls, but the effect of that type of damage should be considered with respect to other design loads and failure modes. For example, the high stresses, and possibly even premature yielding, associated with corrosion damage could significantly reduce the fatigue life of the submarine. Furthermore, loss of hull thickness would inhibit the capability of the hull to withstand dynamic weapons loads. Those aspects of hull corrosion must also be considered when making submarine maintenance decisions.

The work presented in this chapter has been followed by experiments aimed at studying the interaction of corrosion damage and OOC imperfections [31], as well as more complex types of corrosion damage, such as pitting [32]. The results of those experiments, which are described in Chapter 6, will be used to supplement the empirical curves presented here, and to further validate the numerical methodology used in Chapter 7 [25].

also been shown to be similar to that of real pressure hulls. Therefore, it is thought that the residual stresses (Section 2.[illegible]), which were not present in the test specimens, will not influence the relative performance of intact and corroded hulls. These considerations justify the application of the experimental results to real pressure hulls. In other words, the (improved) performance of the test specimens is indicative of the performance of high-strength steel hulls, since those materials have approximately the same degree of strain hardening. Furthermore, the empirical corrosion knock-down curve presented in Figure 4.[illegible] is expected to be similar to one for real hulls with similar levels of OOC and failing by overall collapse.

The cyclic plastic loading of a corroded test specimen represents a severe case: the depth of artificial corrosion ([illegible]%) was much greater than allowable levels in a real pressure hull, and the applied cyclic load was very large with respect to the collapse load (at approximately [illegible]%). Thus, since cyclic loading past the yield pressure has not resulted in considerable cyclic plasticity or premature collapse of the test specimen, it is not likely that those effects are a concern for real pressure hulls failing by overall collapse. All things considered, it is concluded that the experimental results justify the use of corrosion knock-down curves based on the collapse pressure rather than the yield pressure of the hull, even though the latter pressure is more greatly affected by corrosion damage.

The current work was aimed at studying the static collapse strength of corroded pressure hulls, but the effect of that type of damage should be considered with respect to other design loads and failure modes. For example, the high stresses, and possibly even precursive yielding, associated with corrosion damage could significantly reduce the fatigue life of the submarine. Furthermore, loss of hull thickness would inhibit the capability of the hull to withstand dynamic weapons loads. Those aspects of hull corrosion must also be considered when making a thorough risk assessment.

The work presented in this chapter has been followed by an experimental study aimed at studying the interaction of corrosion damage and OOC [illegible], as well as more complex types of corrosion damage, such as pitting [illegible]. The results of those experiments, which are described in Chapter 6, will be used in supplement to the experiments presented here, to further validate the numerical methods described in Chapter 7.

Chapter 6

Experimental study of the interaction of corrosion damage with pressure hull out-of-circularity

The effect of corrosion damage on overall collapse strength of submarine pressure hulls was studied experimentally. Ring-stiffened cylinders were machined from aluminium tubing and loaded to collapse under external pressure. In selected specimens, some of the outer shell material was machined away in large single patches, representing general corrosion. Other specimens had many smaller patches, representing corrosion pitting from the outside of the hull, followed by grinding. Large-amplitude out-of-circularity (OOC) was introduced by mechanically deforming selected cylinders. Clusters of artificial corrosion pits were found to have approximately the same effect on collapse pressure as equal-depth general corrosion covering the same region of plating. General corrosion was found to be most severe when it was "in-phase" with OOC, since, during pressure loading, high compressive stresses resulting from corrosion were compounded by compressive bending stresses associated with OOC, and furthermore, the corrosion tended to increase the geometric imperfection itself. On the other hand, out-of-phase corrosion reduced the effect of OOC, while at the same time the thinning-associated compressive stresses were counteracted by local tensile bending stresses associated with OOC, so that strength reductions were correspondingly smaller. Overall collapse pressures for corroded specimens were reduced by, on average, 0.85% for each 1% of shell thinning. That result is based on a linear approximation of the nonlinear relationship between thinning and collapse pressure. The linear trend-line, which was used to account for the experimental scatter, is based on specimens with 13 to 27% shell thinning, and with a variety of corrosion areas and OOC amplitudes. This chapter is based on the manuscript of a journal paper co-authored with Malcolm Smith, Fred van Keulen, and Theo Bosman. The paper has been submitted to the *International Journal of Maritime Engineering* [24].

Introduction

The critical structural component of a naval submarine, with respect to life-cycle management (LCM), is its pressure hull. This is due to its importance for safe diving operations, the sensitivity of its structural capacity to defects and damage, and the high cost of repairing or replacing damaged sections. The life-cycle of a pressure hull can be limited by the accumulation of fatigue and corrosion defects, and by structural damage resulting from weapons loads or collision. The current work is only concerned with corrosion aspects of LCM.

Hull corrosion can be prevented by using preservatives or impressed current cathodic protection. Nonetheless, it still occurs in practice [12], in either of two forms. With general corrosion, the hull surface is affected approximately uniformly over a large area, and the damage is typically shallow compared to the hull thickness. General corrosion at 10% of the hull thickness would be considered severe. On the other hand, corrosion pitting can penetrate deep into the hull, sometimes through as much as half the thickness, but may be just a fraction of the hull thickness in diameter.

Both types of damage are treated by grinding away the corroded material, leaving a hull with locally reduced thickness. In the case of pitting damage, the affected area may be much larger after grinding due to the size of the grinding wheel and attempts to blend or fair the damaged region with the intact hull. Furthermore, while the highly localized nature of corrosion pitting may mean that a single ground-out pit has a negligible impact on hull strength, closely spaced pits may interact so that the net effect of a cluster of pits is potentially significant.

Hull thickness can be restored using weld overlay, but that procedure is expensive and its secondary effects, including residual stresses, distortions, and changes in material properties, are still being studied [139]. So, in certain circumstances it is preferable to operate the submarine with a hull thickness that has been reduced by corrosion damage.

Conventional design codes allow for only a small amount of corrosion thinning, if any at all [5], mainly because there is a considerable weight penalty to be paid when a general hull wastage allowance is factored into the design. The structural capacity of an in-service hull with an out-of-tolerance case of corrosion is typically assessed by assuming that the entire hull has been uniformly thinned. That conservatism compensates for the uncertainty associated with the effect of a given type and extent of corrosion damage. As a result, cases of ground-out but otherwise unrepaired corrosion damage often require a reduction to the submarine's deep diving depth in order to maintain acceptable safety margins [5,12,13].

The conservatism associated with general corrosion tolerances can be addressed by studying the effect of more realistic, discrete patches of corrosion damage on hull strength. That type of damage was studied experimentally in Chapter 4 [22], whereby general corrosion was applied to aluminium ring-stiffened cylinders by machining away some of the shell material in rectangular patches of uniform depth. The axisymmetric geometries of those specimens is shown in Figure 27, p. 82. The experiments studied the effect of corrosion on overall collapse, characterized by elasto-plastic buckling of the combined shell plating and ring-stiffeners, as well as interframe collapse resulting from inelastic buckling of the shell between stiffeners.

In [22], corrosion damage was found to reduce cylinder collapse strength through early yielding brought on by high stresses in the corroded area. The increased stresses were attributed to higher membrane and bending stresses due to the thinner shell and to additional bending stresses that arose due to the shell eccentricity associated with one-sided thinning. Comparisons between undamaged and corroded test specimens showed a strong correlation between corrosion thinning and the percentage reduction to overall collapse pressure, which was found to be approximately equal to the percentage shell thinning. General corrosion was found to have a much smaller effect on interframe collapse, compared with overall collapse. Heavy ring-stiffeners in specimens failing by interframe collapse provided some reserve strength after the corroded shell had failed locally. That reserve strength was not available with the lighter ring-stiffeners in overall collapse specimens.

In Chapter 5 [23], the experimental study from Chapter 4 [22] was extended to examine the effects of material properties on the strength of damaged hulls by comparing cylinders fabricated from two grades of aluminium. As expected, cylinder collapse strength was found to be sensitive to yield strength. More interestingly, the effect of corrosion damage was found to be related to the degree of strain hardening. Test specimens made from aluminium with a relatively greater strain hardening modulus were less affected by a given corrosion case.

The interaction of general corrosion damage with out-of-circularity (OOC) in hulls failing by overall collapse was studied numerically in [42]. In that paper, Kendrick's finite difference method for determining overall collapse pressures [8] was modified to allow discrete patches of corrosion wastage to be modeled. It was found that the effects of corrosion thinning are not limited to the reduction of the overall bending stiffness of the hull. The load-path eccentricity that results from one-sided thinning effectively increases or decreases the OOC magnitude depending on whether the corrosion is collocated with an inward ("in-phase") or an outward ("out-of-phase") OOC lobe, respectively. That leads to a nonlinear interaction between corrosion and OOC, whereby the effect of a given level of in-phase shell thinning was found to diminish with increasing OOC magnitudes. That was attributed to the relatively smaller OOC-like effect of corrosion when initial imperfections were of greater magnitude.

The analyses in [42] also indicate that overall collapse pressures are markedly more affected by in-phase corrosion compared with out-of-phase corrosion. With in-phase cases, the imperfections introduced by corrosion and OOC are additive, and, under pressure loading, the high compressive stresses that arise at the corrosion due to the thinning itself are compounded by compressive bending stresses associated with OOC. Out-of-phase corrosion reduces the OOC imperfection, and the positioning of the corrosion where the bending stresses associated with OOC are in tension tends to counteract the high compressive stresses that arise in the thinned shell. In some cases, out-of-phase corrosion was found to improve the OOC shape, and the stress field under loading, to an extent that the collapse pressure was greater than a similar model with no corrosion.

The test specimens in [22,23] were produced by machining, so that, other than the corrosion defects, they were nearly shape-perfect. That allowed the effect of corrosion damage to be studied in isolation from other shape defects, but the interaction between OOC and corrosion that was predicted in [42] could not be verified. Furthermore, the earlier experiments were focused on large areas of general corrosion damage, and corrosion pitting was not studied.

The current chapter extends the experiments in Chapter 4 [22] and Chapter 5 [23] to cylinders with more realistic levels of OOC and types of corrosion. Large-amplitude OOC was introduced by mechanically deforming as-machined cylinders with and without general corrosion damage. The current tests also examine the effect of clusters of corrosion pits that have been treated by grinding only. The current work is concerned with overall elasto-plastic collapse, since OOC has the greatest impact on that failure mode, and since interframe collapse pressures in [22] were shown to be less sensitive to corrosion damage. The nominal geometry of the current test specimens is given by Configuration 1 in Figure 27 (p. 82). Photographs of some typical specimens are shown Figure 51 and Figure 52.

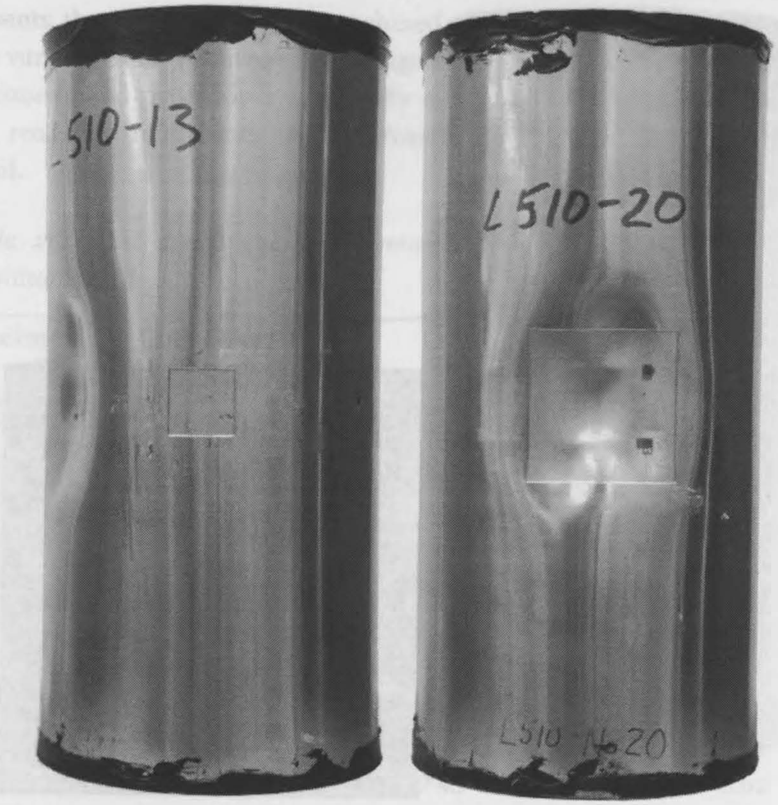

Figure 51: Photographs of cylinders with large-amplitude out-of-circularity and general corrosion damage, shown after testing. L510-No13, with out-of-phase Patch B corrosion, is shown on the left. The right-hand cylinder is L510-No20, with in-phase Patch C corrosion.

The overall goal of the work presented in Chapter 4 [22] and Chapter 5 [23] and the current research is to overcome the uncertainty associated with hull corrosion and its effect on collapse strength in order to reduce the conservatism of current corrosion tolerances. The number of corrosion cases that can be studied experimentally is limited, but numerical models can be used to study any arbitrary pattern of thinning. With that in mind, effort has also been directed at identifying and validating numerical procedures for predicting the effects of corrosion damage, so that numerical models can be used to make assessments of damaged submarine hulls. That work is presented in Chapter 7 [25], where the experimental results from Chapter 4 [22] are used to validate nonlinear finite element (FE) collapse predictions. The current chapter deals only with experiments.

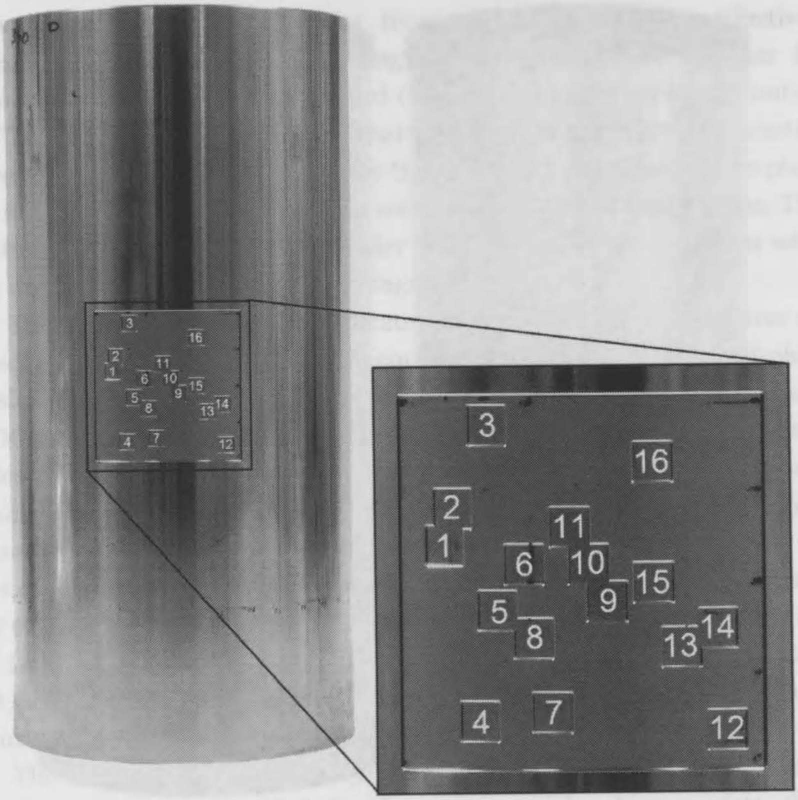

Figure 52: Photograph of L510-N024, with Pitting B damage (general corrosion and pitting), before testing. The pit numbering scheme is shown at the inset.

This chapter begins with a description of the test specimens and experimental procedures, followed by the results of the current testing. The interaction of corrosion and OOC is then discussed, along with a comparison between general corrosion and pitting damage. That is followed by a summary of the entire testing program including results from Chapter 4 [22] and Chapter 5 [23], and then some general conclusions.

Test specimens and procedures

The sixteen cylinder specimens considered here are listed in Table 20 and Table 21. Table 20 shows the type of corrosion damage, and the measured shell thinning (δ_c), OOC magnitude, circumferential yield stress (σ_y), and collapse pressure (P_c) for specimens with large-amplitude OOC. Specimens without corrosion damage are referred to as "intact" cylinders. Table 21 presents the same data for as-machined specimens with corrosion pitting. The various cases of corrosion damage are described in Table 22. The test specimens and procedures are briefly described in the following sections. The reader is referred to the experimental reports in [31,32] for greater detail.

Table 20: Test specimens with general corrosion patches and large-amplitude OOC.

Specimen	Corrosion[a] Patch	δ_c	OOC[b]	σ_y (MPa)	P_c (MPa)
L510-No13	B*	21.2%	0.71%	328	7.55
L510-No14	B	23.9%	0.67%	334	6.93
L510-No17	Intact	N/A	0.39%	306	7.84
L510-No18	Intact	N/A	0.41%	305	7.71
L510-No19	C	17.4%	0.77%	329	6.67
L510-No20	C	18.6%	0.67%	325	6.93
L510-No25	Intact	N/A	0.75%	305	7.13
L510-No26	Intact	N/A	0.94%	310	7.05
L510-No33	Intact	N/A	0.92%	301	7.03
L510-No34	Intact	N/A	0.45%	301	8.02
L510-No35	B	19.0%	0.79%	332	6.58
L510-No36	B*	24.6%	0.97%	331	7.22

[a] An asterisk (*) denotes out-of-phase corrosion; otherwise, the corrosion damage is in-phase with OOC. δ_c is the maximum measured corrosion thinning. The various types of corrosion damage are described in Table 22.

[b] OOC is defined as the maximum measured radial eccentricity at the outside of the cylinder, e_{max}, divided by the nominal mid-plane shell radius, a.

Table 21: Test specimens with corrosion pitting damage and as-machined OOC.

Specimen	Pitting Type	δ_c	OOC	σ_y (MPa)	P_c (MPa)
L510-No21	A	14.4%	0.06%	337	8.65
L510-No22	A	16.2%	0.07%	331	8.98
L510-No23	B	24.1%	0.07%	326	7.63
L510-No24	B	26.5%	0.05%	340	7.62

Table 22: Nominal corrosion damage cases.

Corrosion	Description[a]
Patch B	Single 42×42×0.6 mm (20%) general corrosion patch outside shell
Patch C	Single 100×100×0.4 mm (13.3%) general corrosion patch outside shell
Pitting A	Sixteen 10×10×0.4 mm (13.3%) randomly oriented corrosion pits
Pitting B	Sixteen 10×10×0.4 mm (13.3%) randomly oriented corrosion pits superimposed on a 100×100×0.3 mm (10%) general corrosion patch (23.3% total thinning at pits)

[a] Corrosion patch sizes are specified by the circumferential times the axial extents times the depth. The nominal percentage thinning is shown in parentheses. General corrosion patches and groups of corrosion pits were centred at the mid-length of the cylinders.

Axisymmetric geometry

A CNC lathe was used to machine the axisymmetric geometry of each test specimen from an extruded aluminium alloy tube. The nominal dimensions of the cylinders, which are given by Configuration 1 in Figure 27 (p. 82), are the same as some of the specimens from earlier experiments in [22,23]. The shell plating was proportioned to be relatively stiff compared to the T-section ring-stiffeners in order to promote failure by overall collapse. The thick end rings and tapered end bays were designed to prevent undesired end bay failures, and to provide enough material to bolt the steel end caps that were used during pressure testing.

Out-of-circularity

The design collapse pressure of a pressure hull is determined by assuming that the maximum radial eccentricity, e_{max}, is equal to 0.005 times the hull radius, a, or in the common terminology, 0.5% [5]. Overall collapse pressures are calculated for a range of circumferential wave numbers, n, and the most pessimistic prediction is used for design. It is assumed that the most pessimistic axial mode is a half sine wave over the length of the hull, or m=1. Construction tolerances generally require the OOC of the as-built hull to be less than one-third of the design value, or approximately 0.17% [5]. That allows for growth of OOC during the life of the hull.

In the current study, the OOC of intact cylinders was measured using a coordinate measurement machine (CMM), while laser displacement gauges mounted on a turntable were used to measure the shape of corroded specimens. Measurements were taken at 36 circumferential positions at each stiffener and mid-bay location along the cylinder length. The accuracies of the CMM and the laser displacement gauges are 0.02 and 0.001 mm, respectively. Those accuracies are equivalent to 0.016% and 0.0008% OOC, respectively.

OOC measurements of as-machined cylinders indicated that they were nearly shape-perfect, with maximum values no greater than 0.07% (see Table 21). The machining process resulted in OOC characterized by two complete waves about the circumference of each cylinder (n=2), distributed approximately uniformly over the specimen length (m=0). In contrast, the critical overall collapse mode of the cylinders is m=1, n=3 [22].

With one exception, the cylinders in Table 20 were mechanically deformed to achieve OOC in the critical m=1, n=3 mode, at magnitudes up to twice the design value of 0.5%. The exception is L510-N034, which was designed to study the effect of the axial distribution of OOC. Its intended OOC shape was characterized by an n=3 circumferential mode, and a complete sine wave along the length (m=2).

OOC was applied by deforming the cylinders using a triangular steel frame with bolted joints at its corners. Load was applied at 120° increments by tightening the bolts so that the mid-points of the triangle legs pressed against the cylinder. The desired OOC shape was built up by moving the load frame along the length of the cylinder and incrementally increasing the permanent deformations.

Graphical representations of the final pre-testing OOC for typical cylinders are shown in Figure 53. The images were generated by performing two-dimensional Fourier decompositions of the measured OOC, and applying those nonlinear maps to FE models of the specimens. The Fourier analyses confirmed that the OOC was dominated by the m=1, n=3 mode for all cylinders with that target shape. With most of those cylinders, the OOC amplitude associated with the target mode was an order of magnitude greater than the next largest contributor. In some cases, significant OOC contributions were unintentionally introduced for some higher order modes, especially m=1, n=6 and, to a lesser extent, m=n=3. Those modes are seen as interframe dimples superimposed on the more dominant m=1, n=3 mode in the models in Figure 53. It was also confirmed that the as-measured shape of L510-N034 was dominated by the m=2, n=3 mode.

Corrosion damage

Artificial corrosion damage was applied to selected cylinders by machining away some of the outer shell material in square patches of approximately uniform depth. General corrosion damage was applied to some of the

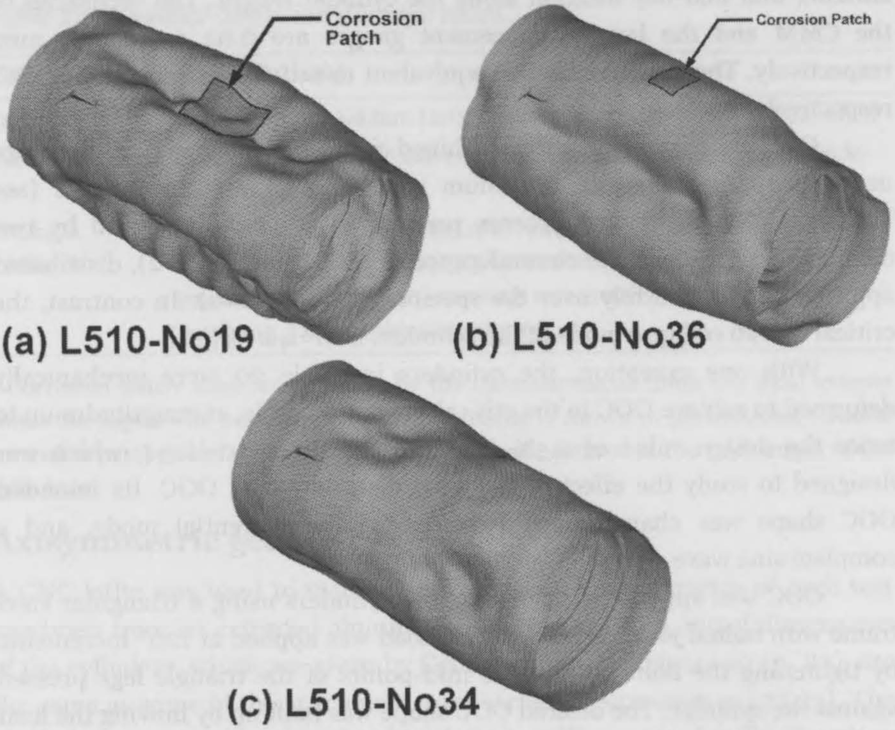

Figure 53: Representation of as-measured OOC, amplified by a factor of 50 for clarity, for the following specimens: (a) L510-No19, with m=1, n=3 *OOC, and in-phase corrosion; (b) L510-No36, with* m=1, n=3 *OOC, and out-of-phase corrosion; and (c) L510-No34, with* m=2, n=3 *OOC, and no corrosion.*

cylinders listed in Table 20. The damage was either in-phase with OOC, whereby the corrosion patch was approximately collocated with an inward lobe of the overall OOC shape, as shown in Figure 53(a), or out-of-phase, whereby the corrosion was applied at an outward OOC lobe, as in Figure 53(b). Patch B was applied in-phase with OOC in two cases, and out-of-phase in two cases. Patch C was always applied in-phase with OOC.

Specimens in Table 21 had sixteen 10×10 mm areas of uniform corrosion, representing corrosion pits after grinding. Each pit was 20% of the frame spacing in breadth. The pits were randomly oriented within a 100×100 mm bounding area, as shown in Figure 54. Cylinders with Pitting A corrosion had only the pitting damage. With Pitting B corrosion, the pits were superimposed on general corrosion covering the bounding area. Pit positions were the same on all specimens with Pitting A and B damage.

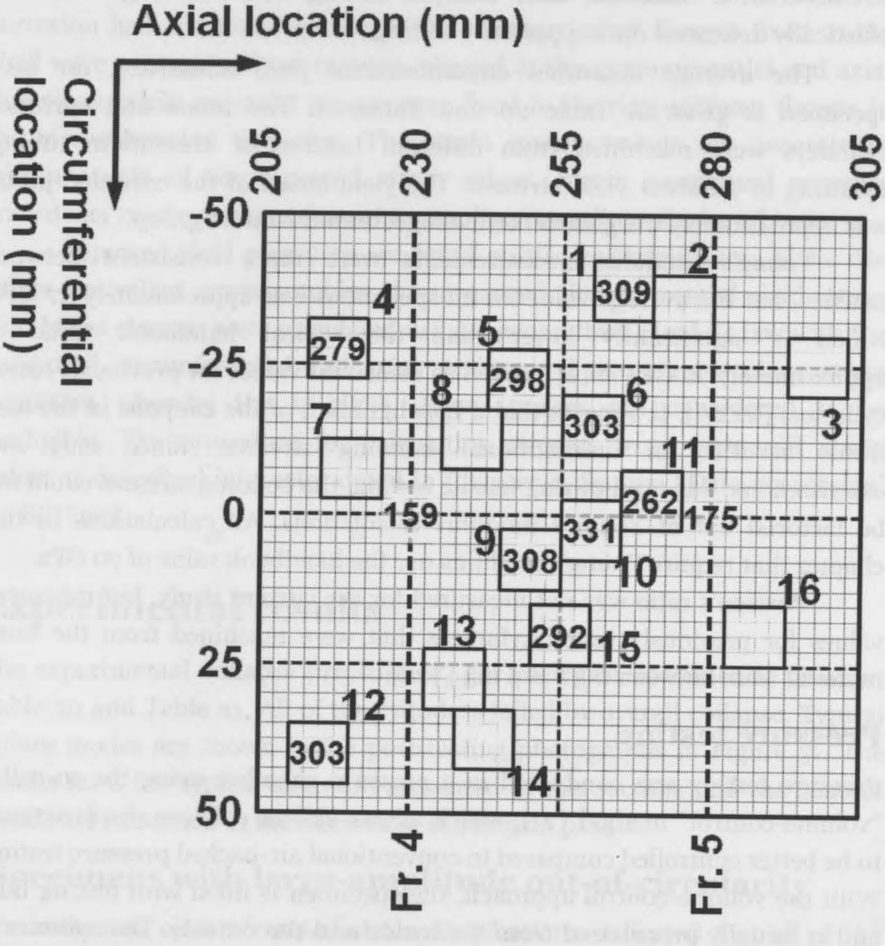
Axial location (mm)
Circumferential location (mm)
205
230
255
280
305
-50
-25
0
25
50
1
309
2
3
4
279
5
298
6
303
7
8
9
308
10
11
262
12
303
13
14
15
16
292
331
159
175
Fr. 4
Fr. 5

Figure 54: Corrosion pit locations and numbering. The thick outer line represents the bounding box and general corrosion patch for Pitting A and B, respectively (see Table 22). Numbers inside pits and at ring-stiffeners are strain-derived von Mises stresses (MPa) outside the shell of L510-No22 at a pressure of 7.13 MPa (see "Specimens with corrosion pitting", p. 146).

Material properties

The specimens were machined from extruded tubes of 6082-T6 aluminium alloy. Previous batches of that aluminium showed an anisotropy, with a yield stress in the circumferential direction that was approximately 10% less than the axial yield stress [22,23]. For the current study, tensile coupons were machined from the thick end rings of each cylinder, in the critical circumferential direction, after collapse testing. The end rings were not plastically deformed during pressure testing.

The average measured circumferential yield stress, σ_y, for each specimen is given in Table 20 and Table 21. The intact and corroded cylinders were machined from different batches of aluminium tubing, resulting in different yield stresses. The yield stress of the corroded group was approximately 9% greater, on average, than the intact group.

Young's modulus measurements were more consistent between batches, but the average value for all specimens was approximately 57 GPa, which is significantly lower than the typical handbook value of approximately 70 GPa [142], as well as measured values for previously tested cylinders [22,23]. It appears that a misalignment of the coupons in the load frame resulted in unintentional bending stresses. Since only one extensometer was used during tensile testing, the bending stresses could not be factored out of Young's modulus calculations. All calculations in this chapter that require Young's modulus use the handbook value of 70 GPa.

Poisson's ratio was not measured for the current study, but measured values for previously tested cylinders that were machined from the same material were between 0.32 and 0.34 [22].

Pressure testing

Pressure testing was conducted in a pressure chamber using the so-called "volume-control" method [21], which allows violent collapse displacements to be better controlled compared to conventional air-backed pressure testing. With the volume-control approach, the specimen is filled with testing fluid and is initially pressurized from the inside and the outside. The cylinder is then loaded by regulating the internal pressure using a series of hoses and valves in order to achieve the desired net external pressure.

In the current tests, a non-conductive mineral oil was used as the pressure testing fluid. Mild steel end caps, 38 mm thick, were attached to both ends of each specimen with bolts and sealed with a polymeric compound. Each specimen was loaded until it collapsed, with the collapse pressure defined as the maximum recorded net pressure. The accuracy of the reported collapse pressures, ±0.09 MPa, is based on the pressure transducers used during testing.

Each cylinder was instrumented with 64 to 72 strain gauges. A typical intact cylinder was instrumented with strain gauges at twelve equally spaced increments about the circumference at the flanges of the two central stiffeners and outside the shell in the central bay. Cylinders with large-amplitude OOC had a row of gauges along the cylinder length to measure the axial distribution of strain outside the shell. Cylinders with artificial corrosion had additional gauges in the damaged area. Gauges fixed to the shell were 2-gauge 90° tee rosettes, aligned in the circumferential and axial directions, while uni-axial gauges were fixed to the ring-stiffener flanges in the circumferential direction. The strain measurements are accurate to within ±0.5% of the reported strain values. Strain gauge and pressure transducer readings were taken at a sampling rate of 100 Hz for all tests.

Reported yield pressures are based on the first occurrence of the von Mises equivalent stress reaching the measured circumferential yield stress. Von Mises stresses were calculated using a generalized Hooke's law with the measured circumferential and axial strains, and assuming a plane stress condition whereby the in-plane shear stresses are considered to be negligible. The procedure for calculating stresses from measured strain values is described in greater detail in Chapter 4, Section "Data processing" (p. 88) [22].

Experimental results

The experimental collapse pressure, P_c, for each test specimen is given in Table 20 and Table 21. All of the cylinders failed by overall collapse. Typical failure modes are shown in the post-testing photographs in Figure 51. The results for a few typical cases are presented in this section, and the general trends are examined in the discussion starting on p. 148.

Specimens with large-amplitude out-of-circularity

The measured circumferential strain distributions indicated that all of the test specimens with large-amplitude OOC (Table 20) failed in the expected overall n=3 collapse mode. Figure 55 shows that the shell bending strains for an intact specimen follow the expected distribution with respect to the initial imperfections. The post-testing photographs in Figure 51 show post-collapse deformations concentrated at one of the three inward OOC lobes, even for cylinders with out-of-phase corrosion. Cylinders with in-phase corrosion failed at the location of shell thinning.

Figure 56 shows measured pressure-strain curves for intact and corroded specimens with similar OOC magnitudes. Shell strains were much greater at the inward OOC lobe compared to the outward lobe for the intact cylinder and the specimen with in-phase corrosion. As expected, large shell strains at the in-phase corrosion patch caused that cylinder to yield earlier than the intact specimen. There was less difference between the strain magnitudes at inward and outward OOC lobes for the cylinder with out-of-

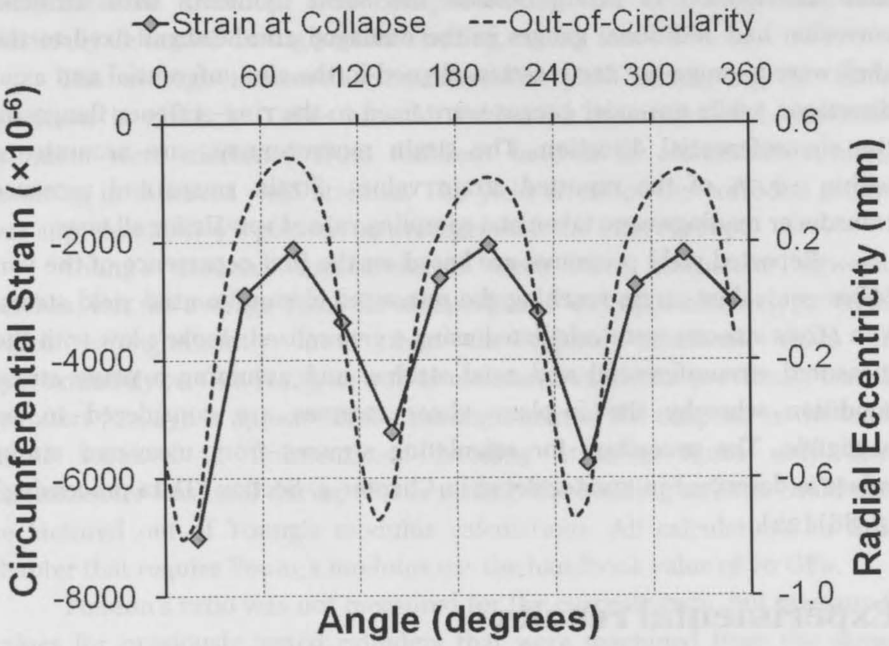

Figure 55: Circumferential distribution of shell strain outside the central bay of L510-N025 at the collapse pressure; the corresponding initial OOC is shown on the secondary vertical axis.

phase corrosion, because the compressive strains resulting from the corrosion damage were offset by tensile bending strains at the outward OOC lobe. That cylinder failed at an inward OOC lobe away from the shell thinning.

The pressure-strain curves in Figure 56, and the collapse pressures listed in Table 20, suggest that the cylinder with in-phase corrosion was only slightly weaker than the intact specimen. Furthermore, the cylinder with out-of-phase corrosion appears to be even stronger than the intact specimen. Those results are misleading, since the material used for the corroded specimens had a yield strength between 7.5 and 9.5% greater than that used for the intact cylinder. The effect of yield stress is dealt with in the discussion.

Specimens with corrosion pitting

The measured strain data indicate that the four cylinders with corrosion pitting failed by overall collapse in the n=3 mode. Post-collapse displacements were concentrated around the corrosion damage, as shown by the post-testing photograph of L510-N022 in Figure 57. Figure 57 also shows

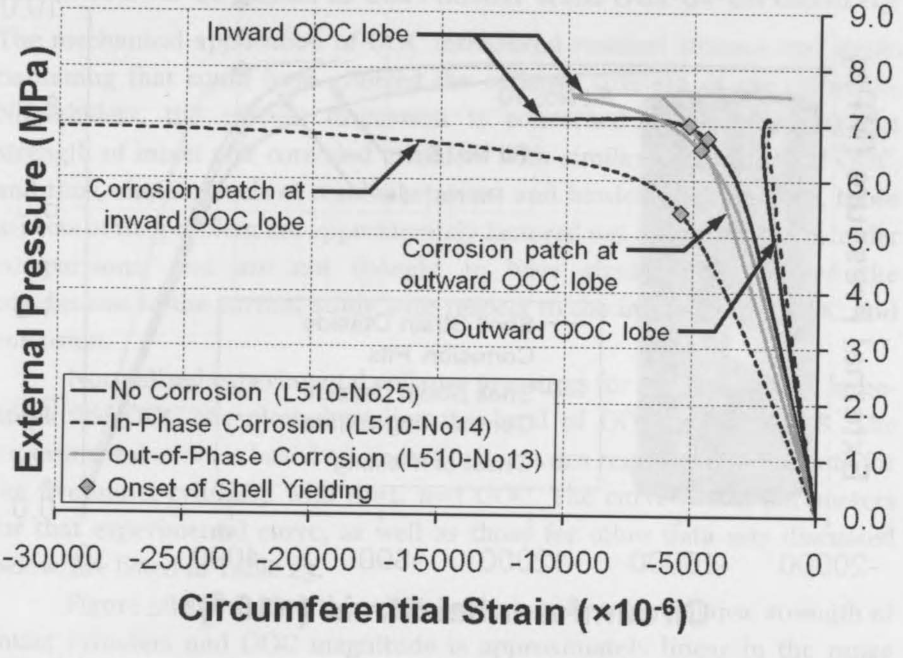

Figure 56: Pressure-strain curves for cylinders with large-amplitude OOC; showing circumferential strains measured on the outside of the shell in the central bay.

selected pressure-strain curves for that specimen. Strain-derived von Mises stresses at instrumented pits are shown in Figure 54. Those stresses are associated with the applied pressure at which the shell first yielded at corrosion pit no. 10.

Figure 54 and Figure 57 show that stresses and strains in the corrosion pits were significantly greater than for the intact shell. Yielding occurred first at the pits, but overall collapse was precipitated by yielding of the intact shell between pits and near the central ring-stiffeners. The shell stresses and strains were greatest at pit no. 10, which was near the centre of the damaged area, and immediately adjacent to two pits. Furthermore, pit no. 10 was situated near the centre of the frame-bay. The corrosion pit with the lowest stress and strain, pit no. 4, was located at the periphery of the damaged area, and was relatively isolated and closer to a ring-stiffener.

The responses of the other specimens with corrosion pitting were similar to L510-No22. The measured strains were greater in the cylinders with Pitting B damage due to the deeper pits and the presence of the general corrosion patch.

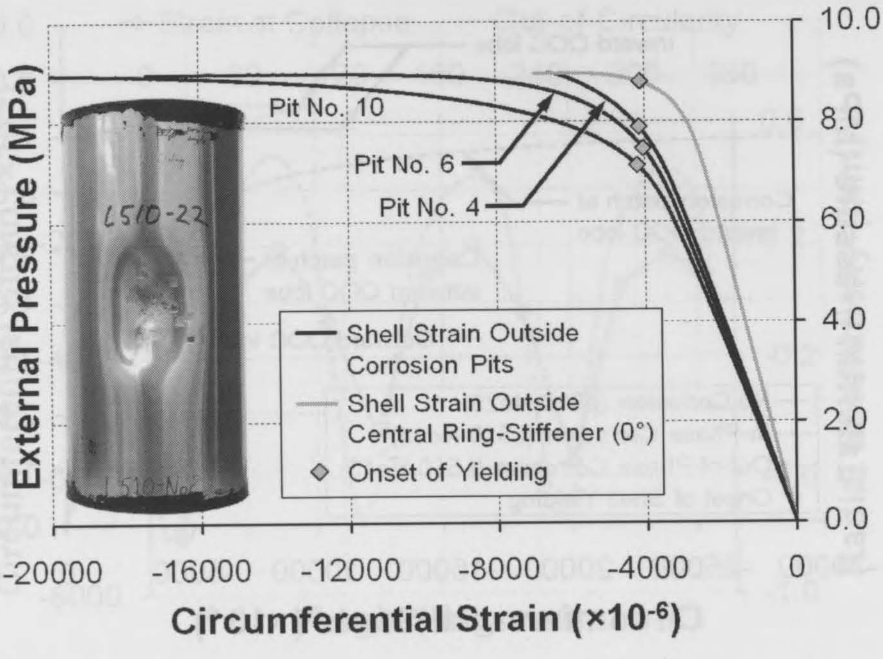

Figure 57: Selected pressure-strain curves for L510-No22 (Pitting A damage).

Discussion

Specimen-to-specimen comparisons in Chapter 5 [23] were made using collapse pressures that were normalized to account for differences in the circumferential yield strengths, as determined from coupon tests. The current chapter adopts the same procedure, whereby the normalized collapse pressure for each specimen is taken as $P_c{}^*=P_c/P_b$, where P_c is the experimental collapse pressure and P_b is the boiler pressure. The boiler formula, $P_b=\sigma_y h/a$, is a simple expression for predicting the onset of yielding in unstiffened pressure vessels. This normalization procedure neglects axial stresses, as well as the material anisotropy discussed earlier; however, FE models show that cylinder collapse pressures are governed by the circumferential material properties [25] (see Chapter 7, p. 155).

The current chapter also adopts the procedure that was used in Chapter 5 [23] to quantify the effect of corrosion damage on collapse strength. In that chapter, a corrosion “knock-down factor”, λ_c, was derived for each corroded specimen. λ_c is taken as the quotient of the normalized collapse pressures for a corroded cylinder and its intact counterpart(s).

Interaction of general corrosion with out-of-circularity

The mechanical application of OOC introduced residual stresses and strain hardening that could have affected the collapse strength of the cylinders. Nonetheless, the current discussion is concerned with comparing the strength of intact and corroded cylinders with similar magnitudes of OOC, and thus, similar levels of residual stresses and hardening. Therefore, those aspects of the problem are approximately factored out of cylinder-to-cylinder comparisons, and are not thought to have significantly affected the conclusions of the current study with respect to the interaction of OOC and corrosion.

Normalized experimental collapse pressures for specimens with large-amplitude OOC are plotted against the level of OOC in Figure 58. The experimental curve is based on linear least squares regression of the data for the five intact cylinders with *m*=1, *n*=3 OOC. The curve-fitting parameters for that experimental curve, as well as those for other data sets discussed below, are listed in Table 23.

Figure 58 shows that the relationship between the collapse strength of intact cylinders and OOC magnitude is approximately linear in the range

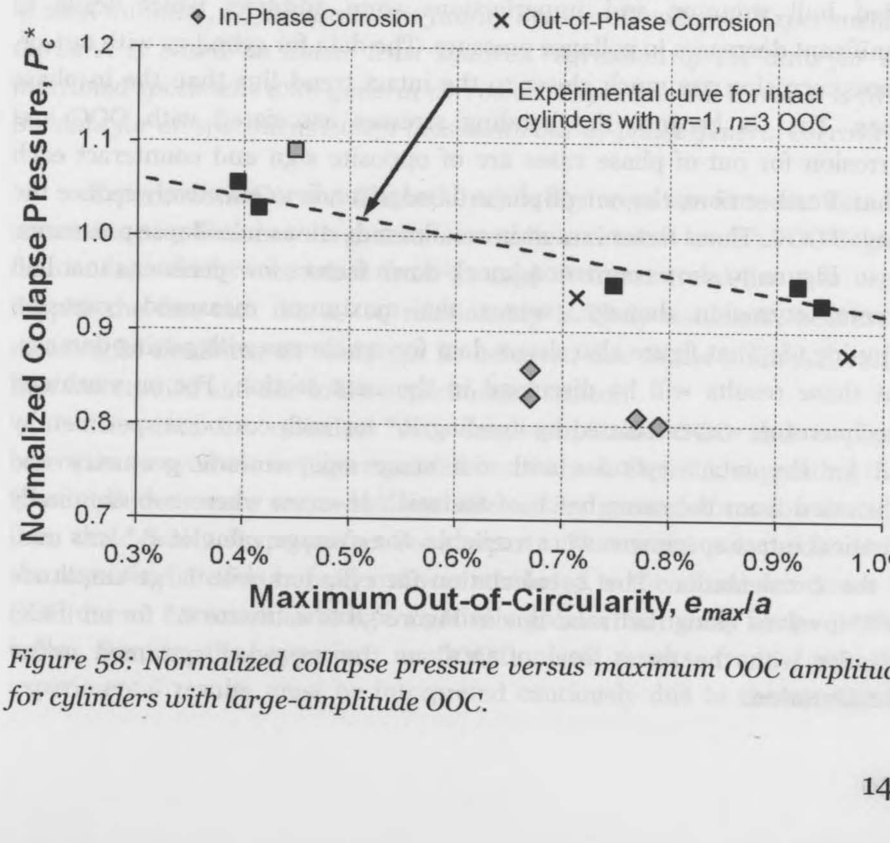

Figure 58: Normalized collapse pressure versus maximum OOC amplitude for cylinders with large-amplitude OOC.

Table 23: Curve-fitting parameters for various data sets[a].

Figure	Variables		Data set	Slope	Intercept	r^2
	x	y		**m**	**b**	
Figure 58	e_{max}/a	P_c^*	Intact m=1, n=3	-20.4	1.12	0.93
Figure 59	δ_c	λ_c	Exp. Curve A	-0.86	0.99	0.72
Figure 59	δ_c	λ_c	Exp. Curve B	-0.85	1.00	0.63

[a] Listing the slope, m, and intercept, b, for the equation: $y=mx+b$. Curve fitting parameters are based on linear least squares regression of the indicated data set. The curve fit improves as r^2, the coefficient of determination, approaches unity.

considered. The strength of the intact cylinder with m=2, n=3 OOC falls above the m=1, n=3 trend-line. That can be explained in general terms by the fact that the OOC of the cylinder did not correspond with the critical m=1 axial buckling mode. More precisely, its greater strength is due to relatively smaller bending stresses that arise under pressure loading for the shorter axial wavelength associated with m=2 OOC.

All of the cylinders with general corrosion damage fall below the intact trend-line in Figure 58. As expected, there is a strong interaction between corrosion damage and OOC. With in-phase corrosion, the effects of one-sided hull thinning and imperfections were additive, which leads to significant decreases in collapse pressure. The data for cylinders with out-of-phase corrosion are much closer to the intact trend-line than the in-phase cases. That is because the bending stresses associated with OOC and corrosion for out-of-phase cases are of opposite sign and counteract each other. Furthermore, the out-of-phase damage tends to effectively reduce the level of OOC. Those factors result in smaller reductions in collapse pressures.

Figure 59 shows corrosion knock-down factors for specimens that had general corrosion damage, versus the maximum measured corrosion thinning, δ_c. That figure also shows data for specimens with pitting damage, but those results will be discussed in the next section. For as-machined specimens, λ_c was calculated by dividing P_c^* for each corroded specimen by P_c^* for the intact cylinder with the same axisymmetric geometry and fabricated from the same batch of material. In cases where two nominally identical intact specimens were available, the average value of P_c^* was used in the λ_c calculation. The λ_c calculation for cylinders with large-amplitude OOC involved using the trend-line in Figure 58 to estimate P_c^* for an intact cylinder with the same level of OOC as the corroded specimen under consideration.

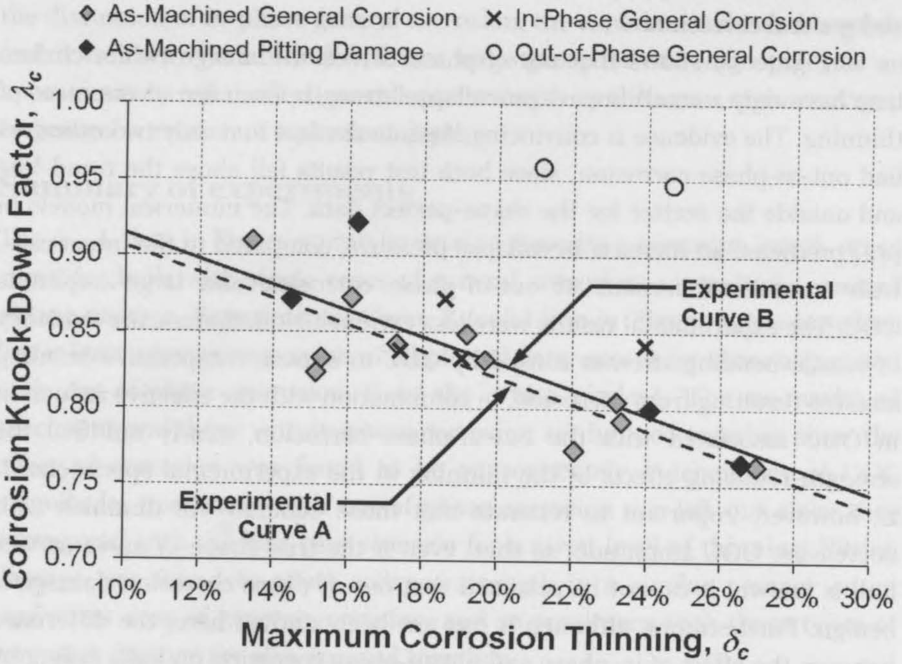

Figure 59: Corrosion knock-down factor, λ_c, as a function of the magnitude of shell thinning, δ_c, for specimens failing by overall collapse. Experimental Curve A is based on linear least squares regression of the data for as-machined specimens with general corrosion. Experimental Curve B is fit to the data for all specimens except those with out-of-phase general corrosion.

Experimental Curve A (dashed line) in Figure 59 was fit to test data for as-machined cylinders with general corrosion and small levels of OOC (gray diamonds), which were taken from [22,23]. A linear trend-line was used, despite the fact that the $\delta_c - \lambda_c$ relationship is likely nonlinear, because a meaningful nonlinear fit could not be achieved due to the limited δ_c-range that was studied and due to the experimental scatter.

The data for cylinders with large-amplitude OOC and in-phase corrosion (× symbols in Figure 59) fall on or above Curve A, suggesting that those cylinders were somewhat less affected by general corrosion damage than their nearly shape-perfect counterparts. That trend was predicted by the numerical models in [42] and was attributed to the effective increase in OOC due to corrosion, which is relatively greater for nearly shape-perfect hulls. Despite the apparent confirmation of results from [42], the experimental results must be interpreted cautiously due to the overlap in scatter between the groups of cylinders with small- and large-amplitude OOC and general corrosion.

Figure 59 shows that out-of-phase corrosion damage (white circles) may have only a small impact on collapse strength, even for severe cases of thinning. The evidence is convincing, despite the fact that only two cylinders had out-of-phase corrosion, since both test results fall above the trend-line and outside the scatter for the shape-perfect data. The numerical models in [42] predicted an increase in collapse pressure, compared to the intact case, with some combinations of out-of-phase corrosion and large-amplitude OOC. The experimental results were less extreme. Nonetheless, the tendency of tensile bending stresses caused by OOC to oppose compressive bending stresses resulting from corrosion, in combination with the effective reduction in OOC associated with the out-of-phase corrosion, nearly nullified the strength-reducing effects of the thinning in the experimental specimens. It is, however, important to reiterate that those benefits will diminish with decreasing OOC amplitude, so that, even if the true shape of an in-service hull is known, it cannot be assumed that out-of-phase corrosion damage is benign. Furthermore, although it has not been studied here, the difference between the effect of in-phase and out-of-phase corrosion on hulls failing by interframe collapse may be negligible.

Comparison of corrosion pitting and general corrosion

The stress at a given corrosion pit would be expected to be affected by the location of the pit relative to other pits, as well as to the ring-stiffeners, and by the depth of corrosion. With complex pitting arrangements, such as the pattern used in these experiments, it is difficult to separate the relative influence of each of those factors. Nonetheless, the experimental data in Figure 54 show that corrosion pitting leads to the greatest stresses when the pits are in close proximity, when they are deep, and when they are located near the centre of a frame bay.

In Figure 59, the $\delta_c - \lambda_c$ data for specimens with pitting damage (black diamonds) are plotted with general corrosion damage data. The bounding area for the corrosion pitting was the same size as Patch C general corrosion. Since several cylinders with Patch C corrosion are included in Experimental Curve A, that curve represents an approximate baseline for general corrosion damage against which the effects of pitting damage can be compared.

All of the specimens with pitting fell on or above Curve A in Figure 59, although only one of the pitting results was outside the scatter of the general corrosion group. That suggests that an area of closely spaced corrosion pits is slightly less severe than an area of general corrosion with the same level of thinning and covering the area that bounds all of the pits. However, as with the discussion of in-phase general corrosion, the experimental trend is weak, and it can only be concluded that a large group of corrosion pits has an approximately equal effect on collapse strength as the same region covered by general corrosion of equivalent depth.

Summary of experiments

The $\delta_c - \lambda_c$ data in Figure 59 can be used to generate a corrosion knock-down curve for hulls with single cases of general corrosion, or multiple cases of pitting damage. Experimental Curve B (solid line in Figure 59) is based on linear least squares regression of all plotted data, except for those associated with out-of-phase corrosion (i.e., the white circles). The as-machined specimens and those with in-phase corrosion are lumped together since the effect of corrosion was found to be approximately independent of OOC magnitude. Specimens with out-of-phase corrosion are left out since they correspond with the best case scenario for a given level of thinning. Pitting damage was found to affect collapse strength in a similar manner as an equivalent area of general corrosion, and so specimens with those types of corrosion damage are also grouped together.

Curve B is slightly offset above Curve A, which is based on as-machined specimens with general corrosion. That difference is consistent with previous observations regarding the greater severity of general corrosion for otherwise shape-perfect cylinders, compared to corrosion pitting and general corrosion of cylinders with large-amplitude OOC. Based on Experimental Curve B, the percent reduction in overall collapse pressure is, on average, equal to 0.85 times the percent corrosion thinning. Curve B intercepts the vertical axis at $\lambda_c=1$, giving it some qualitative validation.

The experiments in [23] showed that the structural and material response of the aluminium test specimens are similar to real pressure hulls made of high-strength steel, and so the trends observed in the current experiments are applicable to real hulls. Nonetheless, the experimental curves in Figure 59 are not intended to be directly used for assessments of in-service corrosion damage since they are based on a limited range of parameters. Furthermore, those curves apply to overall collapse only, while the experiments in [22] showed that the effect of corrosion is related to the hull configuration and failure mode. The recommended approach to assessing in-service damage is to use numerical models that can account for the unique structural configuration, corrosion damage and OOC of the hull. Guidelines for capturing those features in a numerical model, and producing the nonlinear collapse prediction, are presented in Chapter 7 [25].

Conclusions

Corrosion thinning was found to impact overall collapse pressures through higher stresses in the damaged shell, and by changing the effective magnitude of out-of-circularity. In-phase corrosion patches that were preferentially aligned with the dominant out-of-circularity mode were found to be more detrimental to collapse strength than corrosion thinning that was out-of-phase with OOC. The scatter in experimental results was too great to confirm or reject the hypothesis that sensitivity to corrosion thinning diminishes with increasing OOC.

The current work highlights the importance of the interaction of corrosion damage with the actual shape of the pressure hull. When assessing corrosion damage to real submarines, it is necessary to model the true shape of the hull, and the correct location of the thinning with respect to that shape.

Corrosion pitting was found to be most severe when the pits are clustered close together near the centre of a frame bay. A group of pits is approximately equivalent to an area of general corrosion, although pitting damage is less severe, to an extent that depends on the spacing between pits. It is difficult to precisely quantify the difference based on the experiments, due to the level of scatter, but numerical models could be used to extend the experimental study. Nonetheless, structural assessments of real pressure hulls with pitting damage, whereby a group of pits is treated as an equivalent area of general corrosion, are not excessively conservative.

Chapter 7

Development of a numerical modeling methodology for pressure hulls

Nonlinear finite element (FE) collapse pressure predictions are compared to experimental results for submarine pressure hull test specimens with and without artificial corrosion and tested to collapse under external hydrostatic pressure. The accuracy of FE models, and their sensitivity to modeling and solution procedures, are investigated by comparing FE simulations of the experiments using two different model generators and three solvers. The standard FE methodology includes the use of quadrilateral shell elements, nonlinear mapping of measured geometric imperfections, and quasi-static incremental analyses including nonlinear material and geometry. The FE models are found to be accurate to approximately 11%, with 95% confidence, regardless of the model generator and solver that is used. Collapse pressure predictions for identical FE models obtained using each of the three solvers agree within 2.8%, indicating that the choice of FE solver does not significantly affect the predicted collapse pressure. The FE predictions are found to be more accurate for corroded than for undamaged models, and neglecting the shell eccentricity that arises due to one-sided shell thinning is found to significantly decrease the resulting accuracy of the FE model. This chapter was originally published in *Marine Structures* with co-authors Lei Jiang and André Glas [25].

Introduction

Pressure hulls are the main load-bearing structures in naval submarines, commercial and research submersibles, and autonomous underwater vehicles. A typical pressure hull consists of cylindrical and/or conical metal shells with discrete ring-stiffeners distributed along the length and dome bulkheads at the ends. Hydrostatic loading associated with diving results in a primarily compressive stress field in the hull and a failure mode governed by inelastic buckling instability.

The outside of a pressure hull will corrode if the preservative fails or, for submarines, if the acoustic tiles de-bond. If the hull wastage is minor, the corroded material is simply removed by grinding, followed by reapplication of the preservative. More severe cases of hull thinning require restoration of the hull thickness by weld overlay or replacement of the hull plating. Since those repair methods are expensive, a pressure hull may operate with reduced plating thickness in the unrepaired region. The challenge for engineers is to determine the consequences of not restoring the hull thickness on structural strength and stability, in order to establish allowable corrosion thresholds on a particular platform.

Numerical investigations [13,42] aimed at determining the effect of thinning on pressure hull collapse revealed that the subject was poorly understood. Experiments from which the fundamental aspects of the problem could be derived were lacking, so that there was no assurance that the numerical models had considered the critical parameters. This knowledge gap prompted a series of collapse tests on small-scale pressure hull specimens with artificial corrosion damage. The testing program, described in detail in Chapter 4 [22], was aimed at gaining a qualitative understanding of the effects of local thinning on pressure hull strength and stability, and furthermore, at building a database of experimental results for validating numerical models. Twenty small-scale ring-stiffened cylinders, some of which are shown in Figure 60, were tested to collapse under external hydrostatic pressure. The test specimens were machined from extruded aluminium tubing and varied with respect to the basic axisymmetric geometry and the configuration of artificial corrosion.

The main goal of the current chapter is to estimate the accuracy of nonlinear finite element (FE) analysis for predicting the collapse of submarine pressure hulls with and without corrosion damage, so that engineers may use that numerical tool with confidence when making decisions regarding the operational capability of damaged hulls. With that goal in mind, the current chapter presents numerical simulation results for the collapse tests reported in [22], as well as comparisons with the experimental results. A basic FE modeling procedure was identified from previous experience and the literature review in Chapter 2 [20], and was then refined by comparing some of the experimental data with numerical results. Those FE methods were applied to the simulation of the remaining collapse tests and an estimate of their accuracy was derived based on the statistical method suggested in Chapter 2 [20], which is also described

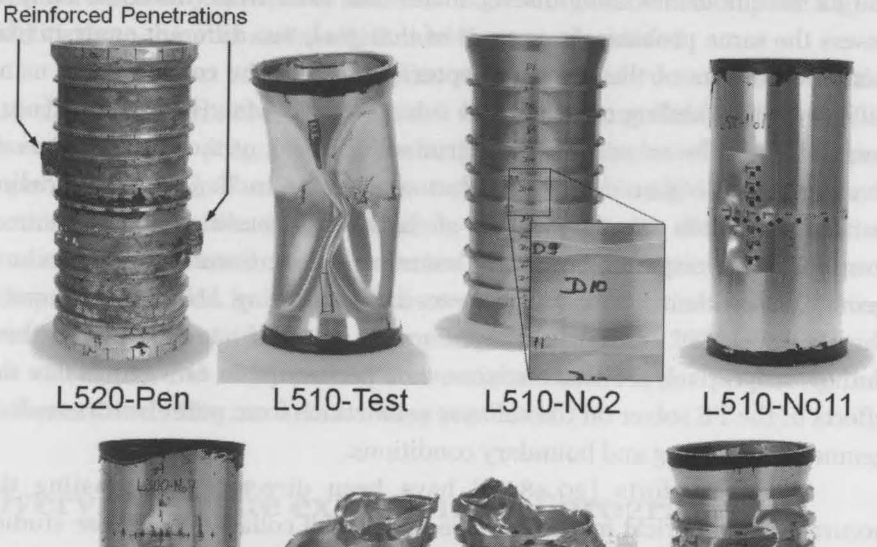

Figure 60: Typical test specimens, before and after collapse testing. Clockwise from top-left: L520-Pen, before testing, with rectangular-section stiffeners and two reinforced penetrations; L510-Test, the unstiffened cylinder after volume-control testing; L510-No2, before testing, showing dog-bone stiffener corrosion at inset; L510-No11, an internally-stiffened cylinder with a large patch of corrosion thinning, after volume-control testing; L300-No1, a short intact cylinder failing by interframe collapse, after volume-control testing; L300-No4, a short cylinder with heavy stiffeners and a small patch of shell corrosion, showing the specimen after conventional pressure testing; L300-No7, a short cylinder with light, internal stiffeners and a small patch of corrosion thinning that failed by overall collapse, shown after volume-control testing.

briefly in the current chapter. The accuracy estimates presented in the current chapter will also be used in support of a program to introduce FE analysis into the pressure hull design procedure by way of a partial safety factor. The proposed procedure for accomplishing that task was presented in Chapter 2 [20].

A secondary goal of the current chapter is to assess the consistency of FE analysis for determining collapse pressures by looking at the sensitivity of the FE results to modeling discrepancies that arise when different analysts assess the same problem. In support of that goal, two different analysts (the first two authors of the current chapter) simulated the collapse tests using different FE modeling methods and solvers (ANSYS [143] and VAST [144], respectively). The accuracy was determined for both of those approaches so that the sensitivities to both analyst and program dependent modeling parameters, such as the choice of boundary conditions and element formulations, respectively, were examined concurrently. Furthermore, geometrically identical FE models were analyzed using ANSYS, VAST and a third solver, MSC MARC [145] (performed by the first, second and third author, respectively). Those analyses were performed in order to isolate the effects of the FE solver on the collapse predictions from other factors such as geometric modeling and boundary conditions.

Previous efforts [20,48,49] have been directed at estimating the accuracy of numerical models for predicting hull collapse, but those studies were focused on intact hulls. In [48], Graham used nonlinear FE analysis to predict the collapse pressures of thirteen pressure hull test specimens. Graham's FE models were based on shell theory and included measured hull dimensions, geometric imperfections, and material properties, where available, as well as explicit simulation of the cold rolling processes in order to capture the resulting residual stress fields and their effect on collapse. Graham's numerical predictions were within ±6% of the experimental collapse pressures. In [49], Graham extended his numerical methodology to a fourteenth test specimen, over-predicting the experimental collapse pressure by 8.5%.

A survey of the state of the art of numerical modeling for pressure hull collapse was presented in [20], including an estimate of the accuracy of the numerical methods that was derived by comparing numerical and experimental collapse pressures that are available in the literature. The experimental-numerical comparisons in [20] include test specimens consisting of cylindrical metal shells under external pressure, with and without ring-stiffeners. A variety of numerical models are represented, including three-dimensional and axisymmetric shell formulations, and finite element and finite difference discretizations. The numerical models considered in [20] include Graham's analyses in [48,49], and some of the FE models described in the current chapter that were presented in an earlier conference paper [51]. When all of the 117 experimental-numerical comparisons were considered, the accuracy of the numerical models was found to be within approximately 16% with 95% confidence. The accuracy was increased to 9%, with the same level of confidence, when only the higher fidelity three-dimensional shell FE models were considered.

The current chapter begins with a brief description of the experimental specimens, methods and results. A more detailed overview of the experimental program is given in [22], which is based on the testing reports in [27-29]. The finite element modeling and analysis methods used in this study are then described, along with the results of some modeling studies. Experimental and numerical results for typical models are compared, followed by a general discussion of the experimental-numerical comparisons. Estimates of the accuracies of the different FE methodologies are calculated and compared to conventional methods for predicting hull collapse. Concluding remarks are then presented.

Overview of the experimental program

Test specimens

Figure 60 shows some typical test specimens considered in this chapter, before or after collapse testing. All of the specimens considered herein are described in Table 24, including the axisymmetric geometry, artificial corrosion damage, material and experimental collapse pressures.

Twenty of the twenty-two specimens considered in this chapter had T-section ring-stiffeners on either the outside or the inside of the shell. Axisymmetric geometries for those models are shown in Figure 27, p. 82. The cylinder dimensions were constrained by the size of the original aluminium tubing, as well as by limitations associated with the minimum shell thickness and maximum length that was achievable with the CNC lathe used to machine the specimens. The cylinders were fabricated in two standard lengths of 300 mm and 510 mm, resulting in the L300 and L510 model series. The shell thickness, stiffener spacing and stiffener scantlings were proportioned to ensure that the desired failure mode was achieved. Cylinders with heavy ring-stiffeners (Configuration 4 in Figure 27) were designed to fail by elasto-plastic collapse of the shell between ring-stiffeners (interframe collapse); those with light ring-stiffeners (Configurations 1-3) were designed to fail by elasto-plastic collapse of the combined ring-stiffeners and shell (overall collapse). Real pressure hulls are proportioned so that the overall and interframe collapse pressures are similar. With the test specimens, the emphasis was placed on ensuring that the desired failure mode was realized during testing, so the test specimens are not simply scaled-down versions of real pressure hull configurations.

Table 24: Summary of test specimens and results.

Specimen	**Axisymmetric configuration**[a]	**Corrosion damage**[b] **Thinning / Area**	**Material batch no.**	**Collapse pressure (MPa)**
L300-No1	Configuration 4	Intact	Batch 1	7.11
L300-No2	Configuration 4	Intact	Batch 1	7.87
L300-No3	Configuration 4	25% / 34×34 mm	Batch 1	6.77
L300-No4	Configuration 4	25%/ 34×34 mm	Batch 1	6.94
L300-No5	Configuration 2	Intact	Batch 3	8.99
L300-No6	Configuration 2	Intact	Batch 3	9.14
L300-No7	Configuration 2	25% / 37×37 mm	Batch 3	7.30
L300-No8	Configuration 2	25% / 37×37 mm	Batch 3	7.11
L510-No1	Configuration 3	Intact	Batch 1	9.05
L510-No2	Configuration 3	Stiffener corrosion	Batch 1	8.59
L510-No3	Configuration 3	Stiffener corrosion	Batch 1	9.25
L510-No4	Configuration 3	Intact	Batch 3	9.79
L510-No5	Configuration 1	Intact	Batch 2	9.08
L510-No6	Configuration 1	Intact	Batch 3	8.48
L510-No7	Configuration 1	20% / 42×42 mm	Batch 2	7.07
L510-No8	Configuration 1	20% / 42×42 mm	Batch 3	7.21
L510-No9	Configuration 1	13.3% /100×100 mm	Batch 2	7.68
L510-No10	Configuration 1	13.3% / 100×100 mm	Batch 3	7.81
L510-No11	Configuration 1	13.3% / 200×100 mm	Batch 2	7.58
L510-No12	Configuration 1	13.3% / 200×100 mm	Batch 3	7.29
L510-Test	Unstiffened	Intact	Batch 2	7.96
L520-Pen	Rect. frames	Reinforced pen.	N/A	9.00

[a] All cylinders had T-section ring-stiffeners, except specimen L510-Test, which was unstiffened and L510-Pen, which had small, rectangular-section stiffeners. The dimensions of the specimens with T-section ring-stiffeners are given in Figure 27.

[b] Specifying the nominal magnitude of shell thinning, unless otherwise noted. Shell corrosion is applied in a rectangular area, orthogonal to ring-stiffeners and centred at mid-length of the cylinder. "Intact" models do not have artificial corrosion. Corrosion area is specified by the axial times the circumferential extents.

Artificial corrosion damage was introduced in selected cylinders by machining away a specific amount of material from either the shell or ring-stiffener. Corrosion damage to the shell consisted of uniformly thinned rectangular patches on the outside of the shell, and was meant to simulate general corrosion rather than pitting. Corrosion was also applied to some cylinders in the form of local flange width reductions at the two central stiffeners, resulting in a "dog-bone" corrosion pattern (see specimen L510-N02 in Figure 60).

In addition to the twenty T-section ring-stiffened cylinders described in [22], two other specimens were tested: a ring-stiffened cylinder with reinforced penetrations, named L520-Pen [27], and an unstiffened cylinder, named L510-Test [28]. Those specimens, which were also machined from aluminium tubing, are shown in Figure 60. They are included in the current work in order to demonstrate the capability of the numerical models to account for other failure modes (elastic buckling in the case of L510-Test) and complex geometry (reinforced penetrations in the case of L520-Pen). The reinforcements on L520-Pen were installed at the penetrations by soldering, which provided a pressure tight seal. L520-Pen was machined from 6061-T6 aluminium tubing, while all other models were machined from 6082-T6 aluminium tubing.

Experimental procedures

Before testing, each specimen was measured for out-of-circularity (OOC) type geometric imperfections at several stations along the cylinder length using a coordinate-measuring machine. Measurements were taken on the outer and inner surface of the specimens at evenly spaced points in the circumferential direction, and along the length of the cylinder at stiffener and mid-bay locations. A discretized mapping of the radial imperfections could then be constructed. The OOC shapes were found to be primarily in modes n=2 and n=3, where n is the number of complete waves about the circumference, with amplitudes between 0.001 and 0.0015 times the shell radius [22].

A discretized shell thickness mapping was also constructed for each test specimen by comparing inner and outer radial measurements. The inner radius measurements were only taken in the middle of the central bay for the first group of cylinder specimens that were tested [27]. For the remaining cylinders [28,29], inner and outer measurements were taken at all stiffener and mid-bay locations, which allowed a more complete map of the shell thickness to be constructed.

The test specimens in [22] were fabricated from three separate batches of aluminium tubing. Material properties for each batch were derived from tensile testing of coupons machined from the original tube, and in some cases from the cylinders themselves after collapse testing. The coupon tests showed that the circumferential yield stress of the cylinders was up to 10% less than the axial yield stress, and furthermore, that there was approximately 10% variation in the material properties between batches. The material batch from which each test specimen was fabricated is given in Table 24, and the corresponding average circumferential and axial material properties for each batch of aluminium are summarized in Table 25. Average circumferential stress-strain curves for each batch are shown in Figure 61. Poisson's ratio was measured for two coupons, giving a value between 0.32 and 0.34.

During testing, the ends of the specimens were sealed with heavy steel end-caps. In earlier experiments [27], the specimens were air-backed during application of the pressure load, so that there was no mechanism to slow down the violent collapse event and the specimens were severely deformed and ruptured (e.g., specimen L300-N04 in Figure 60). Subsequent testing [28,29] involved filling the specimens with fluid in order to mitigate the violent collapse behaviour and to allow the deformation of the specimens to be controlled more precisely, especially near the collapse load. The so-called volume-control test method, described in Chapter 3 [21], allowed the collapse mode and post-collapse behaviour to be studied more effectively. For example, specimens L510-Test, L510-N011, L300-N01 and L300-N07 in Figure 60 were tested with the volume-control method.

Pressure-strain histories were measured during testing using pressure transducers and a large number of strain gauges attached to the test specimens. Intact cylinders were instrumented with strain gauges at eight or twelve equally spaced increments about the circumference at the stiffener flanges, the shell in the central bay and, in some cases, the shell opposite the stiffeners. Cylinders with artificial corrosion had additional gauges in that area. In general, bi-axial tee rosettes were used on the shell and uni-axial gauges were fixed to the stiffeners.

The measured pressure-strain data provide the collapse pressure, the pressure associated with the onset of yielding at specific locations, and also provide insight into the nonlinear behaviour, failure mode and post-collapse behaviour. Furthermore, while the accuracies of the FE models are evaluated by comparing the predicted and experimental collapse pressures, comparison of the measured and predicted pressure-strain history provides information on why the models are correct, or why they are in error. The accuracy of experimental collapse pressures is ±0.09 MPa, and is associated with the accuracy of the pressure transducers. The strain measurements are accurate to within ±0.5%.

Table 25: Summary of tensile testing for coupons taken from the axial and circumferential directions of the test specimens, showing the mean value for each material property and batch of aluminium material.

Material property	**Axial direction**			**Circ. direction**		
	Batch no.			**Batch no.**		
	1	**2**	**3**	**1**	**2**	**3**
Young's Modulus (GPa)	73.2	70.7	74.3	72.7	67.9	80.6
0.2% Yield Stress (MPa)	304	327	317	272	297	303
Tensile Strength (MPa)	373	385	348	333	349	330

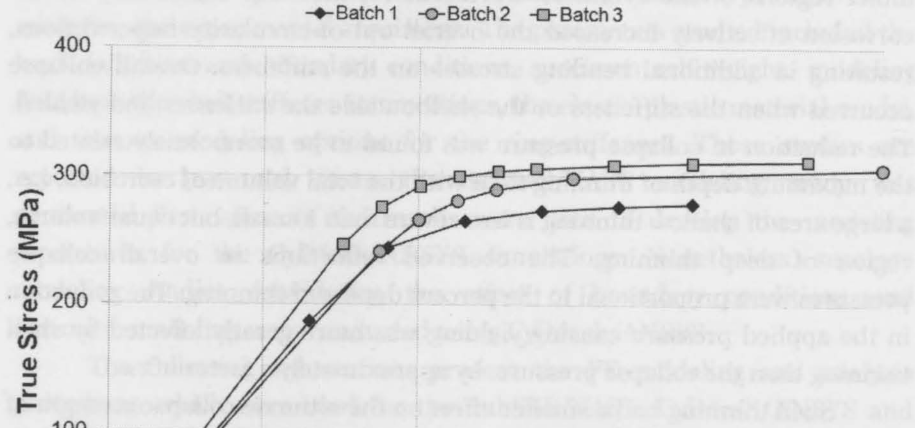

Figure 61: Multi-linear stress-strain curves used with the CylMesh/ANSYS FE models. These curves are based on the average measured stress-strain curve for each batch of material, for tensile coupons taken from the circumferential direction of the test specimens.

Summary of experimental results

Experimental collapse pressures are reported in Table 24. As expected, the short cylinders with heavy ring-stiffeners failed by interframe elasto-plastic collapse (e.g., L300-No1 in Figure 60). All other test specimens failed by overall elasto-plastic collapse (e.g., L300-No7 in Figure 60), except the unstiffened cylinder L510-Test, which failed by elastic buckling. The collapse strength of cylinders with simulated shell corrosion was found to be less than for similar undamaged specimens in all cases, while stiffener corrosion was found to have, on average, a relatively smaller strength-reducing effect on collapse pressure. In general, loss of strength due to corrosion was associated with the early onset of yielding in the region of material loss. For cylinders with shell thinning, early yielding was brought on by high in-plane stresses due to the thinning, as well as by bending stresses due to the eccentricity caused by one-sided thinning.

In models failing by overall collapse, early yielding of the corroded shell resulted in the adjacent stiffeners being loaded more heavily than in intact regions of the cylinders. Furthermore, the shell eccentricity at the corrosion effectively increased the overall out-of-circularity imperfections, resulting in additional bending stresses on the stiffeners. Overall collapse occurred when the stiffeners or the shell outside the stiffeners had yielded. The reduction in collapse pressure was found to be more closely related to the maximum depth of thinning than with the total volume of corrosion, i.e., a large area of shallow thinning is less severe than a small, but equal-volume, region of deep thinning. The observed reductions in overall collapse pressures were proportional to the percent depths of thinning. The reduction in the applied pressure causing yielding was more greatly affected by shell thinning than the collapse pressure, by approximately a factor of two.

Shell thinning had a smaller effect on the ultimate collapse strength of models failing by interframe collapse. Out-of-circularity plays a smaller role in interframe collapse, so that the shell eccentricity at the corrosion patch was less important. Most importantly, however, the heavy ring-stiffeners on the interframe collapse models provided significant reserve strength after the corroded shell failed locally early on in the pressure loading.

Finite element modeling and analysis procedures

Nonlinear finite element analyses were carried out for each of the test specimens in [22] using the finite element codes ANSYS [143] and VAST [144]. VAST is a general-purpose nonlinear FE program developed by Martec Limited over the past three decades under sponsorship of the Canadian Department of National Defence. VAST FE models were generated using a submarine structural modeling program called SubSAS [146], while ANSYS models were created using a C++ code called CylMesh, which was written specifically for the test specimens. The CylMesh/ANSYS and SubSAS/VAST FE modeling was performed by the first two authors of the current chapter. Some of the SubSAS/VAST FE models were converted to the ANSYS and MSC MARC [145] formats, and nonlinear analyses were run with each solver independently as a validation exercise for models with identical meshes, loading and boundary conditions.

Many of the modeling and analysis procedures were selected based on a review of FE methods for pressure hulls reported in the literature, as described in Chapter 2 [20], and from previous experience. Nonetheless, some initial parametric studies were conducted using SubSAS/VAST models in order to investigate the effects of various modeling parameters on the numerical collapse predictions, and to refine the standard procedures for modeling the experimental specimens. The parameters studied included the load definition and boundary conditions, specimen self weight, modeling details at the shell-stiffener intersections, the elastic-plastic material model, and various modeling options for the ring-stiffeners. Those studies are reported in [147-149]. Since the SubSAS/VAST modeling study was performed first, some of the results were used to develop the modeling procedures for the CylMesh/ANSYS simulations. Nonetheless, separate modeling studies considering the effect of boundary conditions and corrosion modeling were conducted using CylMesh/ANSYS.

The following sub-sections present the FE modeling and analysis procedures which were used for the SubSAS/VAST, CylMesh/ANSYS and SubSAS/MARC simulations. The methodologies are broken down into topics covering FE meshes, measured imperfections, material models, *etc*. Each sub-section first presents the standard modeling methods used in the final analyses of the test specimens, and then presents a summary of the modeling studies that led to those standard methods, if applicable. The standard FE modeling and analysis parameters used in the final analyses are summarized in Table 26.

Finite element meshes

Standard methodology

SubSAS and CylMesh were used to generate the FE models for analysis by VAST/MARC and ANSYS, respectively, including the application of measured out-of-circularity and shell thickness data, corrosion damage, loads and boundary conditions.

All FE models used in the final analyses were constructed using 4-node quadrilateral shell elements for the entire model, including the ring-stiffeners. The tapered end sections were modeled with shells with variable nodal thicknesses. Nodes were located at the mid-plane of the shell elements, except in the corrosion patches. Modeling of the corrosion patches is covered separately below. The test specimen with penetrations, L520-Pen, was modeled exclusively with SubSAS/VAST. Both the rectangular-section ring-stiffeners and the penetration reinforcements were modeled using shell elements.

The four-node shell element used in the VAST analyses was developed using the technique of mixed interpolation of tensorial strain components

Table 26: Summary of standard FE modeling and analysis procedures for SubSAS/VAST, SubSAS/MARC and CylMesh/ANSYS analyses.

Model parameter	**SubSAS/VAST**	**SubSAS/MARC**	**CylMesh/ANSYS**
Element type	4-node MITC shell	4-node Mindlin	4-node finite strain shell
Through-thickness integration points	6	11	5
Out-of-circularity	Single Fourier series about circumference and spline curves over length	Single Fourier series about circumference and spline curves over length	Double Fourier series for shell surface and single Fourier series for stiffeners
Shell thickness	Voronoi mapping	Voronoi Mapping	Double Fourier series
Material model (circumferential material properties)	Multi-linear overlay model with kinematic hardening and von Mises yield surface	Multi-linear model with isotropic hardening and von Mises yield surface	Multi-linear overlay model with kinematic hardening and von Mises yield surface
Boundary conditions	Clamped	Clamped	Quasi-clamped
Pressure loads	No follower-force	Follower-force	Follower-force
Axial loads	Concentrated axial loads on end nodes	Concentrated axial loads on end nodes	Edge pressure on end elements
Nonlinear formulation	Co-rotational	Updated Lagrangian	Updated Lagrangian / co-rotational
Path-following scheme	Orthogonal trajectory	Spherical arc-length	Spherical arc-length

(MITC) [150]. That element is free from shear locking and was used with six through-thickness integration points [144]. ANSYS analyses used a four-node finite strain shell element ("SHELL181" in ANSYS) [143], with four in-plane integration points (full integration) and five through-thickness integration points. The MARC FE models used four-node quadrilateral thick shell Mindlin elements ("Element 75" in MARC). The formulation of the bilinear Mindlin elements includes transverse shear effects and prevents locking for thin shell applications [151]. Eleven through-thickness integration points were used in the MARC analyses.

Convergence studies were performed for the SubSAS/VAST and CylMesh/ANSYS models to determine suitable mesh densities for each unique structural configuration. SubSAS/VAST convergence studies are reported in [147-149]. Figure 62 shows the results of a convergence study using CylMesh/ANSYS models of the corroded specimen L510-N07. Each mesh was composed of roughly square shells, and the nonlinear analyses followed the standard methods described in this section. Mesh F produced a converged result, having a collapse pressure within 0.5% of a model with half the mesh density (Mesh D), and was therefore chosen for final analysis. Mesh F had 288 elements about the circumference, 20 elements between frames, and 4 elements on both the stiffener web and flange. Those mesh parameters are typical of all the converged CylMesh/ANSYS FE models. The SubSAS/VAST models used refined meshes in the area of collapse and/or corrosion damage (e.g., see Figure 64) in order to improve computation time compared to globally refined meshes like those used with CylMesh/ANSYS.

Modeling studies

The effectiveness of using various combinations of shell and beam elements in VAST to model the ring-stiffeners for typical intact and corroded models was studied in [149]. It was found that, although the models using beams were reasonably accurate (the collapse pressures were within 2% of the all-shell models), the computational savings associated with the smaller number of nodes and elements were minimal because the FE models with beams required more convergence iterations per load increment than similar all-shell models.

A consequence of modeling ring-stiffeners with shells is that, if the FE model consists of integrally connected branched shells, there will be extra material at the shell-stiffener and web-flange intersections. This can be avoided by more realistic modeling of the stiffeners whereby the web depth is reduced by half the thickness of the shell plating and flange. The web-flange and web-shell connection is then enforced by applying rigid links to

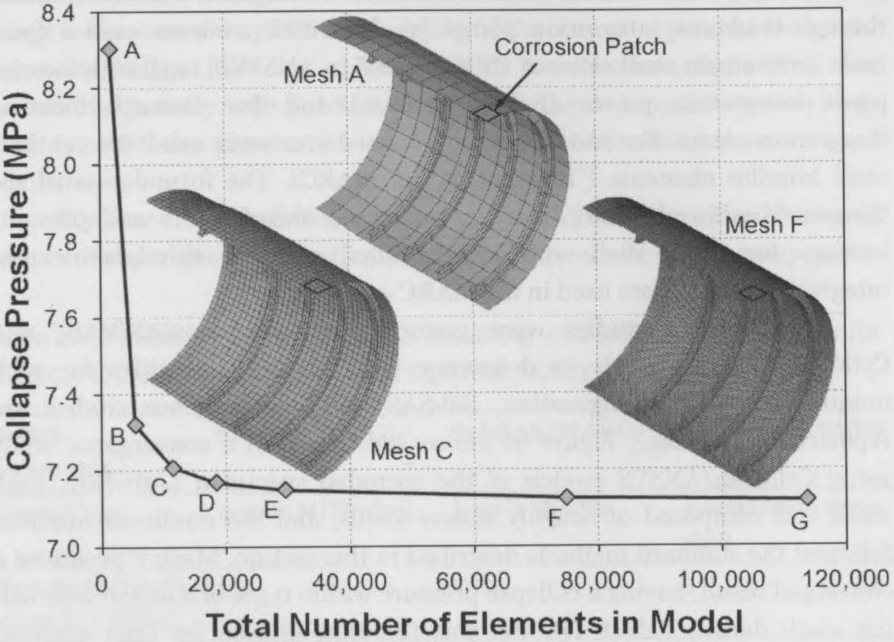

Figure 62: Results of a mesh convergence study for specimen L510-No7, showing the collapse pressures predicted using CylMesh/ANSYS versus the total number of shell elements in the corresponding FE models. Example meshes show only one-quarter of the full FE model for clarity. The corrosion patch elements are highlighted. Mesh F was chosen for final analysis of L510-No7 and similar test specimens.

corresponding node pairs. A study of these effects for specimen L510-No10 showed that the nonlinear collapse pressure predicted by VAST is reduced by 0.65% when the extra material at the shell branches is removed [147]. This small difference can be seen as a validation of the shell theory assumptions for these test specimens and, furthermore, the effect was considered to be small enough that subsequent analyses included the extra material to reduce the amount of effort required to create the models.

Measured out-of-circularity and shell thickness

With both SubSAS and CylMesh, the FE mesh was first created based on the nominal perfect axisymmetric geometry. The out-of-circularity imperfections were then applied to the nodal coordinates based on a continuous nonlinear map (or maps) fit to the discrete OOC measurements. In SubSAS, a single imperfection map was derived by fitting the measured mid-plane shell imperfections, which were derived by averaging the corresponding measurements taken on the inside and outside of the shell, to Fourier series along the circumference and spline curves in the axial direction. This mapping was then applied to both the shell and stiffener nodal positions in the VAST and MARC FE models.

In CylMesh, the radial eccentricity measurements taken outside the shell were fit to a double Fourier series that characterizes the entire two-dimensional shell surface, while one-dimensional Fourier series were fit to the OOC data for individual ring-stiffeners. The double and single Fourier series were then applied to the coordinates of the nodes in the ANSYS FE model that are associated with the shell and stiffeners, respectively. The decomposition for the two-dimensional Fourier series, which consisted of the product of two complete single Fourier series, was accomplished using an iterated method similar to that presented in [152] for one-dimensional Fourier series.

Measured shell thicknesses were applied to the FE models in a manner similar to the out-of-circularity mapping. The FE models were first created based on the nominal shell thicknesses, and the element thicknesses were subsequently adjusted based on maps derived from the measured data. Using SubSAS, the measured thickness data were applied to the VAST and MARC FE models using a Voronoi mapping technique. That entailed partitioning the entire two-dimensional measurement domain for each cylinder into cells corresponding to the measurement sites. The measured thickness values were then assigned to finite element nodes in each cell resulting in a piecewise thickness distribution in both axial and circumferential directions.

With CylMesh, the measured thickness data were fit to a double Fourier series using the iterated method. The Fourier series was subsequently mapped to the ANSYS FE model by adjusting the nodal thickness of each element on the shell surface. When shell thickness data were available for only one bay, CylMesh used a single Fourier series description of the shell in that bay and a uniform thickness elsewhere on the shell corresponding to the mean measured thickness.

Material models

Standard methodology

All FE models used for final analysis incorporated a material model characterized by an isotropic von Mises yield surface and associated flow rule, in combination with a multi-linear stress-strain curve derived from the circumferential coupon test data. The reasons for using the circumferential material properties are described in the next paragraph. Characteristic stress-strain curves were derived for each batch of material by taking the average of all of the curves derived from coupon testing for that batch. Each curve was used in the simulations for all of the test specimens that were fabricated from the corresponding batch of material. The multi-linear stress-strain curves were represented in the VAST and ANSYS FE models using overlay material models with kinematic hardening. The MARC FE models incorporated the multi-linear curves with an isotropic hardening model. Since the VAST and ANSYS FE models were developed independently, the material models were populated with slightly different multi-linear stress-strain curves, even though the same coupon test data were used. The circumferential stress-strain curves used in the VAST and MARC analyses were identical. The stress-strain curves used in the CylMesh/ANSYS analyses are shown in Figure 61.

Modeling studies

An initial study [149] was conducted with SubSAS/VAST FE models in order to determine if a more sophisticated material model was required to deal with the anisotropy mentioned above. Isotropic von Mises material models, of the standard type described in the previous paragraph, were used in collapse analyses with either the axial or the circumferential measured material properties. The results of those analyses were compared with FE models having an orthotropic material model based on Hill's yield criterion [153]. The Hill model requires material data in the principal circumferential and axial directions, as well as the "shear" direction, which is offset 45° from the principal directions.

Nonlinear collapse predictions for specimens L510-N05 and L510-N07, for which the necessary shear-direction tensile testing results were available for the Hill model, showed that the predicted collapse pressures for models using an isotropic yield surface and the circumferential material properties were within 1% of those using the Hill model. Collapse pressures for isotropic models with the axial material data were up to 10% higher than the Hill model results. Furthermore, the Hill and isotropic-circumferential models gave collapse pressures within 3.0 and 3.5% of the experimental values, respectively.

The responses of the test specimens considered herein are dominated by compressive stresses in the circumferential direction at the shell at mid-bay and at the ring-stiffeners, and to a lesser extent, compressive and tensile shell stresses in the axial direction. The magnitude of axial tensile stresses, which arise at the interior of the shell near the ring-stiffeners, may be even greater than the mid-bay circumferential stresses; however, it is generally accepted that local yielding due to high axial stresses at those locations changes the degree of support provided to the shell between frames, but does not lead to collapse [10].

Figure 63 shows a comparison of the von Mises and Hill yield surfaces for L510-N07, along with shell stresses at mid-bay at the centre of the corrosion patch, which were derived from strain gauge measurements taken during collapse testing. Figure 63 shows the similarity between the Hill and isotropic-circumferential yield surfaces in the critical region of the principal stress space, where the compressive circumferential shell stresses are greatest. That explains the close agreement between the material models for predicting the response of the test specimens, despite the inaccuracy of the isotropic-circumferential model in areas with very high axial stresses. Since the isotropic-circumferential material model is accurate with respect to both the Hill model and the experimental data, and requires less tensile testing data, it was used for the final analysis of all test specimens.

Boundary conditions and loading

Standard methodology

The steel end-caps were not explicitly modeled in any of the analyses reported here. Instead, they were included indirectly via boundary conditions applied at the cylinder ends. The choice of boundary conditions, especially the degree of constraint against axial warping of the cylinder ends, can significantly affect overall collapse pressure; however, the boundary condition studies described below in the modeling studies section indicate that the current test specimens were relatively insensitive to the selected constraints, likely due to the degree of resistance that is already provided by the thick end-rings (see Figure 27, p. 82). Nonetheless, the end-caps were found to resist out-of-plane bending (i.e., radial displacements) near the cylinder ends, while allowing some end-warping.

Clamped boundary conditions were used for SubSAS/VAST and SubSAS/MARC models, whereby all nodes at one end of the model were fully constrained and all nodes at the other end were constrained against all translations and rotations except for translation along the axial direction. This convention allowed end-warping at one end of the cylinder. The CylMesh/ANSYS models were simply supported at the ends and at the intersections of the thick cylindrical shell sections with the tapered shell sections. The simple supports at two locations near each end resulted in a "quasi-clamped" condition whereby the ends of the model were supported against out-of-plane bending. A single node at the end of the model was

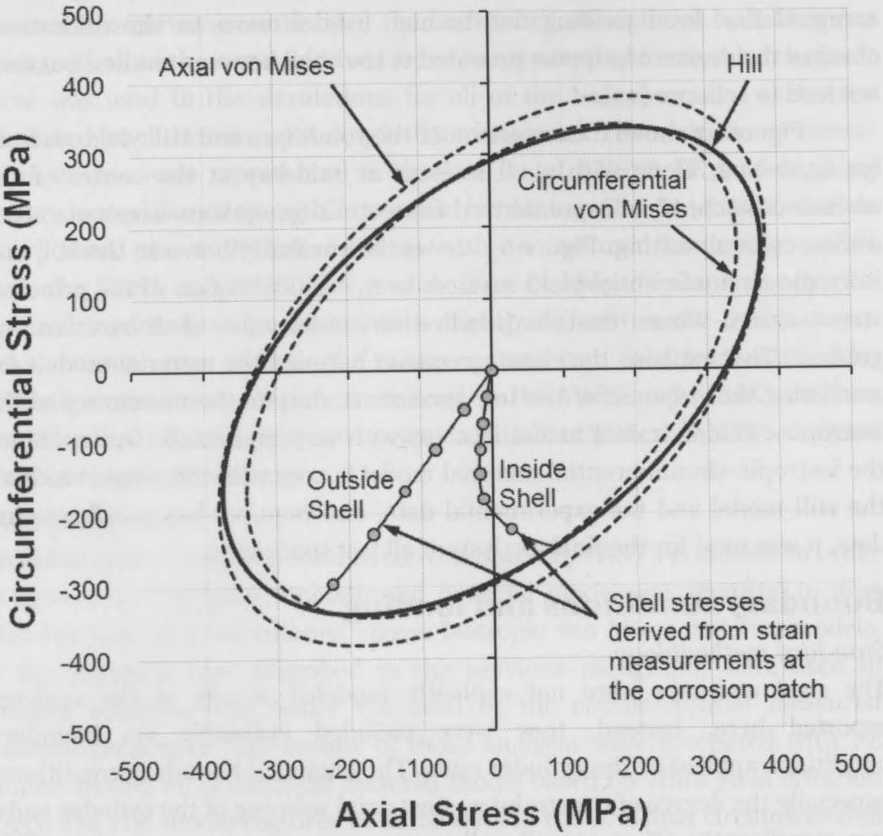

Figure 63: Comparison of isotropic von Mises and anisotropic Hill yield surfaces based on measured material properties for L510-No7. Shell stresses derived from strain measurements taken at the centre of the corrosion patch during collapse testing of that specimen are also shown. The shaded circles on those curves indicate measurements taken at 1 MPa increments of the applied external pressure, starting at 0 MPa at the origin.

constrained in the axial direction to prevent rigid body motion; no other nodes were constrained in that direction so that end-warping was allowed at both ends.

External radial pressure was applied to the shell of each FE model. The effects of live loading (i.e., the follower-force) were not included in the SubSAS/VAST FE analyses, since collapse pressures predicted for one of the test specimens with and without live loading were almost identical. Nonetheless, live loading was considered in the CylMesh/ANSYS and SubSAS/MARC analyses. The forces associated with the pressure loads acting on the end-caps were applied to the FE models via concentrated axial forces at the end-nodes in VAST and MARC models, and by edge pressures on the shell elements at the ends of the model in ANSYS analyses. The nodal forces and edge pressures were computed based on the mid-surface geometry of the shell elements at the cylinder ends. No loads were applied to the flange and web of external stiffeners since both sides of these components were exposed to the same external pressure, thereby producing a net load of zero.

Modeling studies

Separate studies exploring the influence of various boundary condition options on the FE results were conducted for the SubSAS/VAST and CylMesh/ANSYS models. The SubSAS/VAST study considered a clamped (described above) and a simply-supported end condition. The results of that study [147] indicated that the choice of boundary conditions had more influence on the location of failure than on the collapse pressure. The clamped convention, which provides out-of-plane bending resistance similar to the test specimen end-caps, was found to produce collapse modes in agreement with the experimental results, and was employed in the final analyses of all VAST and MARC models.

The CylMesh/ANSYS study examined clamped and simply-supported end conditions, with and without end warping, as well as the quasi-clamped case described above that was meant to more realistically model the support of the end-caps. The quasi-clamped condition was found to give the best predictions of collapse pressure and mode for a number of specimens and was chosen for final analysis of all ANSYS models.

A SubSAS/VAST study was performed to investigate the influence of specimen self-weight, including the steel end-caps and the buoyancy force generated by the pressure testing fluid for air-backed tests, on the collapse pressure of one of the test specimens (L510-N01). The results of nonlinear analyses with and without accounting for specimen self-weight gave collapse pressures that agreed within less than 0.1% [147], and so self-weight was neglected for all final analyses.

Modeling of artificial corrosion

Standard methodology

Twelve of the twenty-two test specimens considered in the present study contained some form of simulated corrosion (Table 24). Regions of one-sided shell thinning introduce step changes in the shell thickness and mid-plane, which presents a problem for conventional shell elements whereby the shell mid-plane is collocated with the element nodes. The corroded regions were modeled using shell element formulations in ANSYS, VAST and MARC that allow the mid-plane of the shell element to be specified relative to the nodal locations. In this way, the cylinder shell, including corrosion patch, could be modeled as a single integrally connected mesh whereby the shell element mid-planes in intact regions were collocated with the nodes, while the mid-planes at corrosion patches were offset from the nodal locations so that the corroded shell was aligned with the inner surface of the intact shell. In this way, the shell eccentricity arising from one-sided thinning was modeled without resorting to artificially tapered elements at the corrosion patch edges, or a separate mesh for the corrosion patch connected to the main shell mesh by rigid links.

When multiple shell thickness measurements were available in the corroded region, the maps were applied using the Voronoi mapping technique for VAST/MARC models. A similar partitioning method was used to apply thickness maps in the corrosion patches for CylMesh/ANSYS models. When only one measurement was available, the thickness in the corroded region was assumed to be uniform. Flange corrosion was modeled by adjusting the coordinates of the flange nodes so as to reduce the width of the flange locally, thus forming the “dog-bone” pattern used in the experimental specimens.

Modeling studies

CylMesh/ANSYS was used to examine the effect of neglecting the shell eccentricity due to one-sided thinning. Two CylMesh/ANSYS models were constructed for each test specimen with shell corrosion: a standard model that accurately represents both the shell thinning and the shell eccentricity at corrosion patches by using the shell offset feature described above, and a second model that incorporates the shell thinning but that neglects the shell offset due to one-sided thinning. Otherwise the models were identical and adhered to the standard modeling procedures described in this section. The results of this study are presented in the discussion under the heading “Prediction of the effects of corrosion damage” starting on p. 191.

Nonlinear solution procedures

Quasi-static incremental application of the load was used for all analyses. In VAST, geometrical nonlinearities were dealt with through an element-independent consistent co-rotational formulation, which is applicable for arbitrarily large displacements and rotations. The ANSYS analyses used an updated Lagrangian formulation in combination with a co-rotational system. The MARC analyses used an updated Lagrangian method to include the nonlinear terms in the curvature expressions.

The nonlinear solution was achieved in ANSYS analyses by iteratively balancing the internal and external forces at a given load increment using a so-called modified Newton-Raphson approach, whereby the tangent stiffness is updated at the beginning of each load increment. VAST and MARC analyses used the full Newton-Raphson method in which the tangent stiffness is updated before each iteration. Arc-length methods were used in order to obtain the structural responses of the models in the post-collapse region. A spherical arc-length method was used in the ANSYS and MARC analyses, while the VAST analyses employed an orthogonal trajectory solution procedure. The latter method is a version of the arc-length method whereby the solution is sought along a line that is orthogonal to the tangent of the load-displacement curve and thereby eliminates the requirement for solving quadratic algebraic equations. A load increment of 0.5 MPa was used to start the solution process in most VAST and MARC analyses, while a typical ANSYS analysis began with a 0.25 MPa increment.

Comparison of experimental and numerical results

The FE-predicted collapse pressures for all SubSAS/VAST and CylMesh/ANSYS analyses using the standard methodologies described in the previous section are reported in Table 27. Those models are referred to as the "standard" models. SubSAS/VAST nonlinear analyses were carried out for each of the test specimens listed in Table 24, and all specimens except L510-Pen were analyzed with CylMesh/ANSYS. Table 27 also includes the CylMesh/ANSYS predictions for the corrosion modeling study described in Section "Modeling of artificial corrosion" starting on p. 173, in which the shell eccentricity at locations of shell thinning was neglected.

Collapse predictions for the FE-solver comparison are reported in Table 28. In that study, SubSAS was used to generate meshes for four test specimens that were subsequently analyzed using VAST, ANSYS and MARC. The FE models are referred to as "geometrically" identical, since the node locations and element connectivity are the same; the material properties, loading and boundary conditions are also identical. Those modeling parameters follow the standard SubSAS/VAST methodology described in Sections "Finite element meshes" (p. 165), "Measured out-of-circularity and shell thickness" (p. 168), "Boundary conditions and loading" (p. 171) and "Modeling of artificial corrosion" (p. 173).

The geometrically identical FE models differ in their solver specific element formulations, material model implementation and solution procedures. Those aspects of the FE predictions are described for each solver in Sections "Finite element meshes" (p. 165), "Material models" (p. 169) and

Table 27: Summary of numerical collapse pressure predictions for standard SubSAS/VAST and CylMesh/ANSYS FE models.

Specimen	**Experimental Collapse Pressure (MPa)**	**Finite Element Collapse Pressure (MPa)**		
		SubSAS/VAST Standard[a]	**CylMesh/ANSYS**	
			Standard[a]	**No Shell Offsets[b]**
L300-No1	7.11	7.19	7.32	-
L300-No2	7.87	7.34	7.51	-
L300-No3	6.77	6.41	6.88	6.99
L300-No4	6.94	6.80	7.12	7.09
L300-No5	8.99	9.61	9.95	-
L300-No6	9.14	9.71	9.93	-
L300-No7	7.30	7.43	7.64	8.02
L300-No8	7.11	7.23	7.47	7.88
L510-No1	9.05	9.45	9.43	-
L510-No2	8.59	8.92	8.93	-
L510-No3	9.25	9.12	9.13	-
L510-No4	9.79	10.54	10.68	-
L510-No5	9.08	8.96	9.32	-
L510-No6	8.48	9.22	9.28	-
L510-No7	7.07	6.94	7.13	7.48
L510-No8	7.21	7.39	7.42	7.79
L510-No9	7.68	7.56	8.01	8.18
L510-No10	7.81	8.57	8.35	8.46
L510-No11	7.58	7.60	7.86	8.06
L510-No12	7.29	7.58	7.83	7.95
L510-Test	7.96	8.22	7.85	-
L520-Pen	9.00	8.95	-	-

[a] FE collapse pressures predicted using the indicated pre-processor and solver, and using the standard modeling and analysis procedures described in Section "Finite element modeling and analysis procedures" starting on p. 164 (see also Table 26).

[b] Collapse pressures predicted by CylMesh/ANSYS FE models whereby the shell eccentricity due to corrosion thinning has been neglected. Otherwise, the FE models were based on the standard methodology.

"Nonlinear solution procedures" (p. 174), respectively. The FE models used in the solver study have slightly coarser meshes than those used for final analysis with SubSAS/VAST, for which the collapse pressures are reported in Table 27.

The numerical failure modes and pressure-strain histories predicted by the standard CylMesh/ANSYS and SubSAS/VAST models were compared with the measured data for each cylinder. Results for a few typical cases are given in the current section for cylinders failing by interframe and overall collapse. FE results for two of the test specimens considered in the solver study are also presented in this section. A discussion of the complete set of FE analyses is presented in the discussion starting on p. 187.

Cylinders failing by interframe collapse

Intact cylinders

Figure 64 shows the short intact cylinder with heavy ring-stiffeners, L300-No1, after testing, as well as a typical SubSAS/VAST FE mesh for that structural configuration. Figure 64 also shows the experimental and predicted pressure-strain responses for the cylinder at the location of initial collapse. The experimental data are characterized by circumferential shell strains that are significantly greater than the strain at the adjacent stiffener. This is indicative of an interframe collapse mode, and is corroborated by the post-testing shape, which shows a classical interframe buckling pattern. The numerical pressure-strain responses are in good agreement, except that initial yielding is delayed in the FE models so that the predicted compressive

Table 28: Summary of numerical collapse pressure predictions for geometrically identical VAST, ANSYS and MARC FE models produced using SubSAS.

Specimen	**Experimental Collapse Pressure (MPa)**	**Finite Element Collapse Pressure (MPa)**		
		VAST[a]	**ANSYS**	**MARC**
L510-No5	9.08	9.04	9.08	9.14
L510-No7	7.07	6.94	7.08	7.13
L510-No9	7.68	7.63	7.76	7.74
L510-No11	7.58	7.71	7.76	7.87

[a] FE models used in these VAST analyses have slightly coarser meshes than those used for final analysis with VAST, for which the collapse pressures are reported in Table 27.

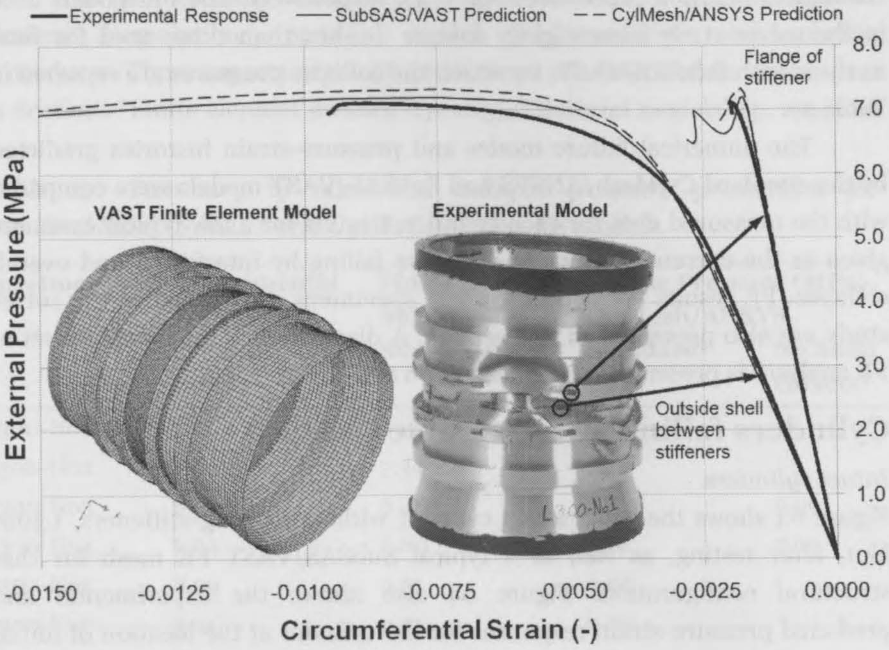

Figure 64: Pressure-strain response for the intact specimen L300-No1, which failed by interframe collapse. Selected circumferential strain histories at the location of failure, as measured in the experiment and predicted by nonlinear FE analyses, are shown.

strains are somewhat smaller than the measured strains in the nonlinear portion of the curves leading up to collapse. Despite that, the SubSAS/VAST and CylMesh/ANSYS numerical models both predicted the collapse load of the test specimen within 3%.

Corroded cylinders

Specimen L300-No3 is nominally identical to L300-No1, except that it has a square patch of artificial corrosion on the outside of the central bay, spanning 70% of the bay width and resulting in approximately 25% thinning of the shell. Experimental and numerically predicted pressure-strain histories in the region of corrosion are shown in Figure 65. In the test specimen, a local strain reversal at the inside of the corroded shell at approximately 5.5 MPa suggests the cylinder has failed at that location. The strain reversal can be attributed to inward bending associated with local plastic buckling. The adjacent intact shell and ring-stiffeners were able to pick up the load shed by the corrosion patch, however, and the test specimen ultimately failed at a considerably higher pressure of 6.77 MPa.

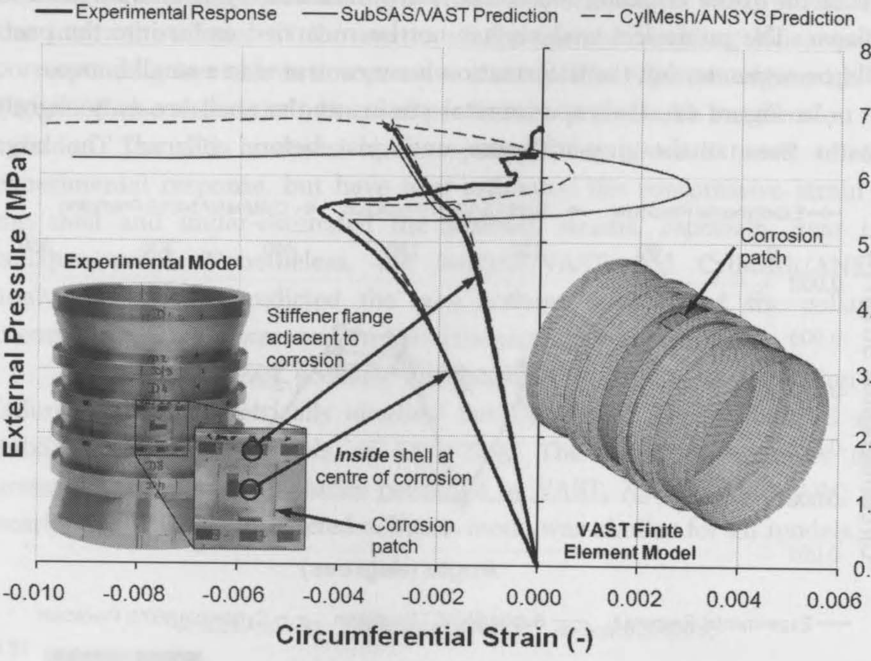

Figure 65: Pressure-strain response for the corroded specimen L300-No3, showing selected circumferential strain histories at the location of failure, as predicted by the experiment and nonlinear FE analyses.

Figure 65 shows that the numerical models correctly predicted the local instability in the corrosion patch, and also captured the increase in stiffener strain that occurred after the corrosion patch failed. The SubSAS/VAST and CylMesh/ANSYS FE models predicted both the local buckling pressure in the corrosion patch and the ultimate collapse load of the test specimen within 5.5%.

Cylinders failing by overall collapse

Intact cylinders

Figure 66 shows the circumferential distribution of strain at a central stiffener, and selected pressure-strain histories, for the long intact cylinder, L510-No5, which failed by overall collapse with n=3 circumferential buckling waves. Also shown are the final deformed shape of the test specimen after testing and the deformed shape of the SubSAS/VAST FE model at the end of the collapse analysis. Overall collapse of the test specimen is indicated by the large deformation of both the shell and ring-stiffeners over the length of the model. The post-collapse behaviour of the test specimen was dominated by one of the three buckling lobes that were indicated by the strain data at collapse. The numerical analysis has not been carried as far into the post-collapse region so that the deformation is concentrated in a smaller area.

In Figure 66, the experimental strains at the shell are only slightly greater than at the ring-stiffeners until just before collapse. The large

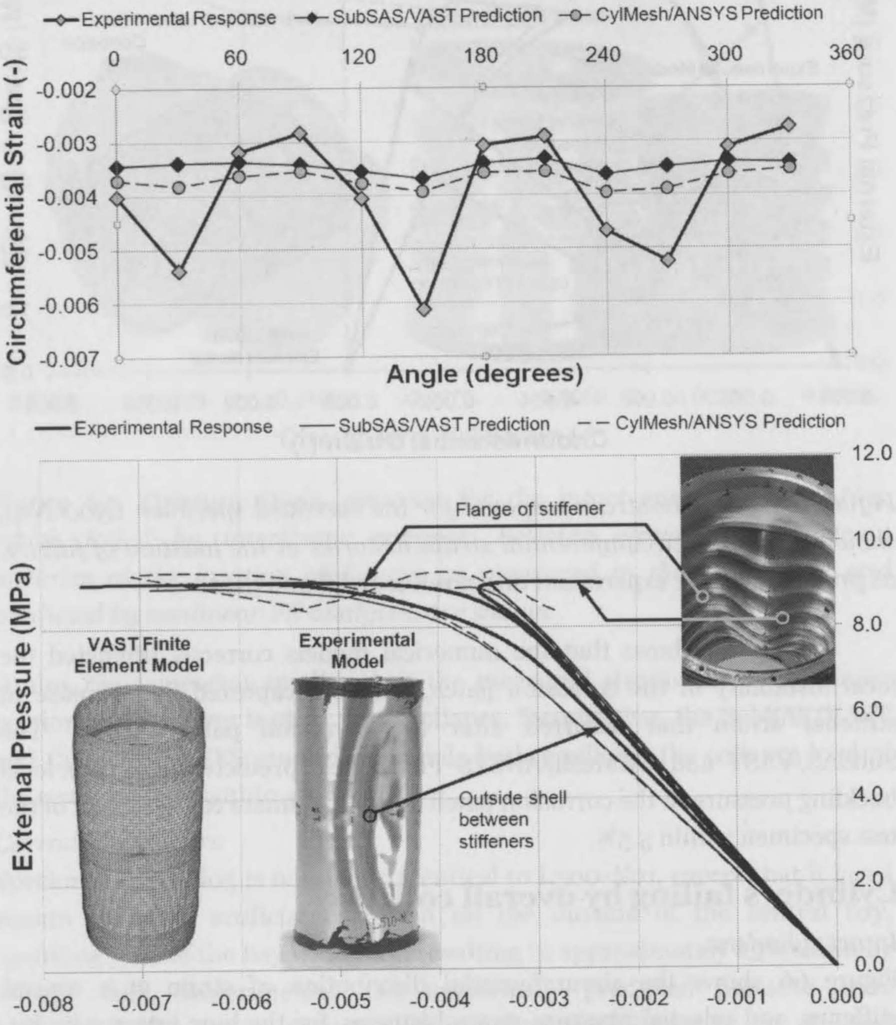

Figure 66: Circumferential distribution of strain at a central stiffener at the experimental and numerical collapse loads (top) and pressure-strain response (bottom) for the intact specimen L510-No5, which failed by overall collapse. Selected circumferential strain histories at the location of failure, as predicted by the experiment and nonlinear FE analyses, are shown.

bending strains that occur during overall collapse result in strain reversal at the internal stiffener at the centre of the inward buckling lobe, and a corresponding increase in compressive strain at the adjacent outward lobe. Figure 66 also shows the numerical predictions at the same locations on the cylinder. The FE analyses have captured the general trend of the experimental response, but have over-estimated the compressive strain at the shell and under-estimated the stiffener strains, especially near the collapse event. Nonetheless, the SubSAS/VAST and CylMesh/ANSYS analyses correctly predicted the *n*=3 collapse mode, and the collapse pressure predictions were within 3% of the experimental value.

Figure 67 shows pressure-displacement curves at the location of failure for the geometrically identical SubSAS/VAST, SubSAS/ANSYS and SubSAS/MARC FE models of L510-No5. The collapse pressures and pressure-displacement histories predicted by VAST, ANSYS and MARC are nearly identical. The predicted collapse mode was similar for all models, as

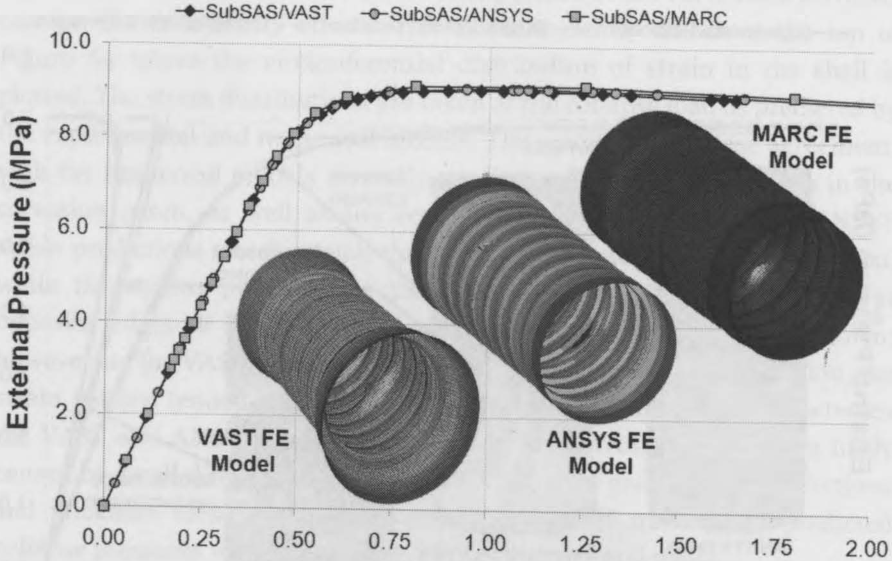

Figure 67: Pressure-displacement responses at the shell at the location of failure for the intact specimen, L510-No5, as predicted using geometrically identical FE models with the VAST, ANSYS and MARC FE solvers. Also shown are the final deformed shapes of the model predicted with those solvers. The radial displacement contour maps superimposed on the deformed FE models are based on different scales for the different solvers.

shown by the final deformed meshes in Figure 67. The predicted collapse pressures agree with each other within 1.2% and with the experimental value within 0.7%. The latter value differs from the 3% agreement mentioned in the previous paragraph since different ANSYS FE models were used in the two experimental-numerical comparisons.

Corroded cylinders

Specimens L510-No7 and L510-No9 are nominally identical to L510-No5, except that they have square patches of corrosion damage on the outside of the shell. In L510-No7, the corrosion spans approximately 85% of the central bay, with approximately 20% thinning. The corrosion patch for L510-No9 is shallower but larger in area, with approximately 13% thinning of the shell over one complete bay in the centre of the cylinder and two half-bays on either side. Pressure-strain plots for the experimental and numerical models are shown in Figure 68 and Figure 69 for L510-No7 and L510-No9, respectively.

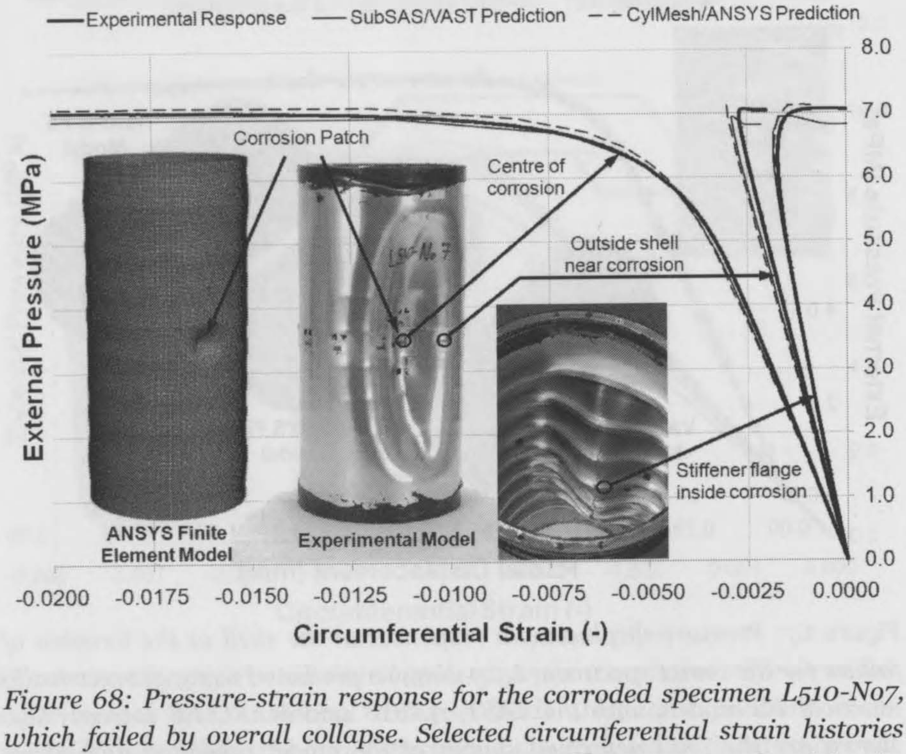

Figure 68: Pressure-strain response for the corroded specimen L510-No7, which failed by overall collapse. Selected circumferential strain histories near the location of failure at the corrosion damage, as predicted by the experiment and nonlinear FE analyses, are shown.

In Figure 68, the compressive shell strains in L510-N07 are shown to be much greater in the corroded area than in the intact shell nearby. This trend, which is common to all corroded test specimens, is magnified as the corroded shell begins to yield and the collapse load is approached. Inward bending of the cylinder around the corrosion patch leads to strain reversal at the stiffener flange directly inside the corrosion patch, as well as the intact shell outside the corroded area. The computed strain histories in Figure 68 indicate that both the SubSAS/VAST and CylMesh/ANSYS models were able to closely predict the nonlinear behaviour in the area of the corrosion patch, as well as the strain reversals associated with the overall collapse mode. The predicted collapse pressures were within 2% of the actual collapse load.

Figure 69 shows that, for L510-N09, the circumferential compressive strains are greatest at the edges of the corrosion patch, where collapse was initiated in the test specimen. This has been attributed to a bending moment induced by the shell eccentricity arising from one-sided thinning. The numerical pressure-strain predictions shown at the bottom of Figure 69 indicate that the shell offset features incorporated in the FE models correctly capture the eccentricity effects. This is more clearly shown at the top of Figure 69 where the circumferential distribution of strain in the shell is plotted. The strain distributions are taken at the collapse load as predicted by the experimental and numerical models. The results are in close agreement, with the numerical models correctly predicting the high local strains in the corrosion patch, as well as the eccentricity effects. The CylMesh/ANSYS strain predictions closely match the pattern measured on the test specimen, while the strains predicted by the SubSAS/VAST model are highest at opposite edges of the corrosion patch, compared to the test specimen; however, as the VAST FE model was loaded into the post-collapse region, the strain pattern tended to match the test specimen. The differences between the VAST and ANSYS strain predictions in the corrosion patch were likely caused by small differences in the representation of geometric imperfections and thickness variations in the corroded area. The numerically predicted collapse pressures were within 4.5% of the experimental result.

L510-N011 had the largest corrosion patch of all models tested, with approximately 13% thinning of the shell over three complete bays in the centre of the cylinder and two half-bays on either side. The test specimen failed by overall collapse in the corroded region, with several smaller interframe buckling lobes superimposed on the overall deformation of the shell and stiffeners. The test specimen is shown after testing in Figure 60, p. 157. It was not loaded as far into the post-collapse region as specimens

L510-No5, L510-No7 and L510-No9, so that the overall collapse mode is not as obvious from the photograph.

The final deformed mesh configurations of the geometrically identical VAST, ANSYS and MARC FE models of L510-No11 are shown in Figure 70. Each FE model has predicted local shell deformation in the corrosion patch

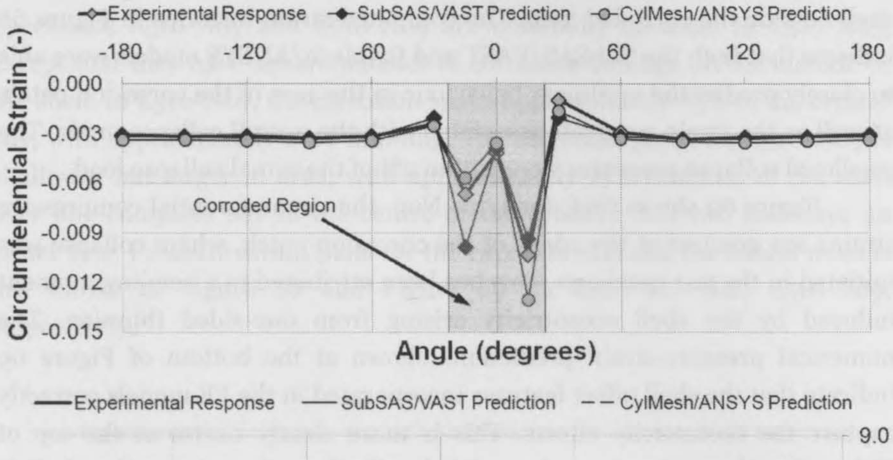

Figure 69: Circumferential distribution of strain at a central stiffener at the experimental and numerical collapse loads (top) and pressure-strain response (bottom) for the corroded specimen L510-No9, which failed by overall collapse. Circumferential strain histories at the location of failure, as predicted by the experiment and nonlinear FE analyses, are shown.

and large stiffener displacements. The VAST and ANSYS collapse modes closely resemble each other, while the collapse mode predicted by MARC is dominated by a different lobe of the interframe deformation pattern in the corrosion patch. The pressure-displacement curves shown in Figure 70, as predicted by each solver, are nearly identical throughout the loading history. The predicted collapse pressures agree within 2% of each other and within 3.6% of the experimental value.

Cylinder with penetrations

The cylinder with reinforced penetrations, L520-Pen, was air-backed during pressure testing, so that it was completely destroyed by the collapse event. An overall collapse mode with n=3 circumferential buckling waves is suggested by the circumferential distribution of strain in the central stiffener, as shown in Figure 71. The experimental collapse mode was aligned so that the two penetrations, which were spaced 180° apart, were collocated with an inward and an outward buckling lobe. FE analysis of L520-Pen was

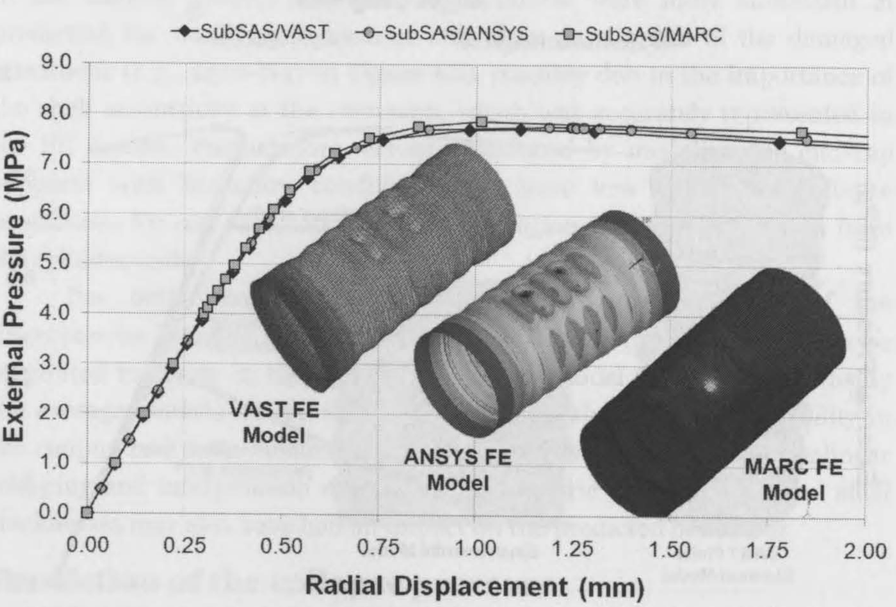

Figure 70: Pressure-displacement responses at the shell at the location of failure for the corroded specimen, L510-No11, as predicted using geometrically identical FE models with the VAST, ANSYS and MARC FE solvers. Also shown are the final deformed shapes of the model predicted with those solvers. The radial displacement contour maps superimposed on the deformed FE models are based on different scales for the different solvers.

performed using SubSAS/VAST. Figure 71 shows that the numerical model has correctly predicted the overall n=3 collapse mode, and the predicted and measured strains are in good agreement despite the simplifications associated with modeling rectangular stiffeners with shells. The predicted collapse pressure was within 1% of the experimental value.

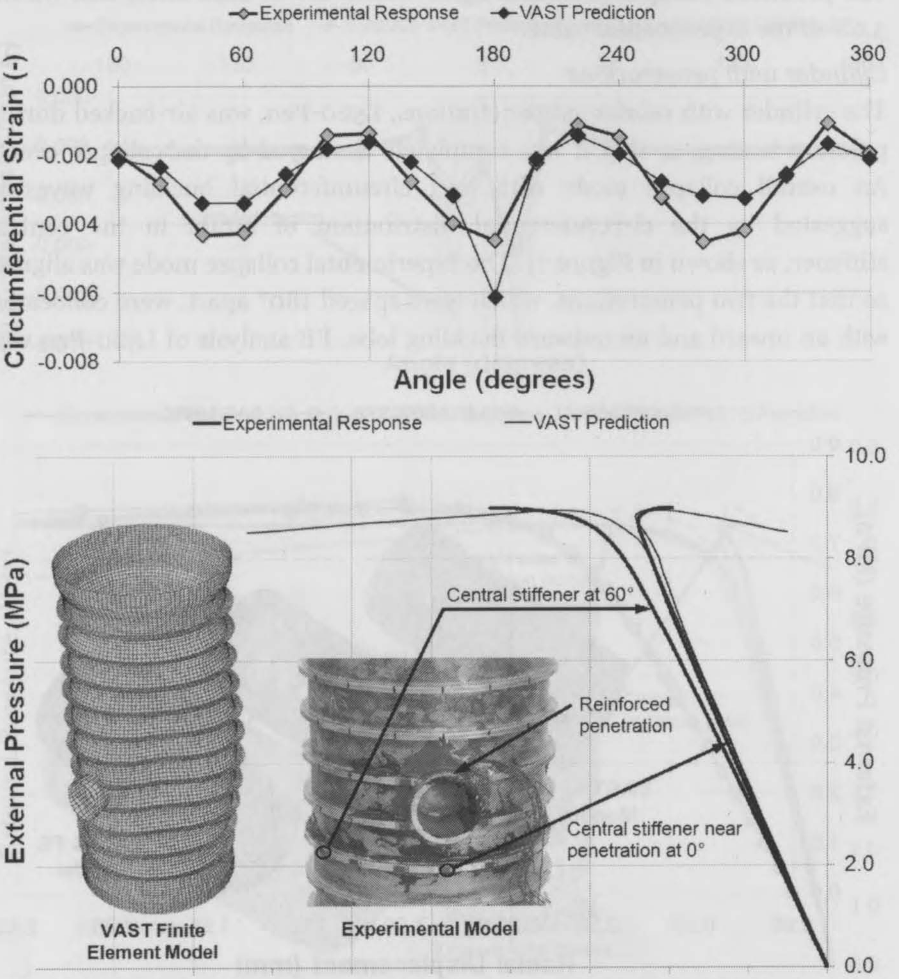

Figure 71: Circumferential distribution of strain at the central stiffener at the experimental and numerical collapse loads (top) and pressure-strain response (bottom) for the cylinder with penetrations L510-Pen, which failed by overall collapse. Circumferential strain histories near the penetration, as predicted by the experiment and nonlinear FE analysis, are shown.

Discussion

Prediction of the nonlinear pressure-strain response

The experimental-numerical comparisons presented above show that the SubSAS/VAST and CylMesh/ANSYS FE models were, in general, successful at predicting the nonlinear response of the test specimens. The intact test specimens were nearly perfectly axisymmetric, so that yielding occurred simultaneously over a large region of the cylinders and the collapse instability followed soon after the onset of yielding [22]. The numerical models sometimes had difficulty accurately predicting the nonlinear behaviour in those models, especially in the ring-stiffeners of models failing by overall collapse (e.g., L510-No5 in Figure 66), so that the collapse load was over-estimated.

With the corroded test specimens, much of the nonlinear behaviour and yielding was concentrated in the corroded area and occurred earlier on in the loading history. The numerical models were more successful at predicting the nonlinear behaviour and ultimate strength of the damaged specimens (e.g., L510-No7 in Figure 68), possibly due to the importance of the shell eccentricity at the corrosion, which was accurately represented in the FE models. Furthermore, errors introduced by modeling the end-cap supports with boundary conditions may have less impact on collapse predictions for corroded models, since the region of failure is isolated from the cylinder ends.

For both intact and corroded models, at least some of the discrepancies between the measured and predicted strain responses can be attributed to errors in the numerical material model associated with using the average material properties for batches that showed some variability in the coupon test data. Furthermore, approximations related to the nonlinear mapping and interpolation of measured geometric imperfections and shell thicknesses may also have had an impact on the predicted behaviour.

Prediction of the collapse pressure

Experimental collapse pressures are plotted against the corresponding standard SubSAS/VAST and CylMesh/ANSYS model predictions in Figure 72. The standard SubSAS/VAST and CylMesh/ANSYS FE models predicted the experimental collapse pressures within ±10% and ±11%, (see also Table 27). The collapse pressures predicted by VAST are scattered around the line of perfect correlation, while the ANSYS models tended to over-predict the experimental collapse pressures to a greater extent than the VAST models. Nonetheless, many of the predictions for both sets of FE models are within,

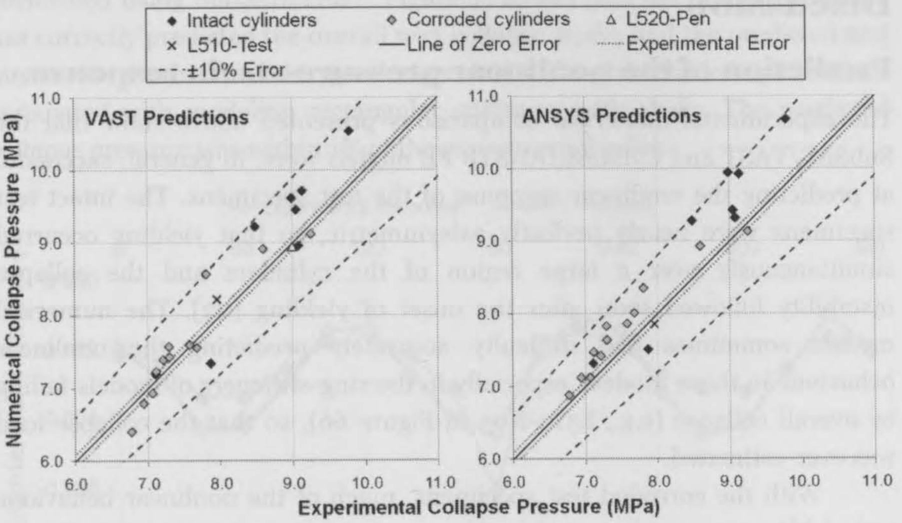

Figure 72: Comparison of experimental collapse pressures with those predicted by SubSAS/VAST and CylMesh/ANSYS FE models, for the test specimens listed in Table 24. The experimental error bounds are associated with the accuracy of the collapse pressure measurements (±0.09 MPa).

or very close to, the experimental error bounds associated with the collapse pressure measurements.

It is convenient to assess the accuracy of a predictive model using metrics, such as those used in Chapter 4 [22] for comparing the test specimens to design formulae predictions, and in Chapter 2 [20] for comparing numerical and experimental collapse loads found in the literature. In those chapters a "modeling uncertainty factor", X_m, was calculated for each collapse prediction by dividing the experimental collapse pressure by the predicted value. The mean value of X_m for a group is called the bias, and is a measure of the ability of the model to, on average, correctly predict the collapse pressure. The coefficient of variation (COV) provides a measure of the scatter in the measured-predicted correlation, and is defined as the quotient of the standard deviation of X_m and the bias.

The bias and COV for various sets of standard SubSAS/VAST and CylMesh/ANSYS models are reported in Table 29. The bias for the entire set of test specimens indicates that VAST and ANSYS have over-predicted the collapse pressures by, on average, less than 2% and 4%, respectively. The subsets of data in Table 29 for the intact and corroded cylinders confirm that both VAST and ANSYS were more successful at predicting the collapse pressure for corroded models.

Table 29: Accuracy of FE collapse pressure predictions using SubSAS/VAST and CylMesh/ANSYS with the standard modeling and analysis procedures.

Sample	**n[a]**	**Bias**	**COV**	**95% prediction interval for X_m[b]**	**Accuracy with 95% confidence**
SubSAS/VAST FE Models					
All specimens	22	0.983	4.3%	$0.893 \le X_{m,n+1} \le 1.074$	10.7%
Intact specimens	8	0.970	5.4%	$0.839 \le X_{m,n+1} \le 1.100$	16.1%
Corroded specimens	12	0.992	3.8%	$0.905 \le X_{m,n+1} \le 1.078$	9.5%
Interframe collapse	4	1.035	3.7%	$0.900 \le X_{m,n+1} \le 1.169$	16.9%
Overall collapse	16	0.970	3.7%	$0.891 \le X_{m,n+1} \le 1.049$	10.9%
CylMesh/ANSYS FE Models					
All specimens	21	0.963	3.7%	$0.886 \le X_{m,n+1} \le 1.039$	11.4%
Intact specimens	8	0.951	5.0%	$0.831 \le X_{m,n+1} \le 1.071$	16.9%
Corroded specimens	12	0.966	2.4%	$0.913 \le X_{m,n+1} \le 1.019$	8.7%
Interframe collapse	4	0.994	3.6%	$0.866 \le X_{m,n+1} \le 1.123$	13.4%
Overall collapse	16	0.951	3.1%	$0.886 \le X_{m,n+1} \le 1.017$	11.4%

[a] n is the sample size, i.e., number of experimental-numerical comparisons.

[b] The prediction interval for a future value of X_m for 95% confidence, based on Eq. (1), p. 17.

The statistical data in Table 6 can be used to derive the overall accuracy of the predictive models. The accuracy is defined by a prediction interval, which gives the range within which a future value of X_m is expected for a given confidence level. Prediction intervals are determined using a t-distribution for populations with a normal distribution where the mean and standard deviation can only be estimated from a finite sample. The t-distribution has the same form as the normal distribution, but with heavier tails to account for the uncertainty of using a finite sample. The prediction interval, with a $100(1-\alpha)\%$ confidence level, for a single future experimental-numerical comparison, $X_{m,n+1}$, is given by Eq. (1), p. 17 [40].

Eq. (1) is valid for a sample of X_m from a normal distribution with sample size, n, bias, $\bar{x}$ and standard deviation, s. α is the area, representing probability, under the tails of the t-distribution. If, for example, the 95% prediction interval is bounded by $0.90 \le X_{m,n+1} \le 1.12$, it would be said that the predictive method is accurate to 12% with 95% confidence. Histograms and probability plots for some of the models presented here show that the distribution of X_m is approximately normal [20].

The 95% prediction intervals for the SubSAS/VAST and CylMesh/ANSYS analyses are given in Table 29. Those data indicate that, based on all of the simulations, the standard SubSAS/VAST and CylMesh/ANSYS models are accurate to 10.7% and 11.4%, respectively, with 95% confidence. Those values are comparable to the 9% accuracy that was estimated for high-fidelity shell models in Chapter 2 [20]. The accuracies are somewhat better for the corroded subset, at 9.5% and 8.7% for VAST and ANSYS, respectively; they are significantly worse for the intact models, at approximately 16% and 17% for VAST and ANSYS, respectively. The better performance of the FE models for corroded cylinders is consistent with comparisons of the predicted and measured nonlinear behaviour, and with the biases and COVs discussed earlier. It is likely that the relatively poor performance of the FE models for intact cylinders is exaggerated due to the near-perfect circularity of the test specimens. Real pressure hulls have out-of-circularity amplitudes on the order of the corrosion thinning considered here, so that a similar level of accuracy can be expected.

Comparison of finite element methods and solvers

For a given test specimen, the standard SubSAS/VAST and CylMesh/ANSYS models (Table 27) gave collapse pressures that agreed with each within approximately 7.5%, and all but two cases agreed within 5%. In all but three cases, the CylMesh/ANSYS models predicted a higher collapse pressure than the SubSAS/VAST models, resulting in the smaller bias for the ANSYS models in Table 29. The data in Table 29 also show that the bias of the SubSAS/VAST group is closer to unity than the CylMesh/ANSYS group, but that the scatter in the ANSYS predictions, as represented by the COV, is less than that of the VAST models. So, while the SubSAS/VAST methodology results in, on average, better collapse predictions compared to the experiments, the CylMesh/ANSYS approach is more consistent. Those factors tended to balance out in the final assessment of accuracy, which was similar for both sets of models (see Table 29).

The ANSYS, VAST and MARC FE solvers predicted similar collapse modes and load-displacement responses for geometrically identical SubSAS generated FE models. The collapse pressures predicted by ANSYS and MARC agreed with the VAST predictions within 2.1% and 2.8%, respectively (Table 28). This implies that solver-specific element formulations and solution algorithms account for a certain portion of the 5-7.5% difference between SubSAS/VAST and CylMesh/ANSYS predictions. The remaining discrepancies are due to the different modeling methodologies, such as the imperfection mapping and boundary conditions.

Prediction of the effects of corrosion damage

The collapse pressures predicted using CylMesh/ANSYS with and without the shell offset feature are listed in Table 27. Except for a single case (L300-N04), neglecting the shell eccentricity at the corrosion patch caused the predicted collapse pressures to be greater than the corresponding values with the eccentricity modeled, and furthermore, caused the error in the collapse prediction to be increased with respect to the experimental value. The discrepancy in collapse pressures predicted with models with and without the shell offset tended to increase with increasing depths of corrosion, up to a maximum difference of approximately 5.4%. Models failing by overall collapse were more sensitive to the shell offset modeling than models failing by interframe collapse. This is due to the previously mentioned reserve strength in the heavy stiffeners in interframe models, and the correspondingly lesser sensitivity to corrosion damage in general.

The statistical methods described above were applied to the CylMesh/ANSYS collapse predictions for test specimens with corrosion. The accuracy is 8.7% with 95% confidence when eccentricity is included (see Table 29) and 12.3% with 95% confidence when eccentricity is neglected. This emphasizes the importance of accounting for the shell eccentricity when assessing corrosion thinning.

When experimental results are not available, an assessment of corrosion damage is often made by comparing a damaged model to an intact model, so that numerical models must be accurate for both cases. The effect of corrosion damage was characterized in Chapter 4 [22] by comparing the collapse pressures for similar intact and corroded test specimens, and plotting the corresponding percent reductions in collapse pressures versus the percent corrosion thinning. That plot is reproduced in Figure 73, with the addition of collapse pressure reductions derived by comparing FE models instead of experimental results. It should be noted that Figure 73 contains data derived from models that failed by overall collapse only.

Figure 73 shows that the numerical models have captured the general trend of decreasing cylinder strength with increasing levels of thinning. Least squares linear regression of the experimental, SubSAS/VAST and CylMesh/ANSYS data yields lines with slopes of 0.995, 1.37, and 1.31, respectively. This indicates that the test data predict a roughly one-to-one correlation between the level of thinning and the reduction in collapse pressure. The numerically-derived curves are more conservative, predicting more severe strength reductions for a given level of thinning. That results from the more prevalent over-prediction of the collapse pressures for intact models compared to corroded models.

Finite element versus design formulae predictions

Contemporary submarine design procedures require the interframe and overall collapse pressures to be calculated separately. For example, in the submarine design manual in [5], interframe collapse pressures are based on a design curve that accounts for interaction between elastic buckling and shell yielding by applying an empirically-derived "knock-down factor" to the classical von Mises elastic shell buckling pressure. The design curve in [5] is fit to the mean of the experimental-analytical comparisons. Overall collapse pressures in [5] are based on a nonlinear elasto-plastic finite difference method [8], which accounts for the influence of out-of-circularity and residual stresses due to cold rolling.

The accuracy of the interframe design curve from [5] and the finite difference method for overall collapse were estimated in Chapter 2 [20] to be 20% and 17%, respectively, with 95% confidence. Those accuracies are based on comparisons with intact test specimens. The accuracy of the finite element predictions for intact models in the current chapter is similar, at 16-

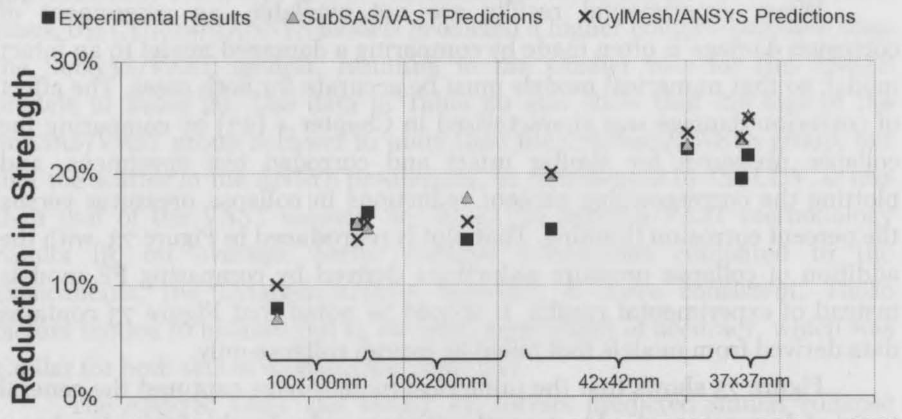

Figure 73: Relationship between cylinder collapse strength and shell thinning for specimens with light, internal ring-stiffeners and failing by overall collapse, as predicted by the experiments and FE models. The patch sizes are shown at the bottom of the chart by specifying the circumferential and axial extents.

17% with the same level of confidence. A modified version of the finite difference method for overall collapse [42] that allows the circumferential extent of corrosion thinning, as well as the associated shell eccentricity, to be included explicitly in the model, was found to be accurate within approximately 60% with 95% confidence [20]. That accuracy may be overly pessimistic due to the influence of two outliers in the experimental-analytical comparisons. When those data are neglected, the accuracy improves to 26% with 95% confidence. Nonetheless, the numerical models for corroded cylinders in the current chapter are significantly more accurate, at approximately 9%.

The numerical models were able to predict interframe and overall collapse pressures for models in this study within 17% and 11%, respectively, with 95% confidence (see Table 29). Some of the test specimens described herein were used in Chapter 2 [20] to derive the value of 17% for the accuracy of the finite difference method for overall collapse of intact hulls, so that result is directly applicable to the current context. The interframe empirical curve in [5] was found to under-predict the experimental collapse pressures for the models in this chapter that failed in that mode by approximately 45%, on average [22]. The empirical curve was built up from experimental data for cylinders with up to 0.5% OOC and residual stresses due to fabrication. Furthermore, corrosion damage was accounted for by using the minimum shell thickness or flange width with the design curve. These factors led to the pessimistic empirical strength predictions for these cylinders, which have small magnitudes of OOC and residual stresses, and a finite region of corrosion.

Conclusions

The standard FE modeling and analysis methods used in this study have been shown to predict the experimental collapse pressures and failure modes of pressure hulls having a variety of structural configurations, failure modes, imperfections, corrosion damage and reinforced penetrations, with an accuracy of approximately 11% with 95% confidence. By comparison, the conventional design methods are accurate to within 20% for intact models, and 26% for models with corrosion damage, with the same level of confidence.

The standard FE models were found to be more accurate at predicting the collapse strength of corroded models than for intact models, and it was shown that it is necessary to model the shell eccentricity at corrosion patches in order to achieve a high level of accuracy. Furthermore, because the FE models, on average, over-predict the collapse pressure of intact models to a greater extent than for corroded models, the FE methods are conservative at predicting the net reduction in collapse pressure due to corrosion damage.

FE models generated using different pre-processing tools and methods, and solved using different programs, resulted in similar accuracies. Neither analyst-dependent modeling choices, such as boundary condition selection, imperfection mapping and mesh structure, nor solver-dependent variables like element formulation and solution algorithms, significantly affected the accuracy of the collapse predictions. Identical models analyzed with the VAST, ANSYS and MARC FE solvers, give agreement within 2.8% of each other. The selection of a model generator and solver may therefore be viewed as producing a small perturbation to a numerical methodology that is common to all models. It is the overall methodology for which credibility is established when looking at the similarity of the numerical results. The similarity in results among different model generators and solvers should therefore not be interpreted as giving the analyst license to deviate from the established methodology.

The test specimens used in the current study were intentionally built to have small imperfections and residual stresses in order to be able to study the effects of corrosion damage in isolation from other strength-reducing factors. It is acknowledged that those factors play an important role in the collapse of real pressure hulls, and require a more complicated numerical model, especially for capturing the effects of residual stresses. Further work is required to validate the FE methods described here against more realistic test specimens before those methods can be used directly in pressure hull design procedures. That being said, similar numerical methods were used in [48,49] to predict the collapse pressures of cold formed and welded pressure hull test specimens, resulting in a similar level of accuracy for collapse predictions.

Chapter 8

Development of a numerical design framework and partial safety factor for pressure hulls

A framework for the design of submarine pressure hulls using nonlinear finite element (FE) analysis is presented in order to improve upon the conventional analytical-empirical design procedure. A numerical methodology is established that allows the collapse pressure of a hull to be predicted with controlled accuracy. The methodology is characterized by quasi-static incremental analysis, including material and geometric nonlinearities, of FE models constructed from shell elements. The numerical methodology is used with ANSYS to predict the results of 47 collapse experiments on small-scale ring-stiffened cylinders representative of submarine hulls. A probabilistic analysis is applied to the experimental-numerical comparisons in order to estimate the accuracy of the FE methodology and derive a partial safety factor (PSF) for design. It is demonstrated that a high level of accuracy, within 10% with 95% confidence, can be achieved if the prescribed FE methodology is followed. Furthermore, it is shown that the PSF for design does not need to be very large, even if a high degree of statistical confidence is built in. The designer can be 99.5% confident that the FE error has been accounted for by dividing the predicted collapse pressure by a PSF=1.134. This chapter is based on the manuscript of a paper co-authored with Fred van Keulen. The paper has been submitted to *Finite Elements in Analysis and Design* [26].

Introduction

This chapter is concerned with the design of naval submarine pressure hulls using nonlinear finite element (FE) analysis. The pressure hull is the main "watertight" structural component of a submarine that houses personnel, propulsion machinery, weapons and sensor systems, and other sensitive equipment. Pressure hulls are designed to withstand the hydrostatic load associated with diving to depths usually measured in the hundreds of meters [4]. Typical pressure hull designs resist those loads using ring-stiffened axisymmetric shells fabricated by cold rolling and welding high-strength steel plates and T-section frames. The mainly compressive stress field under pressure loading, combined with shell-like geometry, leads to a thin-walled structure that is limited by structural instability. The role of the ring-stiffeners is to prevent buckling from occurring before the onset of yielding in the hull plating. The structural capacity of a pressure hull is therefore governed by elasto-plastic collapse, which improves its structural efficiency compared to one failing by elastic buckling.

The conventional submarine design procedure, which is described in the next section, relies on correcting the short-comings of analytical and numerical models using empirical methods, correction factors and pessimistic idealizations of the actual hull geometry. The analytical simplifications, and the inherent scatter associated with experiment results, result in collapse predictions that are only moderately accurate. For example, the empirical design curve used to predict the collapse strength of the hull plating between frames is accurate to within approximately 20%, with 95% confidence [20]. A simple finite difference method that is used to calculate the overall collapse strength of an entire pressure hull compartment is accurate to within 17% with the same level of confidence [20]. Those estimates are based on comparisons with uniformly ring-stiffened test cylinders; larger errors are expected when assessing the complicated geometry of real hulls.

The net result of the modest accuracy and pessimistic modeling assumptions associated with the standard design methodology is a layered conservatism. The current chapter aims to remove some of that conservatism by presenting an approach to pressure hull design that is based on nonlinear finite element collapse predictions. FE analysis can overcome the difficulties associated with modeling complex geometry and structural behaviour. FE models also allow all failure modes, and the interaction between modes, to be considered in one analysis. Furthermore, some initial estimates [20,25,49] suggest that typical FE collapse predictions for pressure hulls are more accurate, within approximately 9-11% with 95% confidence, than the standard design methods. Finally, FE analysis allows the structural capacity of in-service hulls, with known levels of out-of-circularity and other defects or damage, to be more realistically assessed.

There is resistance within the submarine design community to using nonlinear FE collapse predictions. The reluctance is mainly related to two justifiable concerns [5,19]. First of all, until recently [20,25,49], adequate benchmarking of FE predictions against experiments has not been available. Experimental-FE comparisons are needed in order to assess the predictive accuracy of the numerical method; this in turn is required to specify a partial safety factor (PSF) that could then be used in the design of pressure hulls to account for predictive errors. The other concern is related to the analyst-dependent nature of the FE prediction. What makes the FE method a powerful tool is the large range of geometries, materials, loadings and responses that can be modeled. The drawback is that the analyst is required to make choices about each of those aspects of the model, and the correct choice is not always obvious. Two analysts addressing the same problem may come up with different, but equally justifiable results. This second concern is intertwined with the first, since the preferred methodology of the two analysts may lead to different accuracies when compared to test results. Conventional analytical-empirical design methods are also analyst-dependent to a certain extent; however, most of the critical factors, such as boundary conditions, loading, and imperfections, are "hard-wired" into the design equations, so there is less room for error compared to numerical modeling.

The goal of the current chapter is to address both of the above-mentioned concerns, by first setting out a standard FE methodology for producing collapse predictions with a controlled accuracy, and then quantifying the accuracy of that procedure by comparing FE collapse predictions with test results. Those data are then used to develop a PSF for nonlinear FE collapse predictions. It is not within the scope of the current study to define a complete and detailed FE design procedure. Instead, a general FE design framework or philosophy is proposed, and areas requiring more research are identified.

The standard FE methodology used in the current study was developed in Chapter 2 [20] by surveying the literature in order to identify common numerical strategies for predicting the strength of pressure hulls and other buckling-critical shells. The goal was to identify well-established and reliable numerical methods that would be readily available to the submarine designer in commercial FE software packages. The numerical methodology was then refined in Chapter 7 [25] by comparing FE collapse predictions to test results from Chapter 4 [22] for small-scale ring-stiffened cylinders. Of course, the practical modeling experiences of the authors of [25] also influenced the development of the FE methodology.

The modeling study in Chapter 7 [25] involved the use of two different pre-processors and three different FE solvers. The accuracy of the collapse predictions was not found to be very sensitive to using different combinations of those programs, as long as the general methodology was the same. For example, the accuracy of FE models generated using an in-house pre-processing program called CylMesh and analyzed using ANSYS 11.0 [143] was found to be 11.4% with 95% confidence. Predictions based on FE models generated using a submarine structural modeling program called SubSAS [146] and solved using the VAST FE solver [144] were accurate to within 10.7% with the same level of confidence. The current chapter is based on analyses using CylMesh and ANSYS, mainly because validation of a commercially available FE code is of more general interest compared to the SubSAS/VAST software, which is submarine-specific and not widely available. Furthermore, the pre-processing functions performed by CylMesh can be implemented in any general FE pre-processor.

Benchmark test results are based on previous work reported in [22-24,32]. The benchmark data include results for the 21 specimens from Chapter 4 [22] that were used in the FE modeling study in Chapter 7 [25], as well as 26 additional small-scale ring-stiffened aluminium cylinders from Chapter 5 [23], Chapter 6 [24], and additional tests reported in [32]. All of the specimens were tested to collapse under external hydrostatic pressure. Some of the specimens had artificial corrosion defects that simulated real corrosion damage found on in-service hulls. By considering both "intact" and corroded test specimens, the experimental program allowed FE models to be validated for both design-stage and through-life submarine assessments. The design geometry of the test cylinders and photographs of some typical specimens are shown in Figure 27 (p. 82) and Figure 74, respectively. FE simulations of the tests presented in Chapter 4 [22] are reported in Chapter 7 [25]; collapse predictions from the remaining specimens from [23,24,32] are presented in the current chapter.

To the extent possible, the current FE accuracy assessment follows the verification and validation (V&V) procedure proposed by the American Society of Mechanical Engineers for general solid and structural mechanics problems [36]. V&V aims to establish credibility in a numerical model by comparing numerical predictions to benchmark experimental results. A statistical analysis is applied to the experimental-numerical comparisons in order to quantify the accuracy of the FE models. In the present work, the statistical approach is extended to the derivation of the FE PSF; however, that is not the only conceivable approach. Nonlinear FE simulations of pressure hull collapse tests were presented by Graham in [49], where it was suggested that the PSF should be taken as unity plus the maximum relative error for all of the FE predictions. In that paper, the maximum difference between the FE predictions and test results was 8.5%, leading Graham to

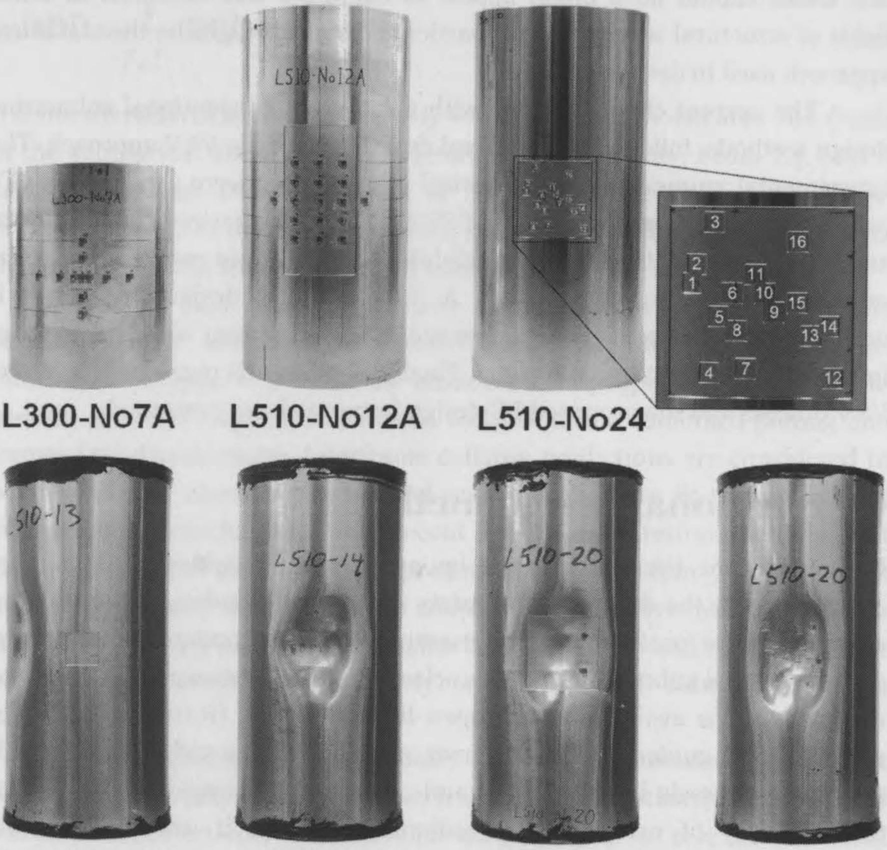

L300-No7A L510-No12A L510-No24

L510-No13 L510-No14 L510-No20 L510-No21

Figure 74: Photographs of typical validation test specimens. Clockwise from the top left: L300-No7A and L510-No12A, as-machined F28 cylinders with Patch A and D corrosion, respectively, shown before collapse testing; L510-No24, an as-machined T6 cylinder with Pitting B damage, shown before collapse testing; L510-No21, with Pitting A damage, after the collapse test; L510-No20 and L510-No14, with Patch C and B corrosion, respectively, in-phase with large-amplitude OOC, shown after testing; L510-No13, with out-of-phase Patch B corrosion, shown after testing.

suggest a PSF of 1.085. The merits of a statistics based PSF, compared with the lower bound approach taken in [49], are discussed in this chapter.

While the main goal of the current chapter, and this thesis in general, is to present a path to modernize submarine design philosophy and methodology, it can also be viewed as a case study for a numerical V&V procedure that has been carried out from beginning to end. In that respect, this thesis should have broad appeal to engineers and scientists in other fields of structural mechanics. Of particular interest might be the statistical approach used to derive the PSF.

The current chapter begins with a review of conventional submarine design methods, followed by a general description of the V&V approach. The experimental, numerical, and statistical methods that were used in the V&V process and the development of a PSF are then summarized. Experimental and numerical results supporting validation activities are compared, and the numerical accuracy is quantified. A finite element design framework is outlined, including a PSF and suggested rules for dealing with design-stage imperfections and material models. Finally, conclusions regarding the entire V&V process and the proposed FE design framework are presented.

Conventional design methods

In some nations, the submarine design procedure is classified, while in other countries, only the design partial safety factors and the design of individual submarines are confidential. For example, the UK standard for structural design of naval submarines [5] is unclassified, likely because it is based on research that is available in the open literature, e.g., [8,10,11,15,154]. The same research guided the development of civilian design codes for externally pressurized vessels in the UK [6] and continental Europe [7]. Despite the inaccessibility of many national submarine codes, it can be said that something like a standard or conventional design practice has evolved. By way of example, the following paragraphs describe, in broad strokes, the pressure hull design methodology prescribed by the UK naval standard in [5].

The deep diving depth (DDD) of a submarine is the standard characterization of its safe structural capacity and operational limit. The design of a pressure hull must ensure that its structural resistance exceeds the applied hydrostatic loading. Loading is characterized by DDD, multiplied by a partial safety factor (PSF), γ_D, that accounts for the risk of errors in depth measurement and manoeuvring. Hull resistance is defined by the design collapse depth (DCD) divided by PSFs γ_c and γ_i, which account for uncertainty related to hull fabrication (i.e., plate misalignments, undersized sections, low-quality welds, *etc.*) and modeling (i.e., systematic and random errors in the predictive model), respectively. The notation for those PSFs is adopted from [5]. DCD is the depth associated with the predicted collapse pressure, P_c, so that

$$\gamma_D \mathrm{DDD} \leq \frac{1}{\gamma_c \gamma_i} \mathrm{DCD} = \frac{1}{\gamma_c \gamma_i} \frac{P_c}{\rho g}. \tag{19}$$

ρ is the characteristic seawater density within the operational area and depth of the submarine, and g is the acceleration due to gravity. From Eq. (19) it can be seen that DDD is arrived at by dividing the predicted collapse pressure by a series of PSFs, and then converting to diving depth by dividing the pressure by the specific weight of seawater.

Pressure hulls have traditionally been designed to fail by inelastic buckling of the hull plating between frames, which is referred to as interframe collapse. It is relatively economical to proportion the frames to prevent sideways tripping and overall collapse of the combined plating and frames [11]. Furthermore, interframe collapse predictions are considered to be very reliable since they are based on a design curve fit to hundreds of laboratory test results [10]. More recent designs are interframe critical, but the interframe and overall collapse pressures are kept within 5 or 10%, which improves efficiency but brings forth concerns about failure mode interaction [15]. The following paragraphs describe how interframe and overall collapse pressures are predicted (separately) using the UK submarine design standard in [5].

Shell buckling is a notoriously difficult phenomenon to predict accurately, especially when factors such as material plasticity, geometric and material imperfections, and residual stresses play a role in the shell behaviour [155,156]. To get around those problems, pressure hulls are designed using a combination of analytical, empirical and numerical methods. Interframe collapse is predicted using an empirical design curve that accounts for the reduction in the classical elastic buckling pressure due to plasticity and imperfections. Figure 3 (p. 5) shows the mean design curve used in [5] along with some of the test data from [10] that were used in its development. The lower bound curve in Figure 3 is used with the civilian codes in [6,7] with a different set of safety factors.

The naval standard in [5] requires overall collapse to be predicted using a nonlinear finite difference (FD) model that predicts the elasto-plastic collapse pressure of a single ring-stiffener and one frame-bay of attached plating [8]. With the civilian codes in [6,7], the overall collapse pressure is based on a simple analytical equation that predicts the onset of yielding in the frame flange. The FD approach allows DDD to be based on the ultimate collapse strength, rather than a first-yield criterion.

The FD discretization is applied about the ring-frame circumference, so that out-of-circularity (OOC) imperfections and the destabilizing effect they have on hull strength can be modeled. The ring-frame cross-section is divided into a series of strips for stress calculations in order to track the progression of yielding as the load is applied. The analysis proceeds by incrementally applying the pressure load and iteratively solving the governing equations, which are based on beam theory, at each load step. The predicted collapse load is taken as the final load increment whereby convergence of the solution is achieved. Correction factors are applied to the solution to account for finite compartment length, interframe deformation of the hull, and failure mode interaction with interframe collapse. The overall collapse pressure used for design is taken as the minimum value for a series of analyses covering a range of simple sinusoidal OOC shapes.

The predictive models for interframe and overall collapse are based on uniformly ring-stiffened cylinders. Since the underlying shell and beam theories are complex, it is impractical to extend the models to complicated geometries without resorting to more sophisticated numerical models (which is, of course, the topic of the current thesis). To account for that, the conventional design procedure requires a single pressure hull compartment, which may consist of a combination of cylinders and cones with various ring-stiffener geometries and spacings, to be idealized as a uniformly ring-stiffened cylinder using the most pessimistic geometry, e.g., the largest frame spacing and hull radius. The conventional methods use simplistic out-of-circularity shapes that may be suitable for design calculations, but that are not representative of the complex shape of real life geometric imperfections. Furthermore, the conventional methods cannot adequately model structural damage due to denting or corrosion. OOC and damage must be accurately modeled when a realistic assessment of an in-service submarine is required.

V&V approach

The current V&V program is aimed at investigating the accuracy of FE predictions for the elasto-plastic collapse of submarine pressure hulls under hydrostatic pressure associated with diving. The study is further concentrated by considering only ring-stiffened cylinders, since they constitute the basic "building blocks" of a pressure hull. In later sections, it will be shown how the loading, geometry and failure modes of pressure hulls were considered when choosing the experimental and numerical methodologies, respectively.

The two components of V&V, verification and validation, are not synonymous. Verification involves ensuring a correct numerical implementation of the underlying physical-mathematical model, whereas validation yields a quantitative assessment of the numerical model accuracy.

Verification studies for the current V&V program are presented in [157]. They are not reported in detail here since the most interesting aspect of V&V is validation. Verification primarily entails checking for errors in the numerical code, and so most of the responsibility for verification lies with the software developer. Nonetheless, the numerical software was indirectly verified in the current study by comparing FE results to classical analytical solutions for elastic buckling of cylindrical shells and ring-stiffened cylinders, as well as the finite difference solution for the elasto-plastic collapse of a ring-frame that was described earlier. CylMesh/ANSYS FE predictions for 140 cylinders and ring-frames were found to be within 8%, on average, of the benchmark analytical or numerical solutions. The FE error was attributed to unavoidable differences between the numerical and benchmark models, rather than problems with the FE software, so that verification was considered to have been achieved.

Verification also involved performing convergence studies on the mesh density for each unique test specimen configuration, as well as for the load increment size. The effect of convergence tolerances within the iterative solution on the collapse prediction was also investigated. The outcomes of those activities were incorporated in the standard numerical methodology described in Section "Numerical methods" on p. 210.

Validation was achieved by comparing FE predictions with test results, and using probabilistic analysis to quantify the accuracy of the FE models. The primary response of interest is the collapse pressure. It was used to characterize the accuracy of a given FE model via the modeling uncertainty factor,

$$X_m = \frac{P_{c,exp}}{P_{c,FE}} \tag{20}$$

where $P_{c,exp}$ and $P_{c,FE}$ are the measured and predicted collapse pressures, respectively. X_m is a standard way to measure the discrepancy between measured and predicted values for any quantity in a reliability analysis [16,37-39]. The probabilistic approach adopted here for quantifying the accuracy of the overall FE methodology based on a set of modeling uncertainty factors is given in Section "Statistical and probabilistic methods" on p. 213.

The main difference between the current V&V approach and the one that is suggested in [36] is related to how credibility is established in the numerical method. The guidelines in [36] suggest that test results should be withheld from the modeler in order to avoid intentional or unintentional tuning of the numerical model. That was impossible in the current context, since the author of this thesis led the experimental team and also performed the FE modeling. Pollution of the FE results by model tuning was avoided by directly applying the numerical methodology developed in Chapter 7 [25] to the validation experiments in Chapter 5 [23], Chapter 6 [24], and [32]. The experiments in Chapter 4 [22] are not considered part of the validation case, since they were used in the development of the FE methodology. The modeling rules prescribe all aspects of the FE prediction, including the geometric modeling, mesh density, boundary conditions and loading, and material model, so there was no opportunity for model tuning.

Experimental methods

In addition to the test results themselves, the experiments provide input data with which to populate the validation numerical models. The input data consist of the general structural configuration of the test specimens, measured geometric imperfections, shell thicknesses and material properties, and information concerning the end-support and loading applied to the specimens. The remainder of this section describes those data, as well as how the tests were performed and the results collected. The experiments are described in greater detail in [22-24,32].

Specimen design

The goal of the validation experiments was to physically simulate the collapse of submarine pressure hulls under controlled laboratory conditions. Several failure modes, structural configurations, and geometric imperfections were considered, as well as the effects of structural damage due to hull corrosion. Corrosion damage was studied by applying artificial thinning to some of the specimens. In that way, the V&V study could be extended to include the types of damage assessments that are often required for in-service hulls. The 9 "intact" and 17 "corroded" validation specimens from [23,24,32] are listed in Table 30, along with any artificial corrosion damage, the type and magnitude of out-of-circularity, and material information. The "calibration" specimens from [22], which were used to develop the standard numerical procedure in Chapter 7, are not listed (see Table 24, p. 160).

Table 30: Descriptions of validation test specimens.

Specimen[a]	**Corrosion**[b]		**Out-of-Circularity**[c]		**Material**[d]	
	Type	δ_c	**Shape/Method**	e_{max}/a	**Grade**	σ_y **(MPa)**
L300-No05A	Intact	N/A	As-machined/CMM	0.09%	F28	171
L300-No06A	Intact	N/A	As-machined/CMM	0.12%	F28	182
L300-No07A	Patch A	26.9%	As-machined/CMM	0.09%	F28	225
L300-No08A	Patch A	24.3%	As-machined/CMM	0.14%	F28	188
L510-No06A	Intact	N/A	As-machined/CMM	0.08%	F28	238
L510-No08A	Patch B	21.8%	As-machined/CMM	0.04%	F28	172
L510-No010A	Patch C	16.1%	As-machined/CMM	0.04%	F28	224
L510-No012A	Patch D	19.6%	As-machined/CMM	0.04%	F28	221
L510-No13	Patch B*	21.2%	m=1, n=3/Laser	0.71%	T6	328
L510-No14	Patch B	23.9%	m=1, n=3/Laser	0.67%	T6	334
L510-No17	Intact	N/A	m=1, n=3/CMM	0.39%	T6	306
L510-No18	Intact	N/A	m=1, n=3/CMM	0.41%	T6	305
L510-No19	Patch C	17.4%	m=1, n=3/Laser	0.77%	T6	329
L510-No20	Patch C	18.6%	m=1, n=3/Laser	0.67%	T6	325
L510-No21	Pitting A	14.4%	As-machined/Laser	0.06%	T6	337
L510-No22	Pitting A	16.2%	As-machined/Laser	0.07%	T6	331
L510-No23	Pitting B	24.1%	As-machined/Laser	0.07%	T6	326
L510-No24	Pitting B	26.5%	As-machined/Laser	0.05%	T6	340
L510-No25	Intact	N/A	m=1, n=3/CMM	0.75%	T6	305
L510-No26	Intact	N/A	m=1, n=3/CMM	0.94%	T6	310
L510-No33	Intact	N/A	m=1, n=3/CMM	0.92%	T6	301
L510-No34	Intact	N/A	m=2, n=3/CMM	0.45%	T6	301
L510-No35	Patch B	19.0%	m=1, n=3/Laser	0.79%	T6	332
L510-No36	Patch B*	24.6%	m=1, n=3/Laser	0.97%	T6	331
L510-No37	Patch E	24.3%	As-machined/CMM	0.06%	T6	305
L510-No38	Patch F	24.0%	As-machined/CMM	0.02%	F28	99

[a] The L510 and L300 series correspond with Configurations 1 and 2, respectively, as shown in Figure 27, p. 82.

[b] Corrosion cases are described in Table 31. An asterisk (*) denotes a corrosion patch that was aligned out-of-phase with large-amplitude OOC; otherwise, the corrosion damage was in-phase with OOC. Corrosion damage was randomly aligned with OOC for as-machined specimens. δ_c is the maximum measured percent corrosion thinning.

[c] m and n are the targeted number of half-waves over the length and complete waves about the circumference, respectively, for cylinders with mechanically applied OOC. OOC magnitude is given by the maximum measured radial eccentricity at the outer shell surface, e_{max}, divided by the nominal mid-plane shell radius, a=121.5 mm.

[d] All cylinders were machined from extruded aluminium tubes of the designated grades. σ_y is the average measured 0.2% yield stress in the circumferential direction.

Each test specimen was a T-section ring-stiffened cylinder machined from an extruded aluminium tube. Four different nominal axisymmetric geometries were used in the testing program, as shown in Figure 27 (p. 82). Configurations 1-3 were proportioned with relatively light ring-stiffeners and a thicker shell in order to promote failure by overall collapse. The large ring-stiffeners in Configuration 4, combined with a thinner shell, produced interframe collapse modes. The thick, tapered end-sections common to all configurations prevented undesired end-bay collapse, and allowed heavy steel end-caps to be bolted on to the cylinders before pressure testing. All four configurations were used in the calibration experiments in [22], while only Configurations 1 and 2 were used in the validation tests in [23,24,32].

The limitations of the machining process resulted in test specimens that were relatively stocky compared to real pressure hulls, but they share same the elasto-plastic collapse mode of failure. The main differences between the test cylinders and real hulls are related to scale and material. As with buckling of other shell structures, pressure hull collapse is sensitive to the relative slenderness of the structure rather than its absolute dimensions, and so dimensional scaling is not a concern [88]. Neither then is the small size of the test specimens. The test cylinders were machined from aluminium, which has a lower Young's modulus and yield stress than the high-strength steel typically used in hull construction. Nonetheless, in Chapter 5 [23] it was shown that the material response of the aluminium cylinders during collapse testing was qualitatively similar to high-strength steel hulls. The main difference between the test specimens and real hulls is that the latter have residual stresses, due to cold rolling and welding, that are not present in the machined test cylinders. The significance of that discrepancy is discussed later on in this chapter.

Artificial corrosion damage

The artificial corrosion cases that were applied to some of the validation specimens are described in Table 31. Table 30 indicates which type of damage was applied to a given cylinder. Some of the corrosion cases are shown in the photographs of test specimens in Figure 74. In most cases, general corrosion damage was introduced by machining away material from the outside of the shell in single rectangular patches of uniform depth (Patches A-D in Table 2). With L510-No37, shell material was removed from both the outside and inside of the shell (Patch E) in order to study the effect of removing the shell eccentricity that arises with the other cases of one-sided thinning. L510-No38 had three patches of general corrosion spaced at

120° increments around the outside of the shell (Patch F), which allowed the interaction of multiple corrosion patches to be studied.

Corrosion pitting followed by grinding was simulated on some cylinders by machining sixteen small patches, 20% of the stiffener spacing in breadth, in a randomly generated pattern (Pitting A, see L510-N021 in Figure 74). In some cases, the pitting damage was superimposed on an area of general corrosion (Pitting B, see L510-N024 in Figure 74). The calibration experiments in [22] considered Patches A-D, as well as ring-stiffener corrosion, which was simulated by locally reducing the flange width of two of the external ring-stiffeners (Configuration 3 in Figure 1).

Out-of-circularity and shell thickness

The out-of-circularity of each specimen was measured using either a coordinate measurement machine (CMM) or by placing the cylinders on a turntable and measuring the radial eccentricities at the outer shell surface using laser displacement gauges. Shell thickness was measured by taking

Table 31: Descriptions of nominal corrosion damage cases.

Corrosion	**Description**[a]
Intact	No corrosion damage
Patch A	Single 34×34×0.75 mm (25%) general corrosion patch outside shell
Patch B	Single 42×42×0.6 mm (20%) general corrosion patch outside shell
Patch C	Single 100×100×0.4 mm (13.3%) general corrosion patch outside shell
Patch D	Single 100×200×0.4 mm (13.3%) general corrosion patch outside shell
Patch E	Two 42×42×0.3 mm (10%) general corrosion patches collocated at the inside and outside of the shell, for a total of 20% thinning
Patch F	Three 42×42×0.6 mm (20%) general corrosion patches outside the shell, uniformly spaced about the circumference at 120° increments
Pitting A	Sixteen 10×10×0.4 mm (13.3%) randomly oriented corrosion pits
Pitting B	Sixteen 10×10×0.4 mm (13.3%) randomly oriented corrosion pits superimposed on a 100×100×0.3 mm (10%) general corrosion patch (23.3% total thinning at pits)

[a] Corrosion patch sizes are specified by the circumferential times the axial extents, times the depth. The nominal percentage thinning is shown in parentheses. General corrosion patches and groups of corrosion pits were centred at the mid-length of the cylinders.

inner and outer radial measurements with the CMM, or by using an ultrasonic thickness (UT) probe. OOC measurements were taken at 36 points about the cylinder circumference at each ring-stiffener and mid-bay location. Thickness measurements were taken on a similar grid, but at mid-bay locations only. The accuracies of the CMM, laser displacement gauges and UT probes are ±0.02 mm, ±0.001 mm and ±0.01 mm, respectively. All of the calibration specimens in [22] were measured using the CMM approach. The final pre-testing shape of each validation cylinder, along with measurement method used to characterize OOC, is specified in Table 30.

Most of the specimens were tested "as-machined", with only the OOC that arose from the machining process. The OOC of those specimens, taken as the maximum measured radial eccentricity, e_{max}, divided by the nominal mid-plane shell radius, a, was less than 0.15% in all cases (see Table 30). The as-machined imperfections were typically characterized by an oval shape with two complete waves about the circumference (n=2) [23,24,32]. The critical overall collapse mode of the L510 series of cylinders (Configuration 1 in Figure 27, p. 82) is associated with three circumferential buckling waves (n=3) [22]. Some of those cylinders were mechanically deformed in order to introduce OOC in the critical n=3 mode and at large amplitudes (between 0.4% and 1%). The interaction of OOC and corrosion damage was studied by deforming corroded specimens so that the corrosion patch was aligned with either an inward OOC lobe ("in-phase" corrosion) or an outward lobe ("out-of-phase" corrosion).

Material properties

The cylinders were machined from two different grades of aluminium alloy tubing: 6082-T6, which is subjected to a T6 heat treatment after extrusion, and 6082-F28, which is an identical alloy that has not been heat treated. Tensile coupon testing showed that both materials are anisotropic, with the yield stress in the axial direction approximately 10% greater than circumferential direction [22,23]. Three tensile coupons were machined from the thick end-section of each cylinder, in the critical circumferential direction, after collapse testing. The end-sections were not plastically deformed during pressure testing, so the tensile testing results are representative of the pre-testing material properties of each cylinder. The average 0.2% circumferential yield stress for each validation cylinder is given in Table 30. The heat treatment improved the strength and consistency of the material, as evidenced by the lower magnitudes and greater variability in yield stress for the F28 cylinders compared to the T6 specimens.

The average measured value of Young's modulus for specimens from Chapter 5 [23] and Chapter 6 [24] were 68 and 57 GPa, respectively. The result from [23], which includes all of the F28 cylinders except for L510-No38, is close to the typical text book value of 70 GPa [142]. The value from [24], which includes all but one of the T6 cylinders, is much lower than expected. Normally, two extensometers are attached to tensile coupons in order to allow unintentional bending stresses to be factored out of Young's modulus calculations. The small size and circular cross-section of the current test coupons allowed only a single extensometer to be used. Thus, it is likely that bending stresses account for the low moduli for the T6 cylinders. Those coupons were tested in a large group using the same test setup, which would explain the consistently low modulus. The F28 specimens were tested separately and may have been relatively free of bending stresses. Poisson's ratio was measured for the calibration specimens, which were machined from the T6 aluminium, and was found to be between 0.32 and 0.34 [22].

Testing procedures

Each validation cylinder was instrumented with approximately 70 strain gauges. A typical cylinder instrumentation plan included twelve uni-axial gauges equally spaced around each of the two central ring-stiffener flanges in the circumferential direction. Those gauges allowed overall collapse deformations to be estimated. Most cylinders also had a similar ring of bi-axial gauges mounted outside the shell between the central ring-stiffeners to track interframe deformations. Areas of corrosion were supplemented with additional gauges, as shown by the pre-testing photographs of L300-No7A and L510-No12A in Figure 74. The strain gauges are accurate to ±0.5% of the measured strain value.

The validation cylinders were tested in a pressure chamber using the so-called volume-control method, which has been shown to allow better control of specimen deformations than conventional air-backed testing, especially during collapse [21]. With the volume-control method, the specimen is filled with testing fluid (mineral oil was used here) and the internal cavity of the specimen is connected to the pressure chamber through a series of pipes and hoses. The system is initially pre-pressurized so that the pressures in the specimen and chamber are equal. The link between the specimen and chamber is then broken by closing a valve, and the specimen is loaded by releasing its internal testing fluid, which creates a pressure differential. Pressure transducers were used to measure the specimen and chamber pressures in order to derive the net pressure on the test specimen. The experimental collapse pressure was taken as the maximum recorded net pressure. The accuracy of the transducers, and thus the experimental collapse pressures, is ±0.09 MPa. Strain and pressure data were collected at a sampling rate of 100 Hz.

All of the cylinders except for L300-No8A were monotonically loaded to collapse. L300-No8A was cyclically loaded past its yield limit ten times before the collapse test was performed in order to determine if the plastic strains would grow indefinitely with constant-amplitude loading.

Numerical methods

The software used to generate and analyze the numerical models, as well as the underlying physical and mathematical models that are implemented in those programs, can be thought of as a numerical tool-kit. The numerical tool-kit is what is being validated, and from a different standpoint, it is the set of modeling rules that must be followed when using the PSF that will arise from the V&V process. The overall numerical strategy, as well as the methodology for specific aspects of the FE modeling, is described below. The reasons for choosing particular approaches over other possibilities (e.g., the choice of shell theory over solid mechanics) were discussed in Chapter 7 [25].

Overall numerical modeling strategy

Each FE model was generated using CylMesh and analyzed with ANSYS. The physical phenomena that were modeled were chosen based on their relevance for predicting pressure hull collapse pressures. The collapse of pressure hulls is associated with large displacements, structural instability and material plasticity [20]. As with other buckling-critical shells, inertia effects do not significantly affect the structural response until the onset of collapse [74-76]. Thus, the FE modeling procedures included material and geometric nonlinearities in a quasi-static analysis based on shell theory. Furthermore, it was assumed that fluid-structure interaction does not significantly affect the static hull response up to the collapse load; that phenomenon was therefore neglected.

Finite element mesh

Each FE mesh modeled the full extent of the test cylinder and consisted of 4-node finite strain shell elements (ANSYS element “SHELL181”) with four in-plane (full integration) and five through-thickness integration points. Meshes were composed of approximately square shell elements in a regular grid, so that the mesh density was uniform over the entire cylinder. A mesh convergence study was performed for each unique combination of axisymmetric geometry and corrosion damage. A converged mesh was defined as one whereby the associated collapse pressure was within 1% of the collapse pressure for a mesh with half the element density. In most cases, the actual mesh convergence was within less than 0.5%. A typical converged mesh was characterized by 288 elements about the circumference of the cylinder, 19 elements between frames, 4 elements through the depth of the stiffener web, and 4 elements across the breadth of the stiffener flange. An example mesh convergence study is presented in [157].

The artificial corrosion damage in some of the validation specimens required specialized modeling. The formulation of SHELL181 allows the shell element mid-plane to be arbitrarily located relative to the nodes. In intact regions, the shell mid-planes were collocated with the nodes. The shell mid-planes in the corroded region were offset to account for the eccentricity with respect to the mid-plane of elements in the adjacent intact region. The resulting shell offset was taken as half the depth of corrosion for cases of one-sided thinning, so that the inside surface of the intact and corroded shell elements were aligned. With the two-sided thinning in L510-N037, the corroded shell offset was based on the difference between the magnitude of outer and inner shell thinning. The shell offset feature was also used to model unintentional shell thinning that was applied at the inside of one of the 20 mm end-bays of L510-N08A through a mistake in the CNC machining [23] (see Chapter 5, Section "Measured geometry", p. 113).

Nonlinear maps of out-of-circularity imperfections and shell thicknesses were derived through two-dimensional Fourier series decompositions of the shape measurement data. The decompositions employed an iterative method to minimize the error introduced by numerical integration over non-uniformly spaced data. The iterative method is based on a similar approach that was presented in [152] for one-dimensional Fourier decompositions. The Fourier maps were applied to the nodal positions (OOC) and shell elements (thickness) of the initially shape-perfect FE models.

Material model

Stress-strain curves for FE analysis were generated by averaging the measured engineering curves for coupons taken from the circumferential direction of each test specimen. The FE material models for specimens from [24,32] were corrected for the artificially low measured Young's moduli. The correction involved subtracting the measured elastic strains, based on the measured value of Young's modulus, and replacing them with elastic strains based on a typical value of Young's modulus of 70 GPa. The resulting engineering curves were used to generate true stress-strain curves, which were implemented via multi-linear material models with isotropic von Mises yield surfaces. Kinematic hardening was used in order to capture the Bauschinger effect. Young's modulus was not modified for specimens from [23] since coupon test results are more reliable. Residual stresses and strain hardening that arose from mechanically introducing OOC in some of the test specimens were neglected.

Loading and boundary conditions

A uniform external pressure load was applied to the shell of each model, with equivalent edge pressures at the cylinder ends to represent the axial load transferred from the end caps. The end-caps, which included plugs that extended 20 mm inside the ends of the cylinders, were not explicitly modeled. Instead, the FE models were simply supported at the cylinder ends, where the end-caps were bolted, and at the furthest extent of the plugs, 20 mm from the ends of the cylinder. Those boundary conditions resulted in a "quasi-clamped" constraint whereby out-of-plane bending was prevented at the cylinder ends, while end-warping was allowed.

Solution procedures

Collapse pressures were predicted with ANSYS using nonlinear quasi-static analysis, including large displacements and material plasticity. Geometric nonlinearities were captured with an updated Lagrangian formulation in combination with a co-rotational system. Loads were applied incrementally, and the follower-force effect was accounted for by updating the direction of the pressure loads after each load increment. The solution at each increment was arrived at through a modified Newton-Raphson approach to iteratively balancing the internal and external forces. Convergence of the incremental solution was considered to be achieved if the L2, or Euclidean, norm of the residual force vector was less than the norm of the applied force vector times a specified tolerance. The verification study in [157] showed that a tolerance of 0.005 is more than sufficient to prevent drift of the nonlinear solution, and so that value was used for all validation analyses.

The arc-length method was used so that the analyses could be continued past limit points and into the post-collapse regions. Load application was controlled by specifying the initial load increment size for the arc-length method. After that, the arc-length method and an automatic time-stepping algorithm in ANSYS were used to control the load application. The arc-length was not permitted to increase beyond the initial value. Furthermore, the automatic time-stepping algorithm automatically reduced the arc-length if a converged solution could not be found at a given load increment. The verification study for the load increment size led to the use of an initial load increment of 0.25 MPa for all validation analyses [157]. The predicted collapse pressure was taken as the maximum limit point in the numerical load-displacement curve. The cyclic loading of L300-No8A before the collapse test was not simulated since it did not apparently affect the collapse pressure [23].

Statistical and probabilistic methods

The end result of the experimental and numerical modeling activities was a set of experimental-numerical comparisons, as quantified for each test specimen by the modeling uncertainty factor, X_m. The goal of typical V&V studies is to use those data to quantify the accuracy of the numerical model. The current study aims to take validation a step further, by using the same data to derive a PSF. Since X_m is the quotient of the measured and predicted collapse pressures, models with $X_m < 1$ have over-predicted the experimental collapse pressure and are unconservative. A PSF should be associated with some critical minimum value of X_m, called $(X_m)_{min}$, that represents the least conservative collapse prediction that can be reasonably expected. Once $(X_m)_{min}$ is determined, the PSF is simply taken as its inverse, i.e., $\mathrm{PSF}=1/(X_m)_{min}$.

A simple approach to determine $(X_m)_{min}$ is to assign it the value of the smallest X_m observation in the validation study. The lower bound approach is essentially what was proposed by Graham for the FE PSF in [49], as discussed in the introduction to this chapter. The problem with the lower bound approach is two-fold. On one hand, the PSF may be overly conservative if the smallest observed value of X_m happens to be an extreme outlier. On the other hand, the sample size may be too small to ensure that the minimum observed value of X_m represents a critical lower bound. In that case, the PSF may be insufficiently conservative. Unless some effort is devoted to studying those two possibilities, it cannot be said that the PSF is too conservative, or not conservative enough, or just right. Those types of descriptions are only possible with a probabilistic approach, whereby the confidence that a given PSF will ensure a safe design can be quantified based on the statistical data resulting from the V&V program. Of course, the adequacy of a given level of confidence is not a straightforward determination, but some ways to deal with that dilemma are discussed later on in this chapter. The remainder of this section is concerned with describing the statistical and probabilistic methodology that is used to quantify model accuracy in general, as well as the level of confidence associated with a PSF.

The first step in the probabilistic analysis is to generate the statistical data. The systematic error, or bias, associated with the numerical procedure indicates how the FE models, on average, over- or under-predict the collapse pressure. The statistical measure of bias is given by the mean value of X_m for the validation cases. The bias may also include some systematic error introduced by the experiments, e.g., error in the collapse pressure measurement. The random component of error, or scatter, in the FE predictions is indicative of how consistent the numerical methodology is over the range of parameters covered by the experiments. The random error also includes the small fraction of experimental uncertainty that cannot be removed by careful measurements before, during and after testing. The statistical measure of random error is the standard deviation of X_m. It is typically presented in a relative manner as the coefficient of variation, COV, taken as the standard deviation divided by the bias.

The bias and COV of a sample are independent of the way the data are distributed over the range of X_m; however, if the validation data are to be used to estimate, for example, the likelihood that a future experimental-numerical comparison will fall within a certain range of X_m, then the probability distribution of X_m must first be determined. Probability plots can show how well a particular sample conforms to an assumed distribution. A probability plot has the random variable on one axis, while the second axis is specially scaled based on the assumed distribution. If the sample data create an approximately straight line on the probability plot, then the assumed distribution is correct [40].

It will be shown in Section "Numerical accuracy assessment" (p. 222) that the X_m data from the validation study conform reasonably well to a normal distribution, and so the remainder of the current section is focused on probabilistic methods for normal distributions. Quantifying model accuracy involves making a prediction of the range of X_m within which it can be expected that a future experimental-numerical comparison will fall. If the true values of the mean and standard deviation of X_m were known, then a normal distribution could be used directly; however, the mean and standard deviation can only be estimated based on a finite sample. The uncertainty associated with that approximation is accounted for by using a *t*-distribution instead of the normal distribution. Those distributions are qualitatively similar, but the *t*-distribution has heavier tails to account for the uncertainty of using a finite sample size.

The overall accuracy of the numerical method is quantified via a prediction interval for X_m, which estimates the range in which a future value, $X_{m,n+1}$, will occur based on a given level of confidence. Such a prediction interval is defined as

$$\overline{X_m} - t_{\alpha/2,n-1} s\sqrt{1+1/n} \le X_{m,n+1} \le \overline{X_m} + t_{\alpha/2,n-1} s\sqrt{1+1/n} \qquad (21)$$

where $\overline{X_m}$ is the sample bias, s is the sample standard deviation, and $t_{\alpha/2,n-1}$ is the t-test statistic for a confidence level of $100(1-\alpha)\%$ and a sample size, n [40]. The accuracy is simply taken as the absolute maximum value of $1-X_{m,n+1}$. For example, a set of experimental-numerical comparisons characterized by the prediction interval $0.85 \le X_{m,n+1} \le 1.20$, for $\alpha=0.05$, indicates that the numerical model is accurate to within 20% with 95% confidence.

A similar prediction interval can be used to estimate the value of $(X_m)_{min}$ for the derivation of the PSF. In that case, $(X_m)_{min}$ is based on a one-sided, lower-bound prediction interval, such that

$$X_{m,n+1} \ge \overline{X_m} - t_{\alpha,n-1} s\sqrt{1+1/n} = \left(X_m\right)_{min} \qquad (22)$$

with $100(1-\alpha)\%$ confidence [40]. Note that the t-test statistic in Eq. (21) is associated with $\alpha/2$ since the prediction interval is two-sided, whereas it is based on α for the one-sided interval in Eq. (22).

Validation results

The results of the validation experiments are reported in detail in [23,24,32]. A specimen-by-specimen description will not be presented here. Instead, the experimental results and numerical predictions, including pressure-strain curves and collapse modes, will be compared for a few typical specimens. A summary of all of the validation results is then presented, followed by an assessment of the numerical accuracy using the probabilistic methodology described above.

Typical experimental-numerical comparisons

Figure 75 shows measured and predicted pressure-strain curves for the as-machined, intact cylinder L300-No6A, which was machined from low yield strength aluminium alloy. A photograph of the specimen after testing and the final deformed shape of the FE mesh at the end of the analysis are also shown in the figure. The experimental and numerical collapse modes are similar, with large deformation of the shell in the central bay, as well as the adjacent ring-stiffeners. The area of overall collapse covers a larger area in the test specimen compared to the FE model, and the centres of the experimental and numerical collapse lobes are offset by approximately 20°.

The pressure-strain plots in Figure 75 are associated with axial and circumferential strains measured (or predicted) at the outside of the shell in the central bay, at the centre of the experimental collapse lobe. The measured and predicted responses are nearly identical in the initial linear region of the curves. Thereafter, the nonlinear response associated with plasticity and large displacements is less pronounced in the FE model, which leads to an approximately 2% over-prediction of the experimental collapse pressure.

L510-No18 is a typical intact cylinder with mechanically introduced OOC. The measured and predicted collapse shapes and pressure-strain

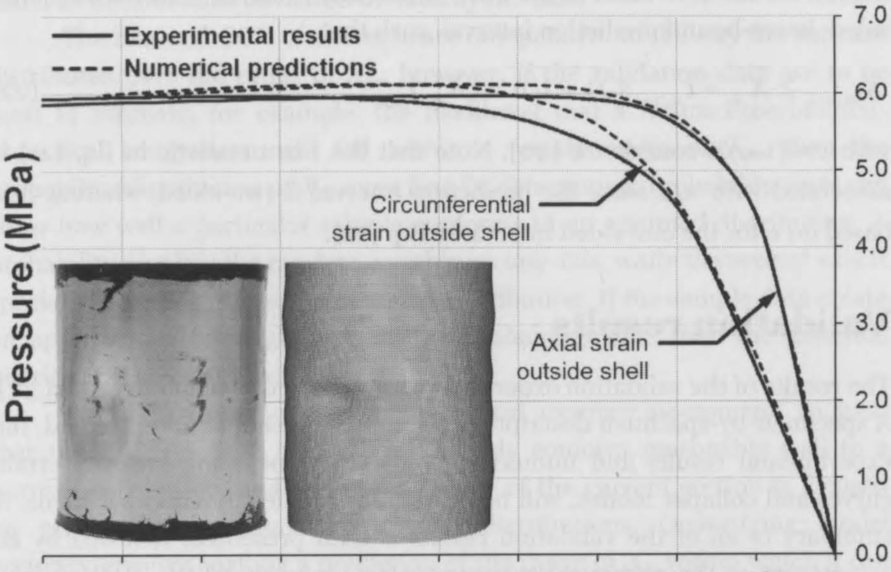

Figure 75: Comparison of experimental and numerical pressure-strain curves for L300-No6A. Strain data are shown for the outside of the shell at the centre of the collapse lobe in Bay 2 (180°). Also shown are a post-testing photograph of the specimen and the deformed shape of the numerical model after the final load step in the analysis. The displacements in the numerical model are scaled by a factor of 10 for clarity.

responses for that specimen are shown in Figure 76. Circumferential strains are shown for the outside of the shell at the centre of the experimental collapse lobe, and for the central stiffener flange at the inward OOC lobe, where collapse occurred, and the adjacent outward OOC lobe. The experimental and numerical collapse modes are similar, with the numerical collapse lobe offset by approximately 10° compared to the test specimen. As with L300-No6A, the FE model has correctly predicted the overall collapse mode, but the experimental collapse deformations extend over a greater area.

The measured and predicted pressure-strain responses for L510-No18 are in good agreement. The FE model has correctly predicted the tensile and compressive bending strains at the inward and outward OOC lobes, respectively. Furthermore, the FE model has captured the strain reversal that occurs at the shell at the centre of the collapse lobe after the peak load has been reached. It is not clear why that strain reversal happened. The strains were not likely measured at the exact centre of the collapse lobe, so that tensile bending strains could have arisen as the buckling lobe grew.

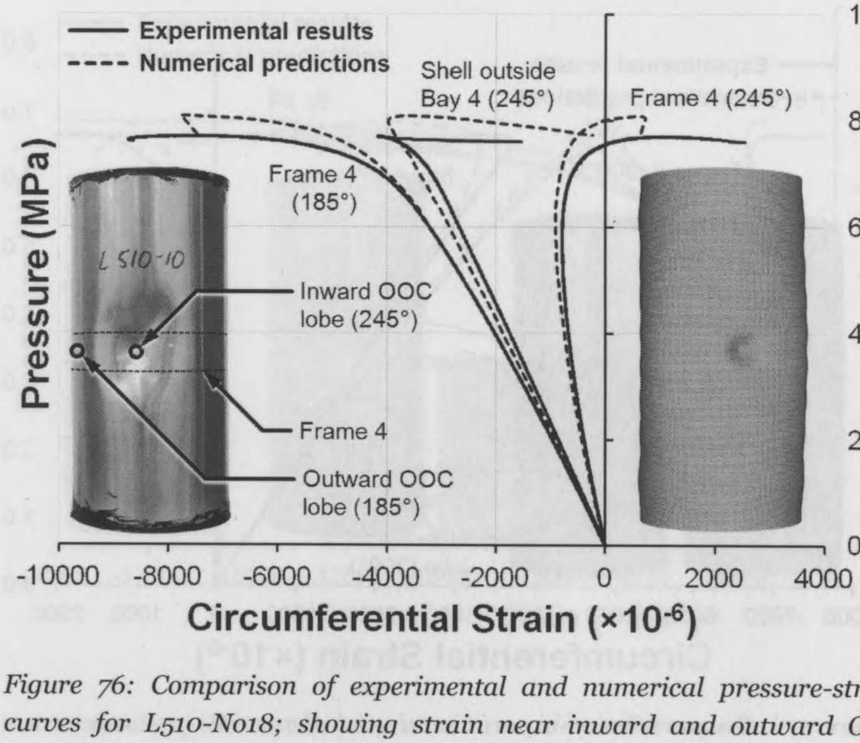

Figure 76: Comparison of experimental and numerical pressure-strain curves for L510-No18; showing strain near inward and outward OOC lobes.

Another possibility is that membrane action dominated the post-collapse response at the centre of the buckling lobe, leading the compressive bending strains to be overwhelmed by larger tensile membrane strains. In any case, the FE model over-predicted the experiment collapse pressure by approximately 4.5%. Some of that error is likely associated with the neglect of residual stresses and strain hardening related to the mechanical application of OOC.

L510-No19 had Patch C general corrosion at an inward lobe of the mechanically introduced OOC, i.e., in-phase corrosion. Experimental and numerical results are shown in Figure 77. The pressure-strain plots are similar to those for L510-No18, except that the shell strain is associated with the centre of the corrosion patch rather than the centre of the collapse lobe. Collapse in both the test specimen and FE model was concentrated within the corrosion patch at one of the circumferential edges. The FE model predicted the location of collapse within 2°. The predicted pressure-strain curves show good agreement with the measured results over the entire nonlinear response up to the collapse pressure, which was predicted within 3%.

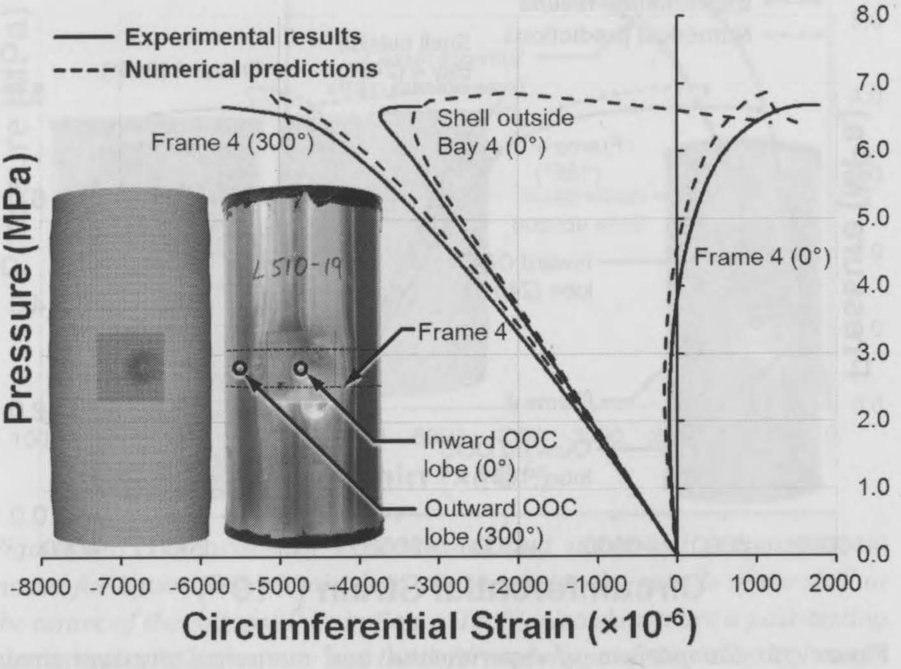

Figure 77: Comparison of experimental and numerical pressure-strain curves for L510-No19; showing strain near the corrosion patch.

Figure 78 shows test results and FE predictions for a typical cylinder with corrosion pitting, L510-No23. The artificial pitting on that cylinder was superimposed on a general corrosion patch. The collapse mode and location predicted by the FE model were nearly identical to the test specimen response, where collapse occurred in the centre of the cluster of corrosion pits. The pressure-strain curves in Figure 78 are associated with strains on the outside of the shell at the centre of two of the corrosion pits at the collapse site. Stiffener strains near the collapse site are also plotted. As with previously discussed specimens, the overall prediction of the pressure-strain curves is good, but the nonlinear response after yielding is somewhat delayed in the numerical model, leading to an approximately 4% over-prediction of the collapse pressure.

Summary of experimental-numerical comparisons

All of the validation specimens failed by overall collapse, with significant deformation and yielding of the shell and ring-stiffeners. Photographs of typical cylinders after testing, showing overall collapse deformations, are

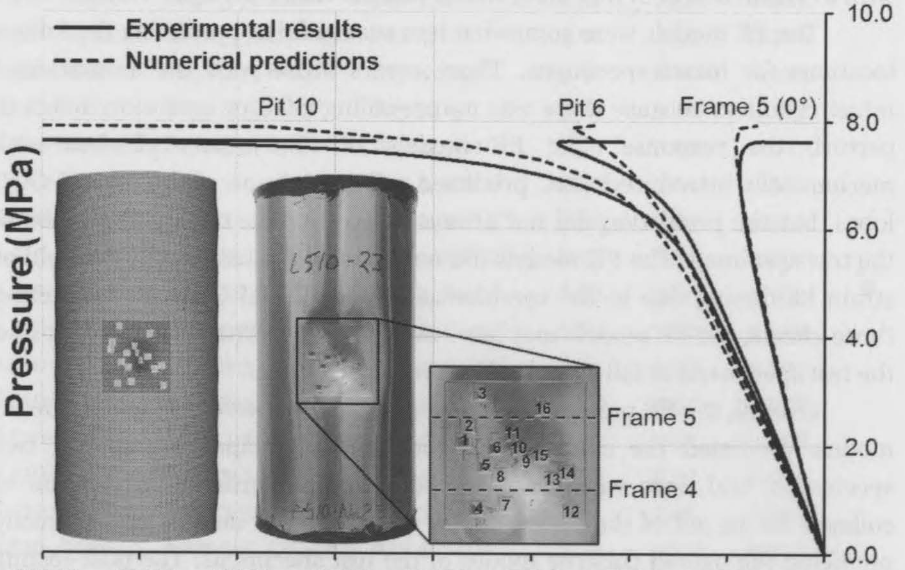

Figure 78: Comparison of experimental and numerical pressure-strain curves for L510-No23; showing strain outside shell at selected corrosion pits, and at the frame flange at the centre of the corrosion patch.

shown in Figure 74 to Figure 78. Table 32 describes where the dominant collapse lobe occurred in the test specimens and the FE models. In general, overall collapse deformations in the test specimens were concentrated at the maximum inward OOC, even for cylinders with corrosion damage that was collocated with an outward OOC lobe (e.g., L510-No13 in Figure 74). Otherwise collapse always occurred at the corrosion damage (e.g., L510-No14, L510-No20 and L510-No21 in Figure 74), except for L510-No8A. With that specimen, collapse occurred near the end of the cylinder, which had unintentional axisymmetric thinning (see Section "Finite element mesh" on p. 210).

The FE models predicted the correct collapse location for all corroded test specimens except for L510-No8A, where the FE model predicted collapse at the corrosion patch rather than the thin end-bay. The discrepancy between the test specimen and numerical model is likely related to using boundary conditions to simulate the support of the end-caps. When collapse occurs near the centre of the specimen, as it did with all of the other specimens, the end conditions are relatively unimportant; however, the interaction between the end-cap and cylinder plays a greater role in collapse with a critical defect in that area, which was the case with L510-No8A.

The FE models were somewhat less successful at predicting the failure locations for intact specimens. Those errors arose with the as-machined intact cylinders because there was no prevailing OOC or corrosion defect to perturb the response. The FE models of the intact cylinders with mechanically introduced OOC predicted collapse at one of the inward OOC lobes, but the prediction did not always agree with the critical OOC lobe in the test specimen. The FE models did not capture the residual stress field or strain hardening due to the mechanical application of OOC. By neglecting those effects, the FE models may have overlooked a perturbation that caused the test specimens to fail at a specific inward OOC lobe.

Overall, the FE predictions of collapse location were very good. The FE models predicted the correct axial location of collapse for all but two specimens, and were within 20° of the actual circumferential location of collapse for 19 out of the 26 validation cases. The FE models also correctly predicted the overall collapse modes of the test specimens. The post-testing photographs and deformed FE meshes in Figure 75 to Figure 78 show that the FE collapse modes are concentrated in a smaller area of the cylinder compared to the test specimens. The volume-control pressure testing method prevents catastrophic failures, but it is unable to completely control the large displacements and accelerations that occur during and after collapse. Thus, the greater extent of the experimental collapse deformations is likely a result of the neglect of dynamic effects in the FE models. Correct prediction of the post-collapse response of a hull is rather academic, since it will be completely destroyed during collapse.

The measured and predicted collapse pressures for each validation specimen are listed in Table 32, along with the corresponding modeling uncertainty factor, X_m. The experimental collapse pressure was over-predicted in all but three cases, and the maximum under-prediction was less than 2.5%. The maximum over-prediction of 9.4% was for L510-No8A. The

Table 32: Summary of experimental and numerical results for validation test specimens.

Specimen	Location of Collapse Lobe		Collapse Pressure (MPa)		
	Exp.	FE	Exp.	FE	X_m
L300-No5A	Bays 1-2, 280°	Bay 2, 223.8°	5.54	5.75	0.963
L300-No6A	Bay 2, 180°	Bay 2, 196.3°	5.98	6.12	0.977
L300-No7A	Bay 2, 0°	Bay 2, 0°	5.56	5.69	0.976
L300-No8A	Bay 2, 0°	Bay 2, 0°	5.06	4.94	1.024
L510-No6A	Bays 3-5, 210°	Bay 7, 8.8°	7.31	7.51	0.973
L510-No8A	Bays 5-7, 120-150°	Bay 4, 0°	4.11	4.54	0.906
L510-No10A	Bays 3-5, 0-25°	Bay 4, 345°	5.97	6.07	0.983
L510-No12A	Bays 4-5, 0-15°	Bay 5, 15°	5.74	5.71	1.005
L510-No13	Bays 3-5, 60°	Bay 4, 56.1°	7.55	7.97	0.947
L510-No14	Bays 3-5, 165°	Bay 4, 159.1°	6.93	7.21	0.962
L510-No17	Bays 3-5, 20°	Bay 4, 246.3°	7.84	8.24	0.952
L510-No18	Bays 3-5, 245°	Bay 4, 256.3°	7.71	8.08	0.954
L510-No19	Bays 3-5, 10°	Bay 4, 8.4°	6.67	6.86	0.973
L510-No20	Bays 3-5, 183.5°	Bay 4, 179.0°	6.93	7.20	0.963
L510-No21	Bays 3-5, 193.7°	Bay 4, 193.7°	8.65	9.37	0.923
L510-No22	Bays 3-5, 0°	Bay 4, 0°	8.98	9.37	0.958
L510-No23	Bays 3-5, 0°	Bay 4, 0°	7.63	7.97	0.958
L510-No24	Bays 3-5, 44.9°	Bay 4, 44.9°	7.62	8.01	0.951
L510-No25	Bays 3-5, 20°	Bay 3, 245°	7.13	7.46	0.955
L510-No26	Bays 3-5, 125-130°	Bay 4, 240°	7.05	7.27	0.970
L510-No33	Bays 3-5, 140°	Bay 4, 16.3°	7.03	7.37	0.953
L510-No34	Bays 5-7, 65°	Bay 6, 65°	8.02	8.37	0.959
L510-No35	Bays 3-5, 0°	Bay 4, 357.8°	6.58	6.93	0.949
L510-No36	Bays 4-6, 300°	Bay 6, 301.4°	7.22	7.59	0.951
L510-No37	Bays 3-5, 0°	Bay 4, 0°	6.68	6.91	0.967
L510-No38	Bays 3-5, 240°	Bay 4, 240°	2.80	2.75	1.019

large error for that specimen is likely related to the previously discussed interaction between the FE boundary conditions and the end-bay thinning. Only one other FE collapse pressure prediction was in error by greater than 5.3%. On the other hand, only two FE predictions fell within the ±0.09 MPa accuracy of the pressure transducers, so the bias clearly exceeds the experimental error bounds.

On average, the FE models over-predicted the experimental collapse pressures by 3.6%. The trend is related to the inability of the FE models to completely capture the severity of the nonlinear response of the test specimens in most cases. In other words, the experimental strains at a given pressure beyond the linear-elastic limit are typically under-predicted. In the case of the intact as-machined cylinders, the effect may be due to the lack of a significant perturbing defect in the FE models that could initiate nonlinear behaviour. That is supported by the better prediction of the nonlinear response and collapse location for specimens with corrosion damage or mechanically introduced OOC. Other simplifications in the numerical models may also have contributed to the general disagreement. For example, an isotropic yield surface was used to model yielding in an anisotropic material. Furthermore, the specimen end-caps were implicitly modeled using boundary conditions, and residual stresses and strain hardening in the models with mechanical OOC were neglected.

Numerical accuracy assessment

As a first step in quantifying the FE model accuracy, the validation data was tested for its normality. A normal probability plot for the X_m data is shown in Figure 79. The plot was produced by listing the X_m data in a vector in ascending order. A z-value was then calculated for each element in the vector, based on its relative percentile position in the vector. For a normal distribution, the magnitude of the n-th vector element is expected to be approximately equal to the bias plus the product of the standard deviation and the z-value, and the X_m and z-value data should form a straight line in the probability plot. The dashed line in Figure 79 was manually fit to the central cluster of data in order to show that most of the data form an approximately straight line, suggesting that the data conform to a normal distribution. The extreme minimum and maximum X_m values fall above and below the trend-line, respectively, indicating a distribution that is somewhat heavy-tailed compared to a true normal distribution. In other words, there are more extreme values in the validation sample than would be expected for a normal distribution. Nonetheless, the normal probability plot data were considered to be sufficiently linear to justify the use of a normal distribution

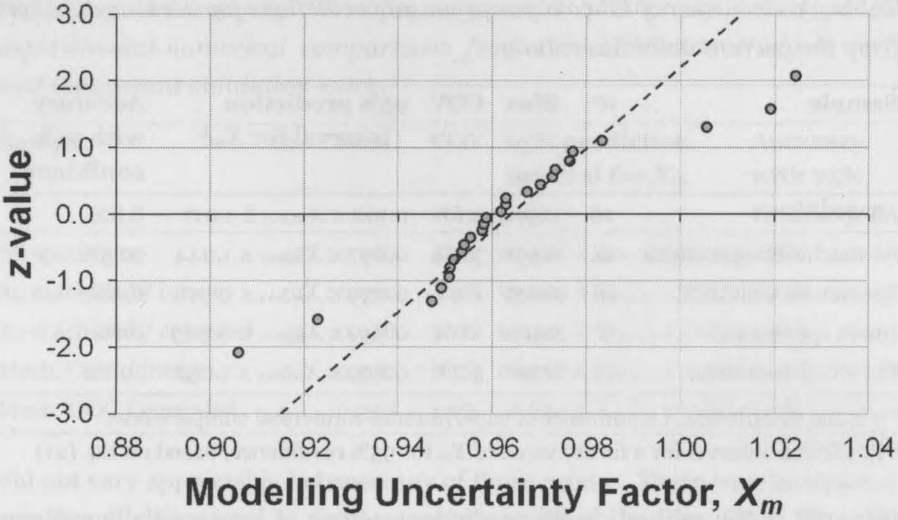

Figure 79: Normal probability plot showing the modeling uncertainty factor for 27 validation cases versus the associated z-value. The dashed line was manually fit to the central cluster of data.

for all further calculations, especially considering that some deviation from a straight line is expected for a sample size less than thirty [40].

The results of the analysis of the validation data using the methodology described in Section “Statistical and probabilistic methods” on p. 213 are summarized in Table 33. Those results include the bias, the COV, a 95% prediction interval for X_m, and the overall accuracy for the entire sample. The same data is also presented for selected sub-sets from the validation sample.

Overall, the accuracy of the validation FE models was found to be 8.8% with 95% confidence. That represents an improvement over the calibration analyses that were presented in Chapter 7 [25], where the accuracy of the same numerical methodology was calculated as 11.4% with 95% confidence. The test specimens were fabricated from several different batches of the aluminium tubing, with between five and ten test specimens per batch. As mentioned earlier, tensile coupons were machined from each test specimen in the validation experiments, so that specimen-specific material properties could be used in the FE models. With the calibration specimens, material testing was performed on a representative sample from each batch, and the resulting material properties were used in all of the FE models associated with the batch. Material variation within a batch was not

Table 33: Accuracy of FE collapse pressure predictions for various data sets from the current validation study.

Sample	***n*[a]**	**Bias**	**COV**	**95% prediction interval for X_m[b]**	**Accuracy with 95% confidence**
All specimens	26	0.964	2.6%	$0.912 \leq X_{m,n+1} \leq 1.017$	8.8%
As-machined specimens	14	0.970	3.4%	$0.897 \leq X_{m,n+1} \leq 1.044$	10.3%
Specimens with OOC	12	0.957	0.9%	$0.939 \leq X_{m,n+1} \leq 0.976$	6.1%
Intact specimens	9	0.962	1.0%	$0.939 \leq X_{m,n+1} \leq 0.985$	6.1%
Corroded specimens	17	0.966	3.2%	$0.899 \leq X_{m,n+1} \leq 1.032$	10.1%

[a] n is the sample size, i.e., number of experimental-numerical comparisons.

[b] Prediction interval for a future value of X_m for 95% confidence, based on Eq. (21).

captured in the calibration FE predictions, which at least partially explains the poorer performance of those models compared to the validation models.

The numerical accuracy was found to be better for specimens with mechanically introduced OOC compared to the as-machined specimens, despite the neglect of residual stresses in the former group of FE models. The improvement is thought to be related to the previously mentioned perturbing effect of large-amplitude OOC imperfections on the FE solution. The FE accuracy was also found to be better for intact cylinders than for corroded specimens. That contradicts the results presented in Chapter 7 [25], where the calibration FE models were found to be significantly more accurate for corroded specimens than for intact specimens, at 8.7% and 16.9%, respectively, with 95% confidence. Specimens with mechanically introduced OOC make up two-thirds of the set of intact validation cylinders, but only approximately one-third of the corroded group. The magnitude of OOC seems to have a greater influence on the numerical accuracy than corrosion damage.

The current validation results were combined with the calibration cases from [25] and the probabilistic analysis was re-applied to the new larger sample. The results of that analysis are presented in Table 34. The bias of the data is the same as for the validation set, but the addition of the calibration data increases the scatter in the results. That, in turn, leads to a decrease in accuracy for the combined data set, at 9.8% with 95% confidence.

The larger calibration/validation sample was broken down into four smaller groups associated with unique combinations of OOC imperfections (as-machined versus mechanically introduced OOC) and corrosion damage (intact versus corroded). The statistical data in Table 34 show that the bias

Table 34: Accuracy of FE collapse pressure predictions based on all experimental-numerical comparisons from the calibration study in [25] and the current validation work.

Sample	n	**Bias**	**COV**	**95% prediction interval for X_m**	**Accuracy with 95% confidence**
All specimens	47	0.964	3.1%	$0.902 \le X_{m,n+1} \le 1.025$	9.8%
As-machined / intact	12	0.961	4.4%	$0.863 \le X_{m,n+1} \le 1.059$	13.7%
As-machined / corroded	23	0.968	3.1%	$0.905 \le X_{m,n+1} \le 1.032$	9.5%
Mech. OOC / intact	6	0.957	0.7%	$0.938 \le X_{m,n+1} \le 0.976$	6.2%
Mech. OOC / corroded	6	0.957	1.0%	$0.930 \le X_{m,n+1} \le 0.985$	7.0%

did not vary appreciably between any of those groups. There was, however, a significant difference in scatter, as represented by the COV. The FE predictions for as-machined specimens in general showed greater scatter, and correspondingly worse accuracies, than the predictions for cylinders with large-amplitude OOC. Furthermore, the presence of corrosion in the as-machined specimens can be seen to dramatically improve the FE prediction. On the other hand, the presence of corrosion damage on cylinders with mechanically introduced OOC did not significantly affect the FE predictions compared to similar intact specimens. Those observations support the previous conclusions that the presence of large-amplitude OOC imperfections or corrosion defects improves collapse predictions, but that OOC imperfections have the greatest influence on the FE accuracy.

Numerical design framework

The goal of this thesis is to propose a framework for the design of pressure hulls using FE analysis. The framework must address two issues that stand in the way of FE design calculations: the lack of FE modeling rules and the lack of a partial safety factor approach consistent with those rules. With a few exceptions, the proposed FE modeling rules consist of the numerical tool-kit described in Section "Numerical methods", starting on p. 210. Of course, grammatical and wording changes are required to frame that numerical methodology in a prescriptive rules format, but that task is beyond the scope of the present study. The tool-kit was developed with the analysis of test specimens in mind, so that emphasis was placed on incorporating measured geometric and material data. The numerical methodology can be applied to assessments of in-service submarines, as long as the hull's current condition is known through sufficient measurements; however, measured data are never available at the design stage. The numerical modeling rules must address that lack of information by providing guidance on design stage imperfections and material models. Those topics, along with permissible numerical modeling codes, are discussed below, followed by the derivation of a PSF for FE analysis.

Numerical modeling rules

Permissible modeling and analysis software

V&V is normally considered to be software-specific, since credibility is established for a particular numerical code, rather than a generic methodology [36]. Strictly speaking then, the proposed modeling rules and corresponding PSF are only applicable to FE models produced using CylMesh and analysed with ANSYS. That interpretation is too restrictive, especially considering that CylMesh is an in-house code that is not suitable for general distribution, and since any generic pre-processing program can create FE models of axisymmetric shell structures.

The modeling study in Chapter 7 [25] showed that the collapse prediction is not very sensitive to the FE solver, even if there is some variation in element formulations and solution procedures. In that study, three FE solvers (ANSYS, VAST and MARC [145]) were used to analyze identical FE models of test specimens. The collapse predictions agreed within 3% of each other in all four cases studied. But then, the full V&V procedure has only been performed for ANSYS. The same degree of credibility has not been demonstrated for the other FE programs, even if the available data indicate that a similar level of accuracy can be expected.

All things considered, it is concluded that the modeling rules are applicable to FE models generated using any pre-processor that can incorporate the methodology specified in the tool-kit, but only ANSYS should be used to produce the numerical collapse prediction.

Geometric imperfections and fabrication tolerances

The treatment of out-of-circularity geometric imperfections is perhaps the most critical difference between FE models for test specimens (or in-service submarines) and those that are to be used to make collapse predictions during the design of the submarine. The strategy proposed here for FE design calculations mirrors the conventional analytical-empirical design methods, whereby conservative OOC shapes and magnitudes are prescribed. Since OOC has its greatest effect on overall collapse [14], it should be applied in the lower-order circumferential modes associated with general instability. Those shapes are also typical of OOC in real hulls, which arises mainly due to longitudinal seam welds in the hull plating [73]. Like the conventional design methodology, collapse simulations should be performed for several FE models with overall OOC in a single circumferential mode, ranging from $n=2$ to $n=6$. The magnitude of OOC should be at the maximum allowable value chosen for design, e.g., the UK standard in [5] requires design calculations to be carried out assuming an OOC magnitude of 0.005 times the hull radius.

FE models with overall OOC shapes sometimes require shorter wavelength imperfections between frames to perturb the hull in the critical interframe collapse mode [14]. In real hulls, those imperfections may be introduced by differential cooling after frame welding, with distortions up to approximately 10% of the hull thickness [73]. So-called interframe nucleators should be superimposed on the overall OOC shape of each FE model in order to ensure that potential interframe collapse modes are revealed. The nucleators should be in the critical elastic buckling mode of the shell, as determined from a linearized FE buckling analysis or a classical buckling equation. Tolerances on interframe distortions are normally required for hydrodynamic considerations. The prescribed amplitude of the interframe nucleators could be associated with those “fairness-of-form” tolerances. Alternatively, the amplitude could be based on the maximum expected weld distortion, e.g., 0.1 times the hull thickness. The design collapse pressure is taken as the minimum value predicted over the range of imperfection shapes.

The nonlinear Fourier mapping technique described in the numerical tool-kit may be used for collapse predictions for in-service hulls if reliable OOC measurements are available. However, it must be understood that by using the measured hull shape, the safety margin implied by using conservative OOC shapes and magnitudes with the design methodology is lost.

In addition to allowances on shape imperfections, a pressure hull design will specify fabrication tolerances on other aspects of the geometry, such as the thickness and mean radius of the hull, and the frame dimensions and spacing. In the conventional design procedure, the geometry used for collapse strength calculations is determined by adding or subtracting those tolerances from the specified values in order to produce the most pessimistic configuration [5]. The use of the so-called “strength” dimensions, rather than the nominal specified values, adds another layer of inherent, but unavoidable conservatism to the design. FE models used for design should incorporate the fabrication tolerances in the same way. Assessments of in-service hulls may be made using measured dimensions if dependable data are available;

however, as with the use of measured OOC data, it must be acknowledged that that choice effectively reduces the hull's safety margin.

Material models and residual stresses

Conventional design calculations are carried out using nominal values for Young's modulus and Poisson's ratio, along with the minimum specified yield stress [5]. FE design analyses should take the same approach. Since submarine steels are typically isotropic [141], it is recommended that the nominal material data be incorporated in a material model with an isotropic von Mises yield surface and kinematic hardening to account for the Bauschinger effect. The calibration study in Chapter 7 [25] showed that approach to be effective for anisotropic materials as well, as long as the smallest yield stress is used in the numerical model. Measured stress-strain data may be incorporated using a multi-linear overlay material model, but that approach reduces the safety margin inherent in the use of minimum specified material properties.

In the present V&V study, residual stresses due to mechanically applied OOC were neglected in the numerical models. The simplification did not significantly affect the accuracy of the numerical models, but the residual stresses in question are not representative of those that occur in real hulls. Residual stresses arise due to two aspects of conventional hull fabrication methods. Cold rolling of the hull plating and ring-stiffeners into circular form leads to a zig-zag pattern of circumferential residual stresses through the hull section. Those stresses can reduce overall collapse pressures by up to 30% [14,73], particularly due to the large compressive residual stresses in the frame flange that hasten the onset of yield. Interframe collapse pressures are thought to be less affected by cold rolling stresses [73], but the interaction has not been studied thoroughly because the interframe empirical design curve implicitly takes residual stresses into account.

Differential cooling rates after welding lead to distortions and residual stresses in the hull. Frame welds result in circumferential residual stresses characterized by yield-level tensile stresses in the heat-affected zone of the plating near the frames, and smaller counter-balancing compressive stresses in the shell between frames [73]. The residual stresses in the frames themselves are in tension, which tends to counteract cold rolling stresses. Welding stresses are not considered in the conventional design method for overall collapse, but like cold rolling stresses, they are implicitly included in the interframe design curve.

Residual stresses can be dealt with in the numerical model in several ways. For example, the fabrication processes themselves can be simulated with the numerical model before the collapse analysis is performed [49], or the residual stresses can be calculated by an analytical method and brought into the numerical model as an initial stress state [16]. Alternatively, predetermined residual stresses can be incorporated in the FE model via "effective" stress-strain (σ-ε) curves [14]. Effective σ-ε curves are generated by numerically simulating uni-axial tension and compression tests on coupons with the correct residual stress field [47]. Early yielding caused by residual stresses is accounted for by softening the material response compared to the stress-relieved state; however, the effect is smeared over entire structural sections, i.e., the plating and the frames.

The authors believe that effective σ-ε curves are the best approach for dealing with residual stresses in the FE analysis because they are significantly easier to implement than a full simulation of fabrication procedures or an initial stress state. Furthermore, it was shown in [47] that effective σ-ε curves were more conservative than a full-simulation approach in all of the cases studied, which included models failing by both overall and interframe collapse. Simple methods for calculating hull stresses due to welding and cold rolling are presented in [73] and [41], respectively. Those stresses could be superimposed on each other and effective σ-ε curves could be generated for the net stress distribution. In that way, residual stresses that arise due to different causes can be accounted for by a single methodology.

Effective stress-strain curves are generated by assuming that the virgin material is elastic-perfectly-plastic. Future work should be directed at studying how effective σ-ε curves could be generated starting from a realistic nonlinear material curve with strain hardening. Furthermore, the effective σ-ε curve approach needs to be validated by comparison with experiments.

Deep diving depth and partial safety factors

The deep diving depth of a submarine, based on a numerical pressure hull collapse prediction, is given by substituting the FE prediction, $P_{c,FE}$, for P_c in Eq. (19) and rearranging the terms, giving

$$\mathrm{DDD} \leq \frac{1}{\gamma_i \gamma_c \gamma_D} \frac{P_{c,FE}}{\rho g}. \tag{23}$$

Since PSFs related to the fabrication quality, γ_c, and the loading, γ_D, are independent of the predictive model, the present work is only concerned with determining an appropriate value of γ_i for FE collapse predictions. The experimental-numerical comparisons described above can be used with the probabilistic methodology outlined earlier to derive γ_I; however, that requires some critical minimum value of the modeling uncertainty factor, $(X_m)_{min}$, to be defined, such that the level of confidence associated with the PSF is sufficiently great.

Figure 80 shows how γ_I varies with the level of confidence for three sets of pressure hull collapse predictions. The data were generated by calculating $(X_m)_{min}$ over a range of confidence levels using Eq. (22). The plotted PSF values are simply the inverse of the corresponding $(X_m)_{min}$ values. The solid curve in Figure 80 is based on results for all of the FE validation cases in Table 32, including predictions for both intact and corroded specimens (i.e., the data for "All specimens" in Table 33). The dashed line is associated with all of the validation cases plus the calibration FE results from Chapter 7 [25] (i.e., the data for "All specimens" in Table 34). Finally, the dotted line shows how a PSF derived for the empirical design curve for interframe collapse [5], using the current methodology, would vary with the level of confidence. The statistical data for the empirical curve were taken from Chapter 2 [20].

In the previous section, it was shown that the accuracy of the validation FE models was better than for the initial calibration results from Chapter 7 [25]. The effect can be seen in Figure 80, where the PSF for a given level of confidence is greater when the calibration results are included with the validation data. The difference is largely due to the greater COV for the combined calibration/validation sample, since the bias of that group of FE models is identical to the validation sample (the size of the sample also affects the PSF calculation). Despite the earlier discussion of polluting the V&V study with model tuning, the combined calibration/validation results have been chosen for use in the derivation of γ_I for FE collapse predictions. That approach is taken because, on one hand, it is conservative, and on the other hand, it improves the credibility of the PSF since the sample size is larger and since a greater number of structural configurations and failure modes are considered.

The bias and COV associated with the design curve from [5] were found to be approximately 1.02 and 8.5%, respectively [20]. The design curve under-predicts collapse pressures, on average, while the scatter around the curve is relatively large compared to the current FE results. In Figure 80, the PSF for the design curve is smaller than the FE PSFs for smaller confidence levels, since the design curve tends to under-predict hull strength while the FE models typically over-predict the collapse pressure. For higher levels of confidence, the scatter in predictions becomes more important than small

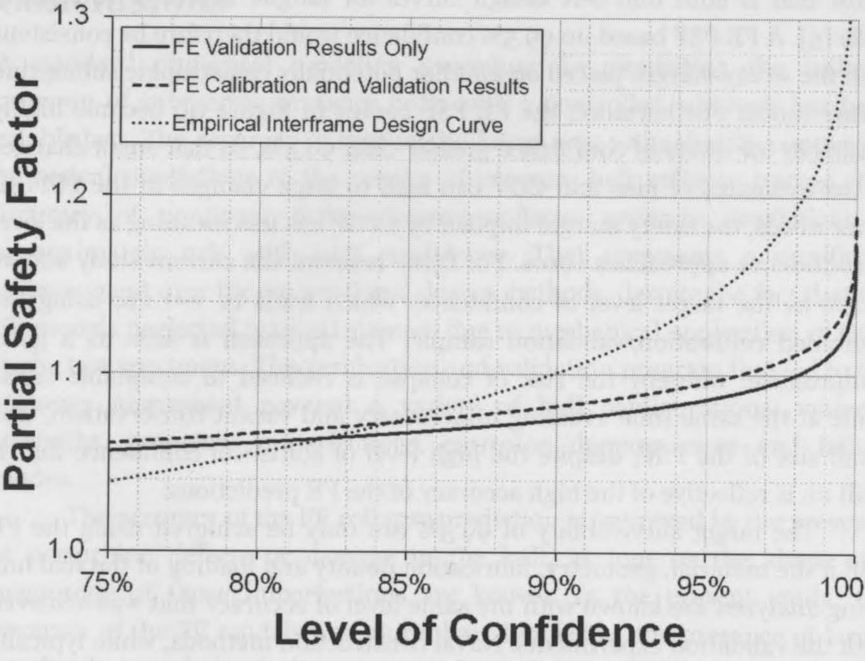

Figure 80: Variation of the partial safety factor with the level of confidence that any future observation of X_m *will exceed* $(X_m)_{min}$*, for FE and design curve predictions of hull collapse.*

differences in bias, so that the PSF for FE predictions can be much smaller than the design curve PSF.

The actual PSF used with the empirical design curve is approximately 1.1 [20]. The value of the PSF is based on the maximum scatter of about 10% in the test results around the elasto-plastic portion of the curve where most pressure hull designs fall [154]. With reference to Figure 80, that PSF gives 90% confidence that the predicted collapse pressure is conservative. The rather modest confidence level is justifiable in the case of the design curve because its credibility has been established through the hundreds of test results on which it is based [10], and because it has been successfully used to design real submarines for decades. The sample size available for FE model validation is an order of magnitude smaller, and furthermore, the direct use of numerical models in the submarine design procedure, to the extent that is proposed here, is a novel concept. For those reasons, a FE PSF associated with a higher level of confidence is warranted.

In Chapter 2 [20], a confidence level of 99.5% was suggested for FE PSFs. That value was chosen because it is associated with an implicit safety factor that is built into *S-N* design curves for fatigue failure of submarine hulls [5]. A FE PSF based on 99.5% confidence would therefore be consistent with the safety margin placed on another potentially catastrophic submarine failure mode. Furthermore, the FE PSF curves in Figure 80 become highly nonlinear for levels of confidence greater than 99.5%, so that small changes in the estimates of bias and COV can lead to large changes in the PSF. In other words, the safety margin implied by a PSF has less meaning as the level of confidence approaches 100%. For those reasons, the current study adopts 99.5% as the target level of confidence, which leads to γ_I=1.134 using the combined calibration/validation sample. The approach is seen as a good compromise, whereby the risk of collapse is reduced to acceptable levels while at the same time avoiding unnecessary and vacant conservatism. The small size of the PSF, despite the high level of statistical confidence that is built in, is reflective of the high accuracy of the FE predictions.

The target survivability of 99.5% can only be achieved using the FE PSF if the material, geometry, fabrication quality and loading of the real hull being analyzed are known with the same level of accuracy that was achieved with the validation experiments. Naval construction methods, while typically of a high quality, cannot meet the standard set by test specimens machined in the shop. (That may not be a disadvantage, since it has been shown that collapse pressures are more accurately predicted by FE analysis when defects are present in the hull. Of course, that means that the actual condition of the hull must be well known.) That is why the additional PSFs γ_C and γ_D are required to account for uncertainty in the condition of the as-built hull and for the loads that will be applied to the submarine during service, respectively. Naval standards like [5] use separate PSFs for those factors, but the civilian pressure vessel codes in [6,7] account for all uncertainties, except for errors in the predictive model, using a single safety factor of 1.5. With those standards, the modeling uncertainty is accounted for using an empirical curve that is offset from the mean curve in [5] so that it forms a lower-bound to all known test results (see Figure 3, p. 5). Essentially, γ_I is built into the lower-bound design curve, and γ_C and γ_D are combined into a single safety factor equal to 1.5. If a similar strategy is adopted for the FE design approach, with γ_I=1.134 and $\gamma_C\gamma_D$=1.5, then the total safety margin on FE collapse predictions is approximately 1.7.

Conclusions

A standard numerical modeling procedure for predicting the collapse pressure of submarine pressure hulls with a controlled accuracy has been established. The accuracy of that methodology was estimated by comparing numerical predictions to the results of pressure hull collapse testing. The accuracy of nonlinear finite element collapse pressure predictions is approximately 10% with 95% confidence. That represents a significant improvement over the conventional design methods, despite the fact that the FE models neglected residual stresses due to mechanical application of OOC to the test specimens. The verification and validation program that led to the accuracy assessment covered a variety of hull configurations, material strengths, geometric imperfections, corrosion damage cases and failure modes.

The accuracy of the FE collapse prediction is improved by the presence of perturbing defects or damage in the hull, as long as the shape and magnitude of those imperfections are known. In the present study, the accuracy of the FE models was more than doubled by the presence of large-amplitude out-of-circularity geometric imperfections in the test specimens, compared to similar but shape-perfect cylinders. The improvement in FE predictions was less dramatic with corrosion damage, especially when combined with large-amplitude OOC. Comparison of secondary responses, namely pressure-strain relationships at critical hull locations, showed that the failure mode and location of collapse can also be predicted with good accuracy.

A framework for a pressure hull design procedure based on FE collapse predictions has been presented. Numerical modeling rules have been established based on the V&V program and supplemented with recommendations for design-stage geometric imperfections and material models. The modeling rules are also suitable for assessments of in-service submarine hulls with known geometric imperfections and damage. A probabilistic analysis was applied to the experimental-numerical comparisons from the V&V program in order to derive a partial safety factor for FE collapse predictions. It was shown that the designer can be 99.5% confident that the FE error has been accounted for if the predicted collapse pressure is divided by a PSF=1.134. The high accuracy of the FE predictions means that the PSF does not need to be very large, even when a conservative degree of statistical confidence is required. Since the proposed FE design framework is based on deterministic analysis, it is compatible with conventional PSFs that are used to correct for errors in hull fabrication and loading.

The current work is focussed on ring-stiffened cylindrical shells, since those structures tend to constitute the critical component of submarine pressure hulls. Nonetheless, future work should be aimed at V&V of other hull elements like ring-stiffened cones, dome ends, and stiffened watertight bulkheads. That would allow FE collapse predictions to be based on system-level models of the entire pressure hull so that interaction between the components is factored into the strength assessment. The recommended approach for dealing with welding and cold rolling stresses in the FE analysis is the use of effective stress-strain curves in the material model. Further work is required to show that the FE accuracy is not affected when residual stresses are treated in that way.

Finally, the FE design methodology presented here represents a potential framework upon which future changes to submarine design standards may be based. The development of a complete and detailed FE design procedure should be undertaken by a panel of experts from government, industry and the research community.

Chapter 9

Conclusions

Conclusions have been presented at the end of each chapter of this thesis. The main findings, including some new conclusions drawn from the context of the entire research program, as well as recommendations and future work, are collected here in the final chapter of this thesis. The conclusions are broken down into categories that do not necessarily correspond with individual chapters.

Conventional design methods

The accuracies of the conventional design methods for interframe and overall collapse were estimated in order to provide a benchmark for numerical collapse predictions. The mean empirical interframe design curve, which is used to predict the governing collapse mode of most submarine hulls, is accurate within 20%, with 95% confidence. The partial safety factor that is used with the design curve gives the designer approximately 90% confidence that the predictive error, especially due to scatter in the test data, has been dealt with. The accuracy of the one-dimensional finite difference model used to predict overall collapse is 17%, with 95% confidence. The accuracy estimates are based on test results for intact hulls without any corrosion or other type of damage.

The strength-predicting effectiveness of the conventional design methods is diminished for hulls with non-axisymmetric defects such as corrosion damage. For example, the interframe design curve under-predicted the experimental collapse pressures of two corroded test specimens by between 69% and 74%. Sufficient test data were not available to estimate the accuracy in a more formal way. The design curve tended to under-predict collapse pressures even for intact specimens from the current test program, by between 15% and 27%. That is attributed to the relatively small levels of geometric imperfections and residual stresses in the current test cylinders compared to the specimens used in the development of the empirical curve. Nonetheless, a significant portion of the error associated with using the design curve for predicting the collapse of the corroded specimens can be attributed to the neglect of the non-axisymmetric nature of the hull thinning.

A larger number of overall-critical specimens with corrosion were tested. The accuracy of the FD method for those specimens was found to be approximately 26%, with 95% confidence. That estimate represents deterioration in accuracy over the intact cases, even though the FD algorithm was modified to allow discrete swaths of thinning to be modeled in the circumferential direction. Furthermore, the accuracy was estimated after two outliers in the data were discarded.

In general, the conventional submarine design methods are conservative. The conservatism is necessary to compensate for the use of empirical methods and simple analytical and numerical models. With the empirical interframe design curve, the large variety of hull configurations, materials and imperfections represented by the test data leads to a high degree of scatter that must be compensated for. The analytical and numerical models used to predict other modes of collapse are restricted to the most idealized hull configurations. Real, complex hulls must therefore be modeled using the most pessimistic geometry. Furthermore, the conventional approach is cautious because each possible mode of failure is considered individually. Interaction between overall and interframe collapse is considered in the numerical approach for overall collapse predictions. Those collapse modes tend to govern the design of the hull. Interaction with other failure modes, like frame tripping, is prevented by over-designing for the non-critical modes.

Pressure testing procedures

A simple method for choosing the pressure testing method, based on the size and stiffness of the test specimen relative to the volume and compliance of the testing fluid, has been presented. A new volume-control test method was developed and implemented in the lab. Compared to conventional testing procedures, the volume-control method improves control over the specimen deformations, especially near the collapse load. The new method dramatically improves the effectiveness of collapse tests by allowing the collapse mode to be measured and, to a certain extent, preserved after the test is completed. The catastrophic failures that plague some conventional test procedures are eliminated with the volume-control method. Those features of the volume-control method are invaluable when comparing measured and predicted strains and collapse modes in numerical model validation exercises.

Complete control of the specimen deformations during collapse is not possible, even with the volume-control method, because typical pressure testing fluids, like water and mineral oil, are too compliant to compensate for the sudden loss of specimen stiffness at collapse. Furthermore, it is possible that, even with an infinitely stiff testing fluid, dynamic snapping is unavoidable due to a limit point in the control variable for all pressure testing methods, i.e., the generalized displacement of the specimen.

Pressure hull corrosion

The aluminium test specimens failed by inelastic buckling of either the shell plating itself (interframe collapse) or together with the ring-stiffeners (overall collapse). Both failure modes combined aspects of axisymmetric plastic collapse with non-axisymmetric buckling. In those ways, the collapse mechanisms in the aluminium cylinders are similar to the failure modes in real high-strength steel pressure hulls. Furthermore, the material response of the aluminium alloy used in the experiments was shown to be similar to high-strength steel, especially with respect to the overall shape of the stress-strain curve and the degree of strain hardening. Therefore, the following conclusions, which are drawn from the current test program, are applicable to real submarine hulls.

Collapse mechanics in corroded hulls

Material loss due to corrosion leads to an earlier onset of yielding in the damaged area of the pressure hull, compared to the undamaged hull. Early yielding is associated with the reduction in cross-sectional area in corroded regions, which leads to higher membrane and bending stresses under pressure loading. Local bending stresses that arise due to the shell eccentricity associated with one-sided thinning further increase the critical stresses in the corroded area. The shell eccentricity effectively increases out-of-circularity imperfections and introduces destabilizing global bending moments that can further reduce collapse strength. Corrosion also leads to early yielding in intact areas of the hull due to load redistribution after the corroded region has yielded. Corrosion damage therefore reduces the elasto-plastic collapse strength of a pressure hull through a complex combination of early yielding and nonlinear geometry effects.

Corrosion damage affects overall collapse pressures to a greater extent than interframe collapse strength. In the experiments, the heavy ring-stiffeners of interframe-critical specimens had significant reserve strength, so that the cylinders were able to carry additional loads after the corroded shell had failed locally. That reserve strength was lacking in the overall-critical specimens. Real submarine hulls are normally designed to be interframe-critical, but with only enough reserve strength in the ring-stiffeners to prevent premature overall collapse. In that way, real hulls are more like the overall-critical than the interframe-critical test specimens. Furthermore, the reserve strength in the frames of real hulls may not be sufficient to accommodate any significant load redistribution once the corroded hull plating has yielded. Thus, real submarine hulls are likely to have a similar sensitivity to corrosion as the overall collapse specimens.

General corrosion damage interacts strongly with out-of-circularity imperfections in overall-critical hulls. The membrane and bending stresses introduced by corrosion work in concert with the OOC bending stresses when the two types of defects are in-phase; the stresses arising from corrosion and OOC tend to counteract each other when they are out-of-phase. Thus, in-phase corrosion has a significantly greater impact on collapse strength than an equivalent out-of-phase case. It is expected that the effect of in-phase corrosion diminishes as the level of OOC becomes larger, due to the relatively greater increase in effective OOC, but that could not be confirmed experimentally due to the level of scatter.

As expected, both corroded and intact hulls were found to be sensitive to material strength; however, corroded specimens were found to be more sensitive to the post-yielding shape of the stress-strain curve, i.e., strain hardening. The strength of corroded cylinders was found to improve with the degree of strain hardening to a greater extent than the intact specimens. Corroded specimens yielded relatively early compared to intact specimens, so that strain hardening had a greater chance to contribute to the collapse strength.

Clusters of ground-out corrosion pits tend to have a similar affect on collapse pressure as an area of equal-depth general corrosion that bounds the same area on the hull. That means that a numerical assessment of corrosion damage, whereby a cluster of pits is modeled as an equivalent area of general corrosion, is not overly conservative. The applied pressure load leads to hull stresses that are greatest in pits that are in close proximity to other pits and near the centre of the frame bay. Therefore, pit concentration and location, along with pit depth, are the critical factors to consider when making a pitting damage assessment.

The consequences of corrosion damage to the ring-stiffeners were found to be less severe than hull thinning; however, only shape-perfect specimens were tested in the current work. Overall-critical hulls with large-amplitude out-of-circularity are more likely to be sensitive to frame damage since the bending strength of the frames plays a greater role in preventing collapse.

Effect of corrosion on hull strength

The experimental results showed a strong correlation between corrosion depth and the reduction in collapse pressure; however, a similar trend was not observed for corrosion area. It is likely that pressure hulls really are sensitive to the size of the corrosion patch (in fact, a recently completed nonlinear finite element study of corrosion depth and area supports that hypothesis [158]); however, the effect was too subtle to be discerned in the test data amongst the experimental scatter.

In the experiments, overall collapse pressures were reduced by, on average, 0.85% for each 1% of general corrosion thinning. That trend is based on test specimens with depths of corrosion between 13% and 27% of the hull thickness, for areas of corrosion less than eight times the frame spacing squared, and for out-of-circularity magnitudes less than 0.01 times the hull radius. The trend was identified by lumping together specimens with a variety of corrosion areas and other geometric imperfections. That approach, along with general experimental scatter, led to some variation around the trend-line. The main conclusion to draw is that, for real pressure hulls, something like a one-to-one ratio of hull thinning to collapse pressure reduction can be expected. The actual strength reduction will depend on the hull geometry, the size and shape of the corrosion patch, and its location on the hull with respect to frames, internal structures and out-of-circularity.

General corrosion damage reduces the yield pressure of the hull by approximately twice the reduction in collapse pressure. Submarine diving restrictions associated with corrosion damage are typically arrived at by comparing collapse pressures, not yield pressures, predicted for the intact and damaged hull. That practice could lead to premature yielding in the corroded area at the restricted diving depth, even though the original safety margin on collapse is retained. The concern is that repeated loading could lead to growth in permanent deformations that would eventually lead to collapse at the restricted diving depth.

One of the corroded test specimens was cyclically loaded past the yield pressure in order to study the possibility of cyclic plastic collapse. Incremental growth in plastic strain at the corrosion damage was found to diminish with each load cycle, and gradually approached zero. The incremental strains tend to die off because the plastic deformations are not great enough to initiate a self-perpetuating feedback loop of large deformations leading to larger bending moments, leading to larger deformations, and so on. The plastic deformation did not apparently affect the ultimate collapse strength of the test cylinder.

Standard finite element modeling rules

A standard finite element methodology was established for predicting the collapse pressure and mode of a submarine pressure hull. The modeling rules were developed through a combination of practical experience, literature review, and comparisons between FE simulations and test results. Only those numerical methods that are well-established and easily accessible by the designer, i.e., available in commercial FE software, were considered. The standard FE modeling rules are described, in abbreviated form, in the following paragraphs.

The standard methodology is based on quadrilateral shell element modeling of the hull plating and ring-stiffeners in a mesh of approximately square elements. A mesh convergence study is performed for each novel hull configuration. A converged mesh is achieved if the predicted collapse pressure is within 1% of an FE model with half the mesh density.

Design-stage calculations are carried out for a range of overall out-of-circularity shapes (n=2 to n=6) at the maximum amplitude allowed by the construction and acceptance tolerances. Short wave-length interframe nucleators, in the critical interframe buckling mode and at an amplitude based on the fabrication tolerance for interframe distortions, are superimposed on the overall OOC shape for each analysis. For through-life hull assessments, discrete data representing measured out-of-circularity and/or shell thicknesses are decomposed into two-dimensional Fourier series. Those continuous, nonlinear maps of OOC and shell thickness are then applied to the nodal coordinates and shell elements, respectively, of the initially shape-perfect FE model. FE models for both design-stage and through-life collapse predictions incorporate geometric tolerances in a pessimistic manner, unless measured data is available and can be included in the model.

Support structures, such as test specimen end-caps or watertight bulkheads in real hulls, are implicitly modeled using boundary conditions. A uniform external pressure load is applied to the shell elements representing the hull plating. Equivalent edge pressures are applied to the shell elements on the ends of the compartment to account for the axial load that is transferred by the end-caps.

Material models are based on the isotropic von Mises yield surface, and are populated with the material properties in the weakest direction. Kinematic hardening is used to account for the Bauschinger effect. Design-stage calculations use the minimum specified material properties in a bilinear elastic-perfectly-plastic material model. Overlay models are used for multi-linear curves based on measured stress-strain data. Residual stresses due to cold rolling of the hull plating and ring-stiffeners are accounted for using effective stress-strain curves.

A Lagrangian and/or co-rotational system are used to account for large displacements and rotations. A quasi-static incremental analysis is performed, with a Newton-Raphson iterative approach to solving the nonlinear equations at each step. The load-displacement response of the hull is followed using an arc-length approach, i.e., generalized displacement control. The follower-force effect is captured by updating the direction of the pressure load at each load increment. The nonlinear analysis is carried far enough into the post-collapse region to ensure that the ultimate collapse pressure has been reached. The predicted collapse pressure is taken as the maximum point on the numerical load-displacement curve.

Corrosion damage assessments require special consideration. General corrosion damage may be idealized as a rectangular patch of uniform thinning if it is impractical to model the actual shape of the affected area. The size of the idealized patch is based on the largest circumferential and longitudinal extents of the real patch, and its depth is equal to the maximum measured thinning.

Where the corrosion damage affects only one side of the hull, the resulting eccentricity of the corroded shell is included in the model. The preferred method involves specifying an offset of the shell mid-plane relative to the element nodes, so that the corroded shell is flush with the inside or outside of the intact hull, as appropriate.

Ground-out corrosion pits are normally modeled individually in the same manner as general corrosion. A group of closely spaced corrosion pits may be modeled as a single patch of general corrosion that extends to the boundaries of the damaged area, with a depth equal to that of the deepest pit in the group.

Care should be taken to ensure that the corrosion damage is positioned correctly on the hull, especially when the measured shape of the hull will be used in the FE analysis. When the true shape of the hull is unknown, assumed design-stage imperfections are used. In that case, the corrosion is aligned in-phase with the OOC to ensure a conservative assessment of its effect on collapse.

Accuracy of finite element collapse predictions

In this thesis, the accuracy of finite element pressure hull collapse predictions was estimated by following, to the extent possible, a formal verification and validation methodology. The author performed both the experimental and numerical modeling for validation. The V&V community discourages that approach since deliberate or accidental tuning of the numerical model may result from the foreknowledge of the test results. That "conflict of interest" was addressed by intentionally tuning the FE models in an initial calibration exercise benchmarked against some of the test data. The standardized numerical procedure was then rigidly applied to the remaining test specimens in a one-specimen, one-analysis approach (after appropriate mesh convergence studies). It was originally intended that only the latter experimental-numerical comparisons would be used in the final accuracy assessment. In the end, all of the experimental-numerical comparisons, including the calibration study data, were used in the validation case, but only because that choice led to a conservative outcome in terms of accuracy and the associated partial safety factor.

One of the main challenges in the current research was to understand, minimize, quantify and justify uncertainty. The error in the FE models was isolated as much as possible by minimizing the experimental uncertainty through careful measurements of test specimen geometry, material and loading. Despite those efforts, it was accepted that a certain degree of irreducible experimental uncertainty would (conservatively) affect the FE accuracy assessment. Error and uncertainty in the FE predictions were minimized by developing modeling rules through systematic study of the effect of modeling and analysis choices on accuracy. Furthermore, FE models with the highest degree of fidelity possible were produced by incorporating the detailed measurements of each test specimen.

Numerical error associated with the discretized finite element solution of the underlying shell equations (as opposed to the total numerical error that includes shortcomings in the physical model itself) was minimized by using well-converged meshes. More advanced methods of quantifying and minimizing the numerical discretization error, such as *a posteriori* error estimation and adaptive meshing schemes, respectively, were not studied. It was felt that the discretization error was sufficiently, if not efficiently, controlled by using well-refined meshes. Furthermore, the main goal of the current work was to estimate the total error in the numerical predictions. Thus, while acknowledging that a certain amount of discretization error plays a role in the FE accuracy, it has been captured in the overall accuracy assessment. In that context, it was felt that more sophisticated estimates of the discretization error would not be useful.

It was accepted that some experimental scatter would be mixed in with the FE error in the experimental-numerical comparisons. The challenge, then, was to identify a strategy to quantify the net uncertainty. For the purposes of this work, that uncertainty is considered to represent the FE error in collapse pressure predictions, even though some experimental scatter is included. Considering the small degree of scatter in the FE predictions, that approach is justified. The uncertainty was quantified by applying a normal probability distribution to the validation data, and using that distribution to predict the range within which the error of a future FE prediction would fall. The standard statistical confidence of 95% was used to quantify FE accuracy. A higher level of confidence was applied to the statistical methodology when it was extended to the derivation of a partial safety factor.

The standard FE methodology is significantly more accurate than conventional analytical-empirical and numerical collapse predictions. The current validation study found that FE predictions are accurate to within 10%, with 95% confidence, for a variety of hull configurations, materials, failure modes, imperfections and corrosion damage cases. That result is in excellent agreement with similarly high-fidelity FE collapse predictions that were collected from the literature, which were accurate to within approximately 9% with 95% confidence. The data from the literature include collapse tests on realistic pressure hull models constructed of cold-rolled and welded steel, which adds credibility to the current accuracy assessment.

The FE accuracy can be expected to be poorest in the absence of a strong geometric perturbation in the model, e.g., large-amplitude out-of-circularity, corrosion damage, or denting. In the current work, the accuracy of FE models for nearly shape-perfect test specimens was approximately 14% with 95% confidence, while FE models for similarly shape-perfect specimens with corrosion damage were accurate to within 9.5%. That stands out against the findings for conventional predictive models, which are significantly less accurate when non-axisymmetric damage is present in the hull. FE models of specimens with large-amplitude OOC were even more accurate, within 7% for both corroded and intact cases.

The prediction of the characteristic collapse mode and location, and the pressure-strain relationships at critical locations, were not used directly in the calculation of FE accuracy. Nonetheless, comparison of measured and predicted responses demonstrate that the FE predictions are not spurious, i.e., that the FE models predict the correct collapse pressure for the correct reasons. FE models are capable of predicting the correct failure mode (i.e., elastic buckling, elasto-plastic interfame or overall collapse) as long as the geometry and material are modeled with sufficient fidelity. The prediction of the correct location of collapse is possible in most cases. As with collapse pressure, it is more difficult to predict the correct collapse location in nearly shape-perfect models compared to those with large geometric imperfections or defects.

In general, prediction of the pressure-strain response was best in the linear-elastic region. In most cases, the nonlinear response was slightly delayed in the FE models compared to the test specimens, leading to an over-prediction of collapse pressure. In fact, the data in the literature support the conclusion that non-conservative collapse predictions are a hallmark of FE predictions for pressure hulls. Despite the high-fidelity nature of the FE models, there are many simplifications related to the material modeling, geometry and end support that could contribute to the over-predictions. Furthermore, the previously mentioned descretization error and shell theory approximations are also a factor in the total numerical model error. It is the opinion of the author that some of the FE error is associated with the neglect of the cumulative effect of small material and geometric defects that tend to perturb the structure and induce collapse. Those defects, which could include impurities, voids and cracks in the material, are difficult to detect and to model, so that it is impractical to prove through experimental-numerical comparisons. Nonetheless, the hypothesis is supported by the improvement in FE accuracy when severe defects are known to exist in the structure.

Predictive accuracy has been established for an over-arching numerical methodology. It can be argued that the methodology has been validated, rather than a particular software program. In the current work, the complete validation study was only performed for the FE models produced using an in-house pre-processor (CylMesh) and the ANSYS solver. On the other hand, it was demonstrated that FE accuracy is relatively insensitive to the pre-processing methods and solver, as long as the overall methodology is the same. Geometrically identical FE models of four test specimens were analyzed with three different FE solvers (ANSYS, MARC and VAST), giving collapse pressures that were in agreement within 2.8% of each other. Furthermore, two sets of FE simulations of twenty test specimens, using different pre-processor/solver combinations (CylMesh/ANSYS and

SubSAS/VAST) gave accuracies of 11.4% and 10.7%, respectively, with 95% confidence. In the end, it is concluded that only the ANSYS solver has been properly validated, but that any capable pre-processor may be used to generate ANSYS FE models.

Numerical design framework

A numerical framework for the design of submarine pressure hulls has been presented. The numerical methodology and the associated partial safety factor are only applicable to conventional ring-stiffened cylindrical pressure hulls made of roughly isotropic metals like steel and aluminium. The effective stress-strain curve approach to dealing with fabrication-induced residual stresses is advocated, but it has not been validated against experiments. Strictly speaking then, the current numerical design framework is only applicable to stress-relieved pressure hulls.

FE models from the literature that included a numerical simulation of cold-rolling before the collapse analysis gave almost the same accuracy as the current modeling work. Furthermore, a separate study from the literature showed that effective stress-strain curves were as effective as full fabrication simulations at capturing the effect of residual stresses on collapse. Thus, it is likely that effective stress-strain curves can be used in the analysis of hulls that are not stress-relieved without affecting the accuracy.

It is also important to note that the collapse of torospherical domes and internal watertight bulkheads that support the hull has not been studied. The design of those structures must still rely on the conventional analytical-empirical methods. Furthermore, the FE accuracy has not been studied for hulls made of non-homogenous materials like composites, which require sophisticated material models to deal with anisotropies and delamination failure modes.

The numerical design framework includes a set of FE modeling rules that can accommodate both design-stage and through-life collapse prediction requirements. The new framework mirrors the conventional methodology, in that it is deterministic, with separate partial safety factors that account for errors in the predictive model, fabrication procedures, and loading. That allowed a PSF to be developed specifically for FE predictions, while retaining the existing PSFs for fabrication and loading errors. Furthermore, the numerical approach to design tolerances and out-of-circularity is based on the conventional procedure.

The statistical approach used to quantify FE accuracy was modified to suit the derivation of a PSF. In that way, the modeling error and the irreducible experimental uncertainty are both included in the PSF. The statistical method accounts for the size of the validation sample and is relatively insensitive to outliers in those data. In that way, it improves upon the traditional lower-bound approach, whereby the PSF is associated with the maximum error observed in the validation program. Furthermore, the statistical approach allows the PSF to be based on a well-defined level of confidence.

The recommended PSF=1.134 gives the designer 99.5% confidence that the FE error is accounted for, provided that the modeling rules are carefully followed. That level of confidence is stringent compared to the PSFs used with conventional methods, but it is justified due to the limited experimental data and the novelty of the numerical design approach. Furthermore, it is consistent with the existing confidence level imposed on fatigue failure predictions, which are associated with a similarly catastrophic outcome if they are incorrect.

Recommendations and Future Work

The level of confidence associated with the partial safety factor used with the empirical interframe design curve has been shown to be relatively modest (90%). The design curve and PSF have been successfully used to design submarines for decades, so the validity of the approach is not in question. On the other hand, the relatively small PSF does not account for all, or even a statistically significant fraction, of the modeling error (i.e., the PSF does not give the designer at least 95% confidence that the predictive error is accounted for). By neglecting some of the uncertainty associated with the design curve, the margin of safety implied by the other PSFs, e.g., for fabrication errors, is eroded. The actual margin of safety implied by the PSFs for the design curve and the other predictive models used in design, such as the finite difference method for overall collapse, should be evaluated in light of the probabilistic approach taken in this thesis.

With respect to pressure testing of buckling-critical shells, the simple equations presented in this thesis can be used to help choose the best testing method for the application. Furthermore, it is recommended that specimen deformations be monitored throughout loading using strain gauges or displacement transducers, even if measures, such as the volume-control test setup, are taken to improve control. Those measurements are needed in order to differentiate between the final post-testing shape of the specimen and the actual collapse mode, since it is impractical to completely control the specimen response during collapse.

Numerical assessments of pressure hull corrosion damage require specialized modeling, as discussed above. Corrosion damage and out-of-circularity were found to interact strongly. Care should be taken to include the as-built out-of-circularity, and the correct position of the corrosion with respect to that shape, in the FE model. The sensitivity of corroded hulls to strain hardening emphasizes the importance of using realistic material models in FE simulations of in-service hulls, especially if an accurate damage assessment is required. If measured material data are unavailable, elastic-perfectly-plastic material models will lead to conservative assessments of the effect of corrosion damage on hull strength. The experiments showed that cyclic plastic collapse of corroded hulls is not likely a concern, so that diving depth restrictions may continue to be based on a collapse pressure, rather than a yield pressure, criterion.

The effect of corrosion damage on hull strength is sensitive to the axisymmetric configuration (i.e., the collapse mode), as well as the location of the damage with respect to out-of-circularity. Furthermore, the response of the damaged hull is influenced by other factors not studied here, such as interaction of corrosion with penetrations and internal structures [159]. It is, therefore, impractical to generate a generally applicable set of corrosion knock-down curves for pressure hulls using, for example, nonlinear FE simulations. It may be possible to produce those types of corrosion curves for individual in-service submarines with known hull configurations and OOC shapes, since the number of parameters that must be studied is significantly reduced. However, if corrosion damage is allowed to accumulate on different parts of the hull, the recommended approach is to use the validated FE methodology presented here to assess the hull in its actual condition.

The proposed numerical design framework is restricted to the analysis of ring-stiffened cylindrical pressure hulls using a particular FE program. Further research is required to extend the FE validation to the other major components of a conventional pressure hull, such as domes and stiffened bulkheads, so that a complete hull can be assessed in a single analysis. In that way, the interaction of a greater number of failure modes and structures could be captured by the FE model, and confidence in the overall design would be enhanced. The modeling of unconventional, but potentially advantageous, hull materials, such as composites, could also be studied. For conventional steel hulls, future work must consider the validity of using effective stress-strain curves to account for cold rolling and/or welding stresses, and the FE predictions should be compared with appropriate test results to ensure that accuracy is not degraded. Finally, the insensitivity of the collapse prediction to the particular FE solver suggests that, in the future, the validation exercise may be extended to any software program, e.g., through limited comparisons with benchmark problems.

The proposed numerical design framework is very similar to the conventional deterministic design methodology. That is intentional, since acceptance of nonlinear FE collapse predictions by the submarine design community is considered a large enough obstacle to overcome by itself, without introducing novelty to the overall design philosophy. In the future, however, it may be desirable to use FE analysis in the context of a hierarchical design procedure (e.g., using conventional methods for optimization, with a final strength assessment by FE analysis) or in a reliability setting. A reliability approach could address all uncertainties in the design, and could make use of the statistical data describing the experimental-numerical comparisons that are presented in this thesis.

The numerical design framework presented herein does not consider many of the finer details that must be addressed in the course of submarine design, such as penetration reinforcement and transitions between cylinders and cones. Those aspects of design must be prescribed by a formal procedure. The current work was largely aimed at establishing credibility and confidence in FE collapse predictions through comparisons with test results. Credibility in a formal numerical design procedure, whether it is based on the proposed framework or some other approach, can only be created through the consensus of a panel of experts from government, industry and the research community.

References

1. R. Burcher, L. Rydill, Concepts in submarine design, Cambridge University Press, Cambridge, 1994.

2. E.C. Tupper, Introduction to naval architecture, Third edition, The Society of Naval Architects and Marine Engineers, Jersey City, 1996.

3. J. Blachut, Developments in strength and stability of shell components used in submersibles, in: W. Pietraszkiewicz, I. Kreja (Eds.), Shell structures: Theory and applications, Volume 2, CRC Press/Balkema, Leiden, 2010, pp. 3-10.

4. Jane's Fighting Ships (http://jfs.janes.com/public/jfs/index.shtml), IHS Global, Access date: 13 December 2011.

5. DPA, SSP 74 Design of submarine structures, Defence Procurement Agency, Sea Technology Group, United Kingdom, 2001.

6. BSI, BS 5500 British standard specification for unfired fusion welded pressure vessels, Issue 5, British Standards Institution (BSI), United Kingdom, 1980.

7. ECCS, Buckling of steel shells: European recommendations, European Convention for Constructional Steelwork (ECCS), Brussels, 1988.

8. S. Kendrick, The influence of shape imperfections and residual stresses on the collapse of stiffened cylinders, in: Proceedings of the conference on significance of deviations from design shape, Institute of Mechanical Engineers, 1979, pp. 25-35.

9. S.B. Kendrick, Analysis of the results of static pressure tests of Chatham submarine models (NCRE Report R218), Naval Construction Research Establishment, Dunfermline, 1955.

10. S. Kendrick, Externally Pressurized Vessels, in: S.S. Gill (Ed.), The stress analysis of pressure vessels and pressure vessel components, Pergamon Press, Toronto, 1970, pp. 405-511.

11. S. Kendrick, Design for external pressure using general criteria, *Int. J. Mech. Sci.* 24 (1982) 209-18.

12. M.J. Smith, Structural modeling and strength assessment of the Victoria-class submarine pressure hull, *Marit. Eng. J.*, Fall 2005 9-13.

13. J.R. MacKay, M.J. Smith, N.G. Pegg, Design of pressure hulls using nonlinear finite element analysis (OMAE2006-92591), in: 25th International conference on offshore mechanics and arctic engineering, American Society of Mechanical Engineers, Hamburg, 2006.

14. D.J. Creswell, R.S. Dow, The application of nonlinear analysis to ship and submarine structures, in: C.S. Smith, J.D. Clarke (Eds.), Advances in marine structures: Proceedings of an international conference, Admiralty Research Establishment, Dunfermline, 1986, pp. 174-200.

15. D. Graham, I. Keron, G. Mitchell, D. Creswell, DRA structural research on submarines and submersibles, in: Proceedings of the Charles Smith memorial conference: Recent developments in structural research, Defence Research Admiralty, Dunfermline, 1992.

16. A.C. Morandi, P.K. Das, D. Faulkner, Finite element analysis and reliability based design of externally pressurized ring stiffened cylinders, *Trans. R. Inst. Nav. Archit.* 138 (1996) 171-88.

17. I. Keron, D. Graham, J. Farnworth, N. Anderson, Recent developments in the analysis and design of submarine structures, in: Advances in marine structures 3, Defence Evaluation and Research Agency, Rosyth, 1997.

18. R.F. Lennon, P.K. Das, The effect of cold forming and welding locked in stress states on the buckling resistance of orthogonally stiffened cylinders, in: Advances in marine structures 3, Defence Evaluation and Research Agency, Rosyth, 1997.

19. D.W. Chalmers, in written discussion of M.J. Smith, J.R. MacKay, Overall elasto-plastic collapse of ring stiffened cylinders with corrosion damage, *Trans. R. Inst. Nav. Archit. Part 1A – Int. J. Marit. Eng.* 147 (2005) 53-61.

20. J.R. MacKay, F. van Keulen, M.J. Smith, Quantifying the accuracy of numerical collapse predictions for the design of submarine pressure hulls, *Thin-Wall. Struct.* 49 (2011) 145-56.

21. J.R. MacKay, F. van Keulen, A review of external pressure testing techniques for shells including a novel volume-control method, *Exp. Mech.* 50 (2010) 753-72.

22. J.R. MacKay, M.J. Smith, F. van Keulen, T.N. Bosman, N.G. Pegg, Experimental investigation of the strength and stability of submarine

pressure hulls with and without artificial corrosion damage, *Mar. Struct.* 23 (2010) 339-59.

23. J.R. MacKay, F. van Keulen, The sensitivity of overall collapse of damaged submarine pressure hulls to material strength, *J. Offshore Mech. & Arct. Eng.* (2012) in press.
24. J.R. MacKay, M.J. Smith, F. van Keulen, T.N. Bosman, Experimental study of the interaction of corrosion damage and out-of-circularity in the collapse of submarine pressure hulls, submitted to *Trans. R. Inst. Nav. Archit. Part 1A – Int. J. Marit. Eng.* (2011).
25. J.R. MacKay, L. Jiang, A.H. Glas, Accuracy of nonlinear finite element collapse predictions for submarine pressure hulls with and without artificial corrosion damage, *Mar. Struct.* 24 (2011) 292-317.
26. J.R. MacKay, F. van Keulen, Partial safety factor approach to the design of submarine pressure hulls using nonlinear finite element analysis, submitted to *Finite Elem. Anal. & Des.* (2012).
27. J. R. MacKay, Experimental investigation of the strength of damaged pressure hulls – Phase 1 (DRDC Atlantic TM 2006-304), Defence R&D Canada – Atlantic, Dartmouth, 2007.
28. J. R. MacKay, Experimental investigation of the strength of damaged pressure hulls – Phase 2: Summary of experimental results (DRDC Atlantic TM 2007-013), Defence R&D Canada – Atlantic, Dartmouth, 2007.
29. J. R. MacKay, Experimental investigation of the strength of damaged pressure hulls – Phase 3 (DRDC Atlantic TM 2008-093), Defence R&D Canada – Atlantic, Dartmouth, 2008.
30. J. R. MacKay, Experimental investigation of the strength of damaged pressure hulls – Phase 4: The influence of material properties on pressure hull collapse (DRDC Atlantic TM 2009-299), Defence R&D Canada – Atlantic, Dartmouth, 2010.
31. J. R. MacKay, Experimental investigation of the strength of damaged pressure hulls – Phases 5 & 6: The influence of out-of-circularity on collapse (DRDC Atlantic TM 2010-239), Defence R&D Canada – Atlantic, Dartmouth, 2011.
32. J. R. MacKay, Experimental investigation of the strength of damaged pressure hulls – Phase 7: The interaction of multiple corrosion

damage cases (DRDC Atlantic TM 2011-034), Defence R&D Canada – Atlantic, Dartmouth, 2011.

33. J. R. MacKay, Experimental investigation of the strength of damaged pressure hulls: Master list of experimental specimens (DRDC Atlantic TN 2011-058), Defence R&D Canada – Atlantic, Dartmouth, 2011.

34. C.T.F. Ross, Pressure vessels under external pressure: statics and dynamics, Elsevier Science Publishing, New York, 1990.

35. B.H. Thacker, S.W. Doebling, F.M. Hemez, M.C. Anderson, J.E. Pepin, E.A. Rodriguez, Concepts of model verification and validation (LA-14167-MS), Los Alamos National Laboratory, Los Alamos, 2004.

36. ASME, ASME V&V 10-2006: Guide for verification and validation in computational solid mechanics, American Society of Mechanical Engineers (ASME), New York, 2006.

37. D. Faulkner, C. Guedes Soares, D.M. Warwick, Modeling requirements for structural design and assessment, in: D. Faulkner, M.J. Cowling, A. Incecik (Eds.), Integrity of offshore structures – 3, Elsevier Applied Science, London, 1987, pp. 25-54.

38. P.K. Das, Reliability based design of submarine structures (OMAE98-1303), in: Proceedings of the 17th International Conference on Offshore Mechanics and Arctic Engineering, American Society of Mechanical Engineers, Lisbon, 1998.

39. P. Thoft-Christensen, M.J. Baker, Structural reliability theory and its applications, Springer-Verlag, New York, 1982.

40. D.C. Montgomery, C.G. Runger, Applied statistics and probability for engineers, Fourth edition, John Wiley & Sons, Inc., Hoboken, 2007.

41. G.C. Mitchell, Overbend prediction for cold-bent beams, *Comput. & Struct.* 24 (1986) 187-96.

42. M.J. Smith, J.R. MacKay, Overall elasto-plastic collapse of ring stiffened cylinders with corrosion damage, *Trans. R. Inst. Nav. Archit. Part 1A – Int. J. Marit. Eng.* 147 (2005) 53-61.

43. S. Aghajari, K. Abedi, H. Showkati, Buckling and post-buckling behavior of thin-walled cylindrical steel shells with varying thickness subjected to uniform external pressure, *Thin-Wall. Struct.* 44 (2006) 904-9.

44. D. Boote, D. Mascia, M. Monti, E. Rizzuto, R. Tedeschi, Elastic instability of thin cylindrical shells: numerical and experimental investigation, *Ocean Eng.* 24 (1997) 133-60.

45. D. Bushnell, Buckling of elastic-plastic shells of revolution with discrete elastic-plastic ring stiffeners, *Int. J. Solids & Struct.* 12 (1976) 51-66.

46. D. Bushnell, Effect of cold bending and welding on buckling of ring-stiffened cylinders, *Comput. & Struct.* 12 (1980) 291-307.

47. L. Gannon, Prediction of the effects of cold bending on submarine pressure hull collapse (DRDC Atlantic TM 2010-065), Defence Research and Development Canada – Atlantic, Dartmouth, 2010.

48. D. Graham, Predicting the collapse of externally pressurised ring-stiffened cylinders using finite element analysis, *Mar. Struct.* 20 (2007) 202-17.

49. D. Graham, A partial safety factor for pressure hull collapse prediction using finite element analysis, in: Warship 2008: Naval Submarines 9, Royal Institution of Naval Architects, Glasgow, 2008.

50. P. Le Grognec, P. Casari, D. Choqueuse, Influence of residual stresses and geometric imperfections on the elastoplastic collapse of cylindrical tubes under external pressure, *Mar. Struct.* 22 (2009) 836-54.

51. L. Jiang, J.R. MacKay, J. Wallace, M.J. Smith, M. Norwood, T. Bosman, Finite element modeling of collapse experiments of ring stiffened cylinders with simulated corrosion damage, in: Warship 2008: Naval Submarines 9, Royal Institution of Naval Architects, Glasgow, 2008.

52. B. Moradi, I.D. Parsons, A comparison of techniques for computing the buckling loads of stiffened shells, *Comput. & Struct.* 46 (1993) 505-14.

53. P. Radha, K. Rajagopalan, Ultimate strength of submarine pressure hulls with failure governed by inelastic buckling, *Thin-Wall. Struct.* *44* (2006) 309-13.

54. C.T.F. Ross, T. Johns, Plastic axisymmetric collapse of thin-walled circular cylinders and cones under uniform external pressure, *Thin-Wall. Struct.* 30 (1998) 35-54.

55. Z. Şanal, Nonlinear analysis of pressure vessels: some examples, *Int. J. Press. Vessels & Pip.* 77 (2000) 705-9.

56. ABAQUS theory and user's manual, version 5.8, Hibbitt, Karlsson, Sorensen, Inc., Pawtucket, 1998.

57. SAS IP, Inc., ANSYS release 9.0 documentation, ANSYS Inc., Canonsburg, 2004.

58. MARC user manual, version K6.2, MARC Analysis Research Corporation, 1996.

59. DISPLAY III & NISA user's manural: I & II, EMRC, Michigan, 1989.

60. C.C. Rankin, A. Brogan, W.A. Loden, H.D. Cabiness, STAGS user's manual, version 3.0 (Report LMSC P032594), Lockheed Martin Missiles & Space Co., Inc., Palo Alto, 1999.

61. Vibration and Strength Analysis (VAST), version 8.5, user's manual, Martec Limited, Halifax, 2003.

62. W.T. Koiter, A comparison between John's refined interior shell equations and classical shell theory, *Z. Angew. Math. & Phys.* 20 (1969) 642-52.

63. A.C. Morandi, P.K. Das, D. Faulkner, Reliability-based design of externally pressurized vessels, *J. Offshore Mech. & Arct. Eng.* 120 (1998) 149-53.

64. E. Ramm, H. Stegmüller, The displacement finite element method in nonlinear buckling analysis of shells, in: E. Ramm (Ed.), Buckling of shells: proceedings of a state-of-the-art colloquium, Springer, New York, 1982, pp. 201-35.

65. M.A. Crisfield, Nonlinear Finite Element Analysis of Solids and Structures, Volume 1: Essentials, John Wiley & Sons Ltd., Toronto, 1991.

66. R.F. Jones Jr., M.G. Costello, T.E. Reynolds, Buckling of pressure loaded rings and shells by the finite element method, *Comput. & Struct.* 7 (1977) 267-74.

67. W.B. Krätzig, D. Jun, On 'best' shell models – From classical shells, degenerated and multi-layered concepts to 3D, *Arch. Appl. Mech.* 73 (2003) 1-25.

68. W. Gilewski, M. Radwańska, A survey of finite element models for the analysis of moderately thick shells, *Finite Elem. Anal. & Des.* 9 (1991) 1-21.

69. H.T.Y. Yang, S. Saigal, A. Masud, R.K. Kapania, A survey of recent shell finite elements, *Int. J. Numer. Methods Eng.* 47 (2000) 101-27.

70. L. Wullschleger, H.-R. Meyer-Piening, Buckling of geometrically imperfect cylindrical shells – definition of a buckling load, *Int. J. Non-Linear Mech.* 37 (2002) 645-57.

71. B. Skallerud, L.I. Myklebust, B. Haugen, Nonlinear response of shell structures: effects of plasticity modeling and large rotations, *Thin-Wall. Struct.* 39 (2001) 463-82.

72. N.F. Knight Jr., S.C. Macy, S.L. McCleary, Assessment of structural analysis technology for static collapse of elastic cylindrical shells, *Finite Elem. Anal. & Des.* 18 (1995) 403-31.

73. D. Faulkner, Effects of residual stresses on the ductile strength of plane welded grillages and of ring stiffened cylinders, *J. Strain Anal.* 12 (1977) 130-39.

74. J. Arbocz, J.H. Starnes Jr., Future directions and challenges in shell stability analysis, *Thin-Wall. Struct.* 40 (2002) 729-54.

75. K.K. Choong, E. Ramm, Simulation of buckling process of shells by using the finite element method, *Thin-Wall. Struct.* 31 (1998) 39-72.

76. C. Bisagni, Numerical analysis and experimental correlation of composite shell buckling and post-buckling, *Composites: Part B* 31 (2000) 655-67.

77. E. Riks, An incremental approach to the solution of snapping and buckling problems, *Int. J. Solids & Struct.* 15 (1979) 529-51.

78. M.A. Crisfield, A fast incremental/iterative solution procedure that handles "snap-through", *Comput. & Struct.* 13 (1981) 55-62.

79. CEN, Eurocode 3 – Design of steel structures – Part 1-6: Strength and Stability of Shell Structures, European Committee for Standardization (CEN), Brussels, 2007.

80. J. Arbocz, H. Abramovich, The initial imperfection data bank at the Delft University of Technology – Part I (Report LR-290), Delft University of Technology, Delft, 1979.

81. K.Y. Sze, X.H. Liu, S.H. Lo, Popular benchmark problems for geometric nonlinear analysis of shells, *Finite Elem. Anal. & Des.* 40 (2004) 1551-69.

82. M.J. Clarke, G.J. Hancock, A study of incremental-iterative strategies for non-linear analyses, *Int. J. Numer. Methods Eng.* 29 (1990) 1365-91.

83. V.I. Weingarten, P. Seide, Elastic stability of thin-walled cylindrical and conical shells under combined external pressure and axial compression, *Am. Inst. Aeronaut. Astronaut. J.* 3 (1965) 913-20.

84. L.R.-L. Wang, Boundary disturbance and pressure rate on the buckling of spherical caps, *Am. Inst. Aeronaut. Astronaut. J.* 6 (1968) 2192-3.

85. J. Singer, D. Bendavid, Buckling of electroformed conical shells under hydrostatic pressure, *Am. Inst. Aeronaut. Astronaut. J.* 6 (1968) 2332-8.

86. M.H. Schneider, R.F. Snell, J.J. Tracy, D.R. Power, Buckling and vibration of externally pressurized conical shells with continuous and discontinuous rings, *Am. Inst. Aeronaut. Astronaut. J.* 29 (1991) 515-22.

87. W. Guggenberger, Buckling and postbuckling of imperfect cylindrical shells under external pressure, *Thin-Wall. Struct.* 23 (1995) 351-66.

88. J. Singer, J. Arbocz, T. Weller, Buckling experiments: Experimental methods in buckling of thin-walled structures – Volume 1, John Wiley & Sons, Inc., New York, 1998.

89. J. Singer, J. Arbocz, T. Weller, Buckling experiments: Experimental methods in nuckling of thin-walled structures – Volume 2, John Wiley & Sons, Inc., New York, 2002.

90. B.I. Sandor, Mechanics of materials, in: F. Kreith (Ed.), The CRC handbook of mechanical engineering, CRC Press, Inc., Boston, 1998.

91. R.V. Southwell, On the analysis of experimental observations in problems of elastic stability, *Proc. R. Soc., Lond., Ser. A* 135 (1932) 601-16.

92. R.C. Slankard, W.A. Nash, Tests of the elastic stability of a ring-stiffened cylindrical shell, model BR-5 (λ=1.705) subjected to

hydrostatic pressure (DTMB Report 822), David Taylor Model Basin, Carderock, 1953.

93. E. Wenk Jr., R.C. Slankard, W.A. Nash, Experimental analysis of the buckling of cylindrical shells subjected to external hydrostatic pressure, *Exp. Stress Anal.* 12 (1954) 163-80.

94. R.C. Slankard, Tests of the elastic stability of a ring-stiffened cylindrical shell, model BR-4 (λ=1.103), subjected to hydrostatic pressure (DTMB Report 876), David Taylor Model Basin, Carderock, 1955.

95. G.D. Galletly, R.C. Slankard, E. Wenk Jr., General instability of ring-stiffened cylindrical shells subject to external hydrostatic pressure – A comparison of theory and experiment, *J. Appl. Mech.* 25 (1958) 259-66.

96. F.J. Schroeder, E.T. Kusterer, An experimental determination of the stability of conical shells, *J. Appl. Mech.* 30 (1963) 144-6.

97. N.M. Goudie, Collapse tests of two full-scale OBERON class dome bulkheads (NCRE Report L12/TG42/71), Naval Construction Research Establishment, Dunfermline, 1971.

98. C.T.F. Ross, W.R. Aylward, D.T. Boltwood, General instability of ring-reinforced circular cylinders under external pressure, *Trans. R. Inst. Nav. Archit.* 113 (1971) 73-82.

99. S.S. Seleim, J. Roorda, Buckling behaviour of ring-stiffened cylinders, experimental study, *Thin-Wall. Struct.* 4 (1986) 203-22.

100. C.T.F. Ross, T. Johns, Buckling and vibration of ring-stiffened cones under uniform external pressure, *Thin-Wall. Struct.* 6 (1988) 321-42.

101. C.T.F. Ross, T. Johns, Vibration and buckling of a thin-walled dome under external water pressure, *J. Ship Res.* 34 (1990) 142-8.

102. C.T.F. Ross, P. Haynes, A. Seers, T. Johns, Inelastic buckling of ring-stiffened circular cylinders under uniform external pressure, *Struct. Dyn. & Vib.* 70 (1995) 207-15.

103. C.T.F. Ross, D. Popken, Buckling of tube-stiffened prolate domes under external water pressure, *Thin-Wall. Struct.* 22 (1995) 159-79.

104. C.T.F. Ross, Inelastic general instability of ring-stiffened circular cylinders and cones under uniform external pressure, *Struct. Eng. & Mech.* 5 (1997) 193-207.

105. C.T.F. Ross, G.A. Waterman, Inelastic instability of circular corrugated cylinders under external hydrostatic pressure, *Ocean Eng.* 27 (2000) 331-43.

106. C.T.F. Ross, A.P.F. Little, K.A. Adeniyi, Plastic buckling of ring-stiffened conical shells under external hydrostatic pressure, *Ocean Eng.* 32 (2005) 21-36.

107. W. Fairbairn, On the resistance of tubes to collapse, *Philos. Trans. R. Soc.* 148 (1858) 389-413.

108. W.F. Blumenberg, The effect of intermediate heavy frames on the elastic general instability strength of ring-stiffened cylinders under external hydrostatic pressure (DTMB Report 1844), David Taylor Model Basin, Carderock, 1965.

109. G.D. Galletly, R.W. Aylward, D. Bushnell, An experimental and theoretical investigation of elastic and elastic-plastic asymmetric buckling of cylinder-cone combinations subjected to uniform external pressure, *Ing.-Arch.* 43 (1974) 345-58.

110. R.W. Aylward, G.D. Galletly, D.G. Moffat, Buckling under external pressure of cylinders with toriconical or pierced torispherical ends: a comparison of experiment with theory, *J. Mech. Eng. & Sci.* 17 (1975) 11-8.

111. D.J. Creswell, Experimental determination of the elastic collapse pressures of some miniature aluminium stiffened cylinders (AMTE Report R78643B), Admiralty Marine Technology Establishment, Dunfermline, 1978.

112. N.G. Pegg, Experimental determination of interframe buckling of a ring stiffened cylinder (DREA TM 89/209), Defence Research Establishment Atlantic, Dartmouth, 1989.

113. T.N. Bosman, N.G. Pegg, P.J. Keuning, Experimental and numerical determination of the nonlinear overall collapse of imperfect pressure hull compartments, in: Proceedings of Warship '93, International symposium on naval submarines 4, Royal Institution of Naval Architects, London, 1993.

114. C.T.F. Ross, M. Humphries, The buckling of corrugated circular cylinders under uniform external pressure, *Thin-Wall. Struct.* 17 (1993) 259-71.

115. C.T.F. Ross, A. Palmer, General instability of swedge-stiffened circular cylinders under uniform external pressure, *J. Ship Res.* 37 (1993) 77-85.

116. C.T.F. Ross, J.R. Sadler, Inelastic shell instability of thin-walled circular cylinders under external pressure, *Ocean Eng.* 27 (2000) 765-74.

117. S.C. Oliveira Jr., I.P. Pasqualino, T.A. Netto, Experimental analysis of metal-composite pipes under external pressure (OMAE2006-92485), in: 25th International conference on offshore mechanics and arctic engineering, American Society of Mechanical Engineers, Hamburg, 2006.

118. A. Liessem, U. Marewski, J. Groß-Weege, G. Knauf, Methods for collapse pressure prediction of UOE linepipe (OMAE2006-92147), in: 25th International conference on offshore mechanics and arctic engineering, American Society of Mechanical Engineers, Hamburg, 2006.

119. C.T.F. Ross, A.P.F. Little, G. Brown, A. Nagappan, Inelastic shell instability of geometrically imperfect aluminum alloy circular cylinders under uniform external pressure, *Mar. Tech.* 45 (2008) 175-81.

120. L. Boichot, T.E. Reynolds, Inelastic buckling tests of ring-stiffened cylinders under hydrostatic pressure (DTMB Report 1992), David Taylor Model Basin, Carderock, 1965.

121. Md. Raisuddin Khan, M.A. Salam Akanda, Md. Wahhaj Uddin, A new approach for instability testing of shells, *Int. J. Press. Vessels & Pip.* 75 (1998) 75-80.

122. J. Blachut, Buckling of externally pressurized barrelled shells: a comparison of experiment and theory, *Int. J. Press. Vessels & Pip.* 79 (2002) 507-17.

123. J. Blachut, Collapse tests on externally pressurized toroids, *J. Press. Vessel Tech.* 125 (2003) 91-6.

124. J.C. New, A nondestructive differential-pressure test for thin shells, *J. Appl. Mech.* 75 (1953) 48-52.

125. W.F. Blumenberg, T.E. Reynolds, Elastic general instability of ring-stiffened cylinders with intermediate heavy frames under external hydrostatic pressure (DTMB Report 1588), David Taylor Model Basin, Carderock, 1955.

126. R.K. Kinra, Hydrostatic and axial collapse tests of stiffened cylinders, *J. Petrol. Tech.* 30 (1978) 668-80.

127. W.R. Midgley, A.E. Johnson Jr., Experimental buckling of internal integral ring-stiffened cylinders, *Exp. Mech.* 13 (1973) 145-53.

128. A.C. Walker, Y. Segal, S. McCall, The buckling of thin-walled ring stiffened steel shells, in: E. Ramm (Ed.), Buckling of shells, Springer, New York, 1982, pp. 275-304.

129. J.E. Harding, P.J. Dowling, A.C. Walker, The buckling design of stringer stiffened shells subjected to combined pressure and axial compression, in: Proceedings 15th annual offshore technology conference, Offshore Technology Conference, Houston, 1983, pp. 267-76.

130. C.D. Miller, R.B. Grove, Current research related to buckling of shells for offshore structures, in: Proceedings 15th annual offshore technology conference, Offshore Technology Conference, Houston, 1983, pp. 277-83.

131. S.K. Tsang, J.E. Harding, A.C. Walker, A. Andronicou, Buckling of ring stiffened cylinders subjected to combined pressure and axial compressive loading, in: Pressure vessels and piping conference, American Society of Mechanical Engineers, Portland, 1983.

132. A.C. Walker, S. McCall, Strength of damaged ring and orthogonally stiffened shells – Part I: plain ring stiffened shells, *Thin-Wall. Struct.* 5 (1987) 425-53.

133. J.J. Giezen, C.D. Babcock, J. Singer, Plastic buckling of cylindrical shells under biaxial loading, *Exp. Mech.* 31 (1991) 337-43.

134. P.A. Frieze, The experimental response of flat-bar stiffeners in cylinders under external pressure, *Mar. Struct.* 7 (1994) 213-30.

135. C.D. Miller, J.F. Vojta, Strength of stiffened cylinders subjected to combinations of axial compression and external pressure, in:

Proceedings of the annual technical session – Structural stability research council: Stability and seismic loading, 1984.

136. G.D. Galletly, K. Pemsing, Interactive buckling tests on cylindrical shells subjected to axial compression and external pressure – A comparison of experiment, theory and various codes, *Proc. Inst. Mech. Eng.* 199 (1985) 259-80.

137. J. Singer, Experimental studies in shell buckling (AIAA-97-1075), in: 38th AIAA/ASME/ASCE/AHS/ASC structures, structural dynamics, and materials conference and exhibit, American Institute of Aeronautics and Astronautics, Orlando, 1997, pp. 1922-32.

138. S.B. Kendrick, Shape imperfections in cylinders and spheres: Their importance in design and methods of measurement, *J. Strain Anal.* 12 (1977) 117-22.

139. C. Bayley, J. MacKay, Strategic research agenda: Verification and validation of numerical welding approaches (DRDC Atlantic TM 2009-170), Defence R&D Canada – Atlantic, Dartmouth, 2009.

140. Online Materials Information Source – MatWeb (http://www.matweb.com), Automation Creations, Inc., Access date: 3 November 2010.

141. C. Bayley, Stress-strain characterization of NQ1 pressure hull material (DRDC Atlantic TN 2007-328), Defence R&D Canada – Atlantic, Dartmouth, 2007.

142. R.D. Hibbeler, Mechanics of materials, Third edition, Prentice Hall Canada, Inc., Toronto, 1997.

143. SAS IP, Inc., Release 11.0 documentation for ANSYS, ANSYS Inc., Canonsburg, 2007.

144. Vibration and Strength Analysis (VAST), version 8.8, user's manual, Martec Limited, Halifax, 2008.

145. MARC 2007r1, User's guide, MSC Software, Santa Ana, 2007.

146. SubSAS: an integrated suite of submarine structural analysis codes user's manual (Martec Software Manual SM-04-14), Martec Limited, Halifax, 2004.

147. L. Jiang, J. Wallace, Submarine structure modeling and analysis for life-cycle management, Phase 2 – Final report (Martec Technical Report TR-07-59), Martec Limited, Halifax, 2008.

148. L. Jiang, J. Wallace, Submarine structure modeling and analysis for life-cycle management, Phase 4 – Final report (Martec Technical Report TR-08-49), Martec Limited, Halifax, 2008.

149. L. Jiang, T. MacAdam, J. Wallace, Structural analyses of phase 3 experimental collapse specimens (Martec Technical Report TR-09-79), Martec Limited, Halifax, 2009.

150. E.N. Dvorkin, K.J. Bathe, A continuum mechanics based four-node shell element for general nonlinear analysis, *Eng. Comput.* 1 (1984) 77-88.

151. MARC 2007r1, Volume A: Theory and user information, MSC Software, Santa Ana, 2007.

152. X. Lin, J.G. Teng, Iterative Fourier decomposition of imperfection measurements at non-uniformly distributed sampling points, *Thin-Wall. Struct.* 41 (2003) 901-24.

153. R. De Borst, P.H. Feenstra, Studies in anisotropic plasticity with reference to hill criterion, *Int. J. Numer. Methods Eng.* 29 (1990) 315-36.

154. S.B. Kendrick, Design of submarine structures, in: C.S. Smith and J.D. Clarke (Eds.), Advances in Marine Structures, Elsevier Science Publishing Co., Inc., New York, 1986, pp. 411-34.

155. G.J. Teng, Buckling of thin shells: Recent advances and trends, *Appl. Mech. Rev.* 49 (1996) 263-74.

156. V.L. Schmidt, Stability of steel structures: General report, *J. Constr. Steel Res.* 55 (2000) 159-81.

157. J.R. MacKay, Verification of numerical models for pressure hull collapse predictions (DRDC Atlantic TM 2011-281), Defence Research and Development Canada – Atlantic, Dartmouth, 2011.

158. B.K. Yuen, T. MacAdam, T.S. Koko, L. Jiang, The effect of general corrosion damage on the collapse strength of submarine pressure hulls (DRDC Atlantic CR 2011-158), Defence R&D Canada – Atlantic, Dartmouth, 2011.

159. L. Gannon, Submarine pressure hull collapse considering corrosion and penetrations (DRDC Atlantic TM 2010-246), Defence R&D Canada – Atlantic, Dartmouth, 2010.

Acknowledgements

First, I thank my PhD supervisor, Professor Fred van Keulen, for challenging me, for leading me down interesting paths, for his patience with the many professional and personal distractions that delayed the completion of my thesis, and for his friendship. Also, my professional managers at DRDC Atlantic, Dr. Neil Pegg and Dr. Malcolm Smith, for giving me the opportunity to pursue my doctorate, and for supporting and contributing to the research.

My doctoral research was part of a collaborative project of the Canadian Department of National Defence (DND) and the Netherlands Ministry of Defence. I am proud to be part of a long-standing naval architecture cooperation between Canada and the Netherlands. It is fitting that I am a Canadian student at a Dutch university, working on a project carried out in both countries. In DND, thanks is due to the submarine engineering directorate for providing research funding. Particularly, Mr. Jocelyn Turgeon, LCdr Helga Budden, and their predecessors at DND have been supportive of my work. In the Netherlands, funding was provided by the Defence Materiel Organisation (DMO). Individual thanks within DMO is due Mr. Adrian van der Made, who saw the value in the research.

I must also thank the co-authors of the papers that make up this thesis, for their professional and scholarly contributions, and for their permission to use the papers herein. In addition to Fred, Malcolm and Neil, whom I have already mentioned, my co-authors include Mr. Theo Bosman of TU Delft, Dr. Lei Jiang of Martec Limited in Canada, and Mr. André Glass of the Netherlands Organization for Applied Scientific Research (TNO). Theo deserves special recognition for his involvement in initiating, planning and carrying out the experiments in his previous careers at DMO and TNO.

Other colleagues who have helped with this research program include Mr. Wim Trouwborst and his staff at TNO, who oversaw the Dutch component of the collaboration. DRDC Atlantic technologists Mr. Alex Ritchie and Mr. Dave Wright were determined in their efforts to prepare, trouble-shoot and perform the collapse tests. Mr. Tom MacAdam and Mr. John Wallace supported the numerical modeling work at Martec Limited. Ms. Marianne Stolker at TU Delft provided essential and timely administrative support, and acted on my behalf while I was in Canada.

Finally, thanks are owed to my family and friends for their encouragement over the last seven years.

Acknowledgements

First, I thank my PhD supervisor, Professor Fred van Keulen, for challenging me, for leading me down interesting paths, for his patience with the many professional and personal distractions that delayed the completion of my thesis, and for his friendship. Also, my professional managers at DRDC Atlantic, Dr. Neil Pegg and Dr. Malcolm Smith, for giving me the opportunity to pursue my doctorate, and for supporting and contributing to the research.

My doctoral research was part of a collaborative program of the Canadian Department of National Defence (DND) and the Netherlands Ministry of Defence. I am proud to be part of a long-standing naval architecture cooperation between Canada and the Netherlands. It is fitting that I am a Canadian student at a Dutch university, working on a project carried out in both countries. In DND, thanks is due to the submarine engineering directorate for providing research funding. Particularly, Mr. Jocelyn Turgeon, LCdr Roger Madden, and their predecessors at DND have been supportive of my work. In the Netherlands, funding was provided by the Defence Materiel Organization (DMO). Individual thanks within DMO is due Mr. Adriaan van der Made, who saw the value in the research.

I must also thank the co-authors of the papers that make up this thesis, for their professional and scholarly contributions, and for their permission to use the papers herein. In addition to Fred, Malcolm and Neil, whom I have already mentioned, my co-authors include Mr. Theo Bosman of TU Delft, Dr. Lei Jiang of Martec Limited in Canada, and Mr. [illegible] of the Netherlands Organization for Applied Scientific Research (TNO). Theo deserves special recognition for his involvement in initiating, planning and carrying out the experiments in his previous careers at DMO and TNO.

Other colleagues who have helped with this research program include Mr. Wim Trouwborst and his staff at TNO, who oversaw the Dutch component of the investigation. DRDC Atlantic technologists Mr. Alex [illegible] and Mr. Dave Wright were [illegible] in their efforts to prepare, instrument and perform the collapse tests. Mr. Tom MacAdam and Mr. John Wallace supported the numerical modeling work at Martec Limited. Ms. Marianne Stolker at TU Delft provided essential and timely administrative support, and acted on my behalf while I was in Canada.

Finally, thanks are owed to my family and friends for their encouragement over the last seven years.

Curriculum vitae

John R. MacKay was born on November 20th, 1977 in Summerside, Prince Edward Island, Canada. He completed his secondary education in 1995, graduating from Kensington Intermediate Senior High, where he received the Canadian Governor General's bronze medal for academics.

John studied engineering at the University of New Brunswick and the Nova Scotia Agricultural College before completing his Bachelor of Engineering degree at Dalhousie University in Halifax, Nova Scotia, Canada in 2000. He specialized in civil engineering, and was awarded the Sexton Distinction (honours) upon graduation. His undergraduate thesis described the connection design for a one-tenth scale steel truss bridge that he designed, fabricated and tested with a team of four other students.

John continued studying civil engineering at Dalhousie University, obtaining his Masters of Applied Science degree in 2003. His masters research involved studying the creep behaviour of fibre-reinforced concrete. It also introduced him to experimental mechanics, a field that he would pursue further, although in a completely different context, while completing his doctoral research.

In 2003, John began his career as a defence scientist at Defence Research and Development Canada (DRDC) in Dartmouth, Nova Scotia. DRDC is the civilian research agency for the Canadian Department of National Defence and the Canadian Forces. In his role at DRDC, John performs theoretical, numerical and experimental research on the structural capacity and operational limits of naval submarines and ships.

In 2005-2006, DRDC granted John one year of leave to begin his doctoral studies at TU Delft. During that time, he lived in Delft, attending courses and working with his supervisor, Prof. Fred van Keulen, at the university. John returned to Canada in 2006, where he continued his doctoral studies part time while resuming his duties at DRDC. John's doctoral research was supported and funded by DRDC, DRDC's collaborative partners in the Netherlands Ministry of Defence, as well as the submarine engineering directorate within the Canadian Department of National Defence. He continues to work at DRDC, and lives in Dartmouth.

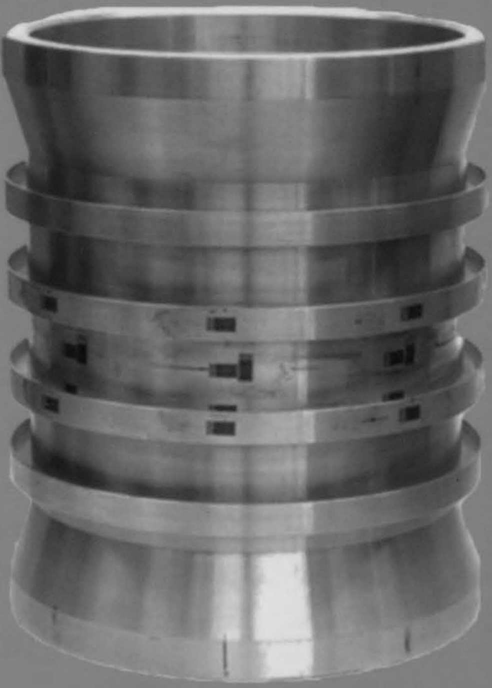

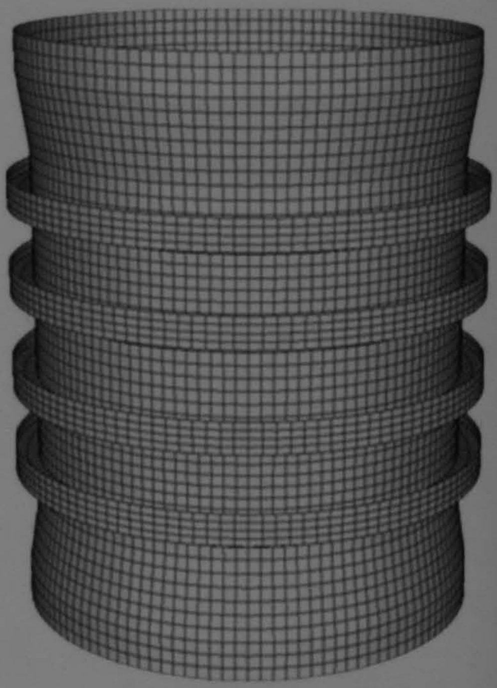

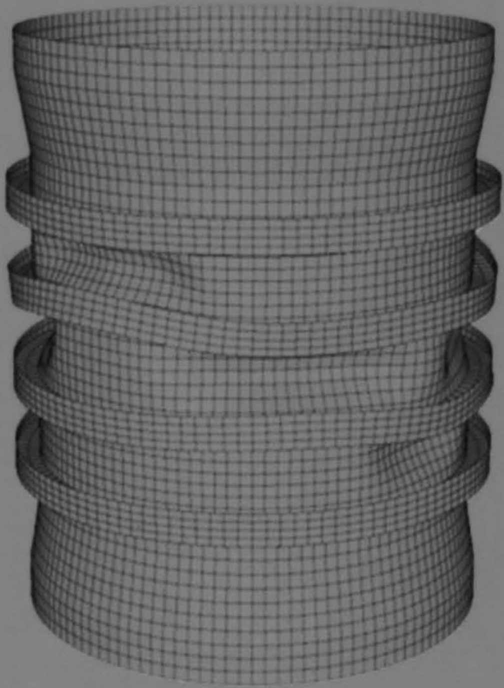

TU Delft Delft University of Technology